FEASIBILITY STUDY OF A SYNTHESIS PROCEDURE FOR ARRAY FEEDS TO IMPROVE RADIATION PERFORMANCE OF LARGE DISTORTED REFLECTOR ANTENNAS

Grant No. NAG-1-859

SEMIANNUAL STATUS REPORT

by

W. L. Stutzman
W. T. Smith

Virginia Polytechnic Institute and State University
Bradley Department of Electrical Engineering
Blacksburg, VA 24061

Virginia Tech Report
EE SATCOM 90-2

August, 1990

Table of Contents

1.0 INTRODUCTION

Surface errors on parabolic reflector antennas degrade the overall performance of the antenna. The errors are in the form of roughness on the surface, deviations of the mean surface from the true parabolic shape, or structural design details such as ribbing, slots between panels, etc.. They cause amplitude and phase errors in the aperture field which lower the gain, raise the side lobes, and fill in the nulls. These are major problems in large space reflector antenna systems. Planned mobile satellite communications systems having limited signal margin need high gain from the space reflectors. Future multiple beam antenna systems requiring spatial isolation to allow frequency reuse could be rendered useless if high side lobes are present. Planned remote sensing missions, such as Mission to Planet Earth and Global Change Technology Initiative, require high beam efficiencies. High side lobes are responsible for noise in remote sensing systems.

Space antenna structures are difficult to build, deploy and control. They must maintain a nearly perfect parabolic shape in a harsh environment and must be lightweight. The restrictions on the structure become more severe as science and technology requirements demand electrically large antennas. There are technologies for building antennas with mechanically adaptive surfaces that can compensate for many

of the larger distortions caused by thermal and gravitational forces. The NASA Hoop/Column 15-meter mesh reflector uses a series of cables to adjust the surface profile to have an error of less than 70 mils. However, as the frequency and size of the reflectors increase, the subtle surface errors become significant and degrade the overall radiation pattern. It is for this reason that another method must be used to further improve the radiation pattern.

Electromagnetic compensation for surface errors in large space reflector antennas can be used to supplement mechanical compensation. In order to implement electromagnetic compensation, some information about the reflector surface or the electromagnetic fields (focal region fields or the radiated far-fields) are required. If accurate surface data are available, the fields information can be computed using diffraction analysis.

Measurements of the necessary data for performing electromagnetic compensation are difficult to obtain. Current methods for accurate measurement of the reflector surface on earth include optical metrology [22] and microwave holography metrology [35]. There are many methods for measuring the radiated far-fields on earth. A technique for determining the far-fields of a space reflector using a free flying probe has been proposed. [44] Recently, focal region field data were measured using the array feed system. [43]

Electromagnetic compensation for surface errors in large space reflector antennas has been the topic of several research studies. Most of these studies try to correct the focal plane fields of the reflector near the focal point and, hence, compensate for the distortions of the over the whole radiation pattern. The compensation is implemented by weighting the elements of an array feed. Of course, perfect compensation would require a very large array. In most of the studies, a precise knowledge of the reflector surface is required (surface shape and the first and second derivatives). At the present,

this approach works on earth but the sensing of the surface errors in space is an especially difficult problem.

An alternative approach to electromagnetic compensation is presented in this study. The proposed technique uses pattern synthesis to compensate for the surface errors. It differs from previous methods in two major respects. First, the previous studies used a global algorithm that tries to correct the entire focal plane field near the focal point and modify the entire radiation pattern. The new pattern synthesis approach uses a localized algorithm in which pattern corrections are directed specifically towards portions of the pattern requiring improvement. The second major difference is that the pattern synthesis technique does not require knowledge of the reflector surface. It uses radiation pattern data to perform the compensation.

Chapters 2 and 3 of this report contain necessary background information required to implement the pattern synthesis compensation technique and discuss past electromagnetic compensation studies. In Section 2.1 the effects of different types of surface errors are analyzed. The information on the effects of surface errors helps to define what types of distorted reflector patterns can be improved with electromagnetic means. Section 2.2 provides insight into what happens to the focal plane fields when the reflector is distorted and scanned. This information is necessary when trying to design an array feed that sufficiently samples the focal plane fields. Section 2.3 reviews past electromagnetic compensation efforts. The kinds of reflector data required to implement the techniques are outlined and the limitations of the methods are noted.

Chapter 3 contains background information on reflector scanning techniques. This information was separated from the discussion in Ch. 2 to emphasize the importance of reflector scanning to the pattern synthesis compensation technique. Section 3.1 evaluates scanning of a reflector by displacing the feed. Section 3.2 examines electronic scanning of a reflector with an array feed. Section 3.3 deals with dual reflector scanning.

All of the above scanning techniques were used to implement the pattern synthesis compensation technique (see Ch. 6).

Chapter 4 presents the pattern synthesis compensation technique algorithm. The technique is based on the iterative sampling method (ISM). In Section 4.1, the ISM is formulated to apply to reflector antennas. Section 4.2 discusses the compensation algorithm and its limitations.

New and existing computer codes were used to analyze reflector scanning and implement the pattern synthesis compensation technique. Chapter 5 contains algorithm descriptions. Section 5.1 discusses the Reflector Analysis Program for Cylindrical Antennas (RAPCA). RAPCA is an infinite cylindrical prime focus reflector code. Patterns with single or array feeds can be computed. The SCANned Reflector Analysis Program (SCANRAP) is discussed in Section 5.2. SCANRAP is used to determine the array feed excitations for electronic scanning of infinite cylindrical prime focus reflector antennas. The SCANRAP excitations are fed into RAPCA to calculate the electronically scanned pattern. The Dual Reflector Analysis Program for Cylindrical Antennas (DRAPCA) is capable of analyzing infinite cylindrical dual reflector antennas with symmetric or offset geometries and single or array feeds. Section 5.3 presents the theory behind the dual reflector analysis and describes the problem geometry. The Reflector Analysis Program (RAP), Version 2.0, is an existing prime focus paraboloidal reflector code. RAP analyzes single feed reflectors with axisymmetric or offset geometries. It was also used to analyze paraboloidal reflectors with array feeds by generating patterns for the individual elements and then superposing the patterns. RAP is outlined in Section 5.4.

The results of this study are contained in Chapter 6. Section 6.1 presents various reflector scanning techniques that are used to implement the pattern synthesis compensation technique. Particular attention is paid to the main beam characteristics

of distorted reflectors. Sections 6.2, 6.3, and 6.4 present several compensation problems for infinite cylindrical prime focus reflectors, prime focus paraboloidal reflectors, and infinite cylindrical dual reflectors, respectively.

From the results in Chapter 6, the pattern synthesis compensation technique was shown to be a feasible method to compensate for pattern irregularities in distorted reflector antennas. The summary and conclusions of this study are presented in Chapter 7.

2.0 REFLECTOR SURFACE ERRORS AND COMPENSATION TECHNIQUES

Surface errors on parabolic reflector antennas degrade the overall performance of the antenna. The errors are in the form of roughness on the surface, deviation of the mean surface from the true parabolic shape, or structural design details (such as ribbing, slots between panels, etc.). They cause amplitude and phase errors in the aperture field which lower the gain, raise the side lobes, and fill in the nulls. These are major problems in large space reflector antenna systems. Planned mobile satellite communications systems having limited signal margin need high gain from the space reflectors. Future multiple beam antenna systems requiring spatial isolation to allow frequency reuse could be rendered useless if high side lobes are present. High side lobes are also responsible for noise. This is especially troublesome for radiometric systems such as in remote sensing applications.

Methods for reducing the distortion of the aperture fields due to reflector surface roughness include:

Direct (mechanical adjustment)

Indirect (electromagnetic compensation)

Hybrid (a combination of both)

Mechanical means of correction for surface roughness typically involves first the sensing of the surface shape and then an adjustment of the main reflector structure to bring it back into shape at selected points. This approach may work well on earth but is difficult in space. Sensing of surface errors is especially difficult in space. Also mechanical correction devices such as motor actuators add weight and complexity to the antenna.

Electromagnetic compensation has been investigated for nearly twenty years. Most methods try to correct the amplitude and phase errors in the aperture field. The majority of work in electromagnetic compensation for distorted reflectors involves the method of conjugate field match (CFM). The CFM method has also been used to scan the main beam of reflectors (Sec. 3.2). The technique uses a multi-element feed array to compensate for amplitude and phase errors in the focal plane field distribution caused by a distorted reflector surface.

Previous investigations into surface error types found in large space reflectors are reviewed in Sec. 2.1. Both random and deterministic errors are discussed. The effects of surface errors and scanning on the focal region fields are evaluated in Sec. 2.2. To perform compensation with an array feed, one needs to adequately sample the focal region fields. Feed location and array feed geometries depend on the distribution of the fields. Section 2.3 is devoted to CFM and other related compensation techniques. The theory behind the previous compensation methods is important when comparing them to the technique proposed in this effort.

2.1 REFLECTOR SURFACE ERRORS

2.1.1 RANDOM SURFACE ERRORS

The available theories concerning random surface errors treat reflectors with rough surfaces (i.e. the surface is not perfectly smooth) using statistical characterizations of the effects of the random errors. Expressions for the gain, SLL, etc. are derived in a "mean" sense.

EARLY WORK FOR UNIFORM AMPLITUDE APERTURES

Perhaps the most referenced work on the topic was written by Ruze. [29] The paper deals with gain reduction due to scattering. Two important results are an expression for the gain of a rough reflector and the frequency dependence of that gain. The expressions are valid for surfaces with small correlation intervals. [30] The aperture illumination is assumed nearly constant over distances on the order of the correlation length. The gain of a rough reflector, G , is given by [29]

$$G \approx G_0 e^{-\overline{\delta}^2} \tag{2.1-1}$$

where G_0 is the gain of the corresponding perfectly smooth reflector given by [29]

$$G_0 = \eta\left(\frac{\pi D}{\lambda}\right)^2 \tag{2.1-2}$$

where η is the aperture efficiency of the reflector, D is the diameter of the aperture, and λ is the wavelength. The exponent in (2.1-1) is [19]

$$\bar{\delta}^2 = \left(\frac{4\pi\kappa\varepsilon}{\lambda}\right)^2 \tag{2.1-3}$$

where ε is the rms surface error. An approximate rule is that the rms error is about one-third of the peak deviation. The factor κ depends on the reflector geometry and is approximately [19]

$$\kappa \approx \frac{4F}{D}\sqrt{\ln[1 + 1/(4F/D)^2]} \tag{2.1-4}$$

where F is the focal length of the reflector. For large F/D ratios, κ is nearly unity, and using (2.1-2) and (2.1-3) in (2.1-1) gives the classic result for a circular aperture [29]

$$G \approx \eta\left(\frac{\pi D}{\lambda}\right)^2 e^{-(4\pi\varepsilon/\lambda)^2} \quad \textit{for large } F/D \ . \tag{2.1-5}$$

This expression shows the expected result that the gain of a rough reflector ($\varepsilon > 0$) is lower than that of a smooth reflector ($\varepsilon = 0$).

The frequency dependence of the gain of a rough reflector may be found from (2.1-5) (assuming a constant η). Initially the gain G increases with increasing frequency (decreasing wavelength). For a certain wavelength λ_{max}, the effects of the surface errors (the negative exponential term) cause the gain to begin to decrease with further frequency increase due to the roughness. The wavelength at which maximum gain occurs (based on (2.1-5)) is [29]

$$\lambda_{max} = 4\pi\varepsilon \tag{2.1-6}$$

and the corresponding maximum gain value is approximately [29]

$$G_{max} \approx \frac{\eta}{43}\left(\frac{D}{\varepsilon}\right)^2 \quad . \tag{2.1-7}$$

TAPERED APERTURE DISTRIBUTION RESULTS

Rahmat-Samii developed a model based on work by Ruze and others that evaluates the average power pattern degradations caused by random surface errors. [30] The model is somewhat more general than Ruze's in that it can handle tapered aperture amplitude distributions and non-uniform rms distortions. The geometry of the model is shown in Fig. 2.1-1. It is assumed that the rms surface error is known in each annular region. The aperture field amplitude distribution is assumed to be of the parabola on a pedestal shape: [30]

$$Q(\rho') = B + C\left(1 - \frac{\rho'^2}{a^2}\right)^p \tag{2.1-8}$$

where $B + C = 1$, a is the radius of the aperture, and $p = 1$ or 2 . The parameter p is used to control the shape of the aperture distribution.

Some important conclusions from Rahmat-Samii's work concern the gain loss and the side lobe degradation. The gain loss correction factor κ in (2.1-4) was computed for different F/D ratios and different edge tapers as a function of ε/λ . The results are plotted in Fig. 2.1-2. The general trend shows that as the F/D decreases, so does κ. Decreasing κ means that the surface errors have decreasing impact on the gain loss of the antenna. It was also found in the study that κ is relatively insensitive to variations in edge taper for given F/D and ε/λ. [30]

Representative plots for side lobe level increase and main beam peak loss versus surface roughness are shown in Fig. 2.1-3. The general trend is for the side lobe levels

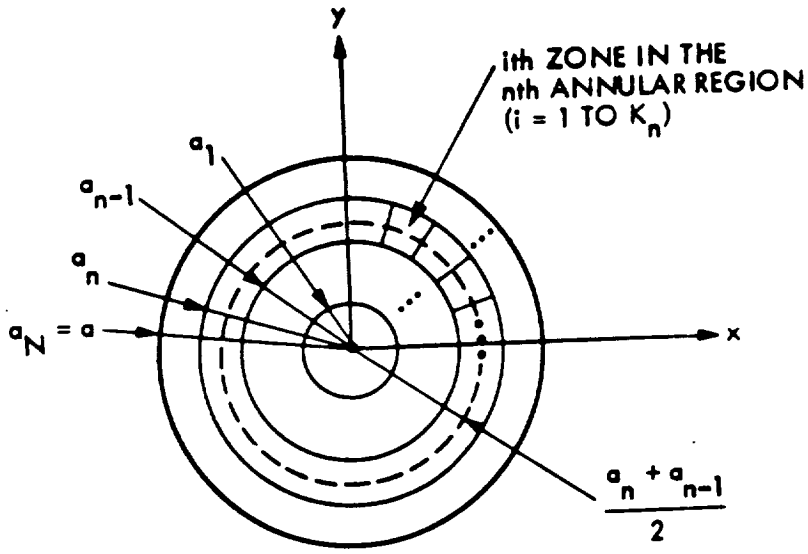

Figure 2.1-1. Reflector geometry model showing the aperture divided into N annular rings. The annular rings are subdivided into K_n zones in the nth ring ($n = 1 \text{ to } N$). [30]

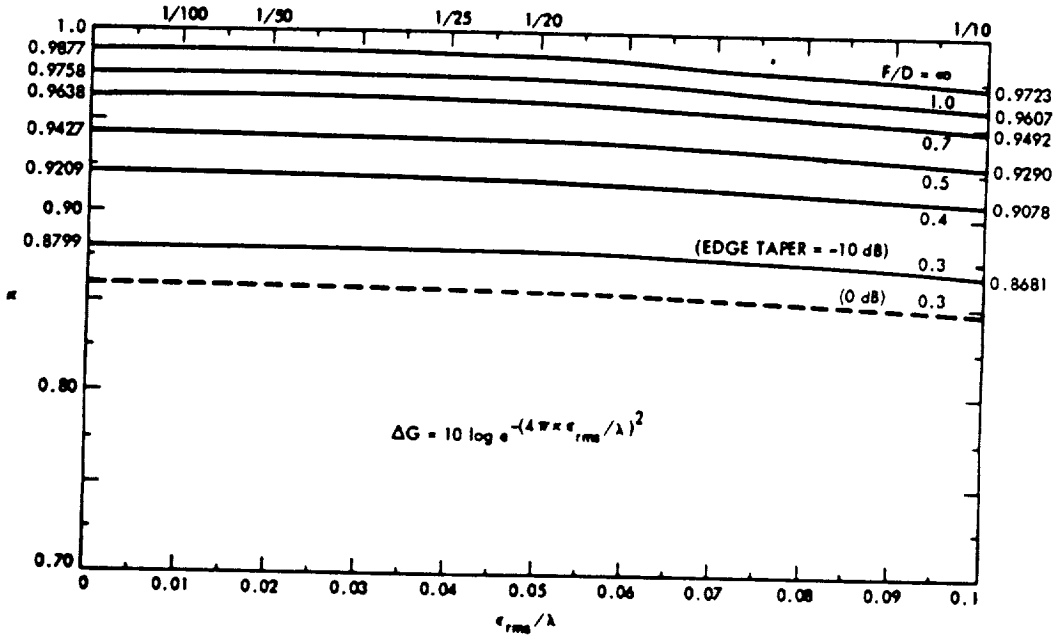

Figure 2.1-2. Plots of the correction factor κ as a function of surface roughness for various F/D values. [30]

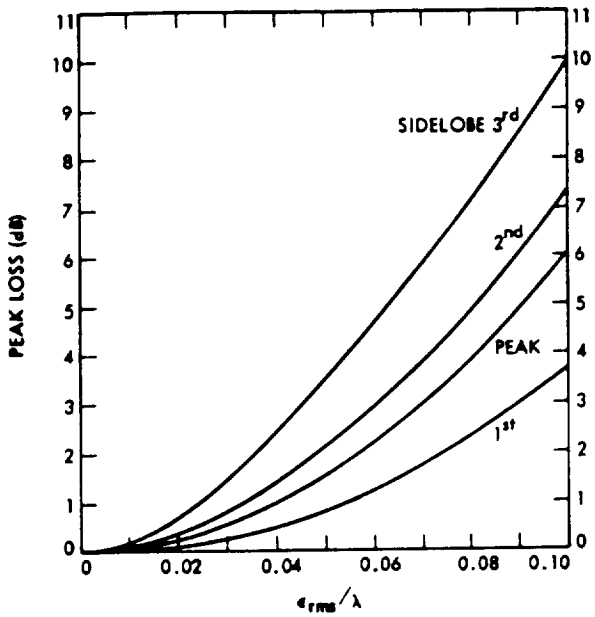

(a)

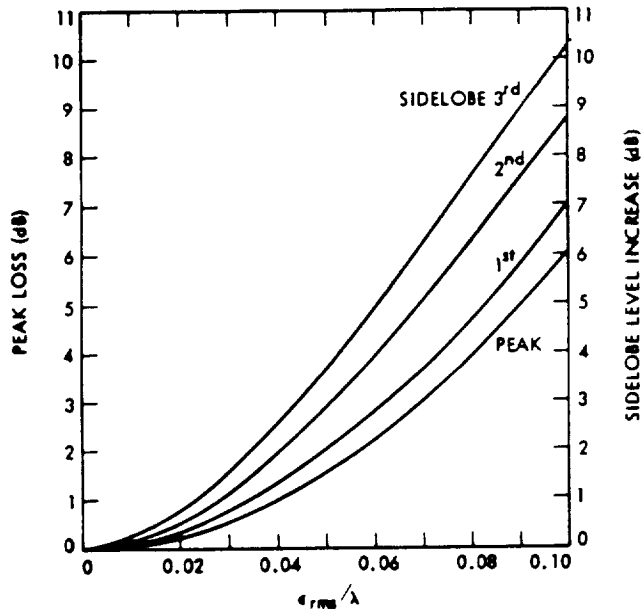

(b)

Figure 2.1-3. Peak gain loss and side lobe level increase as a function of surface errors (ET = – 10dB, F/D = 0.7). (a) P = 1. The levels of the first, second, and third side lobes for the undistorted case are -22.32, -29.35, and -33.83 dB, respectively. (b) P = 2. The levels of the first, second, and third side lobes for the undistorted case are -27.06, -30.83, and -33.85 dB, respectively. [30]

and peak loss to increase as ε/λ increases. An important design consideration from the study is that as the no-error side lobe level decreases, its dependence on the surface ε/λ increases, requiring much smaller ε/λ to maintain the low side lobes. We can also extract a rule of thumb from these plots. The threshold for loss of about 0.5 dB or less and a side lobe degradation of about 1 dB is an rms surface error of $0.05\lambda = \lambda/20$. Larger errors give rapidly decaying performance.

GENERAL ROUGH SURFACE EFFECTS ON THE RADIATION PATTERN

Shifrin presented some very detailed statistical analyses of random phase errors in the aperture. [45] The aperture amplitude distribution is assumed to be uniform in the absence of errors. The statistics of the errors are assumed to be Gaussian and stationary. The mean and variances are constant across the aperture.

Shifrin showed that the presence of phase errors results in smoothing of the radiation pattern. The nulls fill in and the main beam decreases. As the variance of the phase errors increases, a progressive change in the radiation pattern occurs. The pattern changes from an oscillating function to a monotonically decreasing function and the power radiated in the principal direction decreases (the directive properties approach that of an isotropic radiator [45]). As the correlation distance, c, of the phase errors increases across the aperture, the radiation pattern approaches that of a system without errors. [45] For small correlation distance c, the reduction in gain is caused by an increase in side lobe level. [45] Finally, for large correlation distance (as with thermal distortions or ribbed construction techniques), the reduction in gain is caused by an increase in the beamwidth. [45]

2.1.2 RADIAL SURFACE ERRORS

Deterministic surface errors are discussed in Sect's. 2.1.2, 2.1.3, and 2.1.4. The discussion deals mainly with deterministic errors that are periodic.

Dragone and Hogg [9] presented an interesting theory on how phase errors affect the radiation patterns of aperture antennas by using a Fourier series expansion of the phase error. We will present a brief treatment of their approach and findings. Consider a circular aperture shown in Fig. 2.1-4 with an aperture field distribution [9]

$$f(\rho) = [1 - \alpha(2\rho/D)^2]e^{j\psi(\rho)} \tag{2.1-9}$$

where α is the amplitude of a square law taper, ρ is the radial variable, D is the diameter of the aperture, and $\psi(\rho)$ is the phase error (assumed to be a function of radius only). The radiation pattern for this aperture distribution is [9]

$$g(u, \phi) = \frac{D^2}{4} \int_0^{2\pi} \int_0^1 (1 - r^2\alpha) r e^{j\psi(r)} e^{jur\cos(\phi - \phi')} dr\, d\phi' \tag{2.1-10}$$

where $u = (\pi D/\lambda) \sin\theta$ and $r = 2\rho/D$ and ψ is now expressed as a function of r. Upon integrating with respect to ϕ', the expression becomes [9]

$$g(u) = \frac{\pi D}{2} \int_0^1 (1 - r^2\alpha) r e^{j\psi(r)} J_0(ur)\, dr \quad . \tag{2.1-11}$$

If $\psi(r) = 0$ the pattern for no phase error results and it is given by [9]

$$g(u) = 2(1 - \alpha)\frac{J_1(u)}{u} + 4\alpha\frac{J_2(u)}{u^2} \quad . \tag{2.1-12}$$

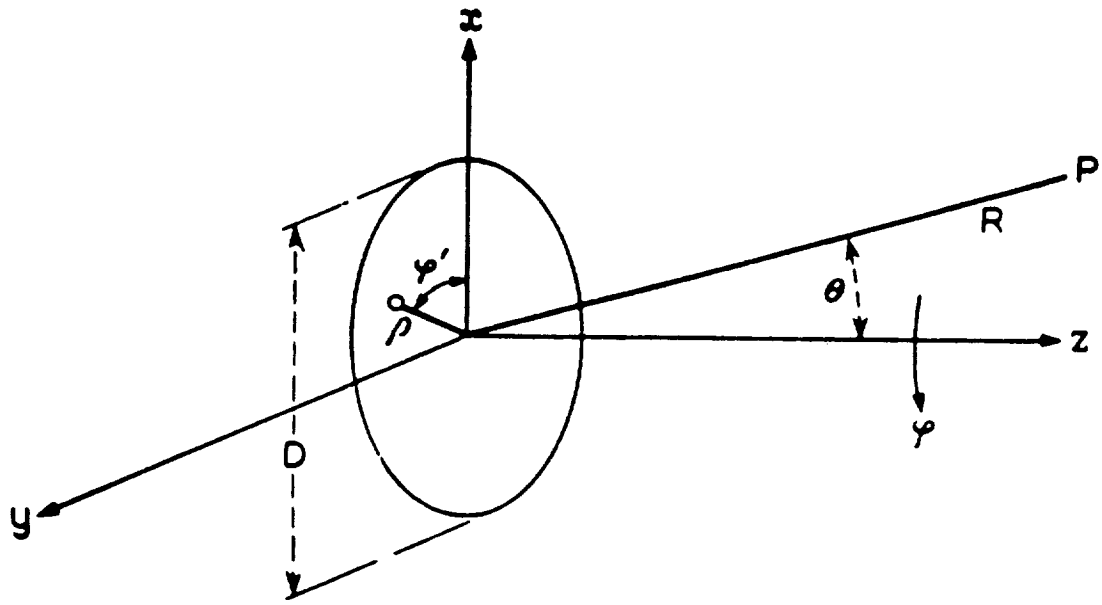

Figure 2.1-4. Circular aperture and the coordinate system. [9]

Figure 2.1-5(a) shows this pattern for $\alpha = 0.684$ which corresponds to a -10 dB edge taper.

For $\psi(r) \neq 0$, $\psi(r)$ could be expanded into a trigonometric Fourier series. First consider a single term of a Fourier series [9]:

$$\psi(r) = \Phi_m \cos(2\pi m r) \tag{2.1-13}$$

where Φ_m is the magnitude of the sinusoidal phase error and m is the number of periods along the aperture radius. The cases for $m = 6$ and $m = 12$ with $\Phi_m = 2\pi/16$ were computed and the radiation patterns are shown in Fig. 2.1-5(b),(c). The patterns show that a sinusoidal phase error causes a large rise in the side lobe level only over a small angular region. The angle where the region is located increases with an increasing number of fluctuations and the amplitude of the rise is dependent on Φ_m. [9] The effects on gain loss as a function of the correlation length of random surface errors (Sec. 2.1.1) can be related to the period of the radial surface error. For the longer period radial surface errors, the gain loss is caused mainly by increasing beamwidth. For the shorter period radial surface errors, the gain loss is caused mainly by increased side lobe level.

Dragone and Hogg related the angular location of the disturbed region in the radiation pattern to the number of periods of the phase error. The angular location of the high side lobe region θ_h is given by the grating formula [9]

$$\sin(\theta_h) = \pm \frac{2m}{n_0} \tag{2.1-14}$$

where $n_0 = D/\lambda$.

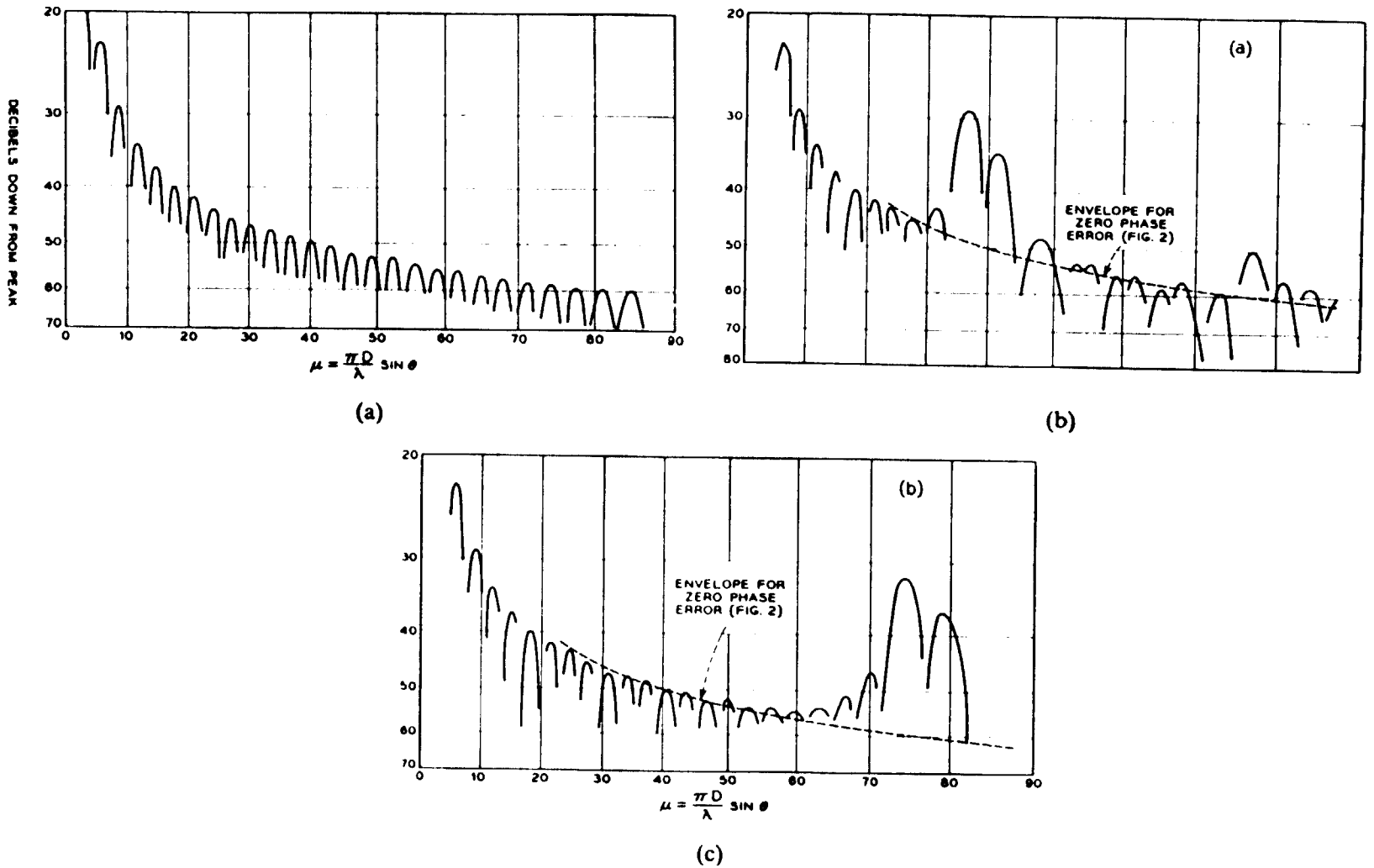

Figure 2.1-5. Radiation patterns of a circular aperture with a -10 dB ET. (a) No error. (b) $\lambda/8$ peak-to-peak sinusoidal phase error with 6 periods along the radius. (c) $\lambda/8$ peak-to-peak sinusoidal phase error with 12 periods along the radius.

2.1.3 AZIMUTHAL SURFACE ERRORS

Azimuthal surface errors arise in large space reflectors primarily from the structural design. A radial rib reflector is an example of a design that gives rise to surface errors that are periodic in an azimuthal direction. The azimuthal surface error for the radial rib reflector gives rise to a periodic scalloped phase error. This scalloped phase error function is sometimes described by the term "pillowing". Analysis for axisymmetric reflectors is presented in this section. Offset radial rib reflectors have also been studied and it was found that they exhibited the same behavior as axisymmetric radial rib reflectors. [18, 28]

Modeling the Radial Rib Reflector

An often used model for the axisymmetric radial rib reflector was presented by Ingerson and Wong. [14] The ribs of the axisymmetric radial rib reflector lie on a parent paraboloid of focal length f_r . The gores between the ribs are modeled as parabolic cylinders of focal length f_g. The f_r and f_g are related by

$$f_r = \frac{f_g}{\cos^2(\pi/N_g)} \tag{2.1-15}$$

where N_g is the number of ribs. The projection of the reflector and the geometry defining a gore are shown in Fig. 2.1-6. The intersection of any plane containing the z-axis and the gores on opposite sides of the reflector define a set of parabolas whose focal lengths, f_c, lie in a continuous distribution; and $f_r \le f_c \le f_g$. [14] The optimum feed location in this distribution was found to be [14]

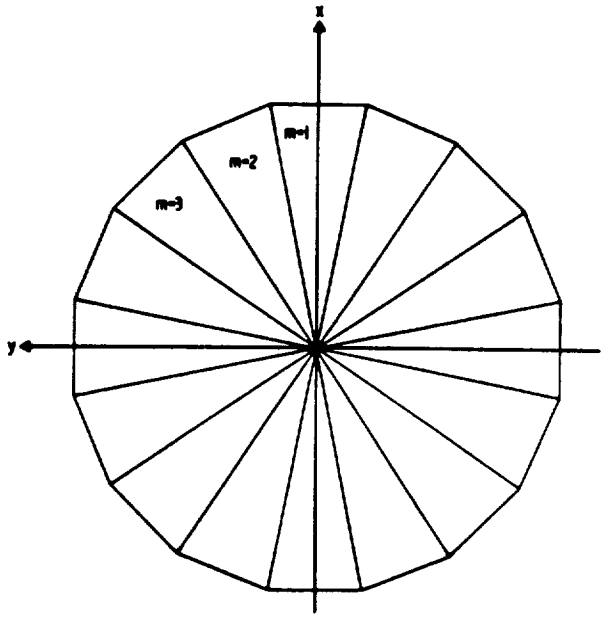

(a)

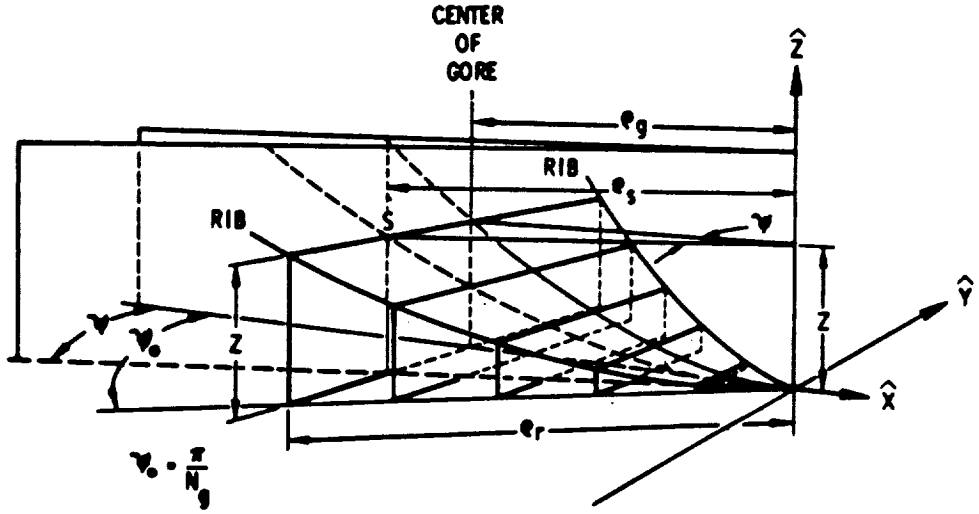

(b)

Figure 2.1-6. The model for an axisymmetric radial rib reflector. (a) The projected aperture of the reflector. (b) The geometry of a gore. [14]

$$f_S \approx f_r \left(1 - \frac{2}{3}\frac{\pi^2}{N_g^2}\right) \tag{2.1-16}$$

where f_S is the distance the feed is from the vertex of the reflector. A later study showed that this formula is good for reflectors up to 60 wavelengths in diameter and that a better feed position can be found which optimizes the boresight gain for larger reflectors. [27]

The azimuthally periodic surface errors caused by the gore model of Ingerson and Wong give the radiation pattern for an axisymmetric radial rib reflector some interesting characteristics. Figure 2.1-7(a) shows the radiation pattern for two "equivalent" reflectors. One is a 100λ diameter smooth paraboloid with $F/D = 0.4$. The other is a 100λ wavelength diameter radial rib reflector with the parent paraboloid of the ribs having $F/D = 0.4$. The feed pattern was chosen to be $\cos^n\theta$ such that the edge taper was -10 dB. The two cuts for the radial rib reflector correspond to the center of the gore ($\phi = 0°$) and a quarter of a way along the gore ($\phi = 5.625°$). The main beam broadened for the radial rib reflector. The effects of the surface errors on the side lobe structure consisted of reducing up to the first eight side lobes and producing a large side lobe envelope further out. The large envelope for far-out side lobes is due to the surface errors exciting pattern expansion terms with Bessel functions J_n of order $n = N_s,\ 2N_s$. [27] Figure 2.1-7(b) shows a computed cross-polar radiation pattern. The effects of the surface errors degrade the pattern somewhat, but the peak cross-pol level still depends mainly on the feed cross-pol level. [27]

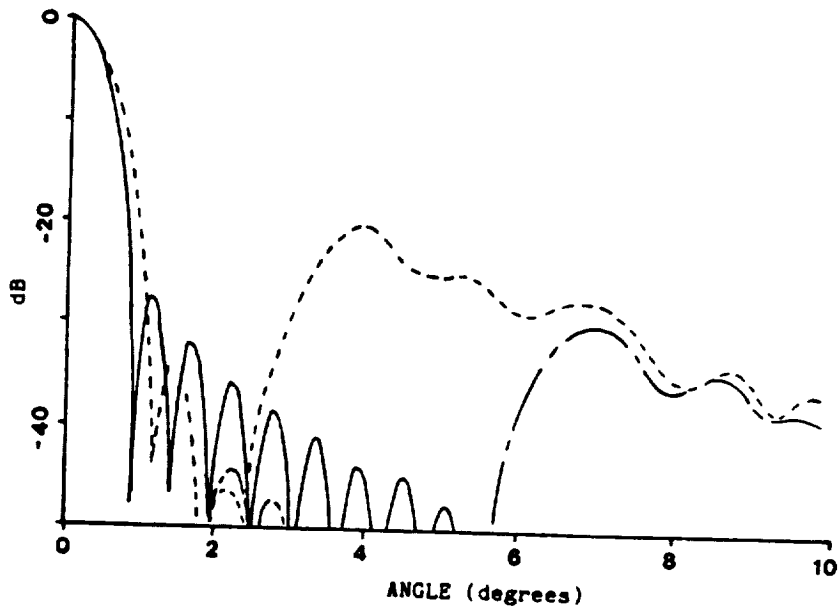

(a)

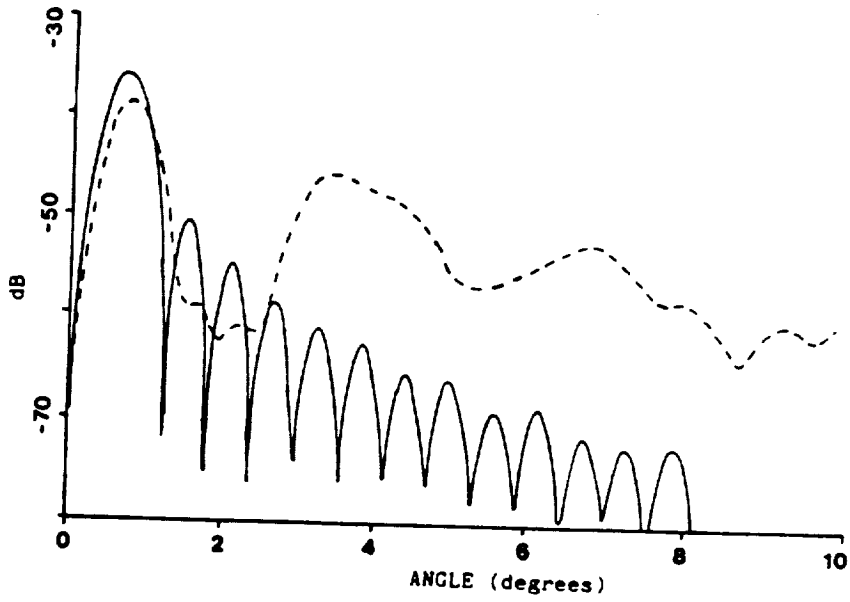

(b)

Figure 2.1-7. Radiation patterns for 100 wavelength diameter reflectors with $F/D = 0.4$ for a smooth paraboloid (solid line) and a ribbed reflector (16 gores) for $\phi = 0°$ (uniformly dashed line) and for $\phi = 5.625°$ (dot-dash line). (a) Copolar pattern. (b) Cross-polar pattern. [27]

PARAMETRIC STUDY OF THE EFFECTS OF THE AZIMUTHAL ERRORS CAUSED BY THE RADIAL RIB REFLECTOR

A parametric study was performed by Olver and Lizius to determine the influence of the electrical and geometrical parameters of a radial rib reflector on the radiation pattern. [27] They found that as the number of ribs increases (for a fixed diameter reflector), the phase errors created by the gores decrease and the radiation pattern tends toward that of a smooth reflector (the surface is approaching that of a smooth reflector). For a fixed number of ribs, as the reflector diameter decreases, the efficiency tends toward that of a smooth reflector, the beamwidth normalized to diameter becomes narrower, the first few side lobes increase, and the gore related side lobe structure decreases. The efficiency of radial rib reflectors was found to be relatively insensitive to variation in the edge taper. This is due to the largest phase errors caused by the gore surface occurring toward the edge where the feed illumination is the lowest and the suppression of the first few side lobes which are normally affected by the edge illumination. Greater distortion from the surface errors occur in reflectors with low F/D ratios and as F/D increases, the pattern tends toward that of a smooth reflector. It was also found that the scanning performance of a reflector using lateral feed displacement is nearly identical to that of a smooth reflector with equivalent dimensions (the analysis was for lateral displacements up to 10 wavelengths).

2.1.4 RADIAL AND AZIMUTHAL SURFACE ERRORS

A reflector structure that gives rise to both radial and azimuthal surface errors is the cross-catenary umbrella reflector. [10] The gore surface is supported by a series of

the points anchored to cross-catenaries between ribs (see Fig. 2.1-8). The gore surface consists of rectangular and trapezoidal warped, ruled facets instead of a triangular section of a parabolic cylinder. The corners of the facets lie on the parent paraboloid of the ribs. This antenna more closely approximates the parent paraboloid than does a radial rib reflector. The tie-point related (azimuthal error) side lobes are generally less significant than those from the radial rib reflectors. [10]

For a symmetrically illuminated cross-catenary umbrella reflector, approximate analysis predicts the grating lobes caused by the surface errors are located at [10]

$$\theta_c \approx \frac{180 m_c \lambda}{\pi \Delta_c} \ ^\circ, m_c = 1, \ 2, \ 3, \ \ldots \tag{2.1-17}$$

for the catenary spacing, Δ_c, and [10]

$$\theta_t \approx \frac{180 m_t \lambda}{\pi \Delta_t} \ ^\circ, m_t = 1, \ 2, \ 3, \ \ldots \tag{2.1-18}$$

for the tie-point spacing, Δ_t.

2.1.5 SUMMARY OF SURFACE ERROR EFFECTS

Section 2.1 reviewed works that deal with how surface errors affect the radiation patterns of reflector antennas. The surface errors give rise to amplitude and phase errors in the aperture plane. For relatively small surface errors the amplitude error effects are minimal. The major effects are caused by the phase errors. Surface errors produce:

- Gain loss

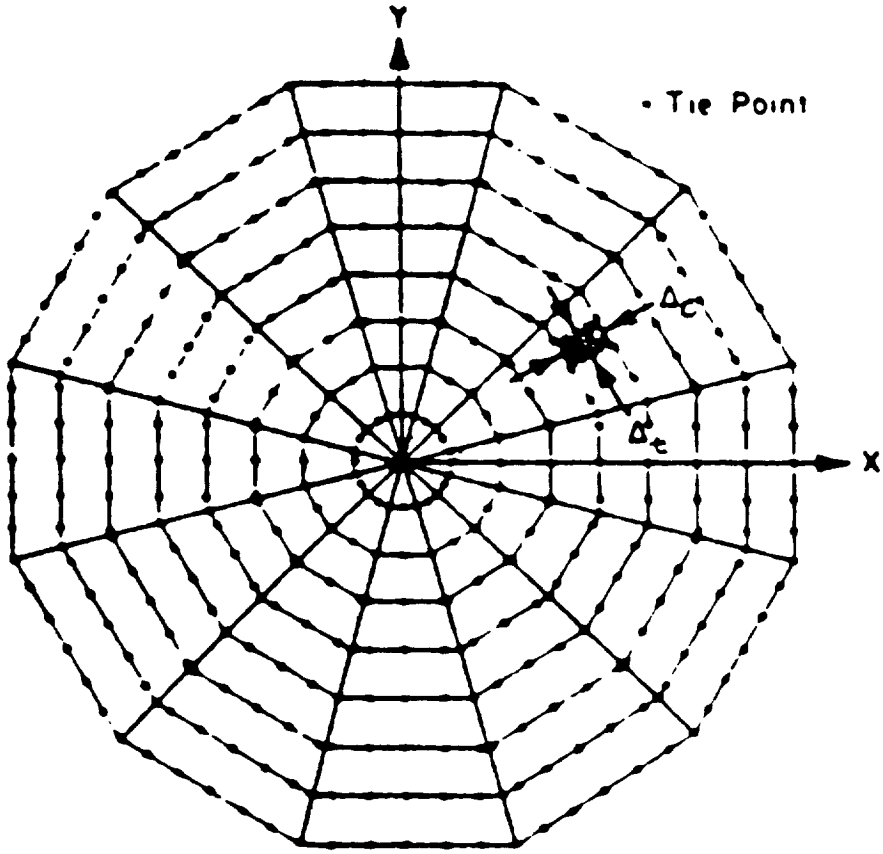

Figure 2.1-8. Geometry of the cross-catenary umbrella reflector. [10]

- Null filling

- Increased side lobe levels

There are two traits that are common to the analyses of the different types of errors in the previous four sections (Sec.'s 2.1.1, 2.1.2, 2.1.3, and 2.1.4):

- As the surface error amplitude increases, the gain loss and side lobes increase.

- As the spatial period (correlation length) decreases, the angular location of the region where high side lobes are produced moves farther away from the main beam.

2.2 *FOCAL REGION FIELDS*

Focal region fields are discussed in this section. Knowledge of the focal region fields and the focal plane distribution (FPD) is essential in understanding the compensation techniques reviewed in Section 2.3 and the scanning theory of Chapter 3. (Note: The terms "focal plane distribution" and "focal plane fields" refer to the fields produced in the plane containing the focal point of the reflector on reception. The term "aperture plane fields" refers to the fields produced in the plane containing the focal point on transmission.) The plots presented in this Section provide insight into how the energy is distributed in the focal region due to rough surface distortion or scanning the reflector. This insight is used to determine the size of the array feed and the element spacing required to capture the scattered energy and coherently combine it to improve the radiation characteristics of the antenna.

The analyses presented in this section assume that the focal plane fields are caused by the physical optics currents induced on the reflectors by an incident plane wave. For large reflectors (focal length and diameter much greater than a wavelength), the FPD may be computed to very good approximation using the P.O. currents out to tens of wavelengths from the focal point. [58] Farther out, the field contributions from secondary currents (currents from one part of the reflector that are induced by radiation from other parts of the reflector) and those arising from the finite size of the reflector must be taken into account. [58] The compensation and scanning techniques discussed in this study are not concerned with these focal plane fields far removed from the focus and the physical optics approximation is considered to be valid.

2.2.1 FOCAL REGION ANALYSIS OF SMOOTH AND ROUGH REFLECTORS

Geometrical optics analysis of a smooth parabolic reflector predicts that the rays of a normally incident plane wave focus to a point, the focal point. This approach is exact as the antenna becomes very large in terms of a wavelength and performs quite well for optical devices. For radio frequency antennas, though, diffraction theory is required for accurate evaluation of the distribution of energy in the focal plane. [31]

AXISYMMETRIC REFLECTORS

Rudge and Davies [31] presented the double Fourier transform compensation technique for a cylindrical reflector (singly curved) with a rectangular aperture. The

coordinate system is shown in Fig. 2.2-1 (Note: The angle and distance variables are defined in the Fig. 2.2-1. The circle in the figure is located in the aperture plane. The circle does not indicate the perimeter of the reflector). In that paper, expressions for the one-dimensional FPD derived using scalar diffraction theory were presented. Assuming that the incident uniform amplitude, uniform phase plane wave was arriving along the antenna boresight, the 1-D FPD was found to be [31]

$$E(x) \simeq 2\hat{p}\,\frac{\sin kx\hat{p}}{kx\hat{p}} \quad , \quad \hat{p} < 0.5 \tag{2.2-1}$$

and [31]

$$E(x) = \pi J_0(kx) \quad , \quad \hat{p} = 1.0 \tag{2.2-2}$$

where $\hat{p}$ is the maximum value of $p = \sin\theta\cos\phi$ which occurs at the reflector rim. Figure 2.2-2 shows some plots of (2.2-1) and (2.2-2).

Rudge and Davies investigated the effects of periodically and randomly distributed errors on the cylindrical reflector. The small reflector surface errors they considered were evaluated as effective phase errors in the aperture distribution. Assuming a periodic phase error of [31]

$$\beta_e(p) = \hat{\beta}_e \cos\left(\frac{N\pi p}{\hat{p}}\right) \tag{2.2-3}$$

where $\hat{\beta}_e$ is the maximum amplitude of the phase error and N is the number of periods of the error across the aperture. The FPD was found to be [31]

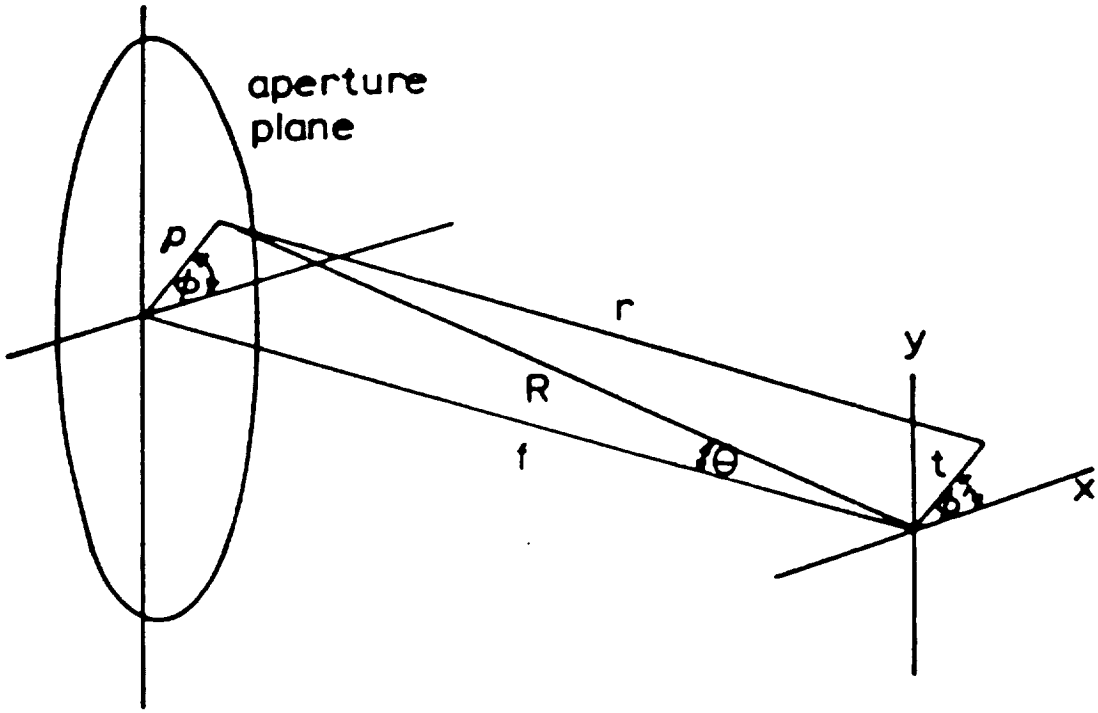

Figure 2.2-1. Coordinate system for the FPD analysis of Rudge and Davies. (Note: the circle in this figure is located in the aperture plane. The circle does not indicate the perimeter of the reflector). [31]

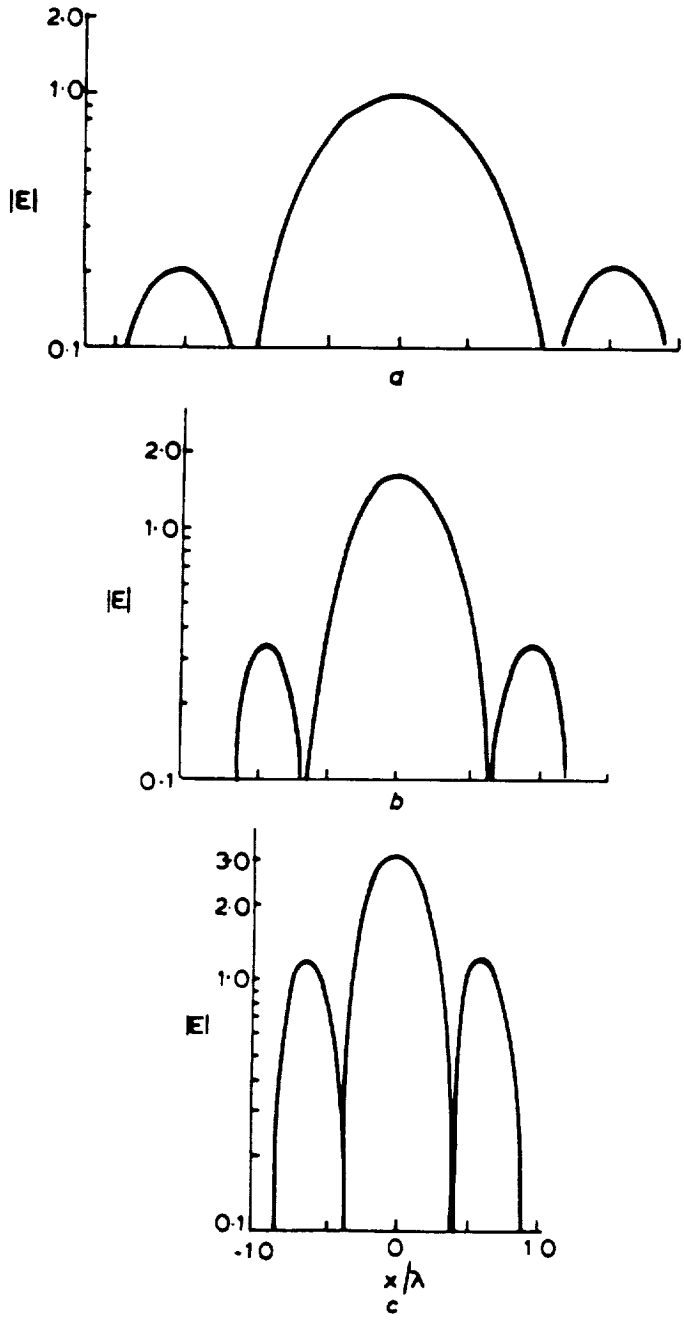

Figure 2.2-2. Focal plane distributions for reflectors with (a) $F/D = 1.0$, (b) $F/D = 0.5$, and (c) $F/D = 0.25$. [31]

$$E(x) = 2\hat{p}\left[J_0(\hat{\beta}_e)\frac{\sin s}{s} + \sum_{n=0}^{\infty} j^n J_n(\hat{\beta}_e) \right.$$

$$\left. \left\{ \frac{\sin(s + nN\pi)}{s + nN\pi} + \frac{\sin(s - nN\pi)}{s - nN\pi} \right\} \right], \quad \hat{p} < 0.5 \tag{2.2-4}$$

and

$$E(x) = \pi\left[J_0(\hat{\beta}_e)(s) + \sum_{n=0}^{\infty} j^n J_n(\hat{\beta}_e)\{J_0(s + nN\pi) + J_0(s - nN\pi)\} \right], \quad \hat{p} = 1.0 \tag{2.2-5}$$

where $s = k\hat{p}x$. The effect of the periodic phase error is to reduce the undistorted FPD and redistribute the energy in a series of grating lobes. An example of an FPD with periodic phase errors is shown in Fig. 2.2-3(a). Rudge and Davies also performed some analysis with random surface errors. Figure 2.2-3(b) demonstrates the effect of random phase errors by showing the mean FPD envelopes for a reflector with the surface rms error shown versus an undistorted reflector FPD.

Rudge and Davies made some important conclusions from their analysis. For reflectors with $F/D > 0.5$, there exists a direct Fourier transform relationship between the aperture plane field on transmission and the focal plane distribution on reception. There also exists a direct Fourier transform relationship between the aperture plane field and the radiation pattern of the reflector on transmission. "The focal-plane field distribution and that of the antenna radiation pattern are therefore identical, being related by a double Fourier transformation." [31] This approximate relationship is exploited in several compensation papers to be discussed in Section 2.3. Using this relationship and knowing the effects of reflector surface errors on the radiation pattern (see Section 2.1.5) Rudge and Davies were able to make the following conclusions [31]: Reflector errors

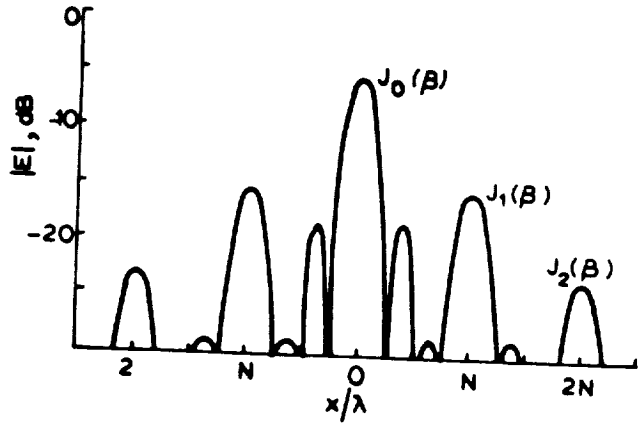

(a)

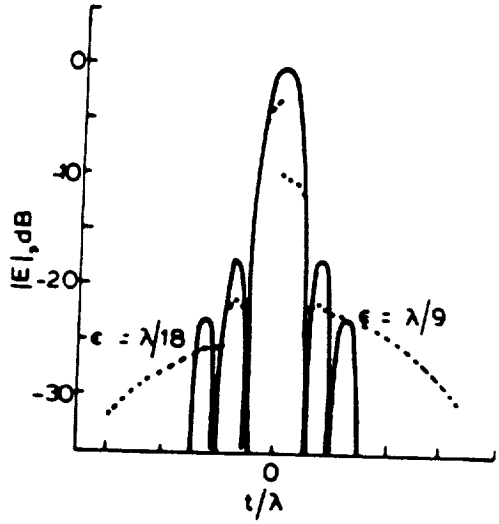

(b)

Figure 2.2-3. (a) The focal plane distribution for a reflector with a periodic phase error. (b) The mean focal plane distribution envelopes for a reflector with random surface errors. [31]

with long spatial periods cause errors in the radiation pattern near the main beam and, hence, (using the above relationship) cause errors in the FPD near the focal point. Errors with short spatial periods cause errors in the radiation pattern in regions far from the main beam and, hence, cause errors in the FPD in regions removed from the focal point.

Blank and Imbriale [4] presented a compensation and beamsteering technique for circular paraboloidal reflectors. They included analysis of the FPD to provide insight into the effects of surface distortions and beamsteering. The focal plane distribution analysis is similar to Rudge and Davies [31] but they extended it to two dimensions. The reflector geometry is shown in Fig. 2.2-4(a). For an incident plane wave, a smooth parabolic reflector with $F/D > 1.0$, the FPD is [4]

$$E(r, \phi') \approx 2\pi(\hat{u})^2 \frac{J_1(kr\hat{u})}{kr\hat{u}} \tag{2.2-6}$$

where $\hat{u} = \sin\hat{\psi}$ and $\hat{\psi}$ is defined in Fig. 2.2-4(a). The FPD for a smooth reflector is plotted in Fig 2.2-4(b). For distorted reflector analysis, an approximation to a gravity-induced distortion was chosen. The reflector is assumed to have a distortion profile of [4]

$$\Delta z = \epsilon \rho^s \cos(L\zeta) \tag{2.2-7}$$

where ϵ is the amplitude of the surface error, s is a real number, ρ is the normalized distance from the z-axis to a point on the reflector normalized to the reflector radius, L is the integer number of periods in the distortion, and ζ is the azimuth angle in the aperture. The FPD for a distorted reflector is shown in Fig. 2.2-5. The spreading of the energy away from the focal point is easily seen in these plots.

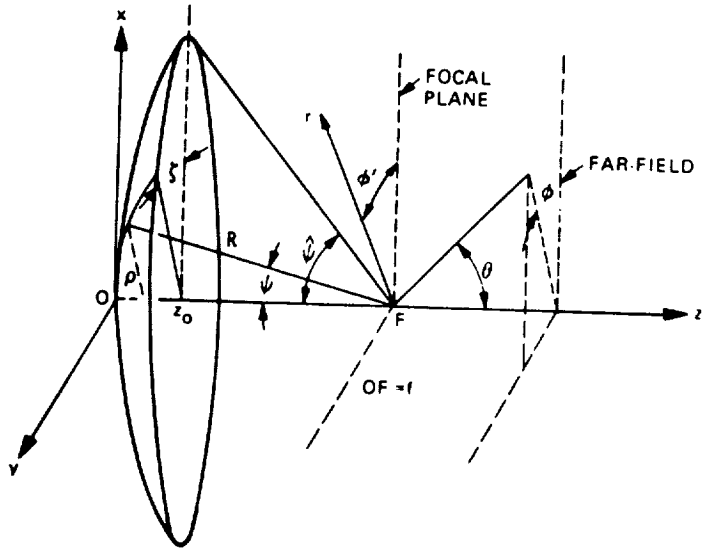

(a)

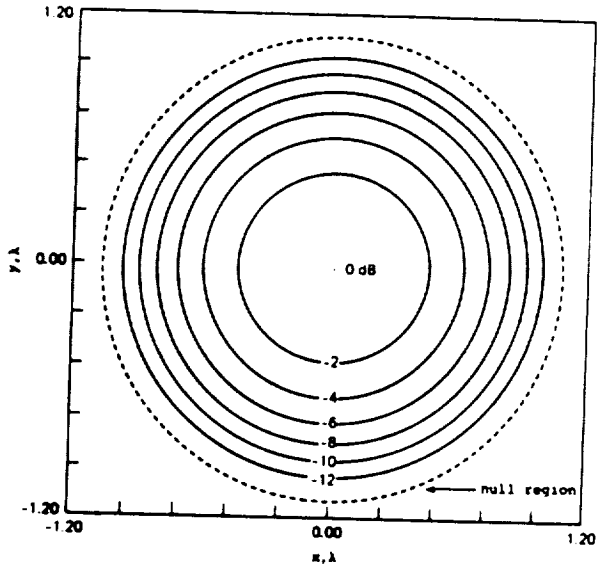

(b)

Figure 2.2-4. (a) The reflector geometry of Blank and Imbriale. (b) Focal plane distribution for a smooth reflector with $F/D = 1.0$. [7]

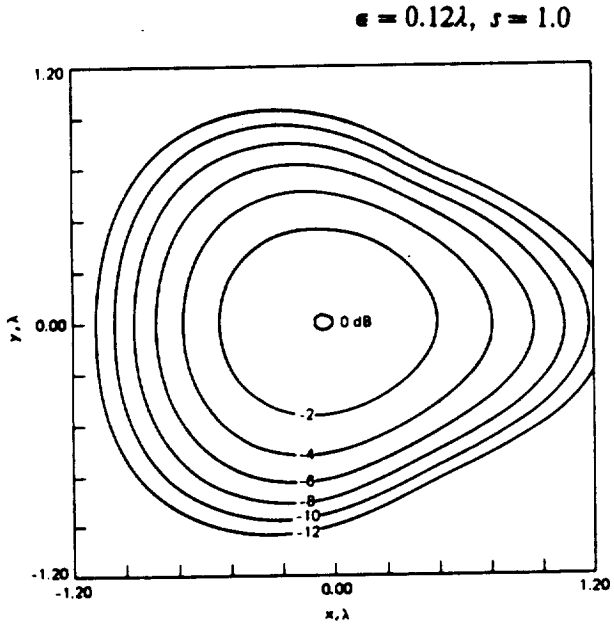

(a)

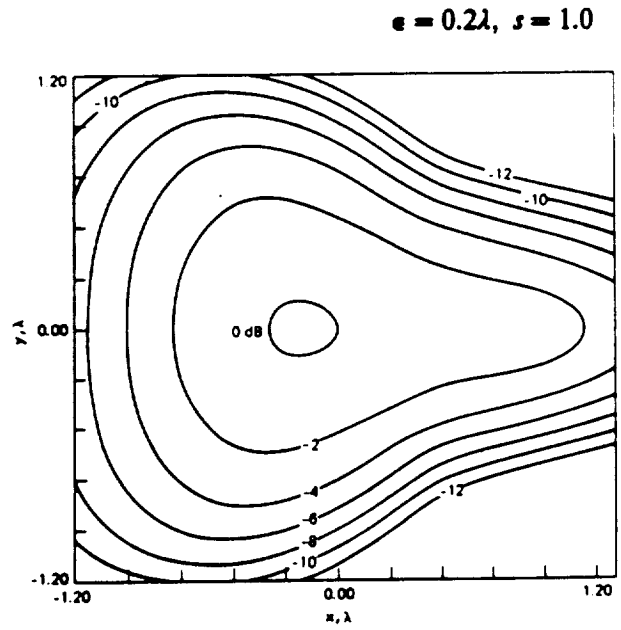

(b)

Figure 2.2-5. Focal plane distributions for a rough reflector with $L = 3$ and the ϵ and s indicated. [7]

OFFSET REFLECTORS

Bem [5] analyzed the focal region field of an offset parabolic reflector. A very important result from his study is that the focal plane fields of an offset reflector of equivalent focal length f' (f' is the distance from the focal point to the reflector surface along the z-axis) are nearly the same as the fields for an axisymmetric reflector with the same focal length $f = f'$. [5]

2.2.2 FOCAL REGION ANALYSIS OF A SCANNED REFLECTOR

Scanning a reflector is implemented by moving the feed away from the focal point or by weighting and possibly moving a phased array feed. The location of the feed or the weighting of the elements of the phased array feed are found through some process that involves a knowledge of the focal region fields when receiving a plane wave incident from the desired scan angle.

SCANNED FOCAL REGION FIELDS, SMOOTH REFLECTOR

Rusch and Ludwig [32] studied the scanning of two paraboloidal antennas with diameters of 34 and 68 wavelengths. The main purpose of the paper was to determine the maximum scan-gain contours and to relate them to the Petzval surface. They presented a plot of the amplitude and phase contours of the focal region fields in the plane of scan (see Fig. 2.2-6) The equiphase contours are separated in phase by 180 electrical degrees. The plots are shown for the cases of reception of a plane wave on-axis and for the angles of 8° and 16° to the right of the reflector axis. For on-axis reception,

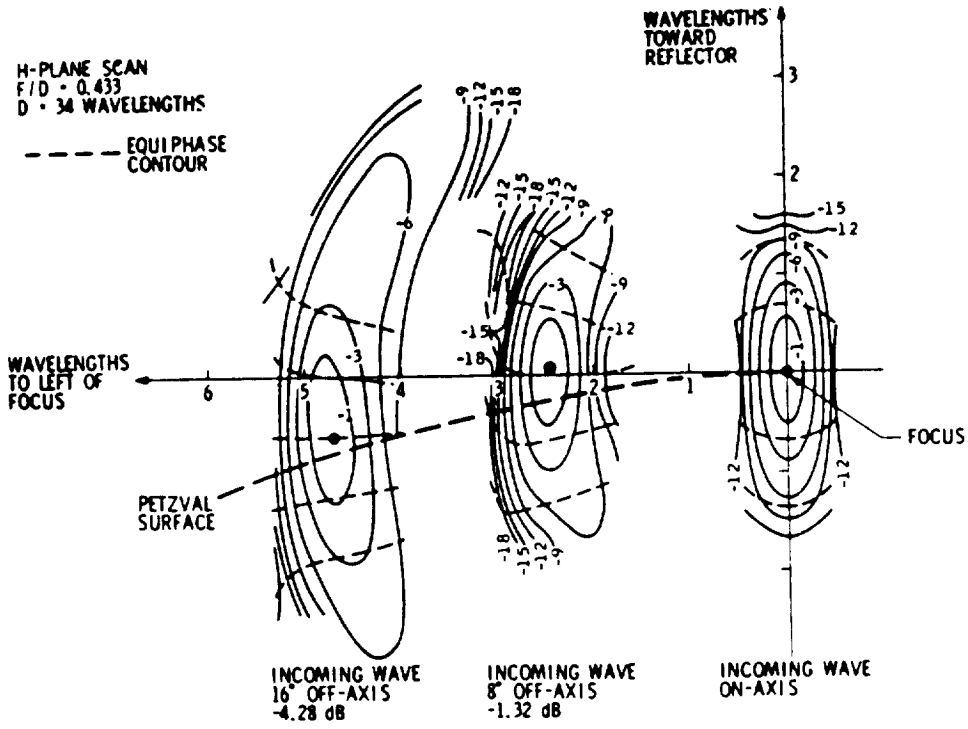

Figure 2.2-6. Amplitude and phase contours of the focal region fields in the plane-of-scan. The scanned plots are for a plane wave incident from the right of the reflector axis. [32]

the maximum focal region field intensity is, as expected, at the focal point. As the scan is increased to the right, the point of maximum field intensity moves to the left of the focal point and eventually away from the reflector. The maximum field intensity decreases as the scan angle is increased. The energy in the focal region is spreading out with increasing scan angle.

Hung and Mittra also presented some focal region field contour plots in their paper on wide-angle scanning. [12] They used the plots to determine the location and element spacing of a feed array used to give improved scanning characteristics. The analysis was performed on a 360 inch reflector with $F/D = 0.48$ at the frequencies f= 18 and 2 GHz. The reflector was scanned at angles $\theta_{SCAN} = 2.5$ and 5°.

The coordinate system used by Hung and Mittra is shown in Fig. 2.2-7. The amplitude contour plots are shown in Figs. 2.2-8 and 2.2-9. Figure 2.2-8 shows the focal region field distribution in the plane of scan while Fig. 2.2-9 shows the focal region fields in planes that are parallel to the focal plane. As expected, the energy spreads out with increasing scan.

SCANNED FOCAL REGION FIELDS, ROUGH REFLECTOR

Blank and Imbriale [4] further illustrated the dispersion of the energy in the focal plane by plotting the FPD for a scanned, rough reflector. The surface error of (2.2-7) was used with $s = 1.0$, $L = 3$, and a scan of approximately half of a beamwidth. The FPD plots for their smooth and rough reflector are shown in Fig. 2.2-10. Comparing to the plot for $\epsilon = 0.12\lambda$ from Fig. 2.2-5, the FPD is seen to be even more distorted than that for a smooth reflector.

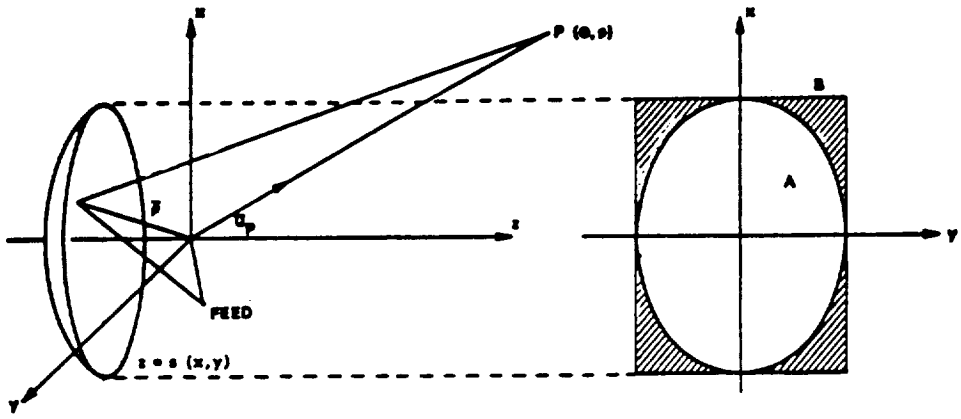

Figure 2.2-7. The reflector geometry for Hung and Mittra's analysis. [12]

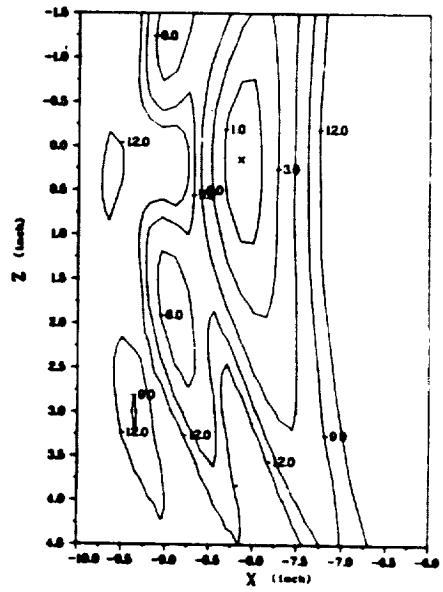

(a)

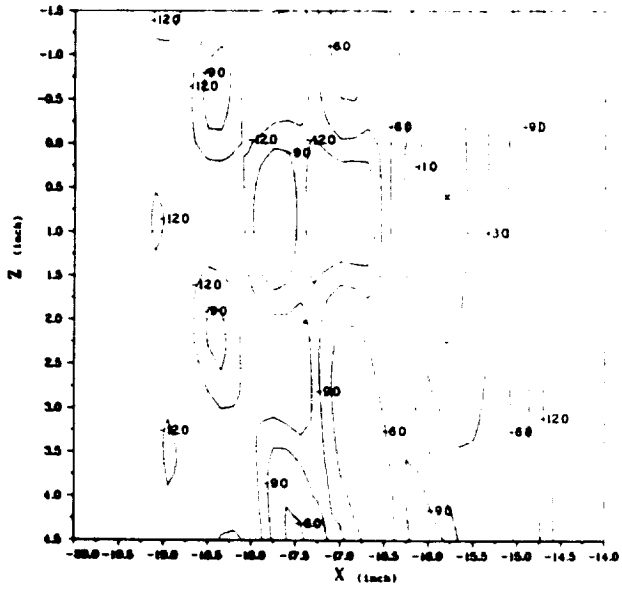

(b)

Figure 2.2-8. Focal region distribution in the plane of scan for 18 GHz case. (a) Incoming wave from 2.5° (24 beamwidths). (b) Incoming wave from 5.0° (48 beamwidths). [12]

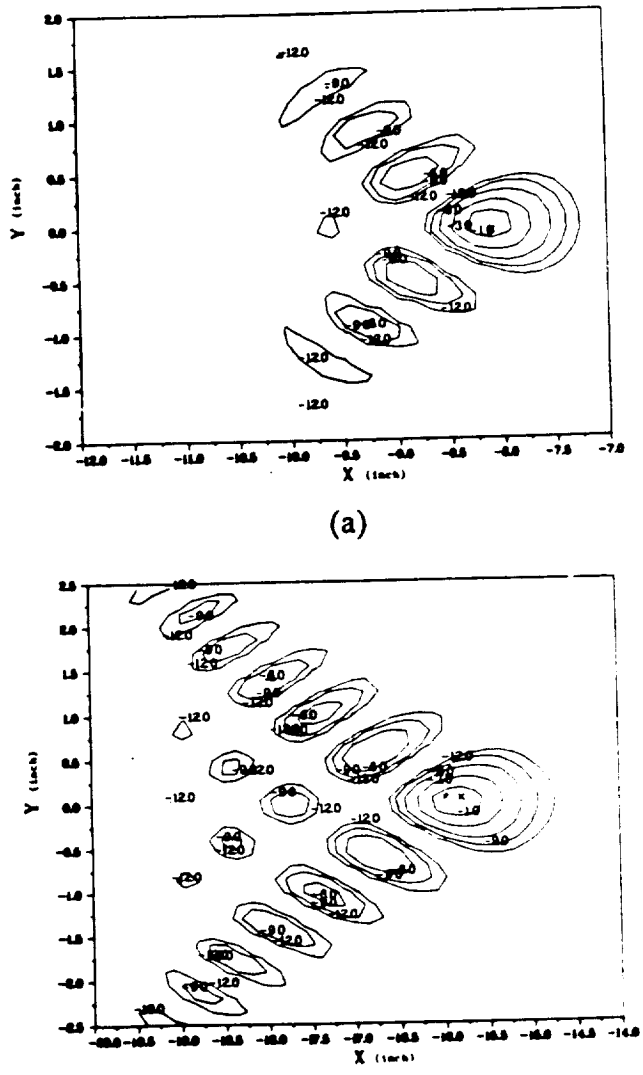

Figure 2.2-9. Focal region distribution in planes parallel to the focal plane for the 18 GHz case. (a) Incoming wave from 2.5°, z = 0.15 inches. (b) Incoming wave from 5.0°, z = 0.6 inches. [12]

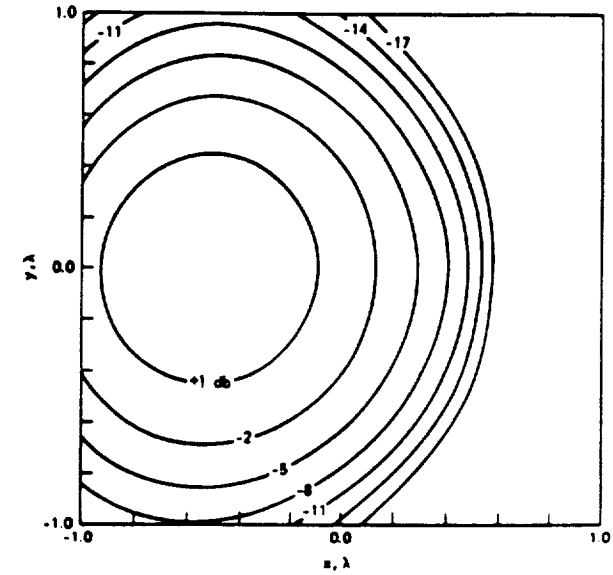

(a)

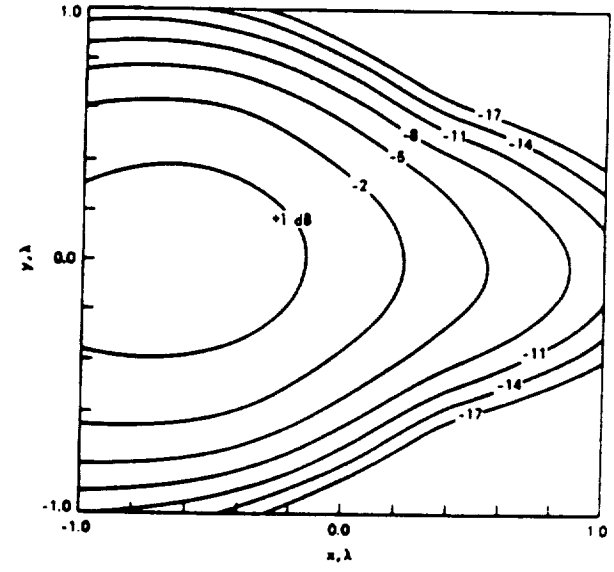

(b)

Figure 2.2-10. Focal plane distributions for scanned (a) smooth and (b) rough reflectors. The distortion profile is that of (2.2-7) with $s = 1$ and $L = 3$. [7]

2.3 PAST ELECTROMAGNETIC COMPENSATION TECHNIQUES

In this section available electromagnetic compensation methods are reviewed. Computational and experimental techniques are presented. All the computational techniques require accurate knowledge of the reflector surface while the experimental techniques do not.

2.3.1 DOUBLE FOURIER TRANSFORM TECHNIQUE

Rudge and Davies wrote one of the earliest and most referenced papers on electromagnetic compensation for surface errors. [31] It followed a work by Davies [11] where techniques for electronic compensation of surface errors were proposed. Rudge and Davies' technique exploits the Fourier transform relationships between the aperture field distribution and the radiation pattern on transmission and the aperture field distribution and the focal plane fields on reception. They showed that the function for the focal plane fields on reception is very similar to the function for the far-field radiation pattern for reflectors fed from the focus with $F/D > 0.5$ [31]

Rudge and Davies' compensation solution requires taking a second spatial Fourier transform (the first being the Fourier transform of the received aperture field by the main reflector to get the focal plane fields) on the signals received by a multiple feed array (see Fig. 2.3-1). The signals produced at the output of the Fourier transforming device correspond directly to the aperture field distribution. [31] If a plane wave is

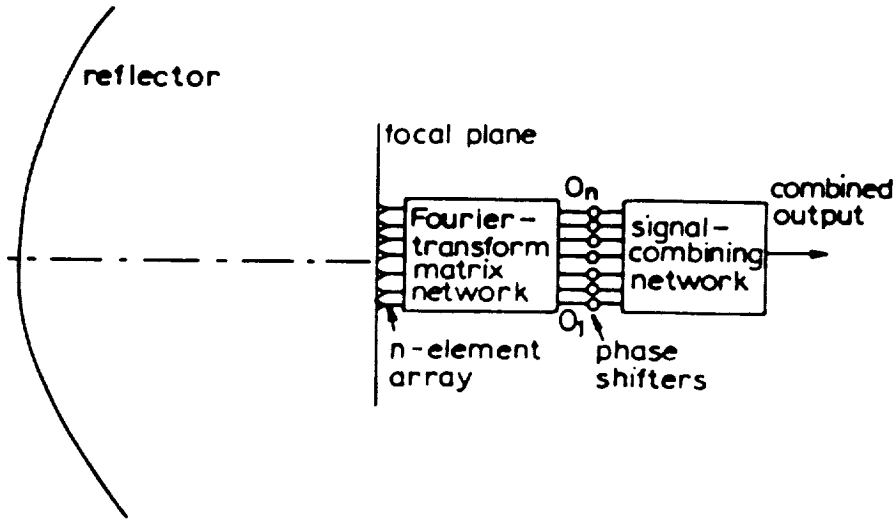

Figure 2.3-1. Feed system for implementation of Rudge and Davies' surface error compensation technique. [31]

incident from boresight, the focal plane distribution for a smooth parabolic cylinder at the input of the Fourier transforming device looks something like a "$\sin x/x$" function. For a smooth reflector, the output signals of the transforming device are uniform in amplitude and phase. For a distorted reflector, the signals are nearly uniform in amplitude and the deviation from constant phase is due to the surface errors. Compensating for the surface errors is performed by measuring the phase at the output of the Fourier transforming network and coherently combining the signals using phase shifters ($O_1 - O_n$ in Fig. 2.3-1). [31]

The initial implementation of Rudge and Davies' compensation method was restricted to one dimension. This allowed the compensation technique to be experimentally implemented via a Butler matrix. The Butler matrix is a device that consists of a matrix of fixed phase shifters and couplers (which are lossless in ideal form) whose output is a sampled spatial Fourier transform of the field distribution applied across the input. [31] Fig. 2.3-2(a) shows an example of the sampled Fourier transform of a hypothetical focal plane distribution. Practical implementation of this feed system requires using a feed array that is small enough to prevent blockage problems. Therefore the only kinds of surface errors this method (and all methods) can compensate for are ones which have slowly changing variations across the reflector surface (giving rise to focal plane errors near the focus, see Sec. 2.2.1). Even though the focal plane field is sampled with a finite aperture, it gives a good approximation to the infinite Fourier transform when the focal plane distribution decay is steep enough. [31]

The Butler matrix feed system with adjustable phase shifters was used in an experiment with a variable-profile parabolic cylinder reflector with $F/D = 0.5$. A second Butler matrix was used as the combining network. The output signal was taken off the port of the second Butler matrix that had maximum output (see Fig. 2.3-2(b) for a schematic of the feed network). The optimum spacing, δ_0 , of the elements is [31]

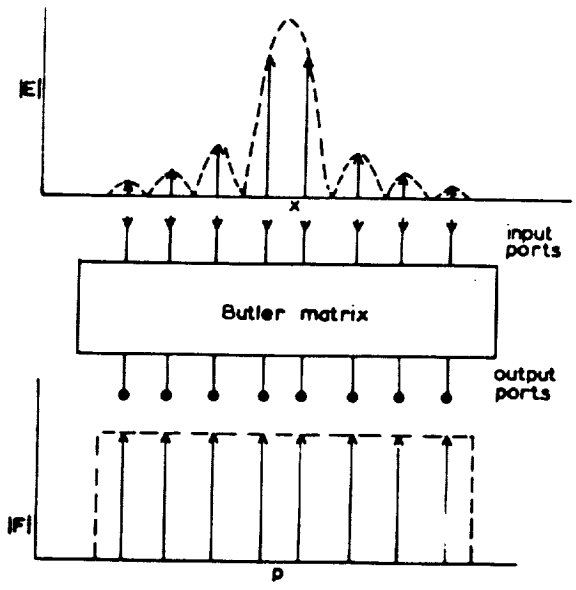

(a)

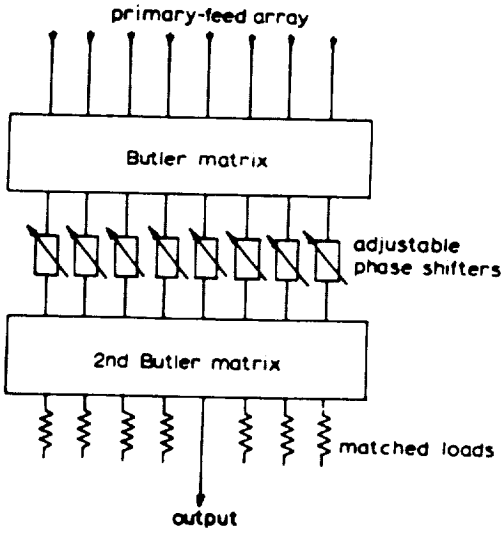

(b)

Figure 2.3-2. (a) Sampled Fourier transform implemented by a Butler matrix. $|E|$ represents the value of the focal plane field at the input of the matrix. $|F|$ represents the corresponding output of the matrix. (b) Schematic diagram for Rudge and Davies' experimental 8-element array feed system. The top Butler matrix takes the Fourier transform of the focal plane distribution. The phase shifters are used to coherently phase the output signals of the matrix. The second Butler matrix is used to recombine the coherent signals. [31]

$$\delta_0 = \frac{\lambda}{2\hat{u}} \tag{2.3-1}$$

where $\hat{u} = \sin\hat{\theta}$ and $\hat{\theta}$ is the angle between the parabola axis the ray from the focus to the reflector edge. This is the maximum separation of the feed array elements which prevents grating lobes from occurring in the angular region subtended by the reflector. [31] The variable-profile reflector built by Rudge and Davies is capable of imposing a phase error, β_e, in the aperture of [31]

$$\beta_e(p) = \hat{\beta}_e \cos\left(\frac{N\pi p}{\hat{p}}\right) \tag{2.3-2}$$

where $\hat{\beta}_e$ is the amplitude of the phase error, N is the number of periods of the phase error across the aperture, $p = \sin\theta\cos\phi$ (see Fig. 2.2-1), and $\hat{p}$ is the maximum value of p at the reflector rim.

The results of experiments using the feed system to compensate for phase errors are shown in Fig. 2.3-3 for the three cases of a smooth and two distorted cylindrical reflectors. The reflectors had $F/D = 0.5$, $D = 180$cm at 10 GHz. Compensation was performed with a Butler matrix with 8 elements. The close Fourier relationship between the focal plane field and the radiation pattern is illustrated in Figs. 2.3-3 (a) and (b) by comparing the magnitude plots. The double Fourier transform method is shown to be very effective in compensating for the surface errors by comparing the Figs. 2.3-3(c), (ii) and (iii), to that of the smooth reflector, Fig. 2.3-3(a), (i).

The authors presented a rule of thumb for determining the compensating range of their adaptive feed. For aperture phase errors with $0 \le \beta_e \le \pi/2$ and with spatial frequency less than $(n-1)/2$, the n-element array feed is able to compensate for errors with [31]

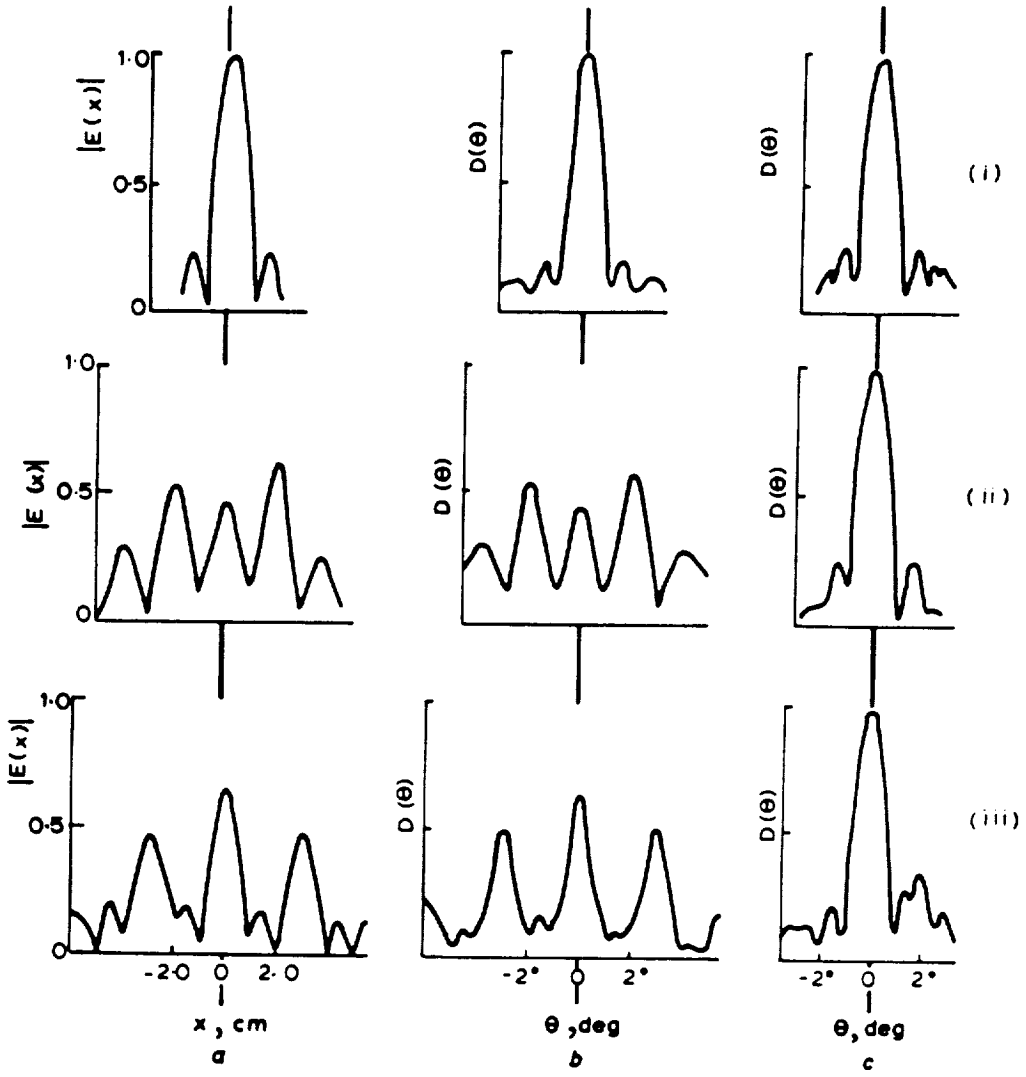

Figure 2.3-3. Experimental results for the variable profile reflector using the feed system of Fig. 2.3-2b. The three cases are for (a) focal plane field, (b) radiation pattern for single feed, and (c) radiation pattern with array feed adjusted for surface error compensation involving (i) no profile errors, (ii) phase errors with $\hat{\beta}_e = 0.5\pi$ and $N = 2$, and (iii) phase errors with $\hat{\beta}_e = 0.4\pi$ and $N = 3$. [31]

$$\hat{\beta}_e N \leq \frac{n-1}{2}\left(\frac{2\delta\hat{u}}{\lambda}\right) \tag{2.3-3}$$

where n is the number of phase-compensated inputs to the summing network and δ is the element spacing.

In their conclusions, Rudge and Davies cited practical problems for implementing their technique in two dimensions. Butler matrices would probably be too hard to build, too lossy, and too expensive for two dimensional problems. They recommended seeking other alternatives to perform the Fourier transform, such as microwave lens or multi-reflector techniques. [31]

2.3.2 CONJUGATE FIELD MATCH TECHNIQUE (COMPUTATIONAL)

Conjugate field match (CFM) for reflectors with array feeds is the most widely published of the surface error compensation techniques. CFM has also been extensively used in reflector scanning analysis. The method is based on maximizing the power received from a given direction. The drawback to the computational CFM technique is that you need an accurate model of the reflector surface.

CONJUGATE FIELD MATCH BACKGROUND

Much of the published work on conjugate field match deals with primary feed horn design. This subsection presents a background summary of the CFM method applied to horn design in preparation for application to reflectors with array feeds.

The CFM formulation was, in part, derived from a study by Midgley [25] dealing with reradiation of a rectangular pyramidal horn. In that study, the conjugate field theorem [25] is used to define complementary waves for which a given antenna receives all the incident power. [25] "If an ordinary aerial emits a certain outward travelling wave $f(jkr - j\omega t)$, it is at least possible to imagine a structure capable of returning a complementary wave $f(jkr + j\omega t)$ of equal strength, in response to which the original aerial is a perfect absorber." [25] For example, consider a reflector feed. If the transmitting field distribution in the feed's aperture is the conjugate of the fields when receiving and either the E-field or H-field is reversed, the feed will absorb all the energy incident upon the aperture. [26] Perfect absorption would correspond to an antenna with an aperture efficiency of 100%. The goal is then to closely match the field transmitted by an antenna to its complementary received field.

A measure of the match of the actual transmitted field of an antenna to its complementary field may be represented by the correlation of the two fields. The correlation of the actual transmitted field and the desired complementary field can be evaluated over a surface enclosing the receiving antenna. [25] The result is an integral expression for the power received by an antenna which, upon normalization, gives the aperture efficiency. [41] The integral expression for the power transmitted to the receiving antenna, P_R, can be derived in two ways. Both solutions are presented here.

First, consider two arbitrary antennas A and B. If A transmits power P_T and B is terminated in a matched load, the power received by antenna B is [25]

$$P_R = \alpha P_T \tag{2.3-4}$$

where α is a constant, $\alpha \leq 1$. It is a consequence of the Lorentz reciprocity theorem and the Friis transmission formula that if B transmits P_T and A is terminated in a matched load, the received power is again P_R in (2.3-4). [25]

Let $\vec{E}_A$, $\vec{H}_A$ be the fields transmitted by A where the transmit power is P_T. Let $\vec{E}_B$, $\vec{H}_B$ be the fields transmitted by B where Midgley now assumes the transmit power is αP_T. [25] The power received by A is now [25]

$$P_{R'} = \alpha^2 P_T \ . \tag{2.3-5}$$

Using (2.3-4) and (2.3-5), [25]

$$P_R^2 = P_T P_{R'} = \left[\int_S \left(\vec{E}_A \times \vec{H}_A \right) \cdot d\vec{S} \right] \left[\int_S \left(\vec{E}_B \times \vec{H}_B \right) \cdot d\vec{S} \right] \tag{2.3-6}$$

where the surface S encloses A, the integral enclosed by the left set of brackets represents the power transmitted by A through S, and the integral enclosed by the right set of brackets represents the power transmitted by B passing through S. The desired integral expression is found by evaluating the elemental power passing through S. The elemental expression is [25]

$$(\delta P_R)^2 = \left[\vec{E}_A \times \vec{H}_A \cdot \delta \vec{S} \right] \left[\vec{E}_B \times \vec{H}_B \cdot \delta \vec{S} \right] \tag{2.3-7}$$

where δP_R is the power crossing an element $\delta \vec{S}$ enclosing A. Using the vector identity [25]

$$\left(\vec{a} \times \vec{b} \right) \cdot \left(\vec{c} \times \vec{d} \right) = \left(\vec{c} \cdot \vec{a} \right) \left(\vec{d} \cdot \vec{b} \right) - \left(\vec{b} \cdot \vec{c} \right) \left(\vec{d} \cdot \vec{a} \right) \tag{2.3-8}$$

in (2.3-7) and factoring gives [25]

$$(\delta P_R)^2 = \left[\left(\vec{E}_B \times \vec{H}_B\right) \cdot \left(\vec{E}_A \times \vec{H}_A\right)\right]\left(\delta\vec{S} \cdot \delta\vec{S}\right) - \left[\left(\vec{E}_A \times \vec{H}_A\right) \times \delta\vec{S}\right] \cdot \left[\left(\vec{E}_B \times \vec{H}_B\right) \times \delta\vec{S}\right] \quad (2.3\text{-}9)$$

The second term in (2.3-9) is zero if $\delta\vec{S}$ is perpendicular to $\vec{E}_A \times \vec{H}_A$ or $\vec{E}_B \times \vec{H}_B$. [25] This condition is satisfied if the surface S is in the far field of A or B. Applying (2.3-8) to the (nonzero) first term in (2.3-9) gives [25]

$$(\delta P_R)^2 = \left[\left(\vec{E}_A \cdot \vec{E}_B\right)\left(\vec{H}_A \cdot \vec{H}_B\right) - \left(\vec{E}_A \cdot \vec{H}_A\right)\left(\vec{E}_B \cdot \vec{H}_B\right)\right]\delta S^2 \quad . \quad (2.3\text{-}10)$$

For linearly polarized antennas with the far field E-fields perpendicular to the H-fields, the second term in (2.3-10) is zero. If the magnitudes [25]

$$\frac{E_A}{H_A} = \frac{E_B}{H_B} = \eta \quad (2.3\text{-}11)$$

where η is the intrinsic impedance of the medium, then (2.3-10) may be written as

$$(\delta P_R)^2 = \frac{\left(\vec{E}_A \cdot \vec{E}_B\right)^2 \delta S^2}{\eta^2} \quad (2.3\text{-}12)$$

which leads to the desired integral expression for the power received by A [25]

$$P_R = \int_S \frac{\vec{E}_A \cdot \vec{E}_B}{\eta}\, dS \quad . \quad (2.3\text{-}13)$$

The aperture efficiency of an antenna can be found by normalizing the fields in (2.3-13). The η in the denominator of (2.3-13) is normalized by multiplying the equation by η.

The transmit field $\vec{E}_A$ is normalized to have unity power. The received field $\vec{E}_B$ is normalized to have unity power intercepted by the aperture of antenna A. [41]

The second solution for finding the power transmitted to the receiving antenna has been used in designing feeds and subreflectors for reflector antennas. [41, 56, 57] The transmission efficiency T for prime focus reflectors is defined as the ratio of the power delivered to a matched load connected to a primary feed to the total power intercepted by the reflector aperture. [41] The efficiency T is found by applying Robieux's theorem of the coupling of two antennas. [60] Wood [60] applied Robieux's theorem to focal plane calculations giving [60]

$$T = \frac{1}{2} \int_{FP} \left[\vec{E}_f \times \vec{H}_{FP} + \vec{H}_f \times \vec{E}_{FP} \right] \cdot d\vec{S} \tag{2.3-14}$$

where $\vec{E}_f$, $\vec{H}_f$ are the fields in the focal plane that would be present if the feed were transmitting and the $\vec{E}_{FP}$, $\vec{H}_{FP}$ are the received focal plane fields for a plane wave illuminating the reflector. The fields incident upon the focal plane are assumed to be normalized to unity power. [60] If the E and H of the E,H pairs are perpendicular, (2.3-14) reduces to (similar to [41])

$$T = K \int_{FP} \vec{E}_f \cdot \vec{E}_{FP} \, dS \tag{2.3-15}$$

where K is a normalization constant. Equation (2.3-15) is the second solution for the P_R and is equivalent to (2.3-13) (when normalized) for fields evaluated in the focal plane.

The expressions in (2.3-14) and (2.3-15) have a unity maximum for the conditions [60]

$$\vec{E}_f = \vec{E}_{FP}^{\,*} \tag{2.3-16a}$$

$$\vec{H}_f = -\vec{H}^*_{FP} \quad . \tag{2.3-16b}$$

Using (2.3-16) in (2.3-14) gives two expressions for the power density integration of the received plane wave or the transmitted wave in the focal plane. The powers are, by definition, normalized to unity and their sum multiplied by the 1/2 gives a maximum of $T = 1$. This implies that the aperture efficiency is maximum for the hypothetical feed that presents a conjugate match to the received focal plane fields over the entire focal plane. [60]

Of course real feeds are of finite size. The surface of integration is then assumed to be the aperture plane of the primary feed instead of the entire focal plane. [41] It is still assumed that the optimum aperture efficiency is realized over the aperture of the feed if the conjugate match conditions of (2.3-16) are met. [60] However, this assumption has not been proved for the limited aperture case. [42]

The array feed implementation of the CFM method is an extension of the primary feed matching. In the array-fed case, the focal plane fields are conjugate matched at a set of discrete locations corresponding to the feed element locations. This implementation is useful for matching the focal plane fields of scanned or distorted reflectors (Secs. 2.3.2 and 3.2). The focal plane fields of scanned or distorted reflectors are spread over a wider region than for unscanned smooth reflectors (see Sec. 2.2). The array feed configuration allows for matching the focal plane fields over a broader area and, hence, providing a higher aperture efficiency.

CFM COMPENSATION

The CFM compensation technique is implemented with a phased array feed. The distorted reflector causes errors in the focal plane fields and the energy is dispersed in the focal plane (see Sec. 2.2.1). The feed array is used to capture the distributed energy and coherently combine it. The individual element excitations, A_i, are set to be proportional to the complex conjugates of the focal plane fields that would be received by the ith feed element given a plane wave incident from the desired direction (boresight if it is not scanned). [4]

There are two ways to determine the required CFM excitations A_i . The A_i may be found by direct computation of the received focal plane fields (In the subsection after the next subsection we call that Direct CFM or DCFM) or A_i may be found by using a reflector far field computer code (In the next subsection we call that Indirect CFM or ICFM). [33]

ICFM AND MODIFIED ICFM WITH IMPROVED SIDE LOBE PERFORMANCE

Reciprocity can be used to show that the ith CFM feed element excitation upon reception of a plane wave is proportional to the secondary field transmitted in the desired direction from a reflector illuminated by the ith feed. [17, 4, 33] Rather than directly computing the focal plane fields to determine the coefficients, the element excitation coefficients are computed indirectly using a far field computer program and invoking reciprocity. This is the basis of the indirect CFM technique (ICFM [2]).

Blank and Imbriale studied array feeds and the use of ICFM to compensate for reflector surface errors. The authors derived some useful design formulas for realistic feed array design. The formulas were based on approximate circularly symmetric, unidirectional feed radiation patterns of the form [4]

$$f(\psi) = \cos^{q_1}(\psi) \quad . \tag{2.3-17}$$

The exponent can be related to the edge taper t of a single feed at the focus ($0 < t < 1$). The exponent, q_1, is approximately [4]

$$q_1 \approx \frac{-8 \ln(t)}{b} (F/D)^2 - 0.5 \tag{2.3-18}$$

where b is a constant that depends on the effective aperture of the feed element. [4] This value of q_1 leads to a minimum element diameter, d_{e1}, for a single feed of [4]

$$d_{e1} \approx \sqrt{\frac{-8 \ln(t)}{b}} (F/D) \tag{2.3-19}$$

for a triangular grid array of circular elements (see Fig. 2.3-4).

The surface errors used by Blank and Imbriale were assumed to have distortion profile Δz, of (2.2-7). This error is based on data for gravity-induced distortions typical of large ground based reflectors. [4] Using this surface distortion profile and the ICFM technique outlined above, the authors looked at the ability to compensate for gain loss for a variety of cases for various combinations of the number of feed elements, N; F/D ratios; distortion profile parameters ε and s (ε and s are empirically determined constants for defining the gravity-induced distortion profile); and feed element parameter b. An edge taper of -10 dB was used in this parametric analysis. The gain loss is referenced to the maximum gain for a circular aperture (49.94 dB for $D = 100\lambda$). Blank and Imbriale found some interesting results during the study. For a single feed, the smaller the values

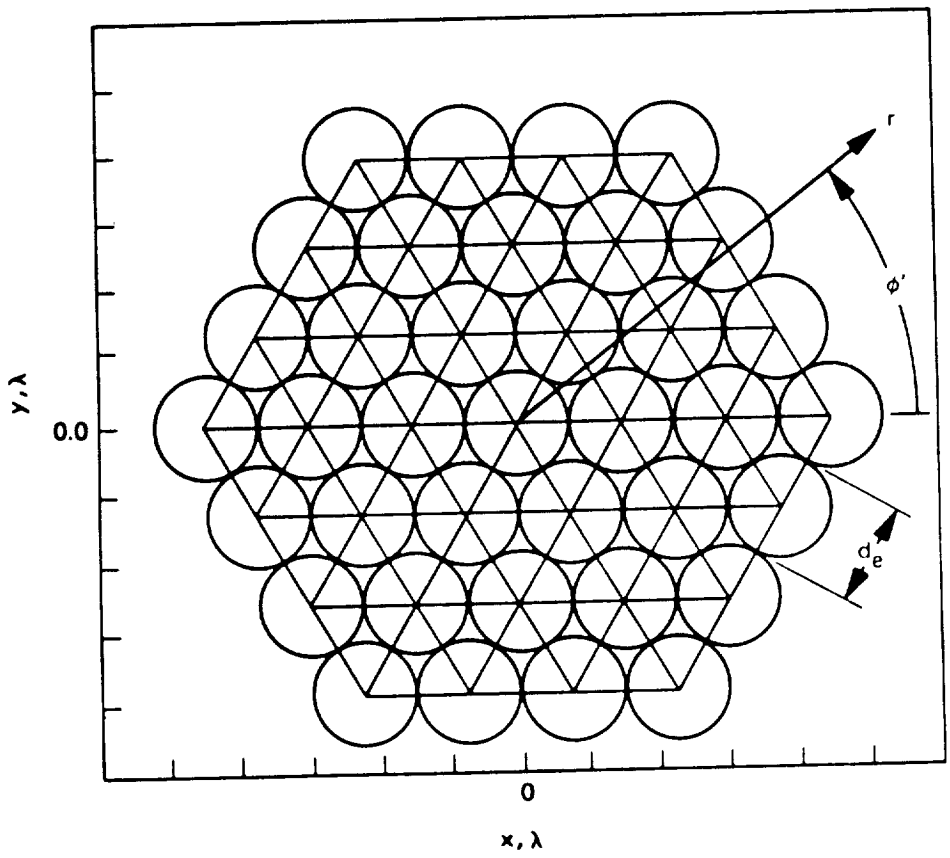

Figure 2.3-4. An example of a 37-element triangular grid array. [7]

of F/D , the smaller were the effects of the distortion whereas for the array feed, the distortion effects are almost independent of F/D for the simulated gravity induced distortion. [7] Gain loss increased with increasing surface distortion amplitude. [7] Also, gain loss is less for errors concentrated at the reflector edge than for more uniformly distributed errors. [4]

Blank and Imbriale used the results of the parametric analysis to derive expressions for the optimum feed element diameters. For $N = 7$ [4]

$$d_{e,N=7} \approx d_{e1} = \sqrt{\frac{9.2}{b}}\,(F/D) \tag{2.3-20}$$

and for $N = 19,37$ [4]

$$d_{e,N=19,37} \approx \frac{1}{3}\,d_{e1} = \frac{1}{3}\sqrt{\frac{9.2}{b}}\,(F/D) \quad . \tag{2.3-21}$$

The feed array configurations using (2.3-20) and (2.3-21) are shown in Fig. 2.3-5.

To illustrate the compensating effects of CFM on a radiation pattern, Blank and Imbriale used a 37-element feed array. The compensated pattern is compared to the badly distorted pattern when a single feed is used (see Fig. 2.3-6).

Rahmat-Samii [33] worked with a modified ICFM algorithm that reduces the side lobe level. Rahmat-Samii's ICFM uses a fictitious feed illumination taper when computing the element excitations. This numerically produces an amplitude taper in the aperture. The resulting secondary fields determined from the set of element excitations lead to an array that compensates for the surface distortions while maintaining a desirable side lobe level. The actual feeds will then be used to compute the far field patterns. [33]

Rahmat-Samii presented a numerical example to demonstrate the compensation algorithm and its effectiveness. A distorted 20-meter deployable offset reflector

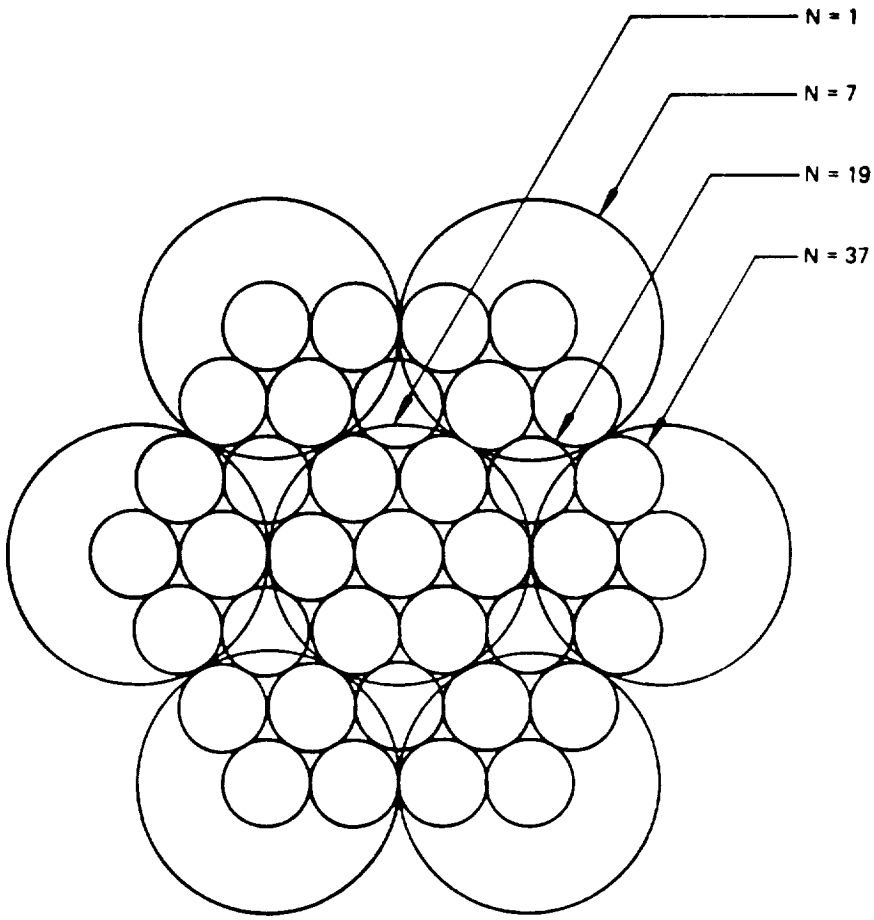

Figure 2.3-5. Optimum feed array configurations for $N = 1, 7, 19$, and 37 elements. [7]

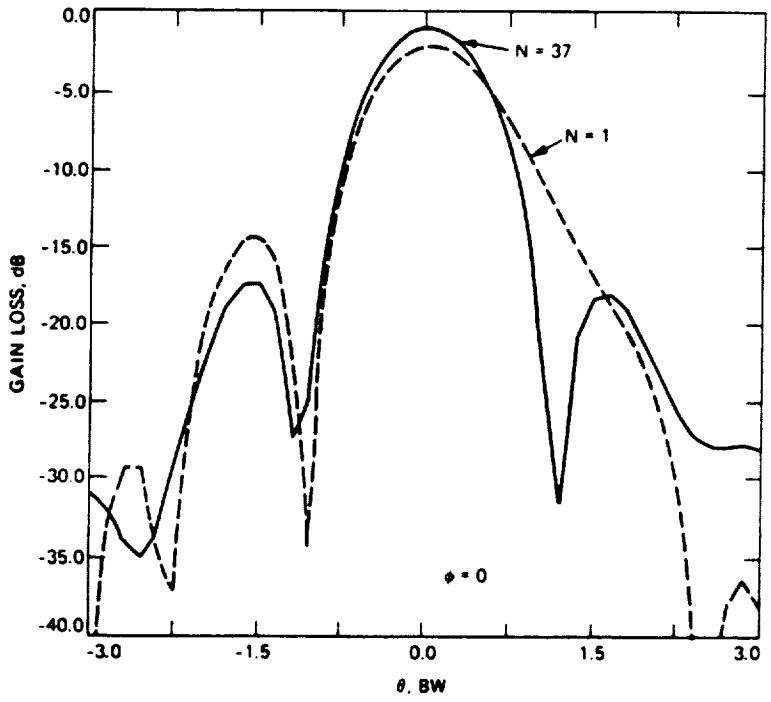

Figure 2.3-6. Radiation patterns for a distorted reflector ($F/D = 1.0$, $\epsilon = 0.12\lambda$, $s = 2.0$). The $N = 1$ plot corresponds to the uncompensated far field pattern using a single feed at the focus ($d_e = 2.1$). The $N = 37$ plot is the compensated pattern using the triangular grid array and CFM ($d_e = 0.71$). [7]

operating at L-band had its edge displaced by 60 mm due to a simulated thermal distortion. A 19-element feed array was used (see Fig. 2.3-7). The uncompensated patterns are shown in Fig. 2.3-8 along with patterns compensated for gain only (similar to Blank and Imbriale's approach [4], ICFM without side lobe control) and ones compensated for gain and side lobe level.

Rahmat Samii also has worked with an experimental CFM technique. This is discussed in Sec. 2.3.4.

DCFM WITH IMPROVED SIDE LOBE PERFORMANCE

Acosta [1] outlined a modified CFM algorithm which has improved side lobe performance. The method uses the received focal plane fields to compute the excitations and is called direct CFM (DCFM). To improve the side lobe levels, Acosta's DCFM algorithm assumes that the incoming plane wave used to compute the focal plane fields is fictitiously amplitude tapered. [1]

Acosta, Zaman, Bobinsky, Cherrette, and Lee [2] compared this modified technique to regular CFM results. The modified CFM coefficients were directly determined by computation of the received focal plane fields assuming the amplitude tapered plane wave is incident upon the reflector. The lower side lobe characteristics of the DCFM were illustrated by numerical example. The reflector antenna with the distortion profile shown in Fig. 2.3-9 was analyzed. Compensation was implemented with the 37-element feed array of Fig. 2.3-9(b). The elements were positioned so that most of the power spread over the focal region by the surface distortion was captured by the array. The plots for the undistorted reflector (single feed), distorted reflector (single feed), and compensated patterns are shown in Fig. 2.3-10. The plots in Fig. 2.3-10 show the improved side lobe structure produced by the modified approach using the amplitude

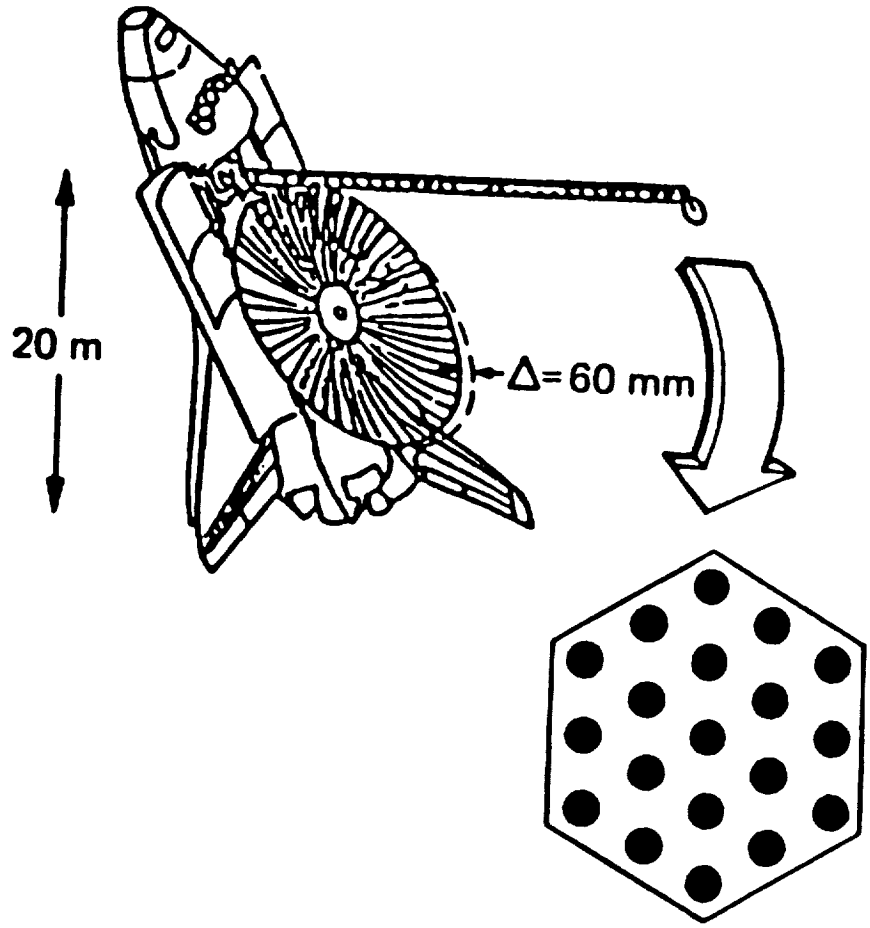

Figure 2.3-7. Reflector geometry with the simulated thermal distortion and the 19-element feed array. [33]

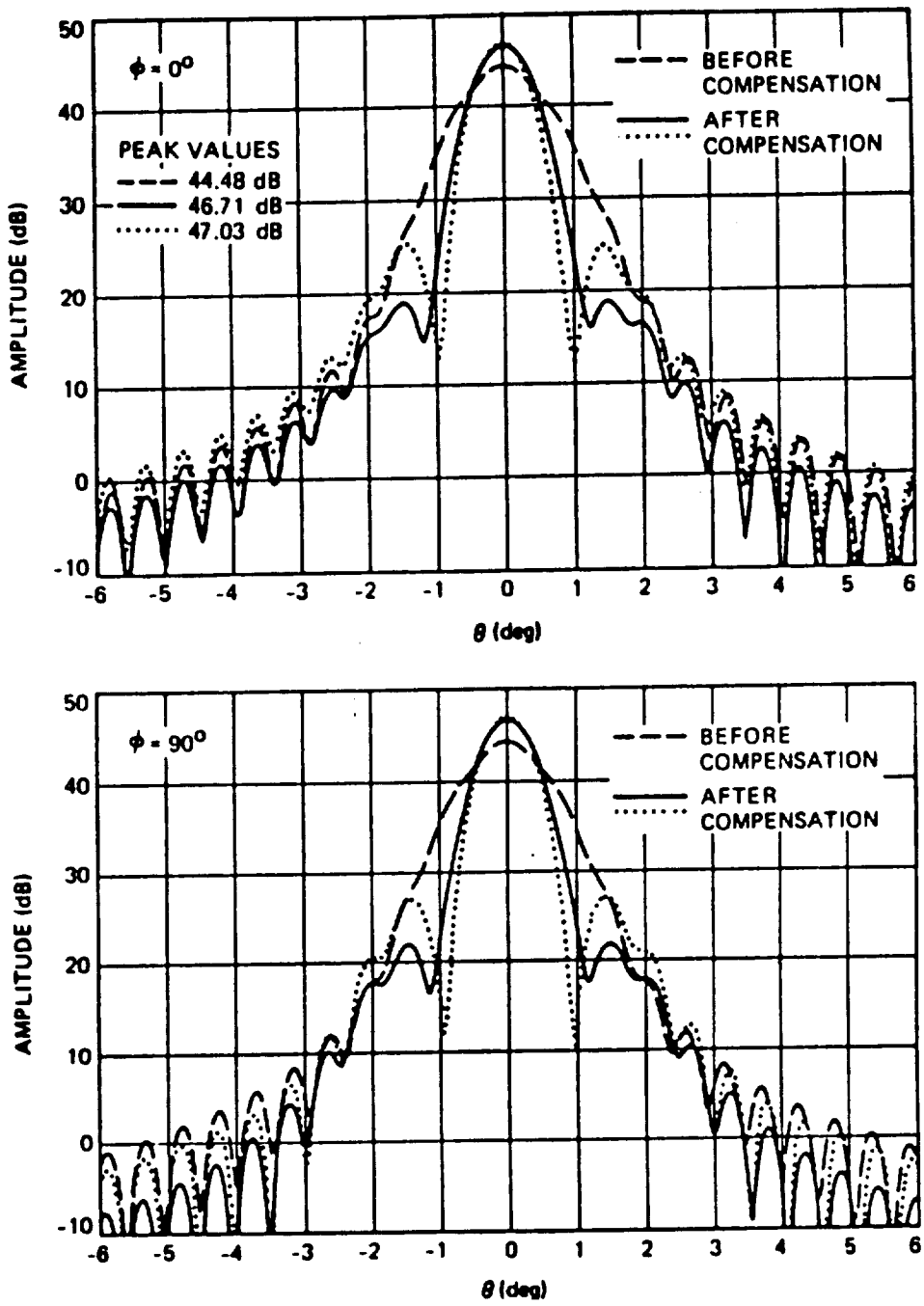

Figure 2.3-8. Radiation patterns for a distorted reflector without compensation (dashed), with compensation for gain only (dotted), and with compensation for gain and side lobes (solid). [33]

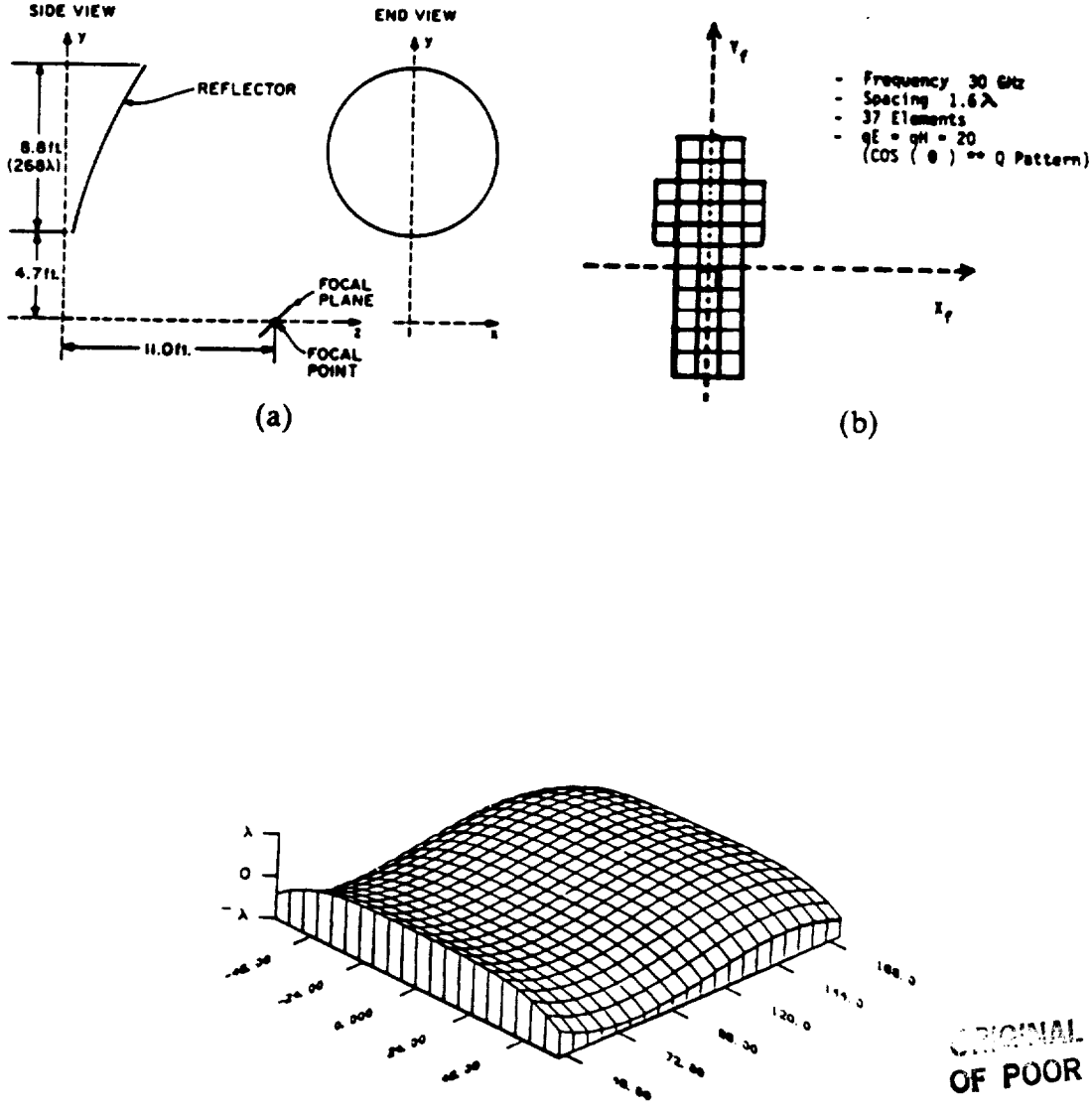

Figure 2.3-9. (a) Reflector geometry for the DCFM analysis. [8] (b) 37-element customized feed array for the DCFM analysis. [2] (c) Distortion profile for the DCFM analysis (height dimension in wavelengths, base dimension in inches, f= 30GHz). [8]

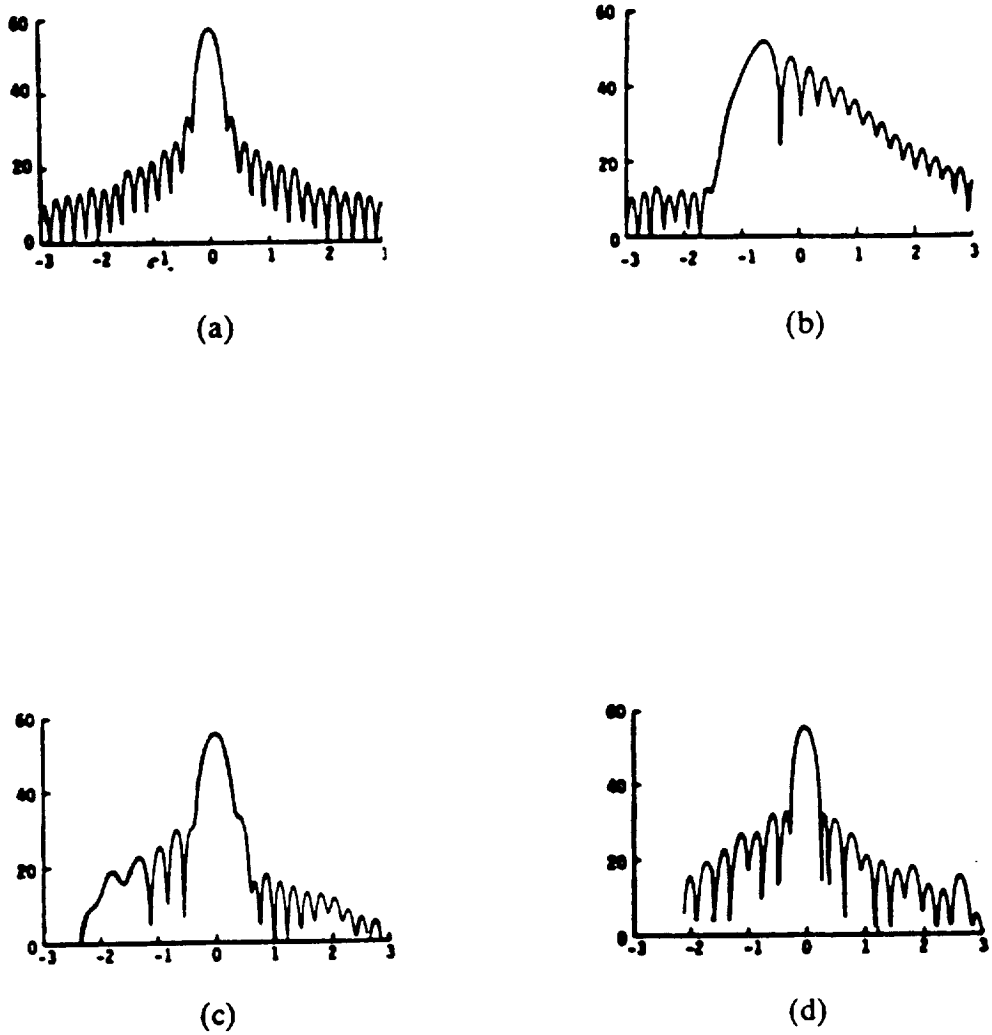

Figure 2.3-10. Radiation patterns for (a) undistorted reflector, single feed; (b) distorted reflector, single feed; (c) distorted reflector, array feed, regular CFM; (d) distorted reflector, array feed, Acosta's DCFM. [2]

tapered plane wave to compute the excitations. Note, however, that the directive gain is about 2 dB lower than the regular CFM approach. [2]

2.3.3 LEAST SQUARED ERROR TECHNIQUE

Bailey [6] developed a method for computing the excitation coefficients of an array feed that give an approximation to a desired aperture field distribution. The author notes that the method could also be implemented by computing the excitation coefficients that approximate a desired far field pattern. The algorithm matches the actual aperture field to the desired aperture field at discrete points. The method of least squares is then used to compute the excitations. [6] As with computational CFM (Sec. 2.3.2), an accurate model of the reflector surface is required.

Aperture field information is used to compute the excitations for the least squared error compensation technique. The aperture fields due to each of the N array elements when transmitting are computed. The desired complex aperture field, $F(x, y)$, is approximated in the xy-plane at I discrete points by [6]

$$F(x_i, y_i) \approx \sum_{n=1}^{N} A_n f_n(x_i, y_i) \quad , \quad i = 1,2,3, \ldots, I \tag{2.3-22}$$

where N is the number of feed elements, A_n is the nth element excitation, and $f_n(x_i, y_i)$ is the field due to the nth element at location (x_i, y_i) in the aperture plane. The number of field points in the aperture I must be sufficiently large to give a representative sample of the aperture distribution. The array may be of arbitrary geometry but for this study planar triangular grid arrays were used. [6] The complex excitations, A_n, are found such that $F(x, y)$ is approximated in a least-squared sense by the N-element feed array. [6]

The quantity G is a measure of the error between $F(x, y)$ and the approximation in (2.3-22) and is defined as [6]

$$G = \sum_{l=1}^{N} \left[F(x_l, y_l) - \sum_{n=1}^{N} A_n f_n(x_l, y_l) \right]^2 . \tag{2.3-23}$$

Minimizing G with respect to A_m for $m = 1,2,3, \ldots, N$ gives [6]

$$\frac{\partial G}{\partial A_m} = -2 \sum_{l=1}^{I} \left[f_m(x_l, y_l) \left(F(x_l, y_l) - \sum_{n=1}^{N} A_n f_n(x_l, y_l) \right) \right] = 0 \tag{2.3-24}$$

which gives N equations with N unknowns. Defining [6]

$$B_m = \sum_{l=1}^{I} f_m(x_l, y_l) F(x_l, y_l) \tag{2.3-25}$$

$$S_{mn} = \sum_{l=1}^{I} f_m(x_l, y_l) f_n(x_l, y_l) \tag{2.3-26}$$

and using (2.3-25) and (2.3-26) with (2.3-24), the problem can be expressed as [6]

$$\begin{bmatrix} B_1 \\ B_2 \\ \cdot \\ \cdot \\ \cdot \\ B_N \end{bmatrix} = \begin{bmatrix} S_{11} & S_{12} & \cdots & S_{1N} \\ S_{21} & S_{22} & \cdots & S_{2N} \\ \cdot & \cdot & \cdot & \\ \cdot & \cdot & \cdot & \\ \cdot & \cdot & \cdot & \\ S_{N1} & S_{N2} & \cdots & S_{NN} \end{bmatrix} \begin{bmatrix} A_1 \\ A_2 \\ \cdot \\ \cdot \\ \cdot \\ A_N \end{bmatrix} \tag{2.3-27}$$

where the unknowns in (2.3-27), A_n, may now be solved for the feed element excitations. Bailey notes that this technique does not maximize the gain nor does it minimize the side lobes but it approximates the desired aperture field distribution and therefore the desired radiation pattern in all angular space within the pattern correction limits of the finite N-element array feed. [6]

Bailey performed a computer simulation to illustrate the compensating capabilities of this technique. He analyzed a single quadrant of the 15-meter hoop/column mesh deployable antenna assuming a frequency of 6.4 GHz and 3.5 inch element spacings.[6] Analysis for smooth, distorted, and compensated reflectors was presented for reflectors with $N = 7$, 19, and 37-element triangular grid feed arrays. The actual surface distortion of the 15-meter hoop/column reflector was measured and the distortion profile is shown in Fig. 2.3-11.

The geometry and initial excitations for a 7-element array feed are shown in Fig. 2.3-12. The radiation pattern for the reflector distortion of Fig. 2.3-11 for the 7-element array-fed case of Fig. 2.3-12 is shown in Fig. 2.3-13. Compensation analysis for the 7-element case showed negligible improvement. [6] The array feed geometry and compensation excitations computed using the method of least squares of (2.3-27) for a 19-element feed are shown in Fig. 2.3-14. The improved radiation pattern for the 19-element compensation case is shown in Fig. 2.3-15. Further compensation analysis was performed with a 37-element feed. The geometry and compensation excitations for the 37-element feed are shown in Fig. 2.3-16. The much improved radiation pattern for the 7-element compensation case is shown in Fig. 2.3-17.

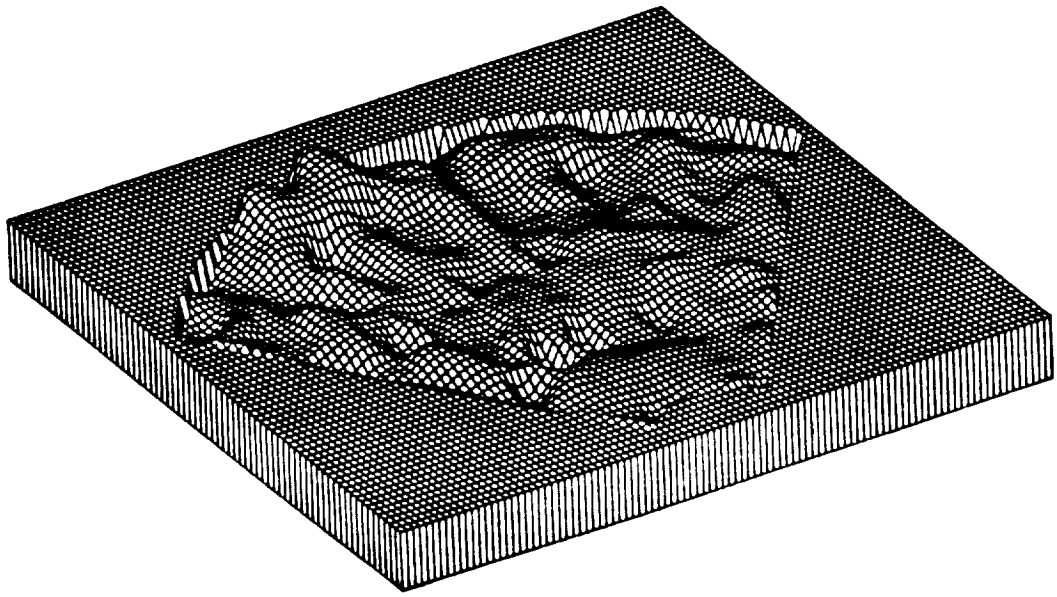

Figure 2.3-11. Exaggerated distortion profile for the single quadrant of the 15-meter hoop/column antenna. The rms of the surface distortion is 0.061 inch. [6]

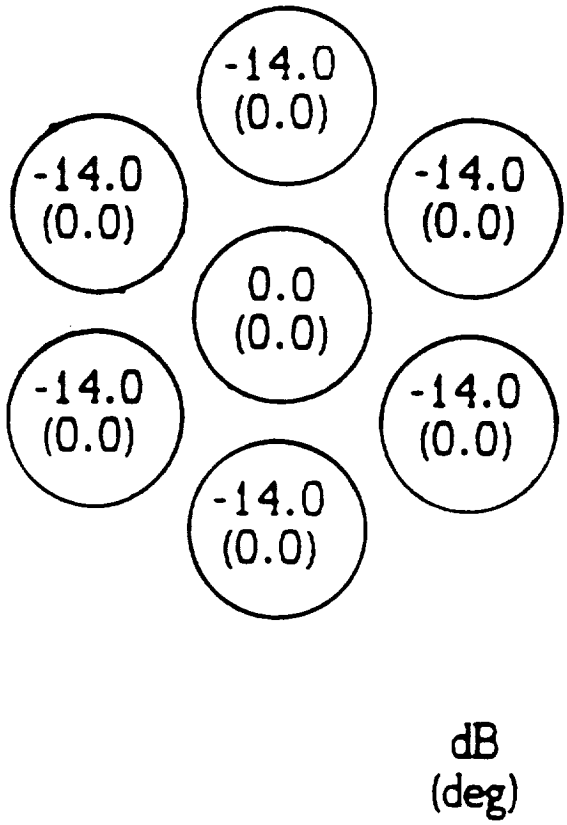

Figure 2.3-12. Geometry and excitation coefficients for the 7-element array. [6]

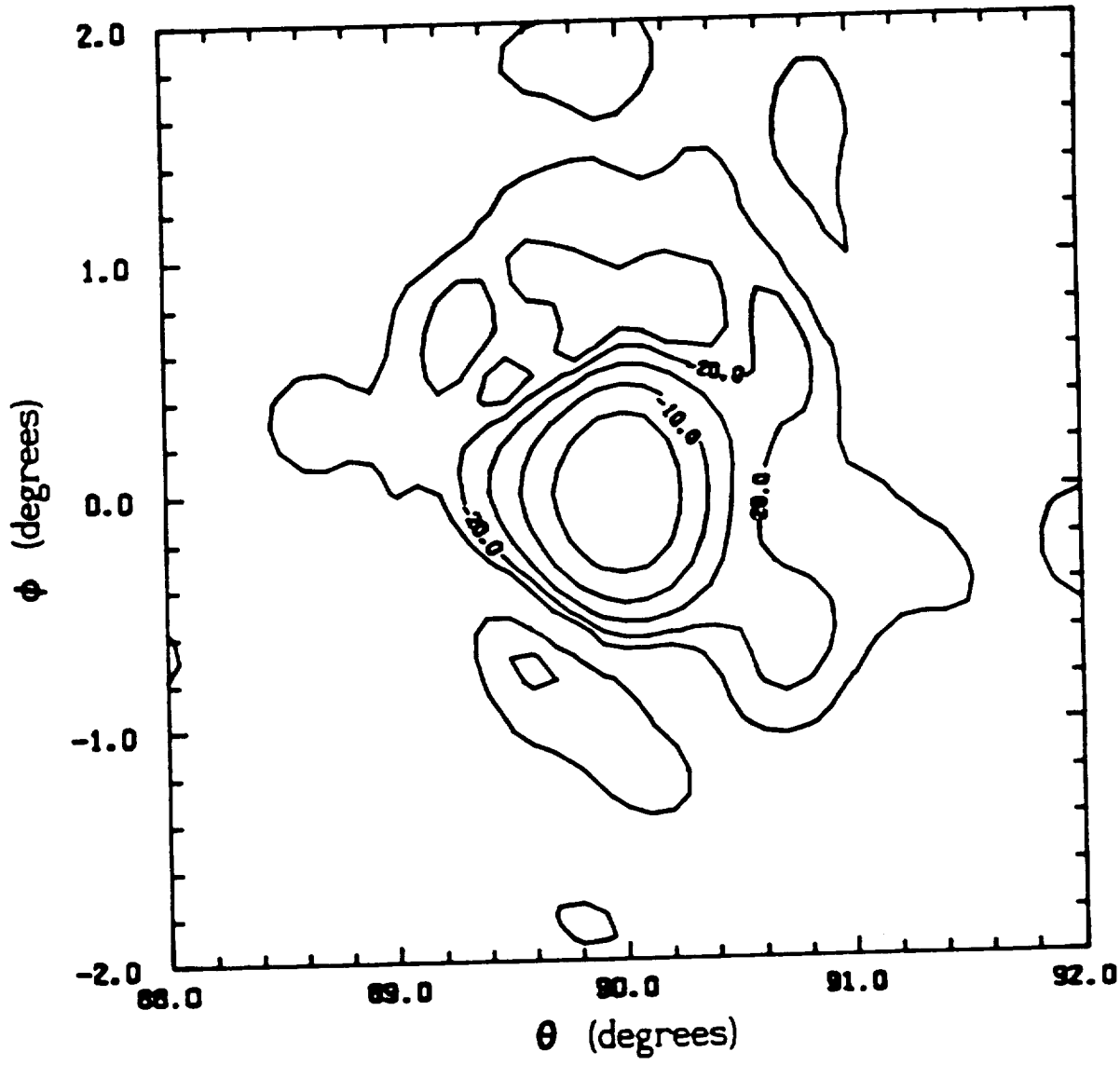

Figure 2.3-13. Uncompensated radiation pattern for the distorted reflector with the distortion profile of Fig. 2.3-11 and the 7-element array feed excited as shown in Fig. 2.3-12. [6]

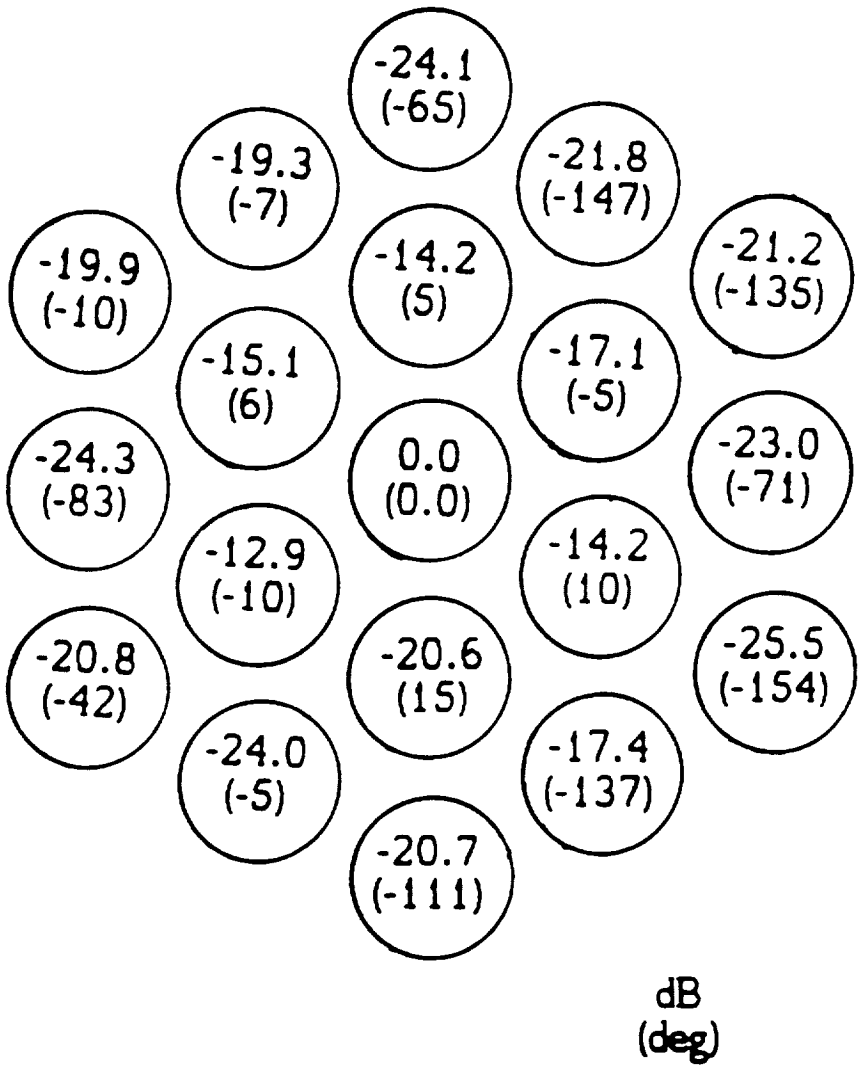

Figure 2.3-14. Geometry and compensation excitation coefficients for the 19-element feed. [6]

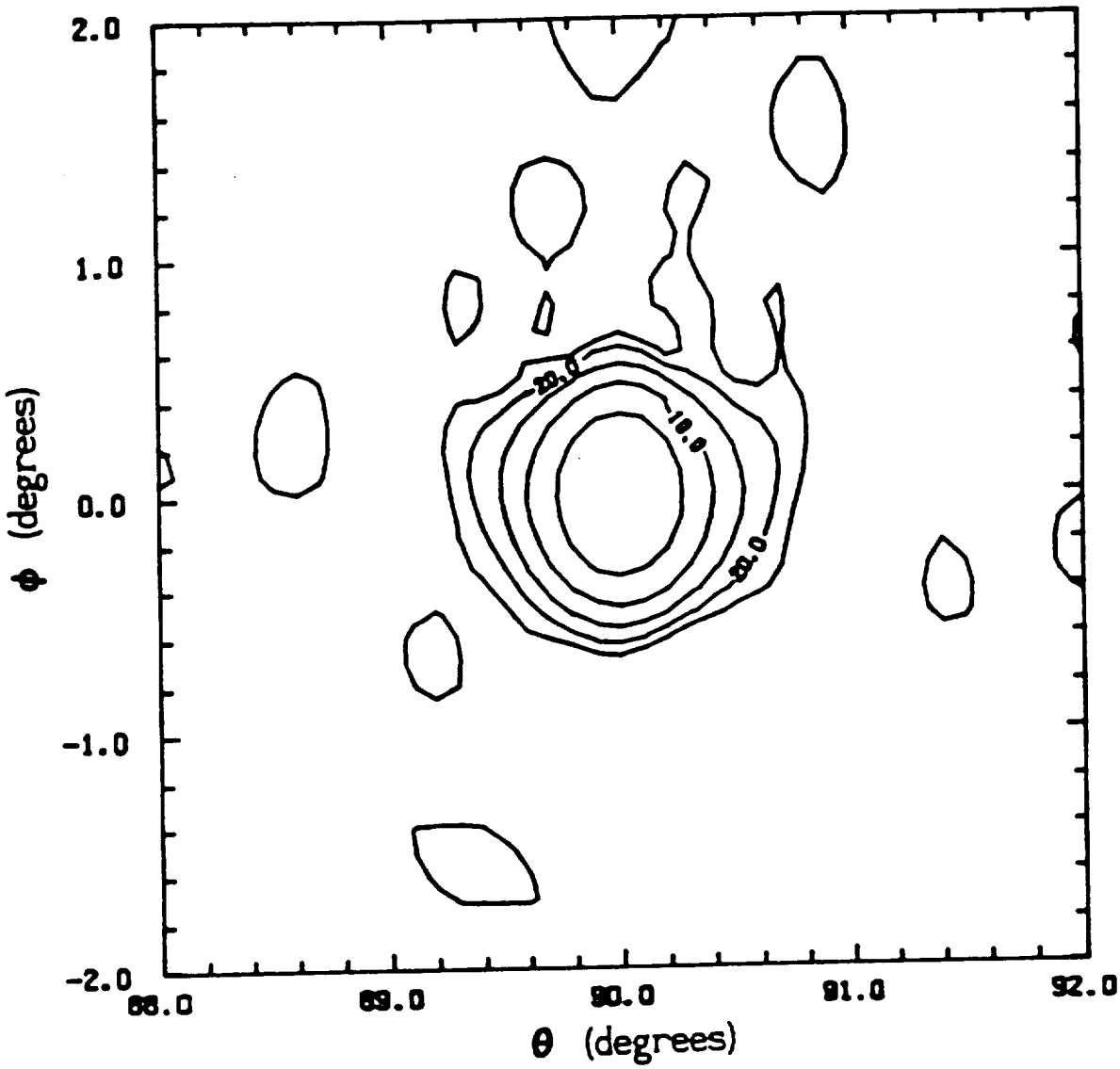

Figure 2.3-15. Compensated radiation pattern for the distorted reflector with the 19-element feed. [6]

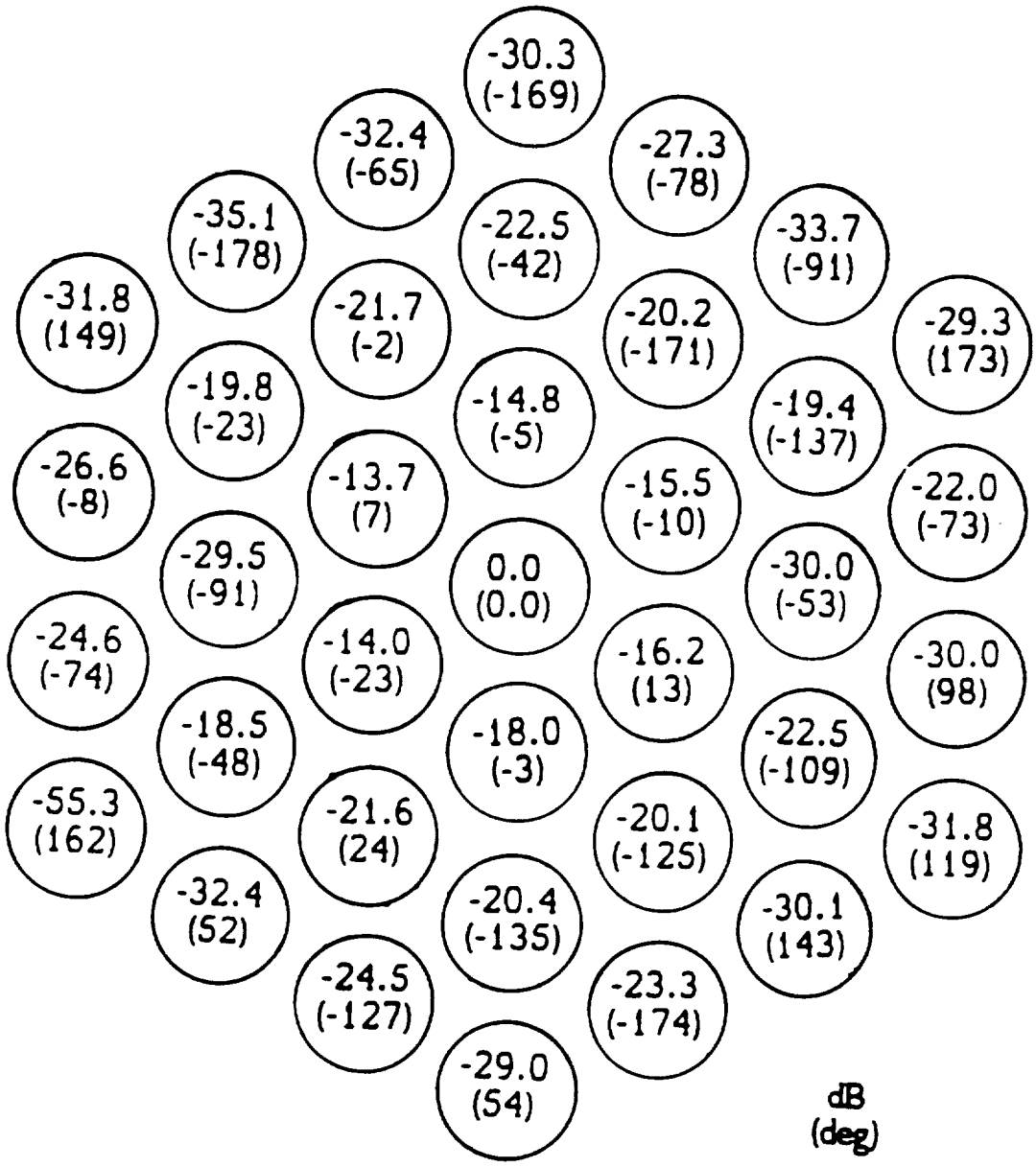

Figure 2.3-16. Geometry and compensation excitation coefficients for the 37-element feed. [6]

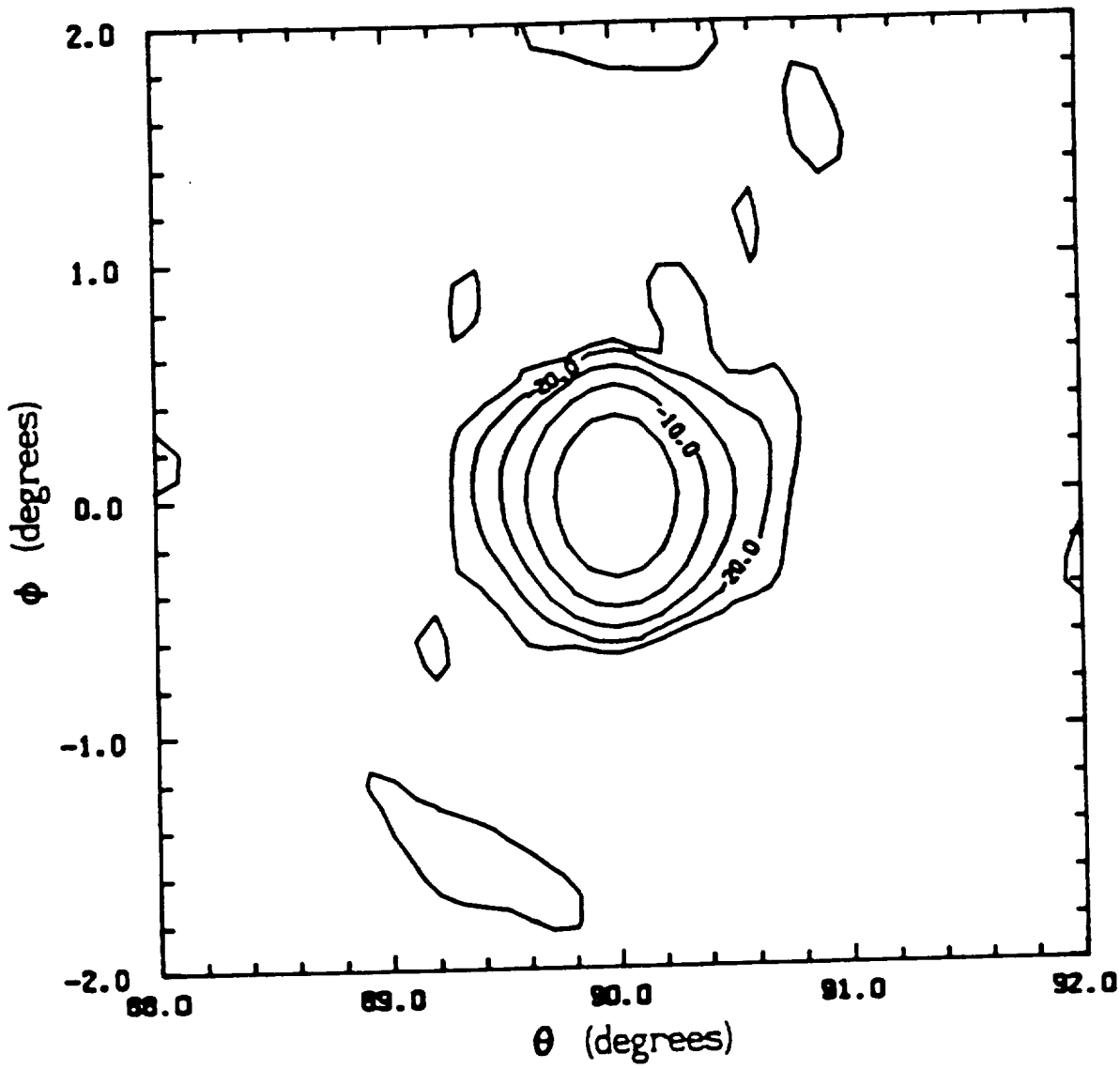

Figure 2.3-17. Compensated radiation pattern for the distorted reflector with the 37-element feed. [6]

2.3.4 CONJUGATE FIELD MATCH TECHNIQUE (EXPERIMENTAL)

Rahmat-Samii [35] performed an experimental implementation of the DCFM compensation method. The experiment follows the same basic theory of the computational DCFM technique (see Sec. 2.3.2). In the experiment, the received focal plane fields for a distorted reflector were measured (instead of computed) and the element compensation excitations were determined using CFM. The advantage of the experimental technique is that the reflector surface shape need not be known.

The experimental CFM study was performed on a reflector that was shaped with that of a simulated thermal distortion. The simulated distorted surface deviates from a smooth parabolic reflector by the [35]

$$f_d = 0.011\left(\frac{2\rho}{D}\right)^3 \cos 2\phi \qquad \text{meter} \tag{2.3-28}$$

which describes the dominant term in a typical thermal distortion. The reflector geometry is shown in Fig. 2.3-18. The feed array consisted of 16 cigar elements in a grid spaced 1.06λ apart at 8.45 GHz. [35] There was an analog phase shifter and variable attenuator behind each element. [35] Considerable effort was spent generating calibration curves for each element so that the desired amplitude and phase excitation for compensation could be implemented despite intercircuit amplitude and phase imbalance. [43]

The algorithm used to implement the experimental CFM approach is shown in Fig. 2.3-19. The experiment showed that the compensated distorted reflector gain improves by 2.5 dB over the uncompensated case. [35] Figure 2.3-20 compares the patterns for the uncompensated and compensated cases.

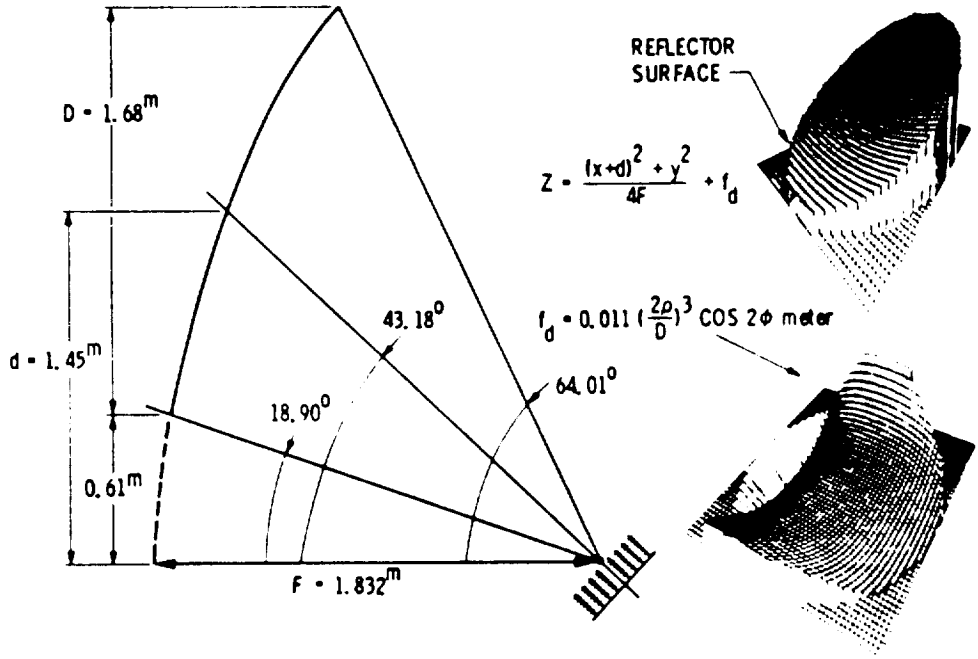

Figure 2.3-18. Reflector geometry and the simulated thermal distortion profile used in the experimental CFM study. The feed array consisted of 16 cigar elements in a grid spaced 1.06λ apart at 8.45 GHz. [36]

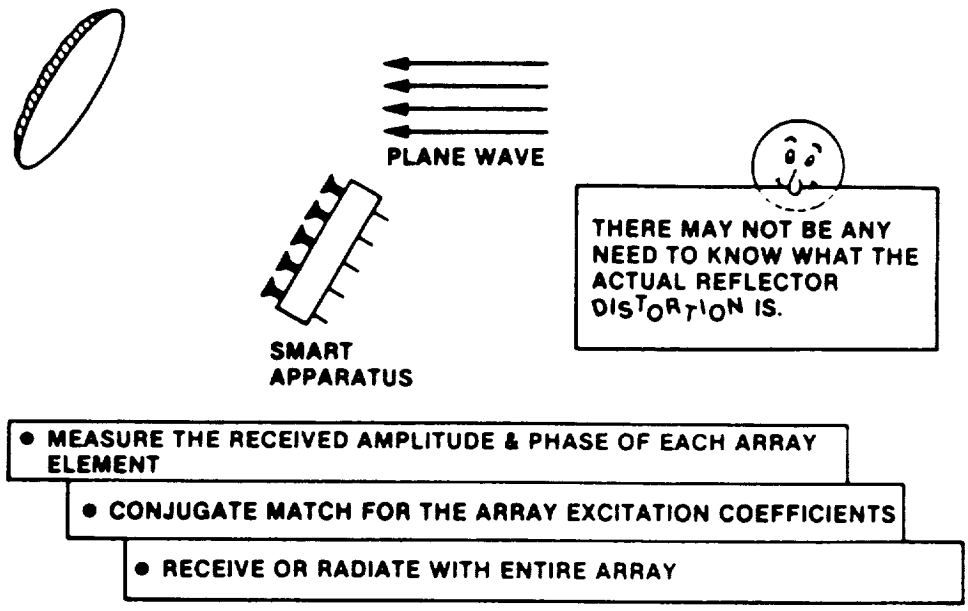

Figure 2.3-19. Algorithm for implementing the experimental CFM technique. [36]

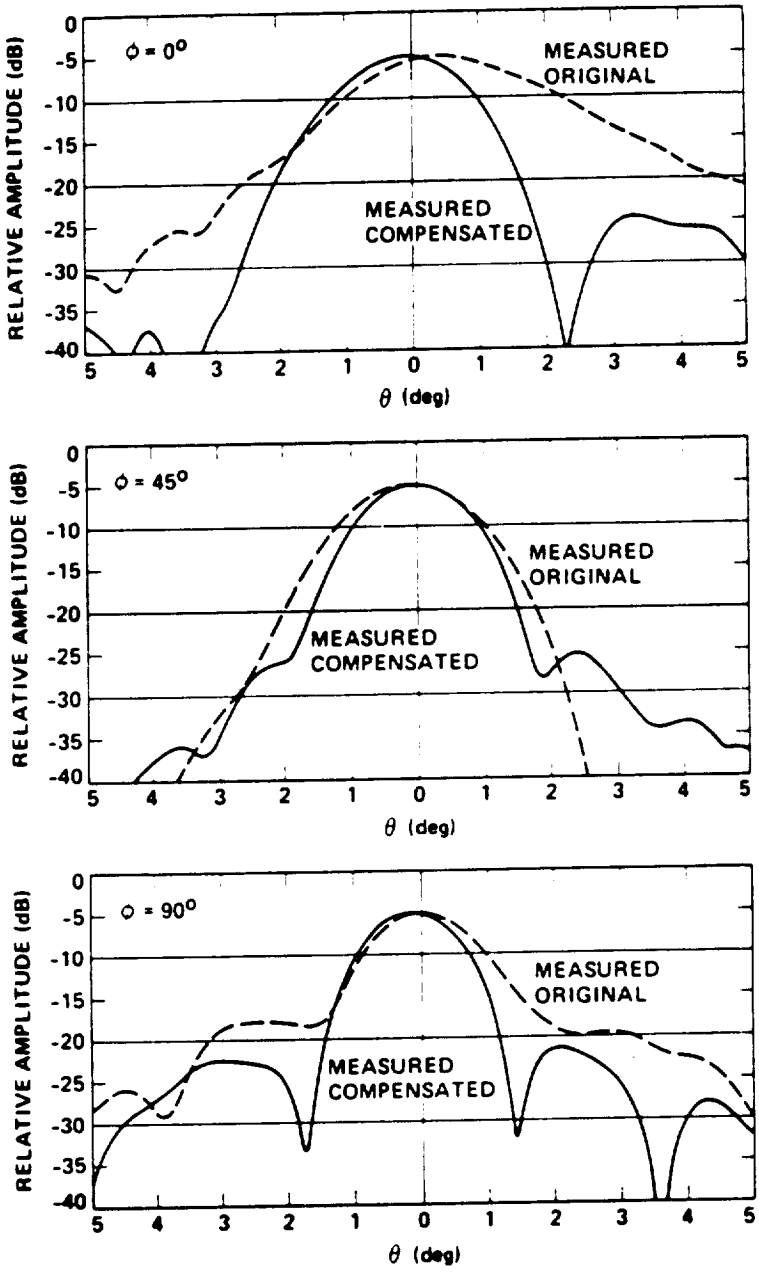

Figure 2.3-20. Measured uncompensated and compensated radiation patterns. The plots are all normalized to -5 dB but the gain of the compensated pattern is actually 2.5 dB higher. [36]

2.3.5 SUMMARY OF COMPENSATION TECHNIQUES

The existing electromagnetic compensation techniques were discussed in this Section. A summary of the techniques is presented in Table 2.3-1. The methods try to correct for errors in the focal plane fields or the aperture distribution and, hence, correct for irregularities in the overall radiation pattern. The compensation techniques allow for some control over the side lobe envelope. They are restricted to compensating for surface errors with long correlation lengths that cause errors in the focal plane fields near the focal point or errors in the radiation pattern near the main beam. The pattern of a rough surface reflector (very short correlation lengths) cannot be improved using electromagnetic compensation.

Rahmat-Samii looked at the effects of random errors in the amplitude and phase of the feed excitations for CFM compensation. [34] He found that with errors of ± 0.5 dB in amplitude and $\pm 10°$ in phase, there were negligible effects on the compensated radiation patterns.

Rahmat-Samii also noted that better improvement can be obtained using larger arrays. [33] This statement is supported by Bailey's results in Sec. 2.3.3. The pattern for the reflector with the 37-element array feed (Fig. 2.3-17) shows improved pattern performance over that of the 19-element array feed case (Fig. 2.3-15).

Table 2.3-1
Summary of the Electromagnetic Compensation Techniques.

Method	Comments	References	Section
Double Fourier Transform	Uses a Butler matrix to take a 2nd Fourier transform. Hard to implement in 3-D.	[31]	2.3.1
Conjugate Field Match (Computational)	The element excitations are the complex conjugates of the received focal plane fields. Requires surface data.	[4, 1, 33]	2.3.2
Least Squared Error	Matches the aperture field to a desired field distribution. Requires surface data.	[6]	2.3.3
Conjugate Field Match (Experimental)	Focal plane fields are actually measured and used to compute the CFM element excitations. Does not require surface data.	[35, 43]	2.3.4

3.0 REFLECTOR SCANNING

The ability to scan a reflector pattern is essential to the pattern synthesis compensation technique (see Ch. 4). There are many methods used to scan reflectors. Displaced feed scanning involves moving the feed from the focal point. Electronic scanning uses a fixed or movable array of feed elements.

This chapter is a literature review of various reflector scanning techniques in preparation for discussion of the pattern synthesis compensation technique, Sec. 4.2. The different methods for scanning a parabolic reflector are outlined. The characteristics of scanned patterns are discussed. The majority of this chapter is devoted to single parabolic reflector antennas but the last section deals with dual reflectors.

3.1 DISPLACED FEED SCANNING

The main beam of a parabolic reflector can be scanned by displacing the feed from the focus. The pattern degrades with increasing scan due to phase errors introduced by

the displacement of the feed. These phase errors limit the range over which the reflector can be scanned.

Approximate scalar analysis for planar and linear apertures has been used to formulate expressions for the phase error caused by displacing the feed and to illustrate the pattern effects of the error. [37, 19] For an axisymmetric parabolic reflector with a feed at the focus, the far-field is (see Fig. 3.1-1) [37]

$$E(\theta, \phi) = \int_0^{2\pi} \int_0^{a} f(r, \phi')\, e^{jk(\rho - \vec{\rho} \cdot \hat{R})} r\, dr\, d\phi' \tag{3.1-1}$$

where a is the radius of the aperture, $f(r, \phi')$ is the effective aperture distribution, ρ defines the parabolic surface as $\rho = 2f/(1 - \cos\theta')$, $\hat{R}$ is a unit vector in the direction of $\vec{R}$, r is the perpendicular distance from the z-axis to the point of integration on the reflector surface, and the constants have been suppressed. Assuming that for small feed displacement the $f(r, \phi')$ is nearly unchanged, the far-field expression becomes [37]

$$E(\theta, \phi) = \int_0^{2\pi} \int_0^{a} f(r, \phi')\, e^{jk(\rho' - \vec{\rho}' \cdot \hat{R})} r\, dr\, d\phi' \tag{3.1-2}$$

where

$$\vec{\rho}' = \vec{\rho} + \epsilon_x \hat{x} + \epsilon_z \hat{z} \tag{3.1-3}$$

$$\rho' = \rho \left[1 + \frac{2\epsilon_x}{\rho} \cos\phi' \sin\theta' + \frac{2\epsilon_z}{\rho} \cos\theta' + \frac{\epsilon_x^2 + \epsilon_z^2}{\rho^2} \right]^{\frac{1}{2}} . \tag{3.1-4}$$

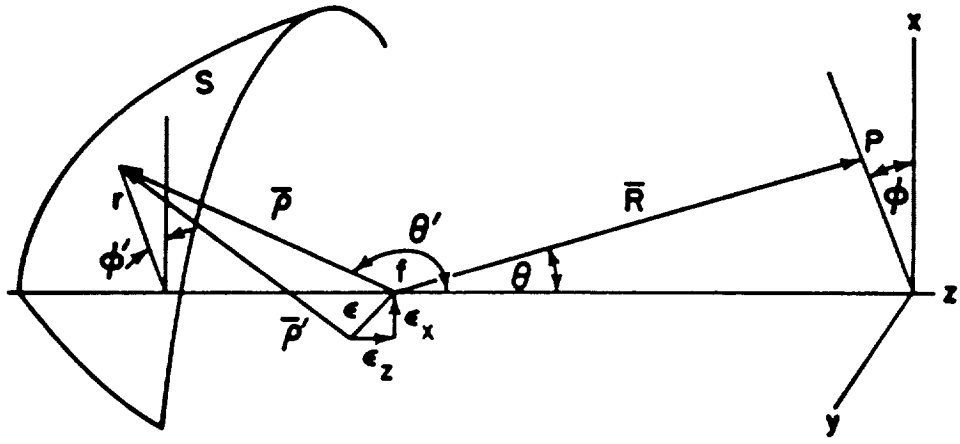

Figure 3.1-1. Geometry of the axisymmetric reflector used to analyze the errors associated with the displaced feed. [37]

3.1.1 PHASE ERROR TYPES

For small feed displacements [37]

$$\frac{\epsilon_x}{\rho} < \frac{\epsilon_x}{f} << 1 \tag{3.1-5}$$

the phase term in (3.1-2) can be approximated by (neglecting terms higher than $O(\epsilon_x^2)$) [37]

$$\begin{aligned} \rho' - \vec{\rho}' \cdot \hat{R} = 2f &- \epsilon_x \cos\phi \sin\theta - \epsilon_z \cos\theta \\ &- \rho \sin\theta' \sin\theta \cos(\phi' - \phi) + \epsilon_x \cos\phi' \sin\theta' \\ &+ \epsilon_z \cos\theta' + \frac{\epsilon_x^2}{2\rho} + \rho \cos\theta'(1 - \cos\theta) \\ &- \frac{\epsilon_x^2}{2\rho} \cos^2\phi' \sin^2\theta' \end{aligned} \tag{3.1-6}$$

where the first three terms are constants with respect to the integral of (3.1-2) and can be taken out of the integral. The next term is the normal phase term of a smooth parabolic reflector with the feed at the focus (see (3.1-1)). The remaining terms represent the phase errors introduced by displacing the feed from the axis.

The fifth term in (3.1-6) represents phase errors that are linear and cubic as a function of x. This is now demonstrated. Since [37]

$$\sin\theta' = \frac{r/f}{1 + (r/2f)^2} = \frac{r}{f}\left[1 - \left(\frac{r}{2f}\right)^2 + \left(\frac{r}{2f}\right)^4 - \cdots\right] \tag{3.1-7}$$

the phase error associated with the fifth term may be written as [37]

$$\delta = \frac{2\pi}{\lambda} u_s r \cos\phi' \left[1 - \left(\frac{r}{2f}\right)^2 + \left(\frac{r}{2f}\right)^4 - \cdots \right] \tag{3.1-8}$$

where [37]

$$u_s = \frac{\epsilon_x}{f} = \tan\theta_s \tag{3.1-9}$$

is a measure of the feed squint. The first term in (3.1-8) is linear as a function of x, $x = r\cos\phi'$. It is represented graphically in Fig. 3.1-2(a). This will cause a pattern shift equal to the feed squint away from boresight. [37] The second term in (3.1-8) is cubic term known as the coma aberration. It is shown in Fig. 3.1-2(b). It has perhaps the most severe impact on the radiation pattern of all the phase error terms. It causes a beam shift in the opposite direction of the linear term and degrades the pattern. [37] The pattern effects of just the cubic error term are shown in Fig. 3.1-3. The patterns in Fig. 3.1-3 are for a one-dimensional aperture. There is an additional exponential term in the far field pattern expression that represents the cubic error. The far field pattern for the cubic error is (following [19])

$$g(u) = \frac{d}{2} \int_{-1}^{1} f(x) e^{j(ux - \Delta L)} dx \tag{3.1-10}$$

where d is the diameter, $f(x)$ is the aperture distribution, $u = (\pi a/\lambda)\sin\theta$, and, for the cubic error, $\Delta L = \delta x^3$. The remaining terms in (3.1-8) are higher order coma terms. For high F/D-systems, they cause negligible contribution to the distortions. [37]

The sixth through eighth terms in (3.1-6) are field curvature terms (functions of r^2) [37] which are represented graphically in Fig. 3.1-2(c). The effects of this quadratic phase error are lower gain, higher side lobes, and filling of the nulls. [19] Figure 3.1-4

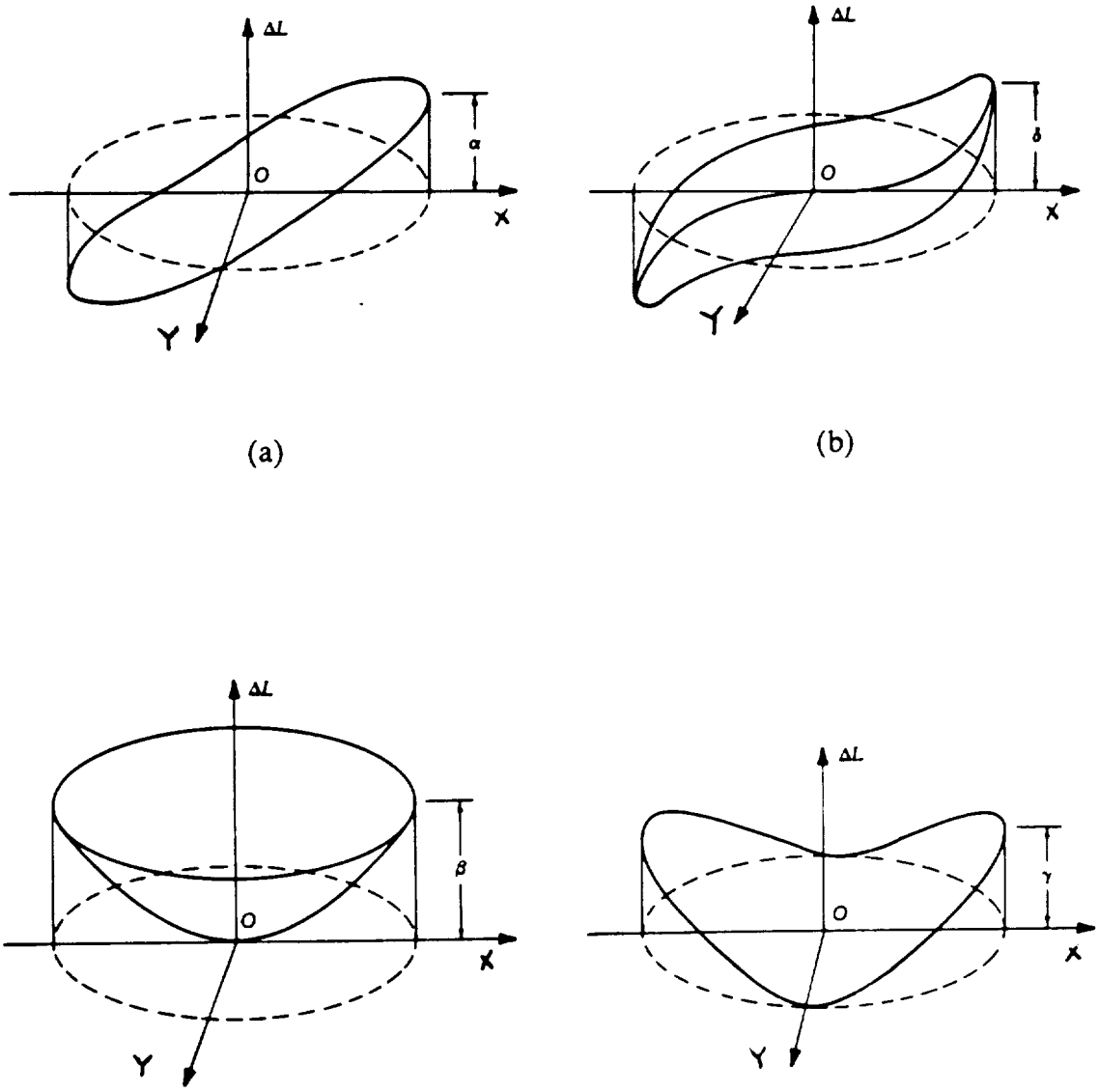

Figure 3.1-2. Phase errors associated with a small displacement of the feed from the focus. The phase errors, ΔL, are shown for the cases (a) linear, (b) coma, (c) curvature of field, and (d) astigmatism. (from [19])

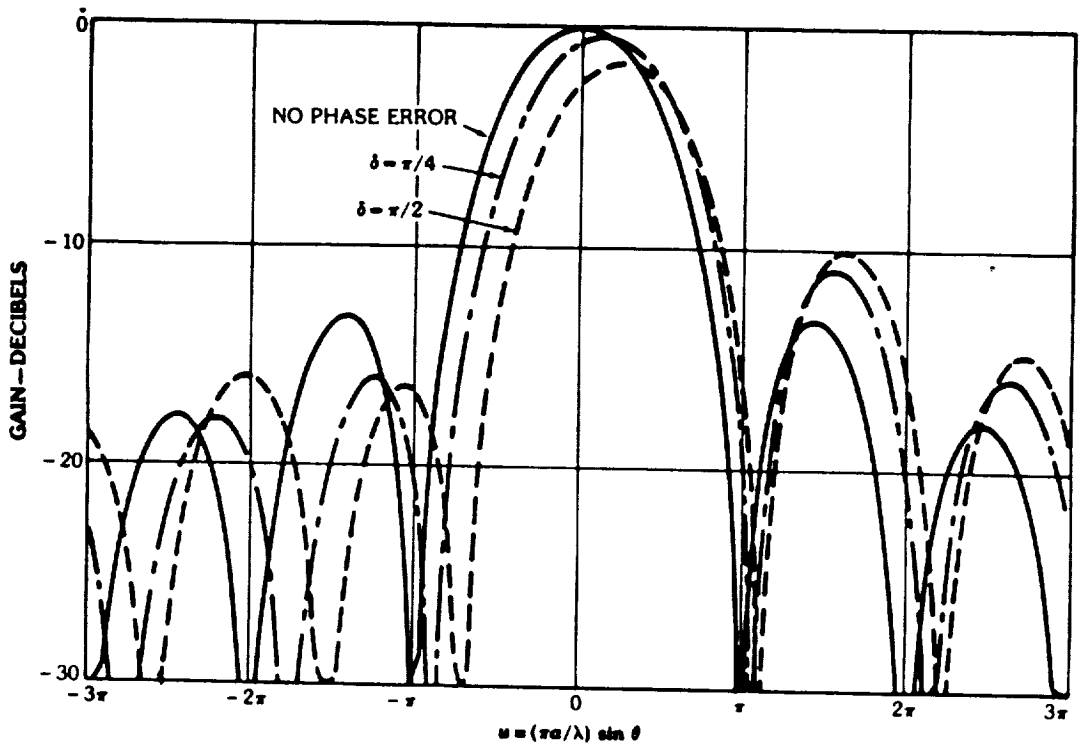

Figure 3.1-3. Pattern degradation due to the coma phase error only for a one-dimensional aperture. For this figure, the error is $\Delta L = \delta x^3$. [19]

shows the effects of just the field curvature terms. Equation (3.1-10) was used to compute the far field patterns of Fig. 3.1-4 with $\Delta L = \beta x^2$. [19] The error is symmetric with respect to the reflector axis so there is no scanning due to the curvature of field. The field curvature may be eliminated by axially displacing the feed parallel to the z-axis to a location corresponding to the Petzval surface from optics. [37] It is found by setting the field curvature terms to zero and solving for the axial displacement [37]

$$\epsilon_z = \frac{\epsilon_x^2}{2f} \quad . \tag{3.1-11}$$

Past studies indicate that the optimum z-displacement for maximum gain actually lies between the focal plane and the Petzval surface. [32, 12] This could be due to the loss from the field curvature phase error terms being overcome by the decrease in spillover. [32]

The last term in (3.1-6) is the astigmatism. It causes an asymmetric distortion in the radiation pattern. The astigmatism is shown in Fig. 3.1-2(d). The effects of the astigmatism are negligible for most parabolic antennas. Following [37], the ratio of the astigmatism to the total coma at the edge is [37]

$$\frac{\text{Astigmatism}}{\text{Total coma}} = \frac{2u_s(f/2a)}{\left[1 + (a/2f)^2\right]^2} \tag{3.1-12}$$

which, for small displacement ϵ_x, is a small quantity and the coma aberration effects would dominate.

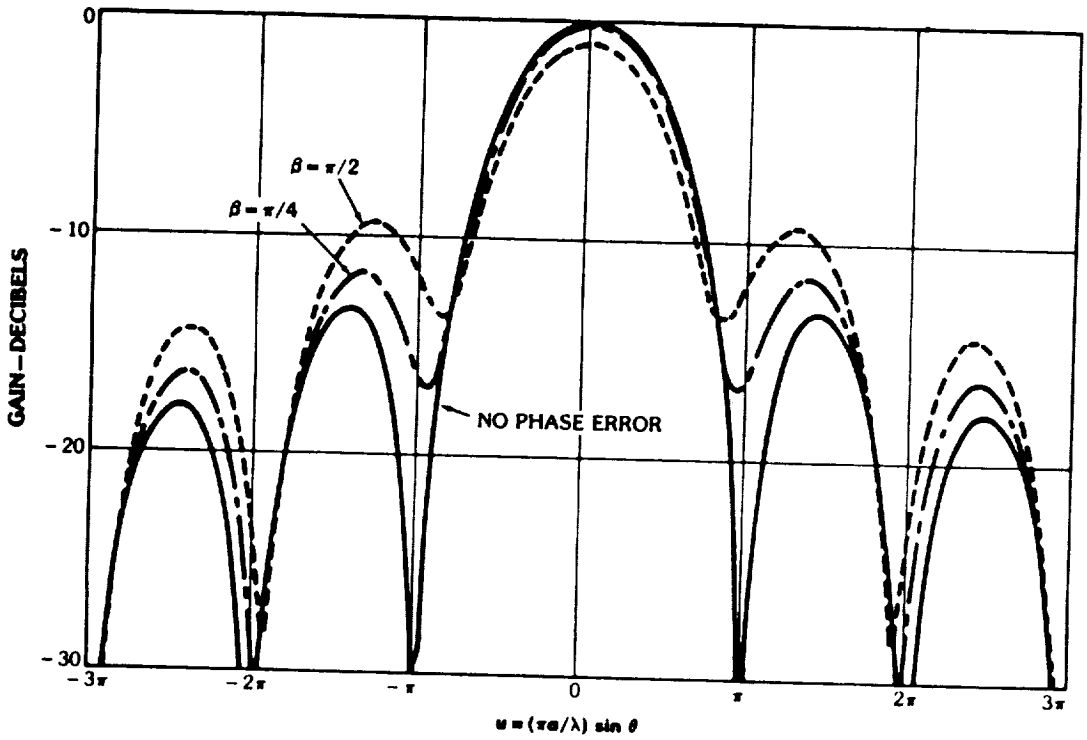

Figure 3.1-4. Pattern degradation due to the field curvature phase error only for a one-dimensional aperture. For this figure, $\Delta L = \beta x^2$. [19]

3.1.2 BEAM DEVIATION FACTOR FOR AXISYMMETRIC REFLECTORS

The scanning of a reflector is often characterized by the beam deviation factor (BDF). The BDF is essentially a measure of the equivalent curvature of the reflector surface. [54] The BDF is defined as [19]

$$BDF = \frac{\theta_B}{\theta_F} \tag{3.1-13}$$

where θ_B and θ_F are the beam scan angle and the feed tilt angle as defined by Fig. 3.1-5. For small feed displacements, the position of the beam maximum for the far field pattern is the value of $u = \sin\theta$ that minimizes the illumination-weighted squared phase error. [37] The minimization of the weighted error of a circularly symmetric aperture distribution leads to the classic result (using the geometry in Fig. 3.1-1) [37]

$$BDF = \frac{\int_0^a \frac{f(r)r^3}{1+(r/2f)^2}\,dr}{\int_0^a f(r)r^3\,dr} \tag{3.1-14}$$

where $f(r)$ is the aperture distribution. Equation (3.1-14) is valid for small scan angles with the feed on the Petzval surface. An approximate formulation for the BDF for small feed displacement is given by [20]

$$BDF = \frac{1+k(D/4f)^2}{1+(d/4f)^2} \tag{3.1-15}$$

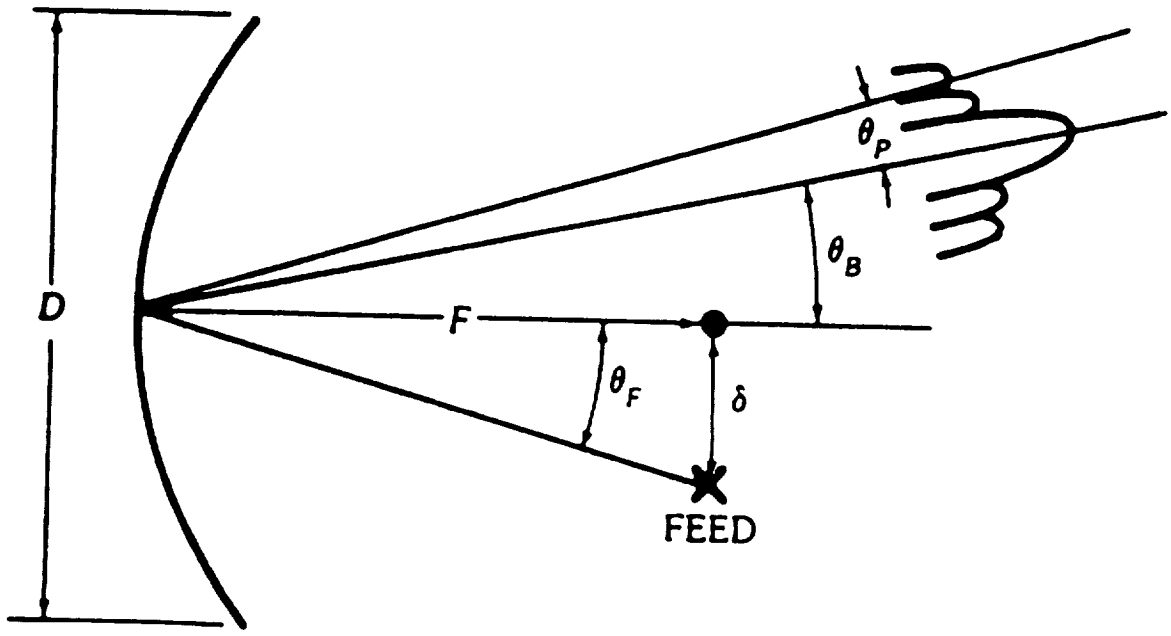

Figure 3.1-5. Angle definitions for the BDF of a symmetric paraboloid. The angle θ_P is the angle measured from the axis passing through the beam directed in the θ_B-direction. [19]

C2

where the diameter of the aperture $D = 2a$, and k is an empirically determined constant such that $0 < k < 1$. The values for k are generally in the range $0.3 < k < 0.7$ and k becomes larger with higher aperture tapering. [20]

The scan limit of a reflector is often chosen to be the angle where the gain drops by 1 dB. Ruze's approximate expression for the scan limit using the 1 dB loss criteria is [37]

$$N_B = 0.44 + 22(F/D)^2 \tag{3.1-16}$$

where N_B is the scan limit in beamwidths. This expression is limited to small angle scans.

Mrstik [24] developed a numerical approach using perturbation analysis in which the gain loss of the scanned beam was related to the rms phase errors introduced by displacing a single feed. [24] The numerical method is valid for any scan angle. Figure 3.1-6 shows plots of the numerical approach compared to (3.1-16). The curves for (3.1-16) give somewhat optimistic values for the scan limit in wide angle scan regions where the approximation used to derive (3.1-16) fails.

Examples of scanned beams are shown in Fig. 3.1-7 for a reflector with $F/D = 0.4$. Note that as the pattern is scanned farther from boresight, the distortion in the pattern increases. The first large side lobe on the axis side of the main beam is known as the coma lobe. The main lobe broadens with increasing scan and the first side lobe on the other side decreases, changes sign, and merges with the main lobe and second side lobe. [37]

The effects of the phase errors can be decreased somewhat by using a higher F/D reflector. This allows for scanning at wider angles. Figure 3.1-8 shows scanned patterns for a reflector with $F/D = 1.0$. Note the improved performance for the higher F/D reflector as compared to the patterns in Fig. 3.1-7. The drawback to using a higher

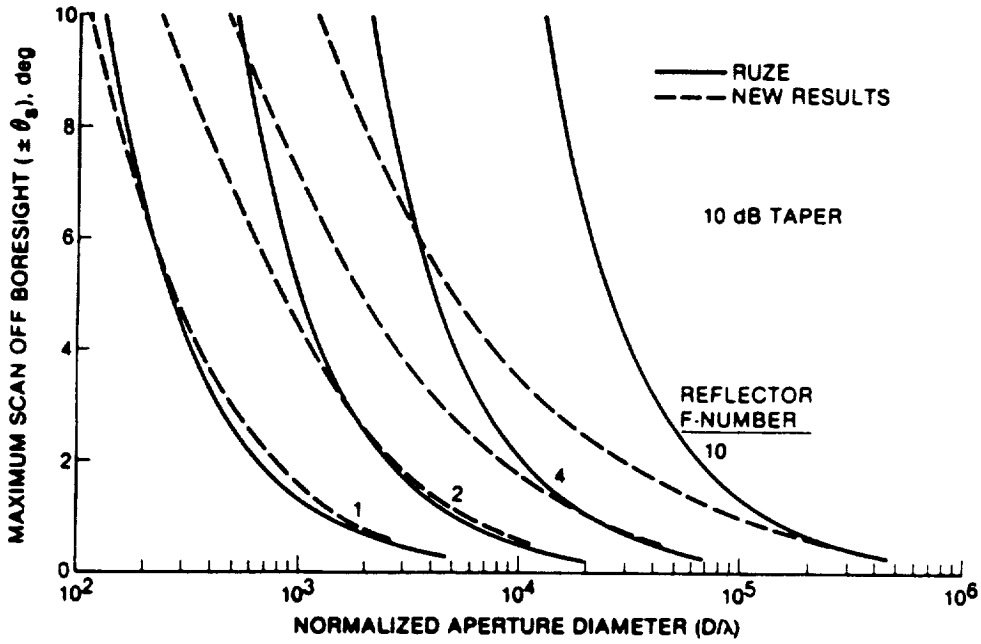

Figure 3.1-6. Scan limit comparing Ruze's approximation from (3.1-16) [37], the solid curves, and Mrstik's numerical approach [24], dashed curves, for a gain loss criteria of 1 dB. Ruze's approximation fails for wide angle scans where the approximations used to derive (3.1-16) fail. (Note: the "reflector F-number" is the F/D ratio) [24]

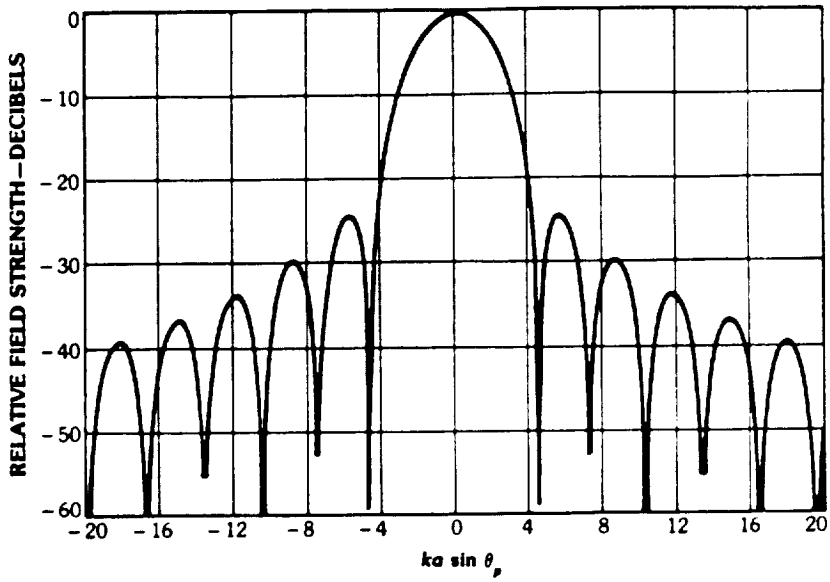

(a)

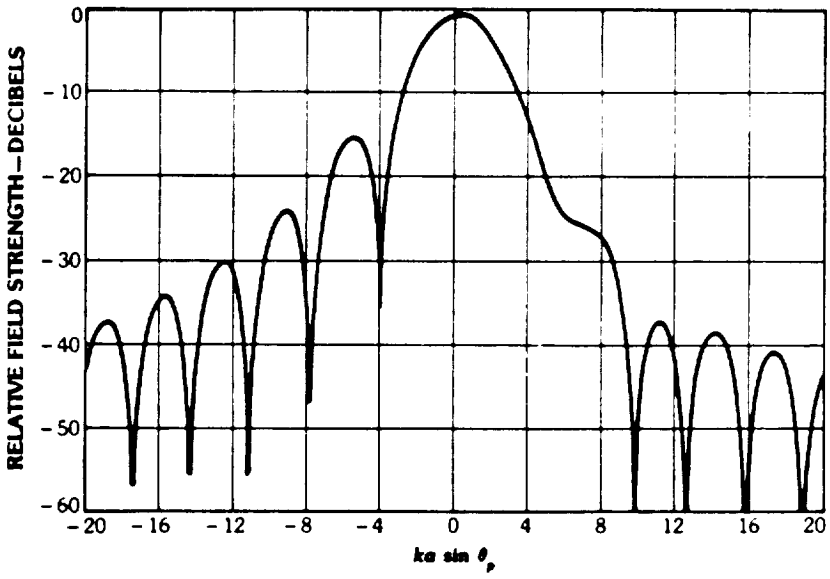

(b)

Figure 3.1-7. Radiation patterns for an axisymmetric ($F/D = 0.4$) reflector with a laterally displaced feed. The patterns are for scans of (a) 0 beamwidths, (b) 2 beamwidths, and (c) 6 beamwidths. The angle θ_p is measured from θ_B (see Fig. 3.1-5). [19]

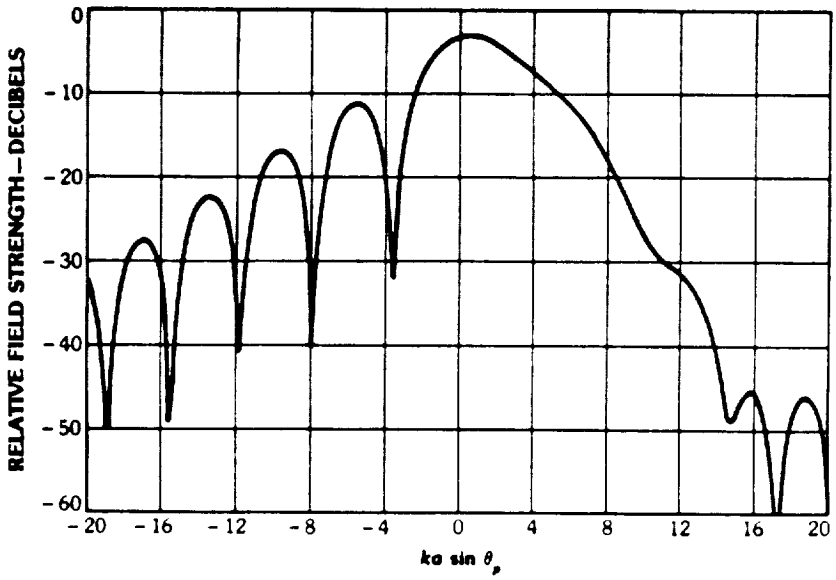

(c)

Figure 3.1-7. (cont.)

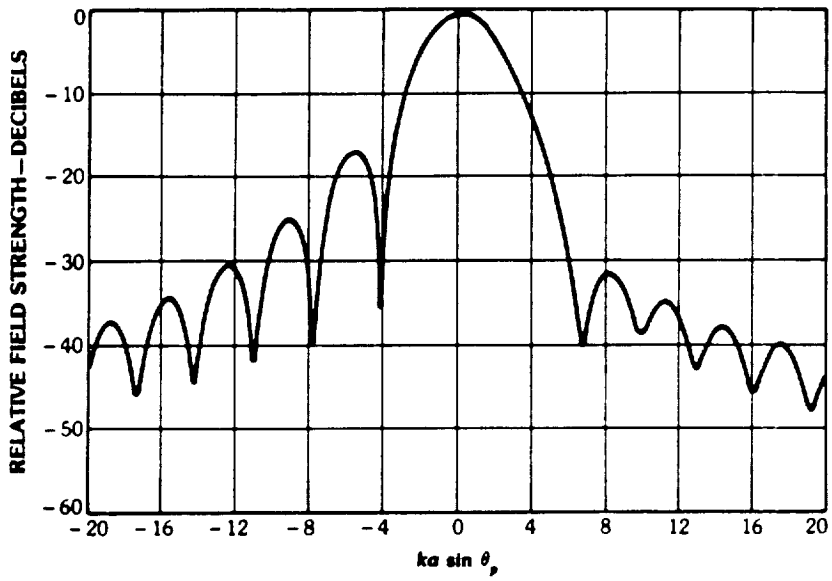

(a)

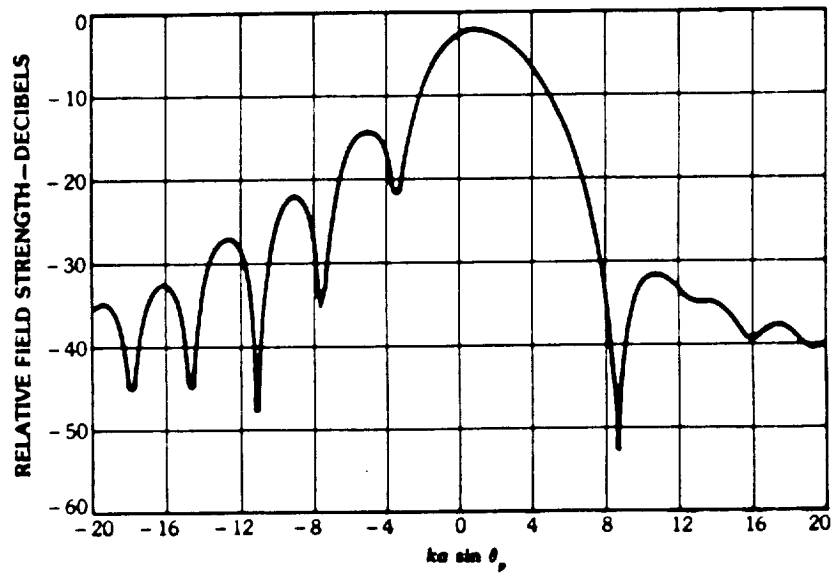

(b)

Figure 3.1-8. Radiation patterns for an axisymmetric ($F/D = 1.0$) reflector with a laterally displaced feed. The patterns are for scans of (a) 8 beamwidth and (b) 16 beamwidths. Note the improvement over Fig. 3.1-7. The angle θ_p is measured from θ_B (see Fig. 3.1-5). [19]

F/D reflector is that it requires a larger support structure for the feed. In addition, it requires a larger feed displacement to scan a given angle than lower F/D reflectors.

3.1.3 BEAM DEVIATION FACTOR FOR OFFSET REFLECTORS

The above discussion on displaced feed scanning pertained to axisymmetric reflectors. Offset configurations are often used to overcome blockage problems. The effects of the phase errors on the scanned patterns of offset reflectors are better characterized by the F/D_P (focal length to diameter of the parent paraboloid) ratio, rather than the actual F/D ratio. [19] The BDF of an offset reflector is computed using the angles defined in Fig. 3.1-9. Equation (3.1-13) is still valid for the angle θ_F measured relative to the ray locating the center of the reflector (the ray locating the center of the dish passes through the focal point along the angle ψ_C) and θ_B located relative to boresight.

3.2 ELECTRONIC SCANNING

Phase errors are the primary cause of distortion in the scanned radiation pattern of a reflector with a single displaced feed. The effects of the phase errors can be somewhat overcome by using an array of feeds. In a receive mode, the array elements are used to capture energy spread over the focal region and coherently combine it.

The studies using array feeds are divided into two main topics. Fixed array feeds are used for small angle scanning of the reflector without mechanical movement.

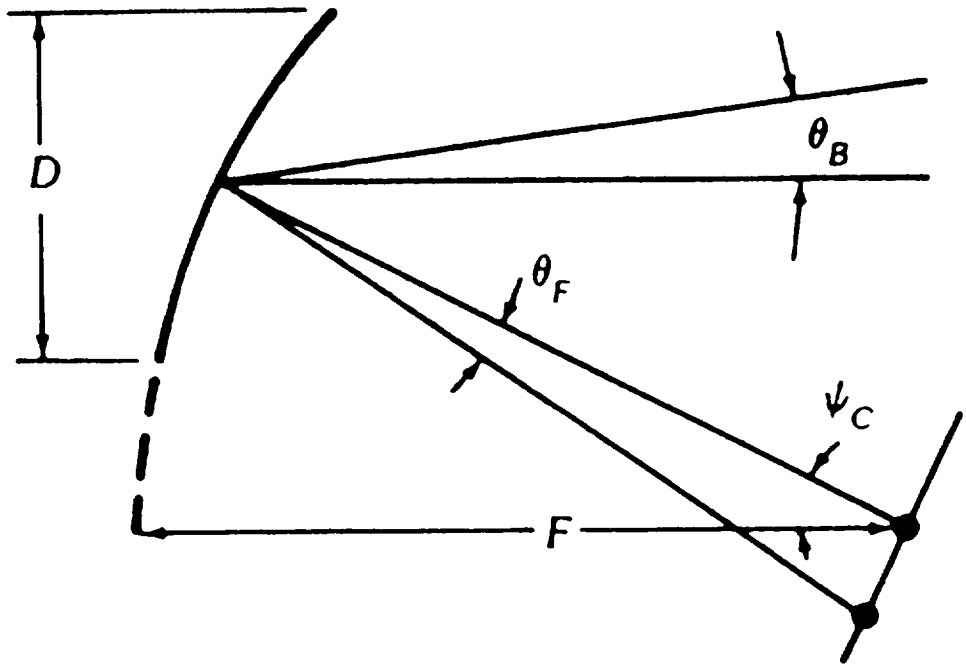

Figure 3.1-9. Angle definitions for the BDF of an offset paraboloid. [19]

Movable array feeds are used for wide angle scanning and are located at some optimum point for a given scan angle.

3.2.1 FIXED ARRAY FEED SCANNING

Of all the configurations, scanning with a fixed array feed is probably the most desirable from a system standpoint since there are no moving parts. A reflector with a fixed moderate size array feed is capable of scanning over a small number of beamwidths. To increase the scanning range significantly would require a very large feed array.

The majority of fixed array feed reflector scanning is accomplished using the method of conjugate field match (CFM) to compute the excitations for the feed elements (see Sec. 2.3.2). The CFM excitations are the complex conjugates of the field received by the ith array element as a result of a plane wave incident on the reflector aperture from the desired direction of scan. [7] The CFM excitations coherently combine the energy and increase the gain. [7] The program SCANRAP (see Sec. 5.2) uses CFM to compute the excitation coefficients for a scanned reflector with an array feed.

Studies were performed by Assaly and Ricardi [3] and Mrstik and Smith [23] on infinite cylindrical reflectors to examine the feasibility of scanning with fixed array feeds. The simpler math of the cylindrical reflectors provides better physical insight into the problem.

A moderate size cylindrical reflector with a fixed array feed was analyzed to examine the parameters associated with the scanning characteristics. [3] The axisymmetric reflector ($F/D = 0.5$, $D = 60\lambda$) had an array feed with various numbers of elements located a distance R from the parabola vertex and in a plane parallel to the

focal plane (see Fig 3.2-1). The feed array elements were symmetrically located at a distance σ from the focus-vertex plane. The σ ranged from -6λ to $+6\lambda$. DCFM (Sec. 2.3.2) was used to compute the feed excitations. The reflector is assumed to be illuminated by a plane wave incident from the desired direction of scan. The complex conjugates of the received signal are used as the DCFM element excitations.

The reflector was scanned from boresight out to $\theta_0 = 8°$. Three cases were evaluated for 21, 16, and 13 elements spaced 0.6λ, 0.8λ, and 1.0λ, respectively, with $R = 24\lambda$. Figure 3.2-2 shows examples of scanned patterns. Note that for Figs. 3.2-2(b) and 3.2-2(c) there are large side lobes. These are due to the larger spacings between the elements. The large element spacing does not allow the array to properly match the focal plane fields of the reflector. The minimum spacing providing satisfactory performance was found to be about 0.7λ . [3]

If the analysis were extended to a three-dimensional problem, the array would have to be increased considerably; the number of elements is n^2 instead of n elements as in the linear array feed for a cylinder. [3] For example, instead of 21 elements as in Fig. 3.2-2(a), about 441 elements would be required.

Mrstik and Smith [23] analyzed very large infinite cylindrical reflectors to determine the feasibility of scanning many beamwidths off boresight with fixed feed arrays. Electronic scanning analysis of these very large reflectors shows that wide angle scanning is not feasible with fixed feeds and further illustrates the problem of requiring unrealistic numbers of feed elements. The pattern results are discussed in Sec. 3.2.2.

One of the reflectors considered in [23] was axisymmetric with $F/D = 1.0$, $D = 1000\lambda$. To continuously scan the cylindrical reflector $\pm 5°$ (± 87 beamwidths) would require a feed array approximately 229λ in diameter with 0.5λ spacing (458 elements). To extend this to a three-dimensional problem would require on the order of 200,000 elements.

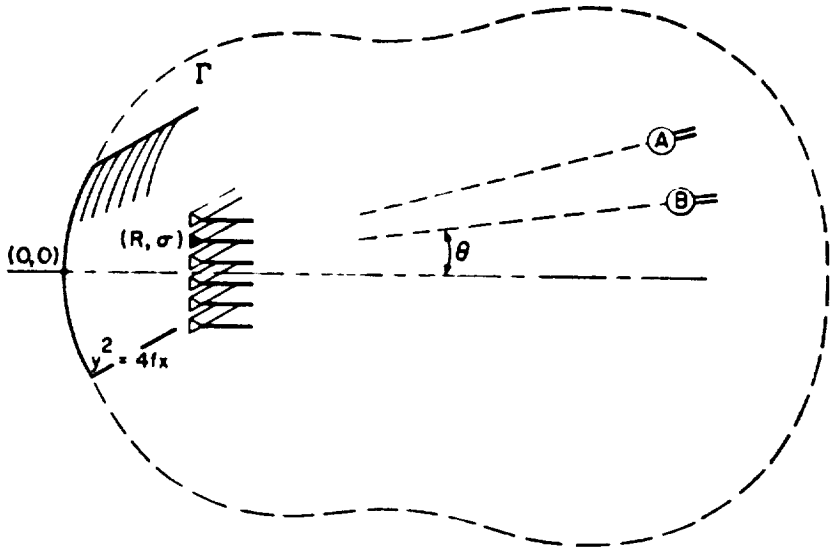

Figure 3.2-1. Geometry of the reflector used by Assaly and Ricardi to analyze the fixed array reflector scanning. [3]

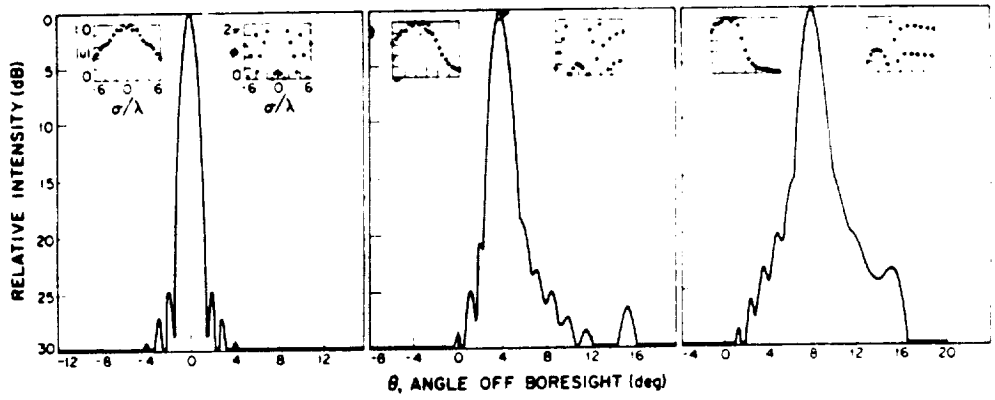

(a)

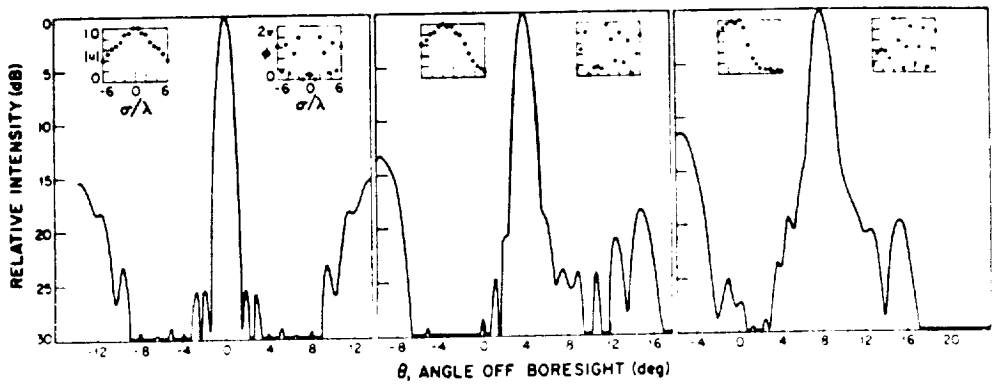

(b)

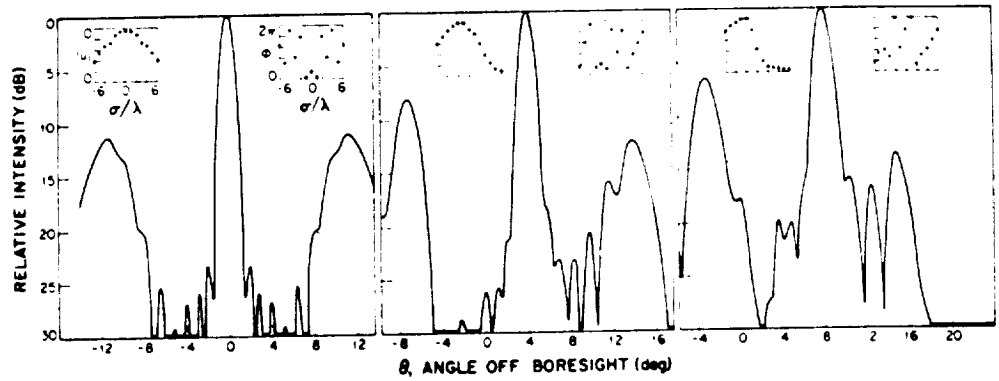

(c)

Figure 3.2-2. Far-field patterns for a cylindrical reflector ($F/D = 0.5$, $F = 30\lambda$) with a linear array feed located $R = 24\lambda$ from the parabola vertex with array feed diameter 12λ and (a) 21 elements with spacing of 0.6λ, (b) 16 elements with spacing of 0.8λ, and (c) 13 elements with spacing 1.0λ. [3]

Electronic scanning with moderate size fixed array feeds was studied by Blank and Imbriale [4, 7] for paraboloidal reflectors. ICFM (see Sec. 2.3.2) is used to determine the element excitations. [7] The reflectors ($F/D = 1.0$) were assumed to be smooth or distorted with [7]

$$\Delta z = \epsilon \rho^s \cos(L\zeta) \tag{3.2-1}$$

where Δz is the deviation in the z-direction of the distorted reflector from a smooth reflector, ϵ is the maximum deviation (λ), s is a real number, ρ is the normalized distance from the z-axis to a point on the reflector, L is the integer number of periodic scallops on the reflector, and ζ is as defined in Fig. 3.2-3(a). The feed array was chosen to be a triangular grid with $N = 7,\ 19,\ 37$ elements with optimal element diameters designed to maximize the gain on axis. [7] The optimal element diameters were determined empirically by evaluating the data from a parametric study. [7] Figure 3.2-3(b) shows the array configurations.

The curves in Fig. 3.2-3(c) show the gain loss as a function of scan angle for various numbers of feed elements and different distortion cases. The curves show that for the optimum gain 7-element case, the spacing of the feeds is too large to allow continuous scanning of a beamwidth. The 19-element case provides continuous scanning over ± 1 beamwidths while the 37-element case extends the continuous scanning to ± 1.8 beamwidths. [7]

3.2.2 MOVABLE FEED ARRAY SCANNING

Scanning a reflector with a movable array feed is not as desirable as the fixed array feed since it requires a moving feed assembly. It does, however, use a much smaller

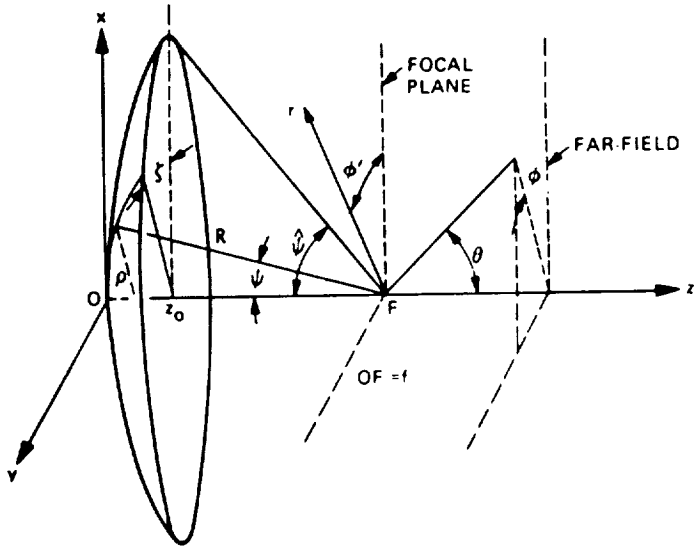

(a)

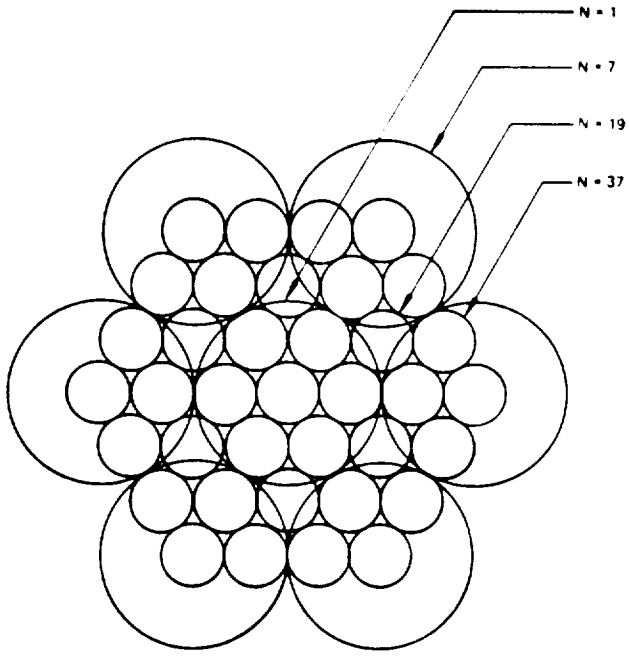

(b)

Figure 3.2-3. (a) Reflector geometry for scanning a paraboloidal reflector with a fixed array feed. (b) Optimum gain array feed configurations. (c) Gain loss as a function of scan angle ($F/D = 1$, $s = 2$, $\epsilon = 0$, 0.12, 0.2). [7]

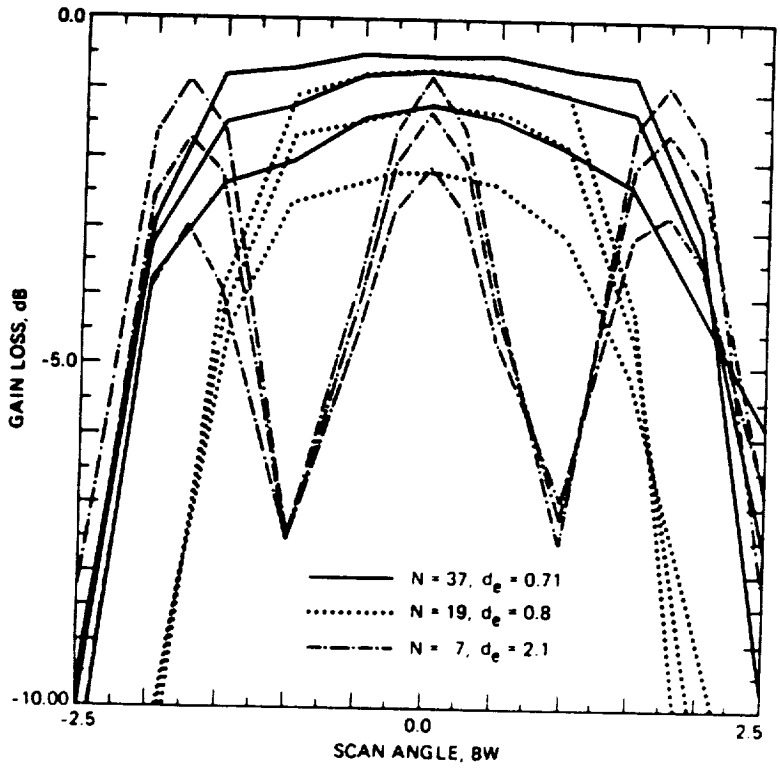

(c)

Figure 3.2-3. (cont.)

array when wide angle scanning is required. The pattern of a reflector using a movable array feed is, of course, much improved over that of a single displaced feed.

Rudge and Withers [38] developed a double Fourier transform technique for scanning a finite cylindrical reflector with a movable array feed. The technique exploits the approximate Fourier transform relationship between the received aperture plane distribution and focal plane fields. For a plane wave received at boresight, the received aperture plane distribution is a constant amplitude, constant phase function and the focal plane fields are of the "$\sin \alpha x/\alpha x$" form. If the focal plane field is acted upon by a device that implements another Fourier transform, the output of the device is again a constant amplitude, constant phase function. In practice, the second Fourier transform has been approximately implemented with a Butler matrix. [38]

The reflector subtends an angle $2\theta^*$ (see Fig. 3.2-4(a)). Rudge and Withers [38] found that as a single feed is moved if it maintains the subtended angle constant $2\theta^*$ (defined in Fig. 3.2-4(b)), that the relationship between the aperture plane fields and the focal plane fields as defined in the new transform plane are related by a Fourier transform as in the unscanned case. For a plane wave received in a direction other than boresight, the plane wave is acted upon by a second Fourier transform in the new transform plane. The output is a constant amplitude function with phase variation that is the complex conjugate of the aperture plane field. [39] Phase shifters can then be used to coherently combine the received signal and feed element amplitude control is not necessary. [38] This method was experimentally implemented with a moderate size cylindrical reflector and scanning of ± 15 beamwidths was achieved. [38]

Hung and Mittra [12] used the CFM method to improve the scanning characteristics of a reflector with a movable array feed. The analysis involved designing the geometry of a moderate size feed array based on the focal region field distribution.

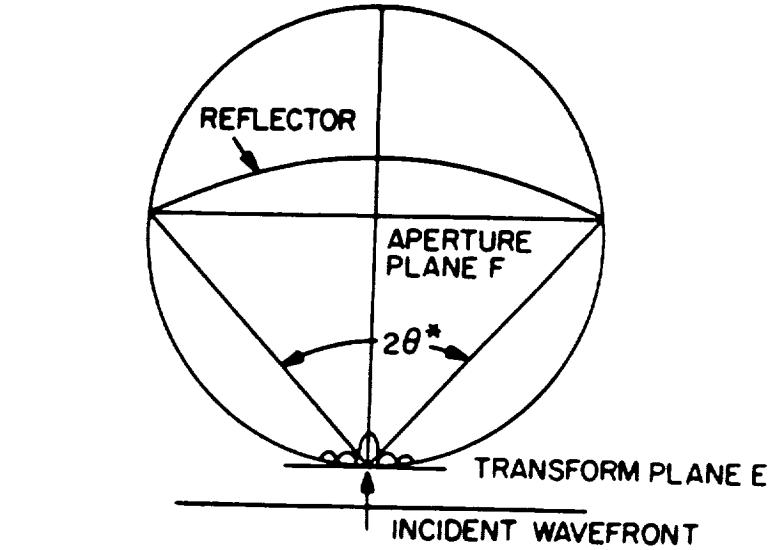

(a)

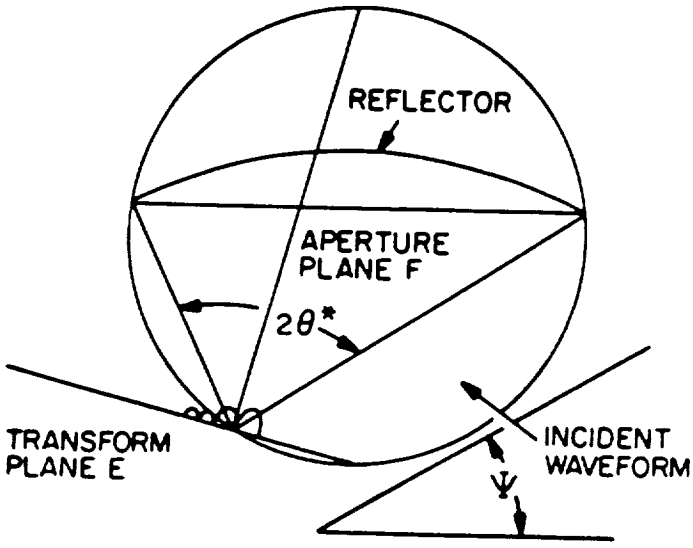

(b)

Figure 3.2-4. Location of the transform planes for a reflector that is (a) unscanned (focal plane) or (b) scanned off boresight. [39]

A large axisymmetric paraboloidal reflector ($F/D = 0.48$, $D = 550\lambda$) was evaluated for wide angle scanning. The focal region field contours are shown in Fig. 2.2-9 for the cases of a received plane wave incident from 2.5° and 5°. From evaluation of the focal plane fields, a 27-element RN^2 triangular array of Fig. 3.2-5(a) was chosen to feed the reflector. [12]

The array center was located in a position that maximized the gain for a given scan location. [12] This optimum location corresponded to the peak of the focal region field distributions from Fig. 2.2-9. The secondary pattern for the cases of no scan, 2.5° scan (24 beamwidths), and 5.2° scan (48 beamwidths) are shown in Fig.'s 3.2-5(b), (c), and (d), respectively. The scanned pattern produced by the array is compared to that of a scanned pattern produced by a single feed.

Directivity optimization has also been used to improve the scanning characteristics of an offset reflector with a movable array feed. [17] Directivity optimization is a method for computing the feed array element excitations that maximize the directivity of the reflector for a given angle of scan. The formula for directivity of a reflector with an array feed was differentiated with respect to the unknown excitations of the array elements. The resulting equation was then solved for the excitations that give optimum directivity.

The reflector that was analyzed with directivity optimization was an offset reflector ($F = 94.87\lambda$, $D = 108.15\lambda$, $F/D_p = 0.38$, Fig. 3.2-6(a)). [17] For a 10 beamwidth scan, the feed was displaced by 10.65λ in the y-direction. Three patterns are plotted in Fig. 3.2-6(b). The results are shown for a single displaced feed and for 19-element triangular grid arrays with either CFM or directivity optimization excitations. As in most of the examples in the paper, the directivity optimization produced patterns with the highest directive gain. [17]

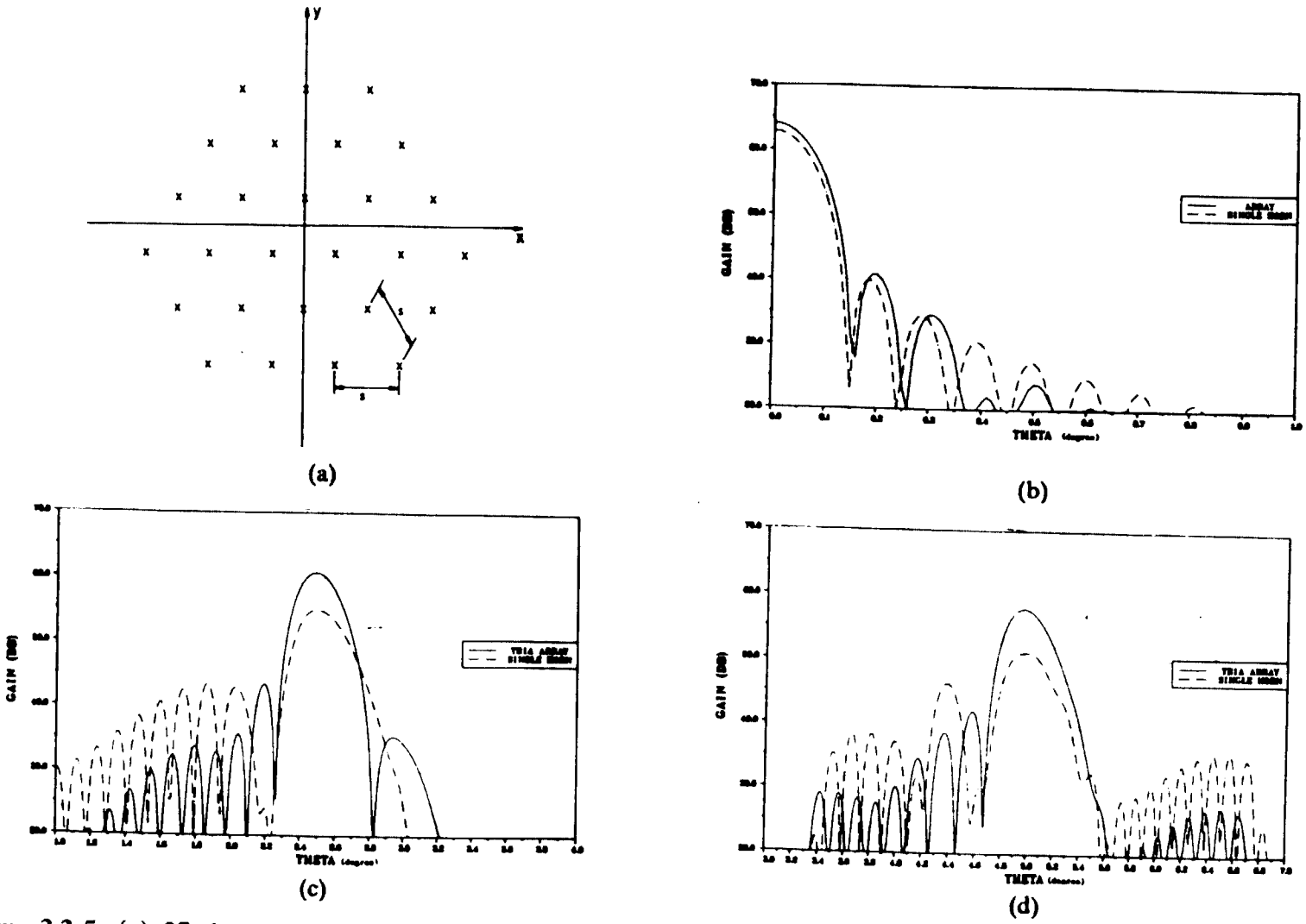

Figure 3.2-5. (a) 27-element RN^2 triangular array used in CFM scanning analysis. Single feed (dashed line) and RN^2 triangular array (solid) patterns for (b) no scan, (c) 2.5 ° scan, and (d) 5° scan. [12]

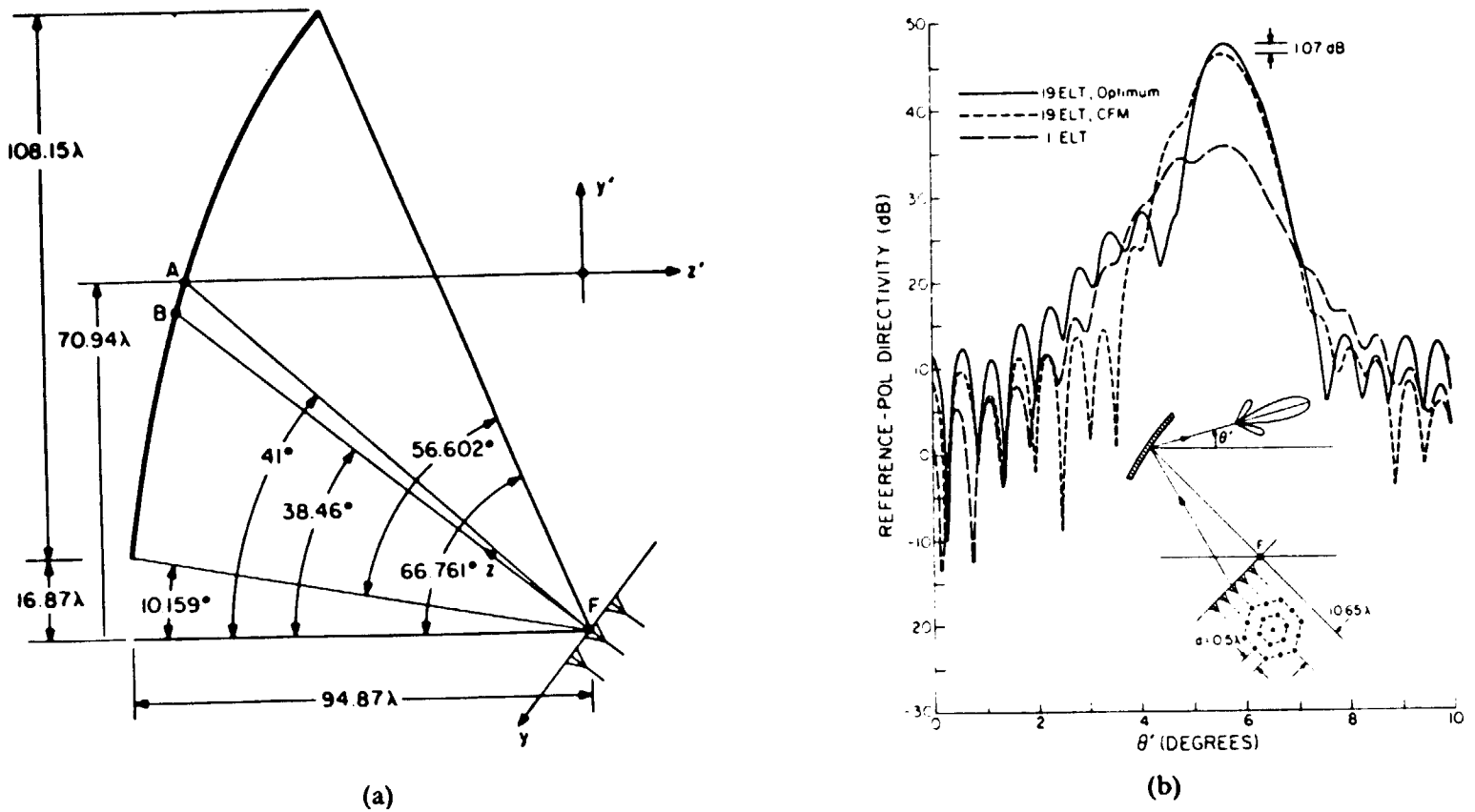

Figure 3.2-6. (a) Offset paraboloidal reflector geometry for directivity optimization scanning analysis. (b) E-plane patterns for the scanned offset reflector using a single feed (long dash), triangular array with CFM (short dash), and triangular array with directivity optimization (solid). [17]

3.3 DUAL REFLECTOR SCANNING

In Sec. 3.1, it was pointed out that the effects of the phase errors associated with scanning a reflector can be decreased somewhat by using a higher F/D reflector. To increase the F/D of a single reflector would require a larger feed structure. A possible alternative is to use a dual reflector with a higher virtual F/D.

The scanned dual reflectors considered for this study are of the classic Cassegrain or Gregorian types. The subreflector is either a hyperboloidal or an elliptical function and the main reflector is paraboloidal. Shaped reflectors were not considered.

Early Cassegrain reflectors were analyzed by the concept of an equivalent parabola. [13] This technique is advantageous as it saves much computational time since only one reflector needs to be analyzed. The main reflector and subreflector are replaced by an equivalent parabolic reflector with focal length F_e (see Fig. 3.3-1). Some important parameter relationships between the dual reflector and the equivalent reflector are [13]

$$\frac{1}{4}\frac{D_m}{F_e} = \tan\frac{1}{2}\phi_r \tag{3.3-1}$$

$$x_e = \frac{y_e^2}{4F_e} \tag{3.3-2}$$

$$\pm\frac{F_e}{F_m} = \frac{\tan\frac{1}{2}\phi_v}{\tan\frac{1}{2}\phi_r} = \frac{L_r}{L_v} = \frac{e+1}{e-1} \tag{3.3-3}$$

where in (3.3-3) the positive sign is for the Cassegrain and the negative sign is for the Gregorian.

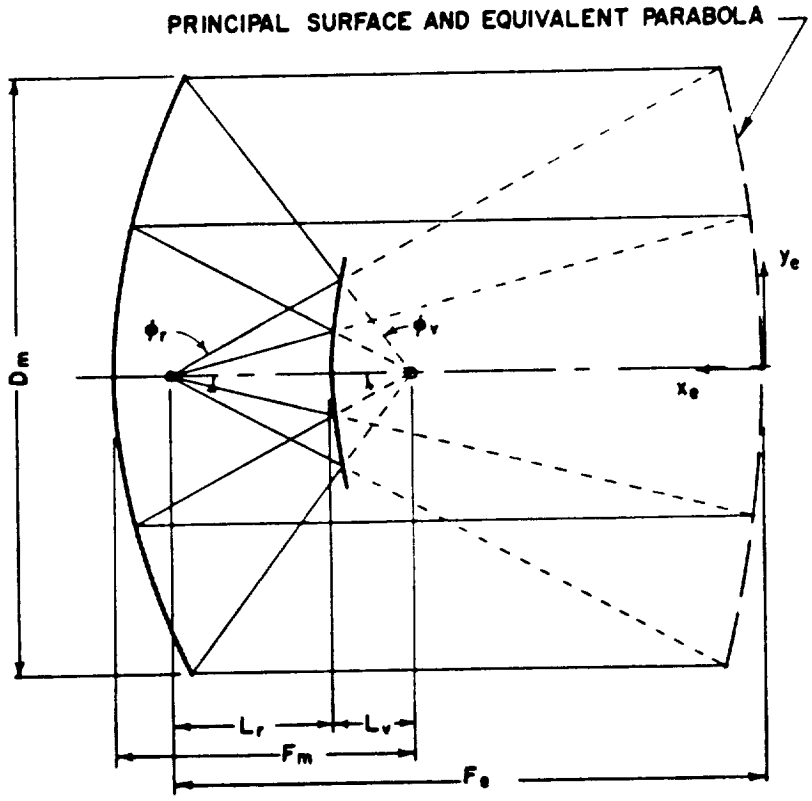

Figure 3.3-1. Geometry of a Cassegrain reflector and its equivalent parabolic reflector. [13]

The pattern of a Cassegrain can be evaluated using the equivalent reflector technique for small angle scans. The coma aberration of the Cassegrain is nearly the same as for the equivalent reflector when the feed is displaced near the focus. [13] For larger scans, however, the equivalent parabola concept fails to provide accurate results [40]; this is discussed further now.

Wong [59] compared the equivalent reflector technique to a PO/PO analysis of a Cassegrain reflector for small scans. Figure 3.3-2(a) shows the geometry of the PO/PO analysis. The feeds were assumed to have a pattern approximated by a $\cos^n\theta$-type power pattern. [59] The results of the study for various values of n and ratios of the subreflector diameter and main reflector diameter showed that the aperture efficiencies of the PO/PO analysis and the equivalent reflector analysis differed by less than 10%. [59] Examples of scanned radiation patterns comparing the two techniques are shown in Fig. 3.3-2(b). The study concluded that the equivalent parabola technique was valid for up to about 4 beamwidth scans. [59]

Rahmat-Samii and Galindo-Israel [40] evaluated the equivalent paraboloid technique for offset Cassegrain reflectors using GTD/PO analysis of the dual reflector. [40] The gain loss as a function of the number of beamwidths scanned is shown in Fig. 3.3-3. The plots in Fig. 3.3-3 compare the characteristics of the Cassegrain, the equivalent paraboloid, and the main reflector by itself. The plots show that the scan performance of the actual dual reflector is somewhere in between that of the equivalent paraboloid and the single main reflector. [40]

Optimum feed locations for prime focus reflectors were related to the Petzval surface in Sec. 3.1. Krichevsky and DiFonzo [15, 16] studied optimum feed locations for Cassegrain and Gregorian antennas. The method for finding the optimum feed locations has two steps. The locus of feed positions that produce a scanned beam in the desired direction is determined with an approximate ray tracing technique. [15] The first order

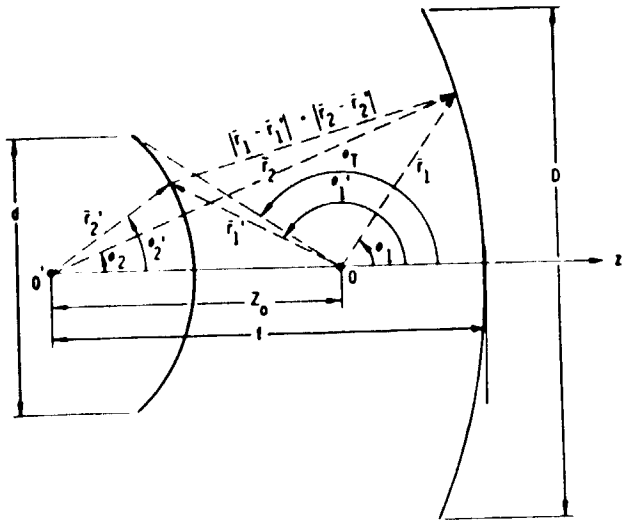

(a)

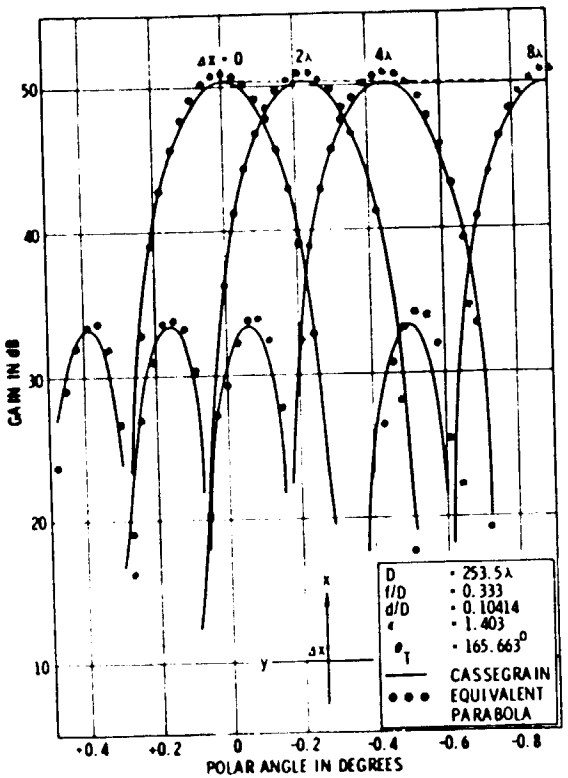

(b)

Figure 3.3-2. (a) Reflector geometry for PO/PO analysis of a Cassegrain reflector. (b) E-plane patterns for the Cassegrain reflector with a laterally displaced feed. The results are for the PO/PO analysis and the equivalent reflector analysis. [59]

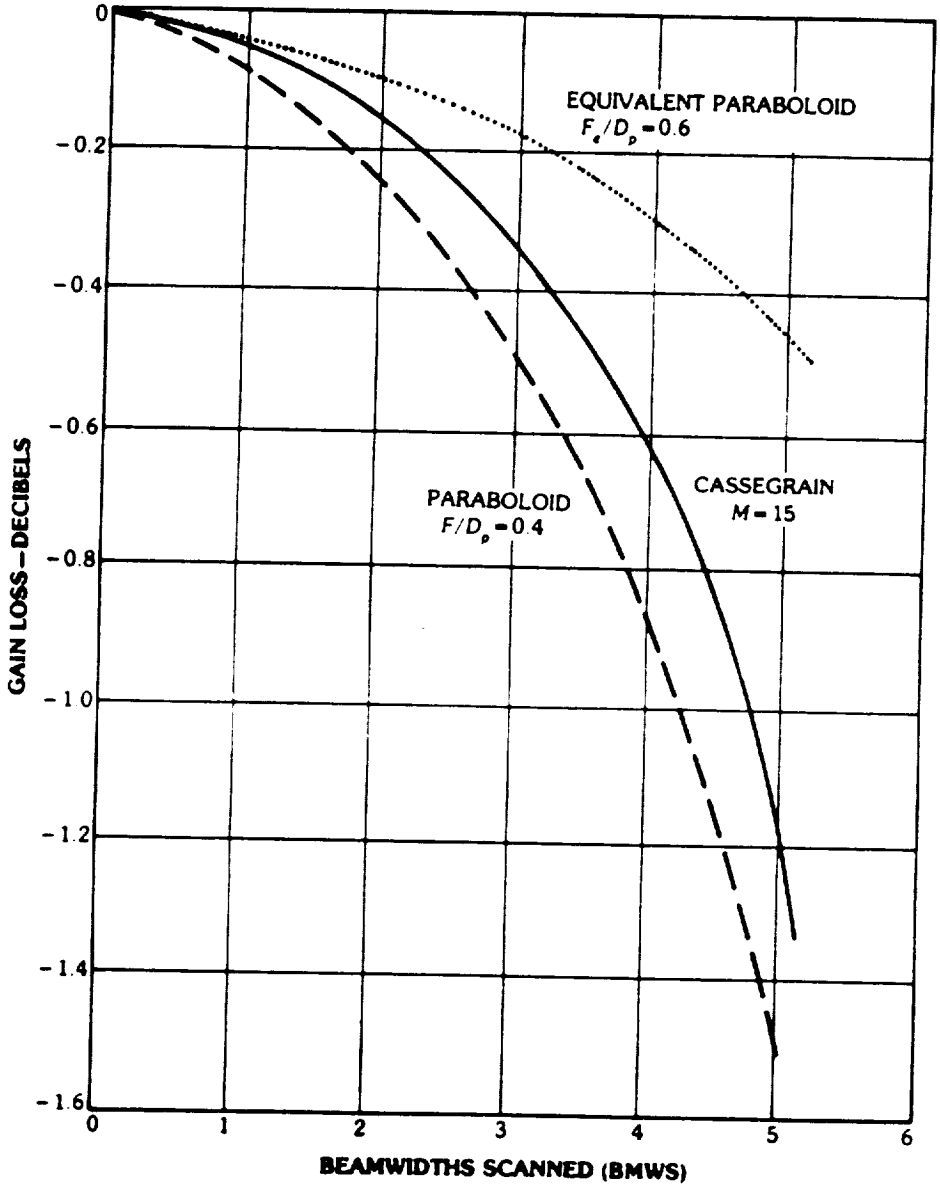

Figure 3.3-3. Gain loss performance for an offset Cassegrain reflector. The plots show the loss characteristics for the Cassegrain reflector using GTD/PO analysis (solid curve), equivalent paraboloid (dotted), and prime focus system using the main reflector (dashed). [19]

approximation of the locus of points for a constant beam scan angle is a straight line (valid for small angle scans). [15] The optimum location for the feed is at the point along the locus that minimizes the phase error for the given direction of scan. [15] Computer analysis of several antenna configurations showed that this method provides the best location for the feed in terms of gain, pattern symmetry, and null depth. [16]

The geometry of an offset Cassegrain reflector is shown in Fig. 3.3-4(a). To a first order approximation, the optimum feed loci of a Cassegrain reflector for given scan angles are located along a line. [15] In Fig. 3.3-4(b), the dashed line represents the first order approximation to the loci of optimum feed locations. To a second order approximation, the optimum feed loci of a Cassegrain reflector are located along a hyperbola. [15] In Fig. 3.3-4(b), the solid hyperbolic curve represents the second order approximation to the loci of optimum feed locations. For a Gregorian reflector, the second order approximation places the optimum feed loci along an ellipse. [16]

Examples of scanned beams as a function of several feed locations for the offset reflector are shown in Fig. 3.3-5. The radiation patterns of the reflectors with their feeds located along the optimum second order curve have the best characteristics.

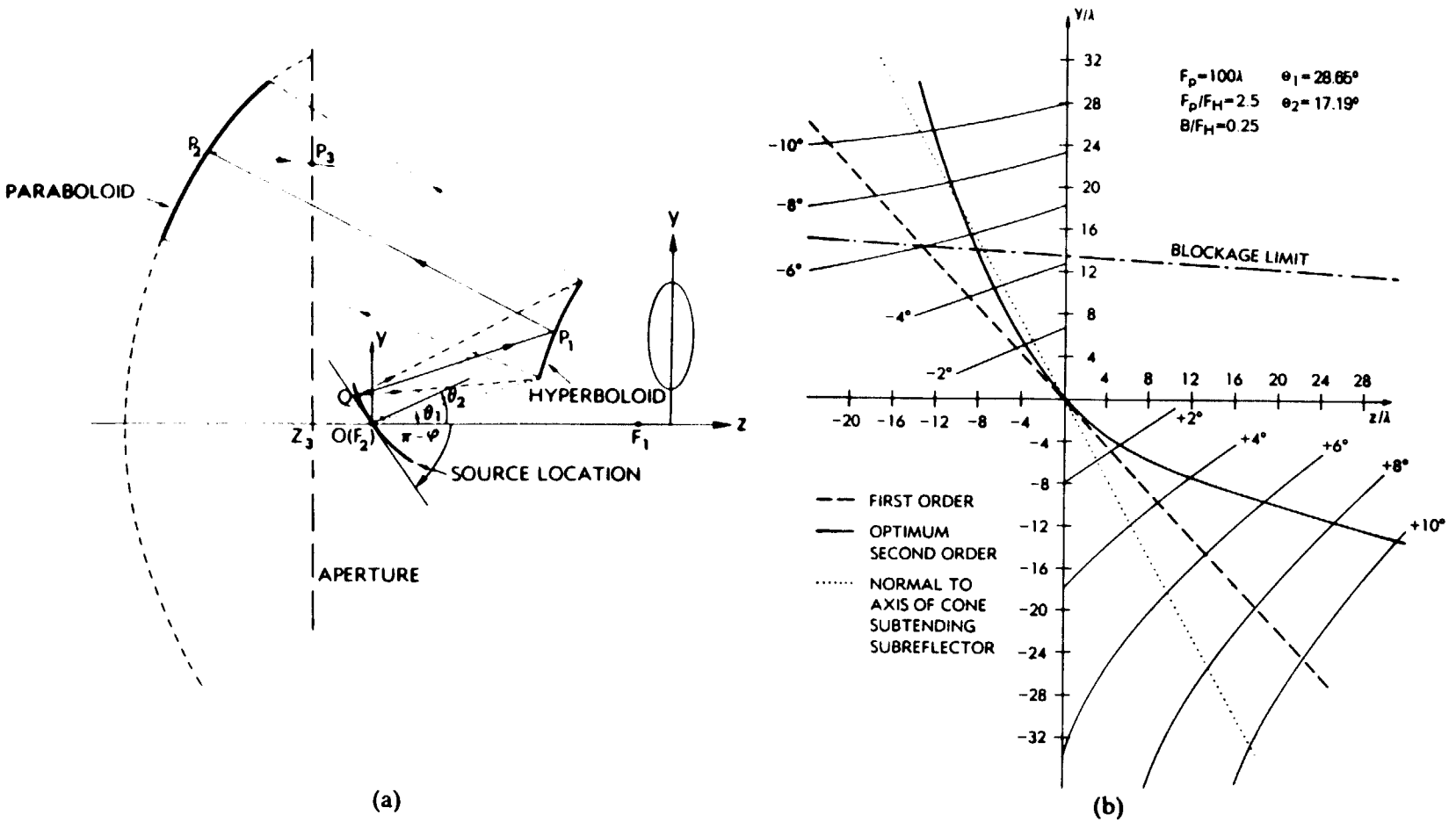

Figure 3.3-4. (a) Reflector geometry for optimum feed location analysis of an offset Cassegrain reflector. (b) Optimum feed loci (both approximations) and constant scan contours for the offset Cassegrain reflector. [15]

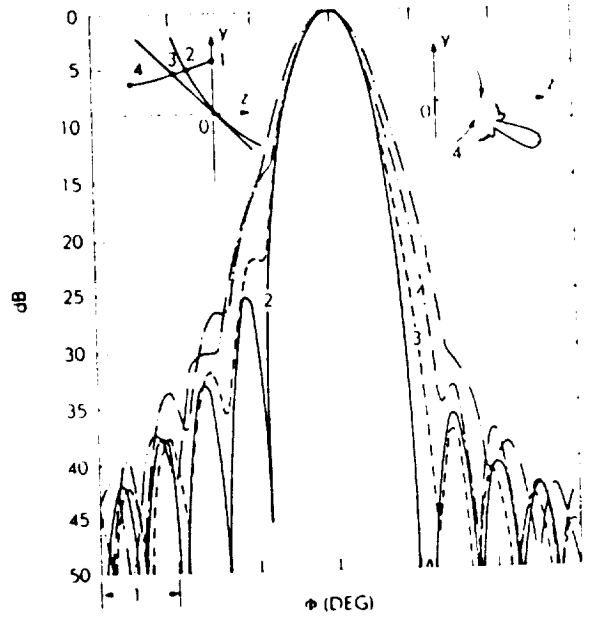

(a)

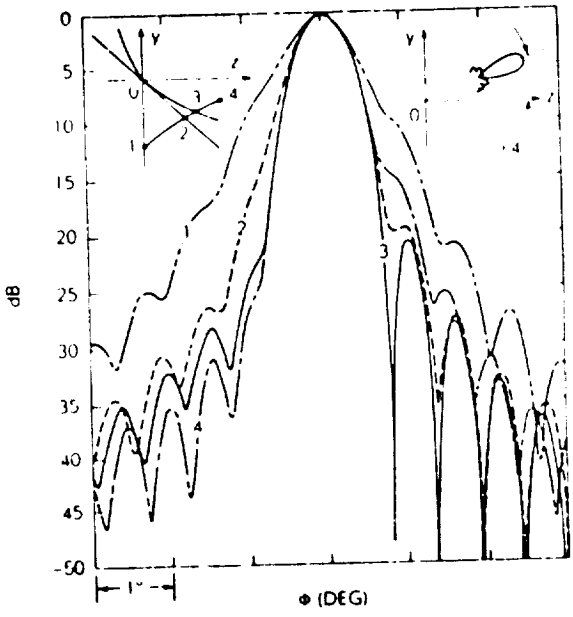

(b)

Figure 3.3-5. Patterns for the offset Cassegrain reflector as functions of feed location. The feeds are located in two arbitrary locations and at the optimum locations for the first order and second order approximations. The patterns are for beams scanned to (a) -4° (first order - point 3; second order - point 2) and (b) +4° (first order - point 2; second order - point 3). [15]

4.0 PATTERN SYNTHESIS COMPENSATION TECHNIQUE

The pattern synthesis compensation technique is based on the iterative sampling method (ISM). The ISM was originally formulated to synthesize shaped radiation patterns for line sources, linear arrays, rectangular apertures, and rectangular arrays. [48, 49, 50, 51] The pattern synthesis compensation technique corrects pattern irregularities caused by surface errors by superposing correction beams with the original distorted pattern. The corrections can be applied in a series of iterations.

In this chapter, the original formulation for ISM is outlined. The ISM is extended for application to reflector problems. This extended ISM is then applied to formulate the pattern synthesis compensation technique.

4.1 ITERATIVE SAMPLING METHOD

4.1.1 ITERATIVE SAMPLING METHOD ALGORITHM

The iterative sampling method for real-valued beam synthesis begins with some original pattern that is an approximation to the desired radiation pattern. The first iteration is to add a series of correction patterns to the original approximate pattern. If the resulting pattern is not satisfactory, more iterations of correction patterns are applied. The total pattern correction is the sum of the weighted correction patterns.

For the ith iteration, the total correction for a linear source is [48]

$$\Delta F^{(i)}(u) = \sum_n a_n^{(i)} G(u - u_n^{(i)}) \tag{4.1-1}$$

where , for a z-directed source, $u = \cos\theta$, $a_n^{(i)}$ is the correction pattern weight, and $G(u - u_n^{(i)})$ is the normalized pattern with a main beam centered at $u_n^{(i)}$ and maximum amplitude of unity. After K iterations, the resultant improved approximation to the desired pattern is [48]

$$F^{(K)}(u) = F^{(0)}(u) + \sum_{i=1}^{K} \Delta F^{(i)}(u) \tag{4.1-2}$$

where $F^{(0)}(u)$ is the original approximate pattern.

The correction pattern for a line source has a correction current $g_n^{(i)}(s)$ related to the pattern by [48]

$$G_{ls}(u-u_n^{(i)}) = \int_{L_{ls}} g_n^{(i)}(s)\exp(j2\pi us)ds \tag{4.1-3}$$

where $s = z/\lambda$ and L_{ls} is the length of the source. The total correction current for the ith iteration for the line source is [48]

$$\Delta f_{ls}^{(i)}(s) = \sum_n a_n^{(i)} g_n^{(i)}(s) \tag{4.1-4}$$

and the total current after K iterations is [48]

$$f_{ls}^{(K)}(s) = f_{ls}^{(0)}(s) + \sum_i \Delta f_{ls}^{(i)}(s) \tag{4.1-5}$$

where $f_{ls}^{(0)}(s)$ is the current distribution of the original approximate pattern.

For a linear array, the corresponding correction current terms $g_{mn}^{(i)}$ are related to the correction pattern by [48]

$$G_{ar}(u-u_n^{(i)}) = \sum_m g_{mn}^{(i)}\exp(j2\pi us_m) \tag{4.1-6}$$

where s_m are the normalized element positions. The total correction for the ith iteration current of the mth element of the linear array is [48]

$$\Delta I_m^{(i)} = \sum_n a_n^{(i)} g_{mn}^{(i)} \tag{4.1-7}$$

and the total current of the mth element after K iterations is [48]

$$I_m^{(K)} = I_m^{(0)} + \sum_l \Delta I_m^{(l)} \tag{4.1-8}$$

where $I_m^{(0)}$ is the current excitation for the original approximate pattern.

A good choice for the weights is [48]

$$a_n^{(l)} = F_d(u_n^{(l)}) - F^{(l-1)}(u_n^{(l)}) \tag{4.1-9}$$

where $F_d(u)$ is the desired pattern. A good choice for the iterative sample points is [48]

$$u_n^{(l)} = \frac{u_n^{(l-1)} + u_{n-1}^{(l-1)}}{2} \quad . \tag{4.1-10}$$

As the number of iterations increases, the pattern approaches the desired pattern to within some acceptable limits and the number of iterative sample points decreases. [48]

The two-dimensional aperture or array problem has a similar formulation except that the single integrals and summations now become double integrals and summations. The patterns and distributions are now bivariate. [50]

4.1.2 APPLICATION OF ISM TO REFLECTORS

In this section, a formulation for extending the ISM to reflectors is presented. Implementing the iterative sampling method with reflector antennas is a difficult problem. With a planar phased array, there is much more control over the amplitude and phase of the radiating currents. With a reflector, the radiating current is an induced current on the surface of the reflector. Scanning of correction patterns is accomplished with feeds displaced from the focal point or by an array of feeds weighted to

electronically scan beams. The amplitude and phase of the scanned pattern currents have inherent amplitude and phase errors that cause the side lobe level and beamwidth to increase with increasing scan. The gain of the scanned correction patterns decreases with increasing scan (see Chapter 3). Furthermore, the radiation pattern is in general a complex valued vector quantity so the phase of the pattern at the iterative sample points is important.

Figure 4.1-1 shows the geometry for an infinite cylindrical reflector with a y-polarized feed. For the ith iteration, the total correction pattern of an infinite cylindrical reflector is

$$\Delta F^{(i)}(u) = \sum_n a_n^{(i)} G_{ref}(u, u_n^{(i)}) \tag{4.1-11}$$

where for this geometry $u = \sin\theta$ (not $\cos\theta$ as for the z-directed sources) and the $u - u_n^{(i)}$ from (4.1-1) has been replaced to emphasize that for the reflector, the radiation pattern is no longer a shifted universal pattern, as is often the case for linear arrays or line sources. The $u_n^{(i)}$ is where the main beam of the nth correction pattern for the reflector is centered. The reflector is assumed to be y-polarized. After K iterations the resultant improved pattern is

$$F^{(K)}(u) = F^{(0)} + \sum_{i=1}^{K} \Delta F^{(i)}(u) \quad . \tag{4.1-12}$$

The correction pattern for the cylindrical reflector is related to the current $g_{mn}^{(i)}$ by (see Ch. 5 for more details)

$$G_{ref}(u, u_n^{(i)}) = \kappa \int_{S_0} \sum_m g_{mn}^{(i)}\left(\vec{H}_{inc},\ S_0,\ x,\ z\right) e^{jk(\vec{\rho} \cdot \hat{R}_1)} dS \tag{4.1-13}$$

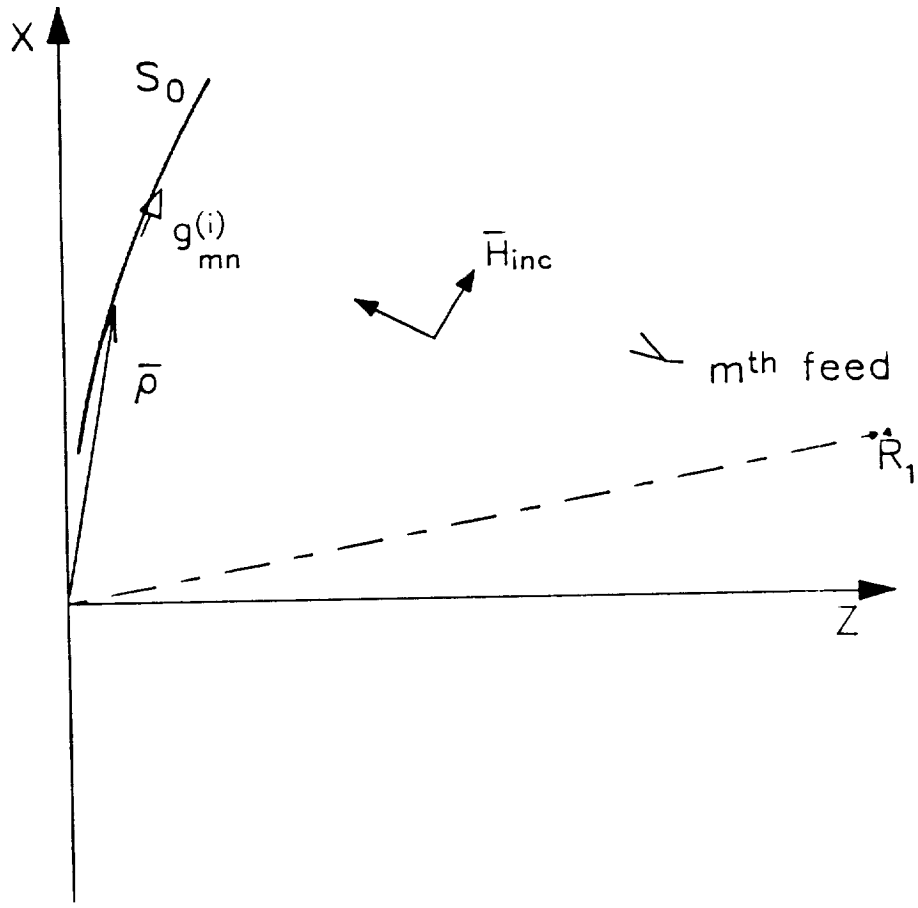

Figure 4.1-1. ISM cylindrical reflector geometry.

where κ is a constant and $\vec{H}_{inc}$ is the H-field incident upon the reflector from the mth feed, $\vec{\rho}$ locates integration points on the reflector surface, and $\hat{R}_1$ is a unit vector in the direction of the observation point. For displaced feed scanning (Sec. 3.1), the $g_{mn}^{(i)}$ in (4.1-13) are all zero except the one that produces the nth scanned beam. For electronic scanning (Sec. 3.2), $g_{mn}^{(i)}$ is the induced current of the mth feed that has been amplitude and phase weighted (for example, using CFM, Sec. 3.2) to compositely produce the nth scanned beam when superposed with the induced currents from the other feeds. The total correction current contribution for the ith iteration of the mth feed is

$$\Delta f_{ref,m}^{(i)} = \sum_n a_n^{(i)} g_{mn}^{(i)} \tag{4.1-14}$$

and the total current on the reflector surface for the mth feed after K iterations is

$$f_{ref,m}^{(K)} = f_{ref,m}^{(0)} + \sum_{i=1}^{K} \Delta f_{ref,m}^{(i)} \quad . \tag{4.1-15}$$

The expression for $\alpha_n^{(i)}$ is similar to (4.1-9). Figure 4.1-2 shows the elements of the nth correction beam weighting scheme for the ith iteration at $u_n^{(i)}$. To allow for an unnormalized correction pattern, the expression from (4.1-9) needs to be divided by the magnitude of $G_{ref}(u, u_n^{(i)})$. Assuming $F_d(u_n^{(i)})$ to be real and positive, the real-valued amplitude of $\alpha_n^{(i)}$ is

$$\alpha_n^{(i)} = \frac{F_d(u_n^{(i)}) - \left| F^{(i-1)}(u_n^{(i)}) \right|}{\left| G_{ref}(u, u_n^{(i)}) \right|} \quad . \tag{4.1-16}$$

The $\alpha_n^{(i)}$ can be positive or negative (the phase of $\alpha_n^{(i)}$ is 0° or 180°). The correction beam must satisfy an in-phase or anti-phase condition with $F^{(i-1)}(u_n^{(i)})$ for correction at $u_n^{(i)}$. The

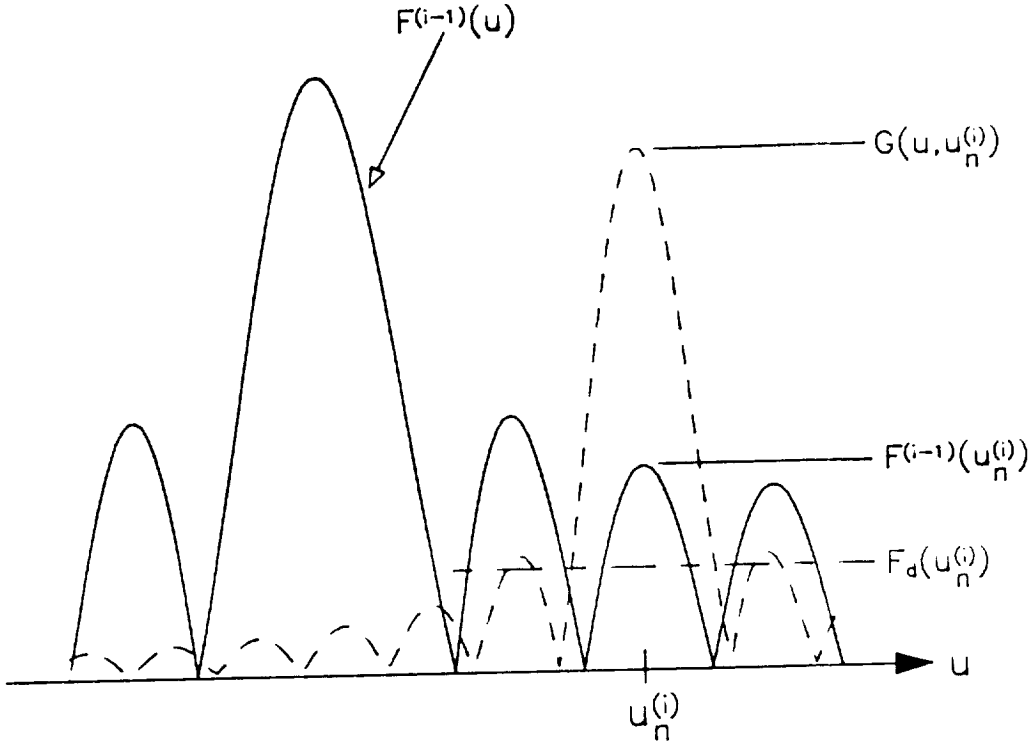

Figure 4.1-2. Representation of elements used in the ISM weighting scheme for the ith iteration at $u_n^{(i)}$. The $F^{(i-1)}(u_n^{(i)})$ is the corrected pattern at the $i-1$ step. $G_{ref}(u, u_n^{(i)})$ is the correction pattern with the peak at $u_n^{(i)}$. $F_d(u_n^{(i)})$ is the desired corrected pattern level at $u_n^{(i)}$.

phase of $F^{(i-1)}(u_n^{(i)})$ must then be equal to or opposite the phase of the weighted correction pattern $\alpha_n^{(i)} G_{ref}(u, u_n^{(i)})$. Therefore,

$$\phi_G + \phi_a + \begin{bmatrix} 0° \\ \pm 180° \end{bmatrix} = \phi_F \tag{4.1-17}$$

and, solving for the weight phase,

$$\phi_a = \phi_F - \phi_G - \begin{bmatrix} 0° \\ \pm 180° \end{bmatrix} \tag{4.1-18}$$

where ϕ_G, ϕ_F, and ϕ_a are the phases of $G_{ref}(u, u_n^{(i)})$, $F^{(i-1)}(u_n^{(i)})$, and the complex part of $\alpha_n^{(i)}$, respectively. From (4.1-16) and (4.1-18),

$$a_n^{(i)} = \alpha_n^{(i)} e^{j\phi_a} \quad . \tag{4.1-19}$$

The three-dimensional reflector problem has a similar formulation except that the single integrals become double integrals and the patterns and current distributions are now bivariate.

The increasing side lobe level and beam broadening are the fundamental limitations to implementing the ISM with reflectors. If several correction patterns are applied in a given iteration, the resultant pattern will equal the desired pattern at the sample points only if the correction patterns are uncorrelated at the sample points. [50] Good results can be obtained only if the correlation between the correction beams is weak at the sample points. The ISM for reflectors is therefore limited to an angular extent over which the side lobe level increase and beam broadening do not cause significant interference between pattern corrections.

4.2 PATTERN SYNTHESIS COMPENSATION TECHNIQUE DESCRIPTION

The pattern synthesis compensation technique is essentially the ISM applied to moderately distorted reflectors. Surface errors cause increased side lobe levels (see Sec. 2.1). The ISM can be used to reduce the side lobe levels.

The pattern synthesis compensation technique differs from most compensation methods in two ways (see Sec. 2.3). It is a localized algorithm in which only the parts of the radiation pattern that do not meet desired specifications are compensated. Most of the other techniques try to use array feeds to correct the focal plane fields near the focal point and, hence, compensate for the distortions of the overall radiation pattern. The other difference is that the pattern synthesis technique does not require reflector surface data. Radiation pattern data are required. If surface data are available, however, the pattern data that are required can be computed.

The correction beam scanning is implemented in two ways. Displaced feed scanning is accomplished by moving auxiliary feeds away from the focal point. For displaced feed scanning, the $g_{mn}^{(0)}$ of (4.1-13) would all be zero except for the feed that corresponds to the nth correction beam. Superposition is performed with the secondary radiation patterns of the individual feeds. This is the easiest analytical implementation of the pattern synthesis compensation technique. Electronic beam scanning with a fixed array feed is a more desirable implementation and probably more practical from a mechanical standpoint. The $g_{mn}^{(0)}$ of (4.1-13) correspond to the induced current of the mth feed that has been amplitude and phase weighted (for example, using CFM, Sec. 3.2) to compositely produce the nth scanned beam when superposed with the induced

currents from the other feeds. Superposition is performed with the induced currents of the composite electronic element excitations.

The amplitudes of the weights $a_n^{(i)}$ are computed assuming the correction patterns $G_{ref}(u, u_n^{(i)})$ are those of a smooth reflector. An extensive scanning study (see Sec. 6.1) showed that for reflectors with moderate surface errors, the main beam peak characteristics did not deviate significantly from those of a smooth reflector. These small deviations in the peak characteristics cause small errors in the $a_n^{(i)}$ calculations but, in general, do not significantly affect the compensation.

The side lobes of distorted reflector antennas are typically higher than those of smooth reflectors (see Sec. 2.1). The vast majority of effort with the pattern synthesis compensation technique deals with side lobe reduction. For side lobe reduction, the correction beam must satisfy the anti-phase condition with $F^{(i-1)}(u_n^{(i)})$ for correction at $u_n^{(i)}$. Therefore, the $\pm 180°$ term from (4.1-18) should be used when computing the ϕ_a.

Pattern phase data are also required for the ISM applied to reflectors. In implementing the pattern synthesis compensation technique, phase data will probably not be available. This problem is overcome with an additional step involving an "amplitude-only" phasor analysis. The auxiliary beam is amplitude weighted using (4.1-16) and steered to the location of the $F^{(i-1)}(u_n^{(i)})$ pattern requiring compensation. A blind guess is made at to the required phase excitation of $a_n^{(i)}$ (a good start is to assume the phase excitation is 0°). By drawing a phasor diagram of the peak of the side lobe before the auxiliary beam is scanned, the peak after scanning, and the (approximately) known amplitude of the $G_{ref}(u, u_n^{(i)})$ pattern, the relative phase, ϕ_r, between the peak of the side lobe before compensation and the scanned correction beam can be determined to a reasonable degree of accuracy (see Fig. 4.2-1). The relative phase is ambiguous as it could lead or lag the phase of the side lobe. This means that ϕ_a from (4.1-18) is

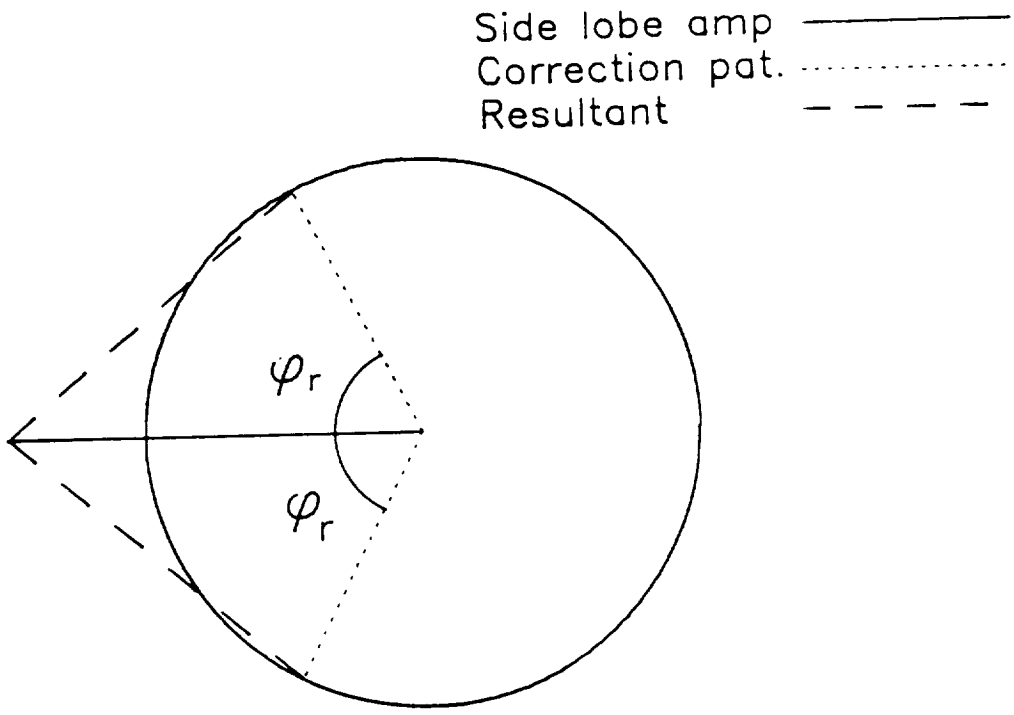

Figure 4.2-1. Phasor analysis to determine the relative phase ϕ_r for compensation. The circle represents the locus of possible values for the correction beam peak. The amplitude measurements lead to an ambiguous phase determination in which the correction beam phase could lead or lag the phase of the side lobe.

$\pm\phi_e$. Therefore, at least one extra step (possibly two) is required to resolve the ambiguity and to set the phase excitation to the proper value for compensation.

The excitation $\alpha_n^{(i)}$ is computed without any knowledge of the surface error. Assuming a smooth reflector when calculating the peak of $G_{re}(u, u_n^{(i)})$ causes a slight error in the phasor determination of the phase ϕ_e. This error reduces the accuracy of the match at the iterative sample point $u_n^{(i)}$. The error is not catastrophic, however, as there is a range of phase values over which reduced compensation is achieved.

Figure 4.2-2 illustrates the range of phases for which reduced or full compensation is achieved when

$$F_d(u_n^{(i)}) = 0.316 \left| F^{(i-1)}(u_n^{(i)}) \right| \tag{4.2-1}$$

(a 10 dB reduction in the side lobe). The side lobe peak is assumed to be normalized to have unity amplitude with phase 0° and is given by

$$f_{SL} = 1 + j0 \quad . \tag{4.2-2}$$

Assuming arbitrary phase, the amplitude of the correction beam peak is (from (4.1-16)) $\alpha_n^{(i)} = -0.684$. The locus of possible values for the weighted correction beam peak is a circle in the complex plane and is given by

$$f_{CP} = x + jy \tag{4.2-3}$$

where $|x + jy| = 0.684$ or

$$x^2 + y^2 = (0.684)^2 \quad . \tag{4.2-4}$$

For a reduction in the side lobe peak, the magnitude of the sum of the peak of the side lobe peak (4.2-2) and the correction pattern (4.2-3) must be less than unity. Otherwise,

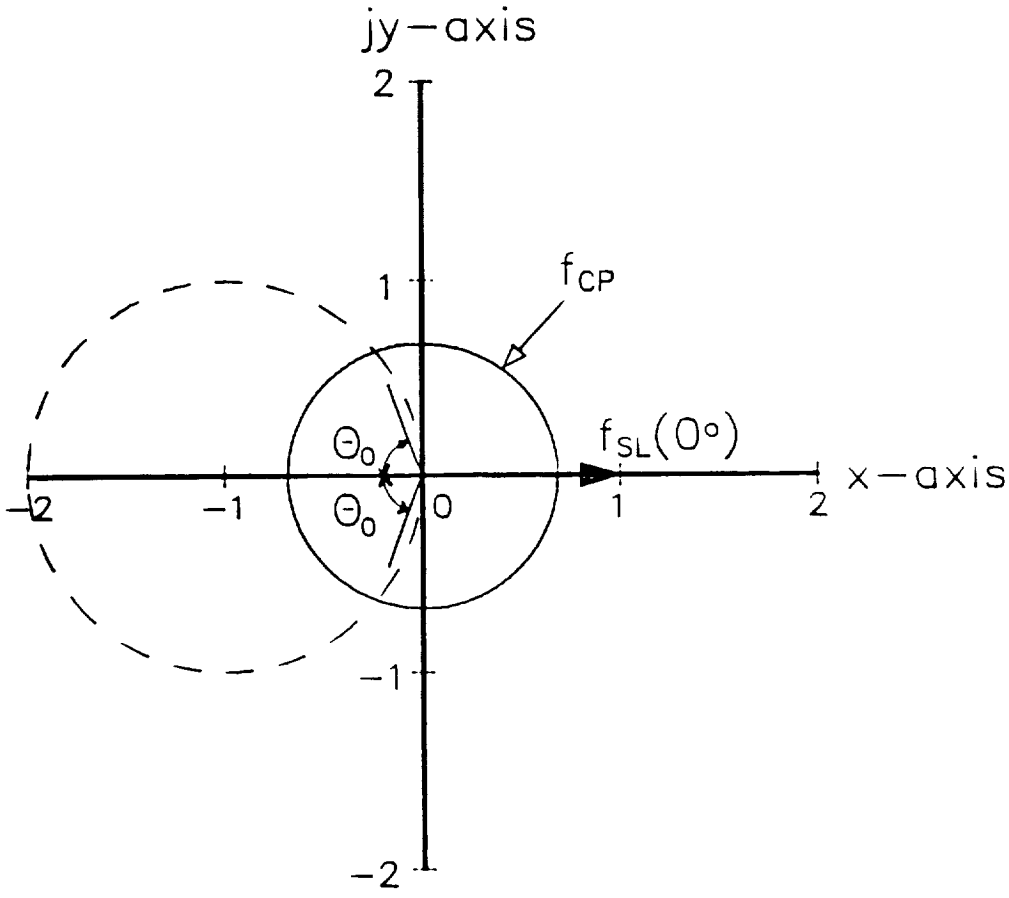

Figure 4.2-2. Graph representing the range of phases for which reduced or full compensation is achieved when trying to reduce the side lobe peak by 10 dB. f_{SL} is the side lobe amplitude and f_{CP} is the correction pattern locus. The range of possible excitation phases for achieving reduced or full compensation is represented by the intersection of f_{CP} and the interior of the dashed circle $180° - \theta_0 \leq |\phi_{CP}| \leq 180°$ relative to the phase of f_{SL}.

destructive interference results and the distorted pattern side lobe peak increases. This is represented by the inequality

$$|(x+1)+jy| \leq 1 \tag{4.2-5}$$

or by its magnitude squared

$$(1+x)^2+y^2 \leq 1 \quad . \tag{4.2-6}$$

Equation (4.2-6) represents the interior of the dashed circle in Fig. 4.2-2 centered at (-1,0) with a radius of unity. The inequality of (4.2-6) must hold for reduced or full compensation. Solving for the points of intersection of (4.2-4) and the interior of the circle of (4.2-6) gives a range of possible phases for which reduced or full compensation is achieved. The actual phase of the weighted correction beam peak must fall in the range

$$180° - \theta_0 \leq |\phi_{CP}| \leq 180° \tag{4.2-7}$$

relative to the phase of f_{SL}. For the above example, $\theta_0 = 70°$.

5.0 COMPUTER CODES

New FORTRAN computer codes and modified forms of existing codes were needed for the compensation analysis. The programs RAPCA (Reflector Analysis Program for Cylindrical Antennas), SCANRAP (SCANned Reflector Analysis Program), and DRAPCA (Dual Reflector Analysis Program for Cylindrical Reflector Antennas) were written to facilitate the two-dimensional analysis of cylindrical reflectors. The program RAP (Reflector Analysis Program [52, 53]) was used to analyze paraboloidal reflectors. RAP was modified slightly to allow rapid evaluation of distorted reflector antennas.

5.1 REFLECTOR ANALYSIS PROGRAM FOR CYLINDRICAL REFLECTORS (RAPCA)

5.1.1 RAPCA ALGORITHM

RAPCA is used to evaluate the radiation patterns for smooth or distorted cylindrical reflectors. The pattern is computed using physical optics. The reflectors can have a single feed element or an array of feed elements. The reflector surface can either be smooth or distorted. Axisymmetric or offset reflectors with the feed elements tilted toward the reflector are possible.

Figure 5.1-1 shows the geometry of a cylindrical reflector. The feeds are assumed to be longitudinally polarized line sources parallel to the y-axis. The xz-plane is therefore the H-plane. Following [47], the feeds are assumed to have radiation patterns that are described by normalized feed radiation patterns $G(\gamma_i)$. For this analysis the normalized feed radiation pattern is defined to be $G(\gamma_i) = \cos^q\gamma_i$. The feeds are assumed to have uniform distribution of intensity in the y-direction.

The radiation pattern for the cylindrical reflector in this study with N feed array elements positioned as shown in Fig. 5.1-1 is given by [23]

$$G_M(\theta) = \frac{\left|\sum_{i=1}^{N} A_i e^{j\phi_i} I_i\right|^2}{\sum_{i=1}^{N} A_i^2} = \frac{P(\theta)}{P_U} \tag{5.1-1}$$

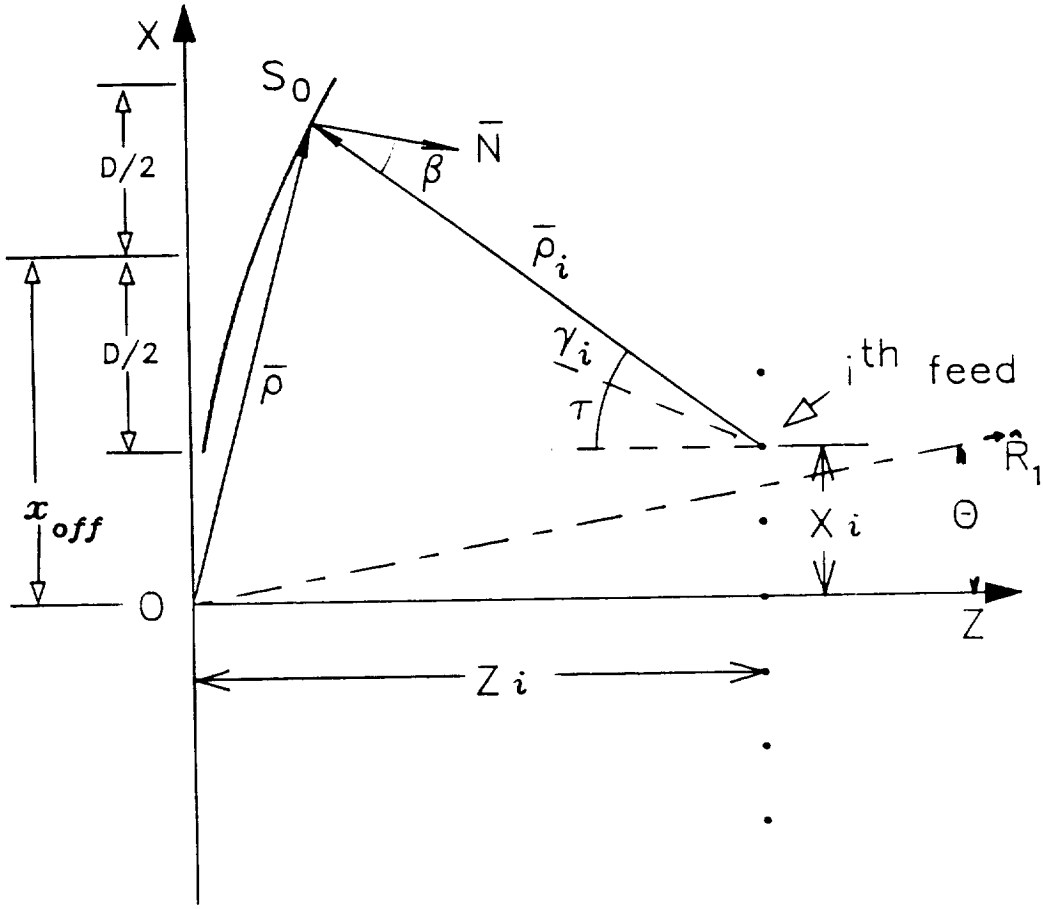

Figure 5.1-1. Geometry of the cylindrical reflector used for the program RAPCA. The reflector is uniform in the y-direction.

where A_i and ϕ_i are the excitation amplitude and phase of the ith feed element, I_i is the radiation integral of the ith element (to be derived below), $P(\theta)$ is the unnormalized power pattern of the reflector, and P_U is the on-axis level one would obtain from a uniformly illuminated aperture with no spillover. The expression for the total reflector system (secondary pattern), $G_M(\theta)$, is computed through superposition of the reflector (secondary) radiation patterns of the individual weighted feed (primary) elements.

The radiation integrals for the individual feed elements can be found from the prime focus cylindrical reflector analysis in [47]. The H-plane radiation pattern is the only one evaluated. The analysis in this study is a special two-dimensional case in which the reflector is assumed to be uniform in the y-direction and the surface errors are also cylindrical. Integration in the y-direction yields a constant that can be normalized out. The H-plane radiation pattern is the only one evaluated. The unnormalized radiation integral for the ith feed element after integrating in the y-direction is given by (from (5-86) in [47])

$$I_i = \int_{S_0} \left[\frac{G(y_i)}{\rho_i} \right]^{\frac{1}{2}} \cos\beta \exp\left[-jk(\rho_i - \vec{\rho} \cdot \hat{R}_1) \right] ds \qquad (5.1\text{-}2)$$

where S_0 is the surface of the reflector and ds is the element of arc length along the cross section of the reflector. This integral can be reduced to an integral in x for the analysis in this study in which only the xz-plane pattern is to be computed. To see this, the terms in the integrand need to rewritten in terms of x.

First, we examine the $\cos\beta$ term. This can be found by taking the dot product

$$-\vec{\rho}_i \cdot \vec{N} = \rho_i \, |\vec{N}| \cos\beta \qquad (5.1\text{-}3)$$

where

$$\vec{\rho}_l = (x - x_l)\hat{x} + (f(x) - z_l)\hat{z} \tag{5.1-4}$$

$$\rho_l = |\vec{\rho}_l| = \left[(x - x_l)^2 + (z_l - f(x))^2\right]^{\frac{1}{2}} \tag{5.1-5}$$

$$\vec{N} = -f'(x)\hat{x} + \hat{z} \tag{5.1-6}$$

$$|\vec{N}| = \sqrt{[f'(x)]^2 + 1} \tag{5.1-7}$$

and $f(x)$ is the function that describes the reflector surface, $f'(x)$ is the derivative of $f(x)$, and z_l is the distance from the z=0 plane to the lth feed element. Factoring (5.1-3) and performing the dot product using (5.1-5) and (5.1-6),

$$\cos\beta = \frac{1}{\rho_l\,|\vec{N}|}\left[(x - x_l)f'(x) + z_l - f(x)\right] \tag{5.1-8}$$

in which the cosine is now in terms of functions of x.

Now we examine the phase terms in the exponent of (5.1-2). Define

$$\Delta = \rho_l - \vec{\rho} \cdot \hat{R}_1 \quad . \tag{5.1-9}$$

The unit vector $\hat{R}_1$ in the xz-plane is given by

$$\hat{R}_1 = \sin\theta\hat{x} + \cos\theta\hat{z} \tag{5.1-10}$$

Evaluating the dot product in (5.1-9),

$$\Delta = \rho_l - x\sin\theta - f(x)\cos\theta \tag{5.1-11}$$

which is also in terms of functions of x.

The angle γ_l is

$$\gamma_i = \tan^{-1}\left(\frac{x - x_i}{z_i - f(x)}\right) - \alpha_f \tag{5.1-12}$$

where α_f is the tilt angle of the feed elements.

All the terms in the integrand have been rewritten in terms of x. Everything is a constant with respect to y and the y-integration may be performed giving a constant that will be accounted for when the radiation integral is normalized. The single integral that is left is in terms of *ds*. This may be rewritten in terms of *dx* by introducing the Jacobian in the xz-plane. The relation is

$$ds = \sqrt{[f'(x)]^2 + 1}\; dx = |\vec{N}|\, dx \quad . \tag{5.1-13}$$

The limits of integration are $\{x_{off} - D/2,\ x_{off} + D/2\}$. Using (5.1-5), (5.1-8), (5.1-11), (5.1-12), and (5.1-13) in (5.1-2), the radiation integral for the *i*th feed element is

$$I_i = C\int_{x_{off}-D/2}^{x_{off}+D/2} \left[\frac{G(\gamma_i)}{\rho_i}\right]^{\frac{1}{2}} [f(x) - z_i - (x - x_i)f'(x)]\,\frac{1}{\rho_i} \times \exp[-jk\{\rho_i - x\sin\theta - f(x)\cos\theta\}]\, dx \tag{5.1-14}$$

where the constant C is a normalization constant. From [23],

$$C = \sqrt{\frac{1}{2\pi D}} \quad . \tag{5.1-15}$$

Equation (5.1-14) is the radiation integral evaluated by RAPCA. It has the arbitrary function $f(x)$ defining the reflector surface. For the special case of an axisymmetric parabolic cylinder reflector,

$$f(x) = \frac{x^2}{4F} \tag{5.1-16}$$

where F is the focal length of the parabolic cylinder and $x_{off} = \alpha_f = 0$. Using this in (5.1-14) gives [23]

$$I_l = \sqrt{\frac{1}{2\pi D}} \int_{-D/2}^{D/2} \left[\frac{G(\gamma_l)}{\rho_l} \right]^{\frac{1}{2}} \left[\frac{x x_l}{2F} - \frac{x_l^2}{4F} - z_l \right] \times \frac{1}{\rho_l} \exp\left[-jk\{\rho_l - x \sin\theta - \frac{x^2}{4F} \cos\theta\} \right] dx \tag{5.1-17}$$

The function describing the reflector surface used in the analysis of this study was chosen to be a distorted parabolic cylinder reflector. The particular surface distortion used sets up a surface error corresponding to a sinusoidal phase error in the equivalent PO aperture plane current assuming the feed is at the focal point.

For a smooth reflector with the feed at the focus (see Fig. 5.1-1 for the geometry), d, the sum of the distance from the focal point to a point on the reflector surface and the distance from the point on the reflector to the aperture plane (containing the focal point), is a constant $2F$ (F is the focal length). The equation for d is

$$d = \rho_0 + F - f(x) \tag{5.1-18}$$

where ρ_0 is the distance from the focal point to a point on the reflector

$$\rho_0 = \sqrt{x^2 + (F - f(x))^2} \tag{5.1-19}$$

$f(x)$ is the function defining the reflector surface, and $d = 2F$ for the smooth parabolic reflector. For the distorted surface, a sinusoidal variation in d as a function of x is required to implement the desired sinusoidal phase error in the equivalent PO aperture plane current. The expression for d for a distorted reflector is

$$d = 2F + \zeta = F - f(x) + \rho_0 \tag{5.1-20}$$

where

$$\zeta = \Gamma \cos\left(\frac{4\pi m x}{D}\right) \tag{5.1-21}$$

where Γ is the amplitude of the distortion, m is the number of periods along the radius of the aperture, and D is the diameter of the aperture. Substituting (5.1-19) into (5.1-20) and solving for $f(x)$ gives

$$f(x) = \frac{x^2 - 2F\zeta - \zeta^2}{4F + 2\zeta} \quad . \tag{5.1-22}$$

This surface error produces a phase error in the projected aperture plane equivalent current, Φ_E, given by

$$\Phi_E = \phi_e \cos\left(\frac{4\pi m x}{D}\right) \tag{5.1-23}$$

where $\phi_e = (2\pi/\lambda)\Gamma$. The periodic nature of the surface error creates a region of high side lobes over an angular location determined by the spatial frequency (m) of the surface error (similar to the radial error from Sec. 2.1.2). [9]

5.1.2 RAPCA INPUT AND OUTPUT

The program RAPCA requires two input files which are denoted by the logical file numbers (LFN) 20 and 21. LFN 20 contains feed and reflector input data and defines the type of Gauss-Legendre quadrature to be used for the radiation integral. The

reflector may be smooth or distorted with the surface distortion defined by (5.1-18). The reflector may be offset and have up to 10 feeds with arbitrary locations and tilt angles. LFN 21 contains the weights and zeroes for the Gaussian integration. The output file is designated by LFN 10. Table 5.1-1 shows the form for LFN 20 and LFN 21. Table 5.1-2 contains descriptions of the input variables for LFN 20. Table 5.1-3 shows the format for inputting the weights and zeros of the Gaussian integration. Appendix A.1 gives an example of a cylindrical reflector analyzed by RAPCA.

5.2 SCANNED REFLECTOR ANALYSIS PROGRAM (SCANRAP)

5.2.1 SCANRAP ALGORITHM

The program SCANRAP uses the method of conjugate field match (CFM, Sec. 2.3.2) to find the excitations of the feed array elements necessary to scan the reflector to a given angle θ_0. SCANRAP computes the received focal region fields of the array feed elements for a plane wave incident from the desired angle of scan, θ_S . The excitations for scanning the reflector to θ_S are the complex conjugates of the received focal region fields at the locations of the feed elements. [33] The reflector is assumed to be smooth when computing the excitations. These excitations for a smooth reflector are then used with the distorted reflector to scan a correction beam to the region in the radiation pattern requiring compensation.

Table 5.1-1.

RAPCA input file formats for LFN 20 and LFN 21.

LFN 20

NFEEDS				
$AEXCIT_1$	$PEXCIT_1$	XFEED(1)	ZFEED(1)	TFEED(1)
$AEXCIT_2$	$PEXCIT_2$	XFEED(2)	ZFEED(2)	TFEED(2)
.	.	.	.	.
.	.	.	.	.
$AEXCIT_{NFEEDS}$	$PEXCIT_{NFEEDS}$	XFEED(NFEEDS)	ZFEED(NFEEDS)	TFEED(NFEEDS)
Q	PERRMX	PERRCY		
DIAM	OFFSET	FOCAL		
THETAB	THETAE	THETAI		
NORDER				

LFN 21

ZEROS(1)	WEIGHT(1)
ZEROS(2)	WEIGHT(2)
.	.
.	.
ZEROS(NORDER)	WEIGHT(NORDER)

Table 5.1-2.

RAPCA input variable description for LFN 20.

ARGUMENT	TYPE*	DESCRIPTION
NFEEDS	I	Number of feeds: Initially limited to 10 or less
$AEXCIT_i$	R	Excitation amplitude for ith feed (linear)
$PEXCIT_i$	R	Excitation phase for ith feed (degrees)
XFEED(i)	R	X-coordinate of ith feed (λ)
ZFEED(i)	R	Z-coordinate of ith feed (λ)
TFEED(i)	R	Tilt of the ith feed (°)
Q	R	Feed pattern exponent ($\cos^q\theta$)
PERRMX	R	Phase error amplitude (°)
PERRCY	R	Number of cycles for the phase error
DIAM	R	Reflector diameter(λ)
OFFSET	R	Reflector offset dimension (λ)
FOCAL	R	Focal length of the reflector (λ)
THETAB	R	Far-field beginning angle (°)
THETAE	R	Far-field ending angle (°)
THETAI	R	Far-field increment angle (°)
NORDER	I	Order of Gaussian quadrature

I: FORTRAN INTEGER
R: FORTRAN REAL NUMBER

Table 5.1-3.

RAPCA input variable format for LFN 21. Only the positive half of Gauss quadrature zeros and their corresponding weights are input. RAPCA uses symmetry to fill the ZEROS and WEIGHT arrays. The elements are real variables.

positive, largest root→	ZERO(1)	WEIGHT(1)
	ZERO(2)	WEIGHT(2)
	.	.
	.	.
positive, smallest root→	ZERO(M)	WEIGHT(M)

(M = NORDER/2)

Figure 5.2-1 shows the geometry for the SCANRAP analysis. A linearly polarized plane wave is assumed to be incident on the cylindrical reflector with the E-field y-polarized. The expressions for the incident fields are

$$\vec{E}_i = E_0 e^{-jkr}\hat{y} \tag{5.2-1}$$

$$\vec{H}_i = \frac{E_0}{\eta} e^{-jkr}(\cos\theta_S \hat{x} - \sin\theta_S \hat{z}) = \frac{E_0}{\eta} e^{-jkr}\hat{h}_i \tag{5.2-2}$$

where E_0 is the magnitude of the E-field and θ_s is the angle of incidence of the plane wave and also the angle of desired scan. The scattered E-field from the reflector is given by [47]

$$\vec{E}_r = \frac{1}{4\pi j\omega\varepsilon}\int_{S_0}\left[\vec{J}\cdot\nabla(\nabla\psi) + k^2\vec{J}\psi\right]dS \tag{5.2-3}$$

where S_0 is the surface of the reflector,

$$\psi = \frac{e^{-jk\rho}}{\sqrt{\rho}} \tag{5.2-4}$$

for the parabolic cylinder reflector, ρ being the distance from the elemental current on the reflector to the point of evaluation, and [47]

$$\vec{J} = 2\hat{n}\times\vec{H}_i = J\hat{y} \quad . \tag{5.2-5}$$

With the given incident fields of (5.2-1) and (5.2-2), $\vec{J}$ only has a y-directed component and does not depend on y. It can be shown that for the infinite cylindrical reflector of Fig. 5.2-1 with a y-polarized feed

$$\vec{J}\cdot\nabla(\nabla\psi) = 0 \quad . \tag{5.2-6}$$

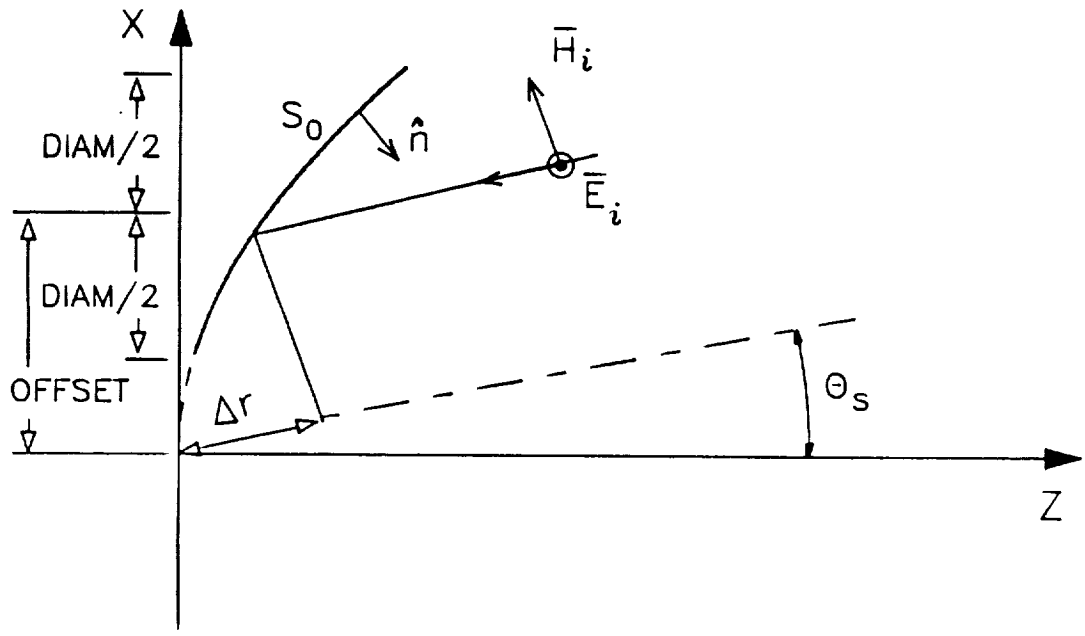

Figure 5.2-1. Geometry of the cylindrical reflector used for the program SCANRAP. The reflector is assumed to be a smooth parabolic cylinder that is uniform in the y-direction.

The expression for the scattered E-field in (5.2-3) reduces to

$$\vec{E}_r = \frac{k^2}{4\pi j\omega\varepsilon}\int_{S_0}\vec{J}\psi dS \quad . \tag{5.2-7}$$

The received field at the ith feed location is found using the infinitesimal scattered E-field. [47] The infinitesimal field intensity from (5.2-7) is given by

$$dE_r = \frac{k^2}{4\pi j\omega\varepsilon} J\psi dS \quad . \tag{5.2-8}$$

(Note: the vector notation has been dropped as the E field only has a y-component. In addition, the feed is also y-polarized so there is no need to account for any polarization mismatch loss.) The magnitude of the Poynting vector of the incremental field intensity at the ith feed is [47]

$$|S_r| = \frac{1}{2}\left(\frac{\varepsilon}{\mu}\right)^{\frac{1}{2}}|dE_r|^2 \quad . \tag{5.2-9}$$

The incremental received power of the ith feed is then [47]

$$dP_r = |S_r| G_f(\theta,\phi)\frac{\lambda^2}{4\pi} \tag{5.2-10}$$

where, for the infinite cylindrical reflector, the feed radiation pattern is defined as

$$G_f(\theta,\phi) = G(\gamma_i) \tag{5.2-11}$$

and is assumed constant in the y-direction. The incremental received voltage of the ith feed is proportional to the square root of the received power given by

$$dV_i = \alpha\sqrt{dP_r} \tag{5.2-12}$$

where α is a constant of proportionality. Using (5.2-8), (5.2-9), (5.2-10), and (5.2-11) in (5.2-12), the incremental received voltage is

$$dV_i = C\sqrt{G(\gamma_i)}\,\vec{J}\,\psi dS \tag{5.2-13}$$

where all constants are absorbed by the constant C. The constants are not important to this analysis as the final results will be normalized. The total received voltage for the ith feed is found by integrating (5.2-13) along the entire surface of the parabolic cylinder reflector. The integral is

$$V_i = C\int_{S_0} \sqrt{G(\gamma_i)}\,J\psi dS \tag{5.2-14}$$

where

$$dS = dy\,ds \tag{5.2-15}$$

and ds is the element of arc length along the cross section of the reflector. The y-integral from (5.2-14) yields a constant for this cylindrical analysis (also absorbed into C). The integral is expressed in terms of dx instead of ds by using the Jacobian. The surface function of a smooth parabolic cylinder is given by (5.1-16) and is repeated here

$$f(x) = \frac{x^2}{4F} \tag{5.2-16}$$

where F is the focal length. Using (5.2-16) in (5.1-13), ds can be rewritten as

$$ds = \left[1 + \left(\frac{x}{2F}\right)^2\right]^{\frac{1}{2}} dx \quad . \tag{5.2-17}$$

Using (5.2-17), the integral of (5.2-14) becomes

$$V_i = C\int_{l/2-OFFSET}^{l/2+OFFSET} [G(\gamma_i)]^{\frac{1}{2}} J\psi\left[1+\left(\frac{x}{2F}\right)^2\right]^{\frac{1}{2}} dx \quad . \tag{5.2-18}$$

The excitation for the ith feed to scan the reflector to angle θ_s is then, using (5.2-18),

$$A_i e^{j\phi_i} = V_i^* \tag{5.2-19}$$

where A_i and ϕ_i are the amplitude and phase of the excitation, respectively, and the star denotes the complex conjugate (Note: this is essentially (3) from [23] with a constant weighting function).

This algorithm for computing the excitations follows the DCFM approach (see Sec. 2.3.2). The received focal region fields were computed directly. The complex conjugates of the received fields were were then output as the array feed element excitations. SCANRAP computes the excitations using (5.2-19). The excitation with the largest value of A_i is normalized to unity and is used as a phase reference of zero degrees. The other excitations are then scaled to this normalized maximum excitation.

To evaluate the integral of (5.2-18), all the quantities of the integrand must be in terms of x. The expression for γ_i in terms of x is given in (5.1-12). The function ψ in (5.2-4) is a function of ρ which is a function of x as shown in (5.1-5).

The induced current $\vec{J}$ can also be expressed as a function of x using (5.2-5). The geometry of Fig. 5.2-2 is used to find the expression for $\vec{J}$. The intersection of the x-z axes is assumed to be the phase reference. The plane wave is incident from angle θ_i. Variables corresponding to the ray passing through the origin are denoted by the "0"-subscripts. The variables corresponding to the ray passing through the point being evaluated by the integral are unsubscripted.

Using the intersection of the xz-axes as the phase reference, the H-field of (5.2-2) can be rewritten with an absolute phase term as

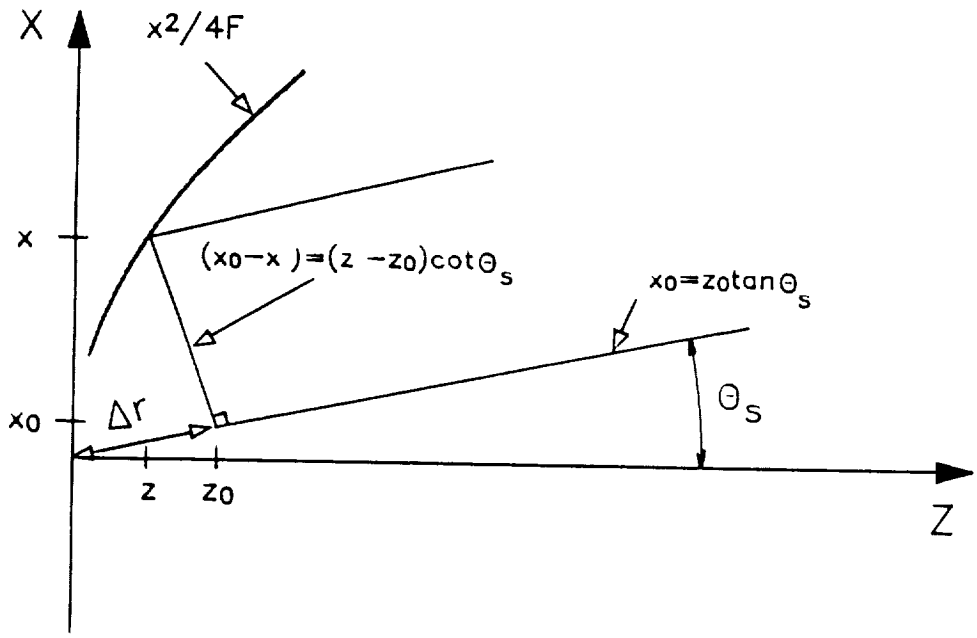

Figure 5.2-2. Geometry used to find Δr in terms of x.

$$\vec{H}_i = \frac{E_0}{\eta} e^{+jk\Delta r}(\cos\theta_S \hat{x} - \sin\theta_S \hat{z}) \quad . \tag{5.2-20}$$

The Δr-term needs to be written in terms of x. The two lines defined by

$$x_0 = z_0 \tan\theta_S \tag{5.2-21}$$

$$(x_0 - x) = (z - z_0)\cot\theta_S \tag{5.2-22}$$

and solving (5.2-22) for x_0,

$$x_0 = (z - z_0)\cot\theta_S + x \tag{5.2-23}$$

will be used to find an appropriate expression for Δr. Substituting (5.2-23) into (5.2-21) and factoring gives

$$z_0 = \frac{z\cot\theta_S + x}{\tan\theta_S + \cot\theta_S} \quad . \tag{5.2-24}$$

Using Fig. 5.2-2, the path length difference Δr is

$$\Delta r = \frac{z_0}{\cos\theta_S} = \frac{z\cot\theta_S + x}{\cos\theta_S[\tan\theta_S + \cot\theta_S]} \tag{5.2-25}$$

which can be simplified using trigonometric definitions for the tangent and cotangent. The expression in (5.2-25) becomes

$$\Delta r = x\sin\theta_S + z\cos\theta_S \quad . \tag{5.2-26}$$

Therefore, substituting (5.2-16) into (5.2-26) gives the desired result for the phase term of the incident H-field of

$$\Delta r = x \sin\theta_S + \frac{(x)^2}{4F}\cos\theta_S \quad . \tag{5.2-27}$$

The final step in expressing $\vec{J}$ in terms of x is to evaluate the cross product of (5.2-5). Using (5.1-6) and (5.1-7), the surface normal is

$$\hat{n} = \frac{1}{\sqrt{1+\left(\frac{x}{2F}\right)^2}}\left[-\frac{x}{2F}\hat{x}+\hat{z}\right] \quad . \tag{5.2-28}$$

Using (5.2-28) and (5.2-2), the cross product of (5.2-5) is

$$\begin{aligned}\hat{n}\times\hat{h}_i &= \frac{1}{\sqrt{1+\left(\frac{x}{2F}\right)^2}}\left[-\frac{x}{2F}\hat{x}+\hat{z}\right]\times\left[\cos\theta_S\hat{x}-\sin\theta_S\hat{z}\right] \\ &= \frac{\cos\theta_S-\frac{x}{2F}\sin\theta_S}{\sqrt{1+\left(\frac{x}{2F}\right)^2}}\hat{y}\end{aligned} \quad . \tag{5.2-29}$$

If the amplitude of the incident H-field is normalized to unity, the current density, using (5.2-20), (5.2-27), and (5.2-29) in (5.2-5), is [23]

$$\vec{J} = 2\hat{y}\,\frac{\cos\theta_S-\frac{x}{2F}\sin\theta_S}{\sqrt{1+\left(\frac{x}{2F}\right)^2}}\,e^{jk\left[x\sin\theta_S+\frac{x^2}{4F}\cos\theta_S\right]} \quad . \tag{5.2-30}$$

The current expression in (5.2-30) is used in (5.2-18) and the required current excitation for the ith feed is then found with (5.2-19)

5.2.2 SCANRAP INPUT AND OUTPUT

The program SCANRAP requires two input files which are denoted by the logical file numbers (LFN) 20 and 21. LFN 20 contains feed and reflector input data and defines the type of Gauss-Legendre quadrature to be used for the computation of the feed element excitations. The reflector is assumed to be smooth and can be offset. The feed can have up to 10 elements with arbitrary locations and tilt angles. LFN 21 contains the weights and zeroes for the Gaussian integration. It is the same as LFN 21 used by the program RAPCA. The output file is designated by LFN 10. Table 5.2-1 shows the form for LFN 20 and LFN 21. Table 5.2-2 contains descriptions of the input variables for LFN 20. Refer to Table 5.1-3 for the format of LFN 21. Appendix A.2 gives an example of computing the excitations of an array feed for a given scan angle.

5.3 DUAL REFLECTOR ANALYSIS PROGRAM FOR CYLINDRICAL REFLECTORS (DRAPCA)

5.3.1 DRAPCA ALGORITHM

DRAPCA is used to evaluate the radiation patterns for dual cylindrical reflector antennas. The radiation pattern is computed using geometrical theory of diffraction (GTD) analysis for the scattered field from the subreflector and physical optics/aperture integration (PO/AI) for the main reflector. The dual reflector can have multiple feeds.

Table 5.2-1.

SCANRAP input file formats for LFN 20 and LFN 21.

LFN 20

NFEEDS		
XFEED(1)	ZFEED(1)	TFEED(1)
XFEED(2)	ZFEED(2)	TFEED(2)
.	.	.
.	.	.
XFEED(NFEEDS)	ZFEED(NFEEDS)	TFEED(NFEEDS)
Q		
DIAM	OFFSET	FOCAL
THETAS		
NORDER		

LFN 21

ZEROS(1)	WEIGHT(1)
ZEROS(2)	WEIGHT(2)
.	.
.	.
ZEROS(NORDER)	WEIGHT(NORDER)

Table 5.2-2.

SCANRAP input variable description for LFN 20.

ARGUMENT	TYPE*	DESCRIPTION
NFEEDS	I	Number of feeds: Initially limited to 10 or less
XFEED(i)	R	X-coordinate of ith feed (λ)
ZFEED(i)	R	Z-coordinate of ith feed (λ)
TFEED(i)	R	Tilt of the ith feed (°)
Q	R	Feed pattern exponent ($\cos^{q}\theta$)
DIAM	R	Diameter of the aperture (λ)
OFFSET	R	Aperture offset dimension (λ)
FOCAL	R	Focal length of the reflector (λ)
THETAS	R	Scan angle (°)
NORDER	I	Order of Gaussian quadrature

I: FORTRAN INTEGER
R: FORTRAN REAL NUMBER

The subreflector surface is assumed to be a hyperbola (Cassegrain) or an ellipse (Gregorian). The main reflector is a parabola and can either be smooth or distorted. The distorted main reflector surface is the same as described in Sec. 5.1.1, equations (5.1-18), (5.1-19), and (5.1-20). Axisymmetric, single offset, or dual offset reflectors with tilted feed elements are possible.

Figure 5.3-1 shows the geometry of a dual cylindrical reflector. The feeds are assumed to be linearly polarized line sources parallel to the y-axis. As in Section 5.1, the feeds are assumed to have radiation patterns described by $G(\gamma_i) = \cos^q \gamma_i$. Also, as in Section 5.1, the radiation pattern for a dual cylindrical reflector with N feed array elements is given by (equation (5.1-1) is repeated here for convenience) [23]

$$G_N(\theta) = \frac{\left| \sum_{i=1}^{N} A_i e^{j\phi_i} I_i \right|^2}{\sum_{i=1}^{N} A_i^2} \tag{5.3-1}$$

where A_i and ϕ_i are the excitation amplitude and phase of the ith feed element and I_i is the radiation integral of the ith element (to be derived below). The total radiation pattern, $G_N(\theta)$, is the superposition of the weighted radiation patterns of the individual feeds. (Actually, the superposition is performed in DRAPCA with the induced currents on the main reflector as this is computationally much more efficient).

There are two coordinate systems used to evaluate the dual cylindrical reflector (see Fig. 5.3-1). The radiation pattern coordinate system is centered at F0 with the positive x-axis pointing up and the positive z-axis pointing to the right. The feed coordinate system is centered at F1 and it is located by the tilt of the interfocal axis (β) and the leftmost foci of the ellipse or hyperbola. The positive z-axis of the feed coordinate system is along the ray from F1 to the center of the subreflector.

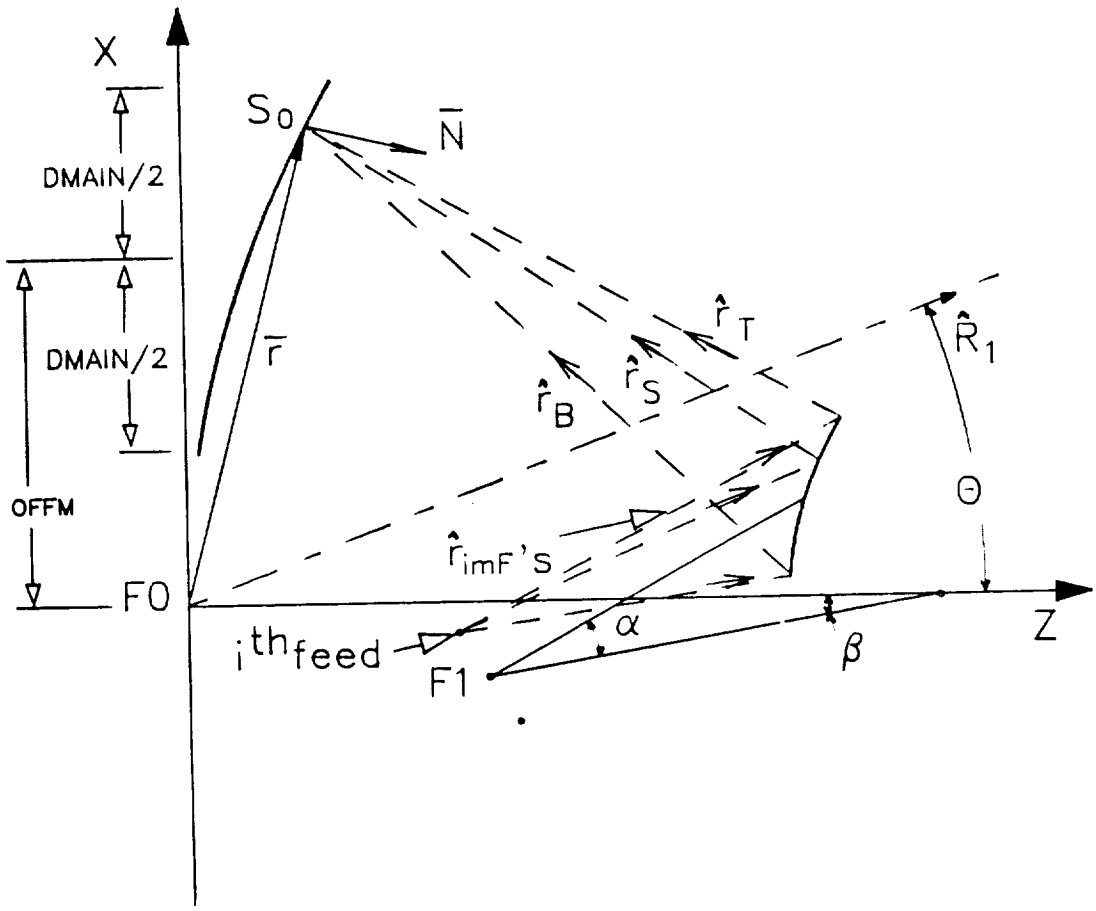

Figure 5.3-1. Dual cylindrical reflector geometry. This is the geometry DRAPCA uses to analyze the two-dimensional problem.

DERIVATION OF THE UNNORMALIZED RADIATION INTEGRAL

The radiation integrals for the individual feed elements can be found by extending the prime focus cylindrical reflector analysis in [47]. The analysis for this program is a special case in which the reflectors are assumed uniform in the y-direction. Integration in the y-direction yields a constant that can be normalized out. The remainder of the unnormalized radiation integral for the *i*th feed is (following [47])

$$I_i = \int_{S_0} \vec{J}_i e^{jk(\vec{r}' \cdot \hat{R}_1)} \, ds \tag{5.3-2}$$

where $\vec{J}_i$ is the induced PO current on the main reflector and S_0 is the surface of the main reflector. The integral along the profile of the main reflector surface, ds , can be replaced by an integration in x by making the substitution from (5.1-13). The integral can be rewritten as

$$I_i = \int_{OFFM-DMAIN/2}^{OFFM+DMAIN/2} \vec{J}_i e^{jk(\vec{r}' \cdot \hat{R}_1)} \, |\vec{N}| \, dx \tag{5.3-3}$$

The PO current $\vec{J}_i$ has three components: a GTD component from the top edge of the subreflector ($\vec{J}_T$) , a GTD component from the bottom edge of the subreflector ($\vec{J}_B$), and a GO (specular) component from the subreflector surface ($\vec{J}_S$) The total PO current is then

$$\vec{J}_i = \vec{J}_T + \vec{J}_B + \vec{J}_S \ . \tag{5.3-4}$$

The PO current is related to the H-field incident upon the main reflector. The PO current for the *ith* feed is given by $2\hat{n} \times \vec{H}_{i_m}$ for $m = T,B,S$. Each component of the

H-field can be expressed in terms of the incident E-field as (constants will be normalized out)

$$\vec{H}_{lm} \propto \hat{r}_m \times \vec{E}_{lm} = \hat{r}_m \times \hat{y} E_{lm} \tag{5.3-5}$$

where E_{lm} is the complex E-field amplitude. The induced PO current for the mth component is

$$\vec{J}_{lm} \propto \hat{n} \times \hat{r}_m \times \hat{y} E_{lm} \quad . \tag{5.3-6}$$

The cross product can be simplified. Referring to Fig. 5.3-2, the cross product in (5.3-6) is

$$\hat{n} \times \hat{r}_m \times \hat{y} E_{lm} = E_{lm} \sin \xi \hat{y} = E_{lm} \cos \chi \hat{y} \tag{5.3-7}$$

but

$$E_{lm} \cos \chi = - E_{lm} (\hat{r}_m \cdot \hat{n}) = - E_{lm} \frac{\hat{r}_m \cdot \vec{N}}{|\vec{N}|} \quad . \tag{5.3-8}$$

Equation (5.3-8) can be substituted into (5.3-4) to give

$$\vec{J}_l = (- E_{lT} \hat{r}_T - E_{lB} \hat{r}_B - E_{lS} \hat{r}_S) \cdot \frac{\vec{N}}{|\vec{N}|} \tag{5.3-9}$$

which when used in (5.3-3) produces the desired form

$$I_l = \int_{OFFM-DMAIN/2}^{OFFM+DMAIN/2} (- E_{lT} \hat{r}_T - E_{lB} \hat{r}_B - E_{lS} \hat{r}_S) \cdot \vec{N} e^{jk(\vec{r}' \cdot \hat{R}_1)} \, dx \tag{5.3-10}$$

which is the unnormalized radiation integral for the ith feed evaluated by DRAPCA.

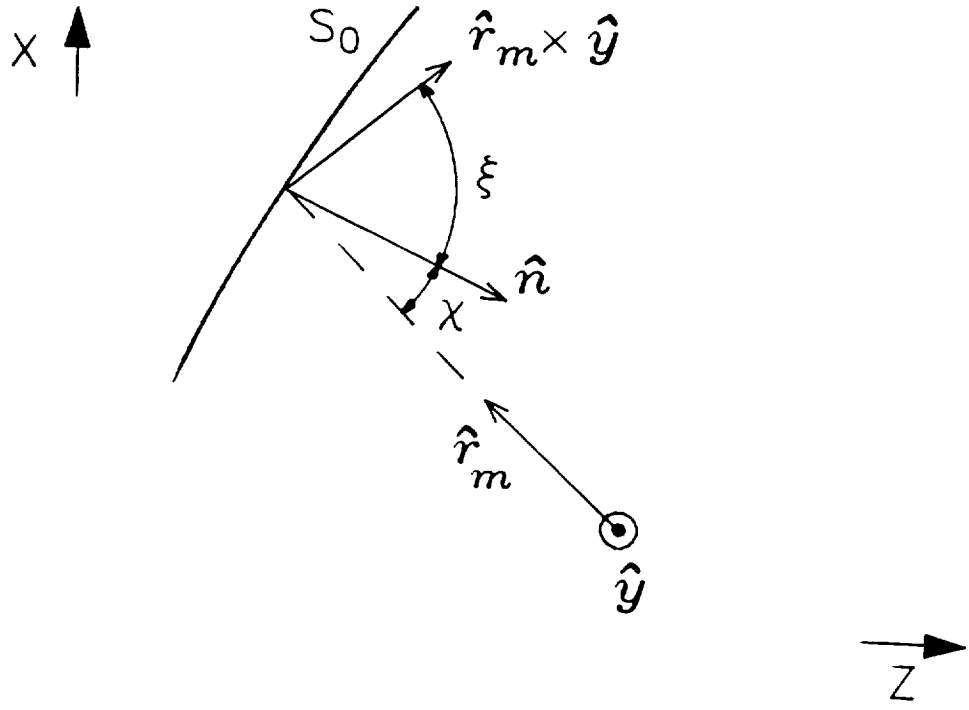

Figure 5.3-2. Vectors used to simplify the cross product expression of (5.3-7).

E-FIELD EXPRESSIONS FOR PO CURRENT CALCULATIONS

The problem remains to find expressions for the E-fields incident upon the main reflector. The GTD fields from the top and bottom edges of the subreflector are of the same form. The GO field from the subreflector surface has a distinct form.

The GTD E-field incident upon the main reflector is found by analyzing each of the subreflector edges as if it were an infinite half-plane. The incident E-field of the ith feed due to one of the edges is given by (using [55])

$$E_{im} = - D_{\parallel} E^F_{im} \frac{1}{\sqrt{r_m}} e^{-jkr_m} \tag{5.3-11}$$

where $m = T$ or B, $D_{\parallel}$ is the uniform theory of diffraction (UTD) coefficient and E^F_{im} is the field from the ith feed incident upon the subreflector edge. The E^F_{im} is defined as (any constants will be normalized out)

$$E^F_{im} = \left[\frac{G(\gamma_{im})}{r_{imF}} \right]^{\frac{1}{2}} e^{-jkr_{imF}} = \left[\frac{\cos^q \gamma_{im}}{r_{imF}} \right]^{\frac{1}{2}} e^{-jkr_{imF}} \tag{5.3-12}$$

where γ_{im} is the ith feed angle in the direction of the top or bottom edge. Substituting (5.3-12) in (5.3-11),

$$E_{im} = - D_{\parallel} \left[\frac{\cos^q \gamma_{im}}{r_{imF}} \right]^{\frac{1}{2}} \frac{1}{\sqrt{r_m}} e^{-jk(r_m + r_{imF})} \quad . \tag{5.3-13}$$

The UTD diffraction coefficients are found using the subroutine in Appendix G.9, [55].

The GO E-field incident upon the main reflector is determined using ray optics. The GO E-field component corresponds to the ray reflected from the specular point on the subreflector. The cylindrical GO E-field incident upon the main reflector is [55]

$$E_{lS} = -E_{lS}^{F}\left[\frac{\rho_1}{\rho_1 + r_S}\right]^{\frac{1}{2}} e^{-jkr_S} \tag{5.3-14}$$

where E_{lS}^{F} is the field incident upon the subreflector as defined in (5.3-12), ρ_1 is the radius of curvature of the reflected wavefront, and the minus sign accounts for the reversal of the E-field vector upon reflection from the subreflector. Using(5.3-12) in (5.3-14) gives the desired formulation of the GO component

$$E_{lS} = -\left[\frac{\cos^{q}\gamma_{lS}}{r_{lSF}}\right]^{\frac{1}{2}} e^{-jkr_{lSF}}\left[\frac{\rho_1}{\rho_1 + r_S}\right]^{\frac{1}{2}} e^{-jkr_S} \quad . \tag{5.3-15}$$

The radius of curvature of the reflected wavefront is computed using [55]

$$\frac{1}{\rho_1} = \frac{1}{r_{lSF}} + \frac{2}{\rho_c \cos\theta'} \tag{5.3-16}$$

where ρ_c is the radius of curvature of the subreflector at the specular point and θ' is the angle of incidence or reflection at the specular point.

5.3.2 DRAPCA INPUT AND OUTPUT

The program DRAPCA requires two input files which are denoted by the logical file numbers (LFN) 20 and 21. LFN 20 contains feed and reflector input data and defines the type of Gauss-Legendre quadrature to be used for the radiation integral. The main reflector may be smooth or distorted with the surface distortion defined by (5.1-18). The dual reflector may be offset or dual offset. The subreflector may be hyperbolic or elliptical. There may be up to 10 feed elements with arbitrary locations and tilt angles. LFN 21 contains the weights and zeroes for the Gaussian integration. It is the same as

LFN 21 used by the program RAPCA. The output file is designated by LFN 10. Table 5.3-1 shows the form for LFN 20 and LFN 21. Table 5.3-2 contains descriptions of the input variables for LFN 20. Refer to Table 5.1-3 for the format of LFN 21. Appendix A.3 gives an example of a Cassegrain reflector analyzed by DRAPCA.

5.4 REFLECTOR ANALYSIS PROGRAM (RAP), VERSION 2.0

5.4.1 RAP ALGORITHM

RAP is used to evaluate the radiation patterns for prime focus paraboloidal reflector antennas. The radiation pattern is computed using PO/AI. The reflector surface can be smooth or distorted. The projected aperture can have arbitrary shape. The reflector may be offset. Feeds displaced from the focus and tilted are possible. References [46] and [53] describe the algorithm in detail.

RAP, 2.0, has a surface interpolation routine that can be used to evaluate distorted or shaped reflectors. Interpolation, however, is computationally time consuming. Evaluation of the analytical distortion is much faster than for an interpolated surface. The RAP subroutine REFLEC which analyzes the surface function was modified slightly to evaluate distorted reflectors with analytical expressions. The equations defining the surface and derivatives of the surface were changed to allow pattern computation for distorted reflectors.

Table 5.3-1.

DRAPCA input file formats for LFN 20 and LFN 21.

LFN 20

NGTD				
NFEEDS	ISYS			
$AEXCIT_1$	$PEXCIT_1$	XFEED(1)	ZFEED(1)	TFEED(1)
$AEXCIT_2$	$PEXCIT_2$	XFEED(2)	ZFEED(2)	TFEED(2)
.	.	.	.	.
.	.	.	.	.
$AEXCIT_{NFEEDS}$	$PEXCIT_{NFEEDS}$	XFEED(NFEEDS)	ZFEED(NFEEDS)	TFEED(NFEEDS)
Q	PERRMX	PERRCY		
DMAIN	OFFM	FOCAL		
DSUB	ECC	TWOC	OFFS	OFFF
THETAB	THETAE	THETAI		
NORDER				

LFN 21

ZEROS(1)	WEIGHT(1)
ZEROS(2)	WEIGHT(2)
.	.
.	.
ZEROS(NORDER)	WEIGHT(NORDER)

Table 5.3-2.

DRAPCA input variable description for LFN 20.

ARGUMENT	TYPE*	DESCRIPTION
NGTD	I	Controls the subreflector analysis: NGTD = 0 - GTD is used NGTD = 1 - GO is used
NFEEDS	I	Number of feeds: Initially limited to 10 or less
ISYS	I	Defines the feed input location: ISYS = 1 - F1 coordinates ISYS = 2 - Primed coordinates
$AEXCIT_i$	R	Excitation amplitude for ith feed (linear)
$PEXCIT_i$	R	Excitation phase for ith feed (degrees)
XFEED(i)	R	X-coordinate of ith feed (λ)
ZFEED(i)	R	Z-coordinate of ith feed (λ)
TFEED(i)	R	Tilt of the ith feed (°)
Q	R	Feed pattern exponent ($\cos^q\theta$)
PERRMX	R	Phase error amplitude (°)
PERRCY	R	Number of cycles for the phase error
DMAIN	R	Main reflector diameter (λ)
OFFM	R	Main reflector offset (λ)
FOCAL	R	Focal length, main reflector (λ)
DSUB	R	Subreflector diameter (λ)
ECC	R	Subreflector eccentricity
TWOC	R	Interfocal distance (λ)
OFFS	R	Subreflector offset (λ)
OFFF	R	Feed phase center offset (λ)
THETAB	R	Far-field beginning angle (°)
THETAE	R	Far-field ending angle (°)
THETAI	R	Far-field increment angle (°)
NORDER	I	Order of Gaussian quadrature

I: FORTRAN INTEGER
R: FORTRAN REAL NUMBER

Two types of distorted surfaces were evaluated. Both had periodic errors. Both produce regions of high side lobes with a level dependent upon the amplitude of the errors; the location of the high side lobes depends on the frequency of the error across the surface.

The distorted surface function is found in a similar manner to the distorted surface function used by RAPCA (see Sec. 5.1.1, (5.1-22)). Figure 5.4-1 gives the reflector system geometry. For this geometry, the distance d is

$$d = r' - z' \tag{5.4-1}$$

where

$$r' = \sqrt{(\rho')^2 + (z')^2} \tag{5.4-2}$$

z' defines the surface function, and for a smooth parabolic reflector, $d = 2F$. Following the derivation of the cylindrical error in Sec. 5.1.1, the distorted surface is defined to be

$$d = 2F + \zeta = r' - z' + \zeta \quad . \tag{5.4-3}$$

Substituting (5.4-2) into (5.4-3) and solving for z', the distorted reflector surface expression is

$$z' = f(\rho, \rho_a, \phi_a) = \frac{\rho^2 - (2F + \zeta)^2}{4F + 2\zeta} \tag{5.4-4}$$

where ρ, ρ_a, and ϕ_a are the cylindrical coordinates defining the surface (see Fig. 5.4-2), F is the focal length, and ζ is the function describing the surface error. This reduces to the equation of a smooth paraboloid for the no error case of $\zeta = 0$.

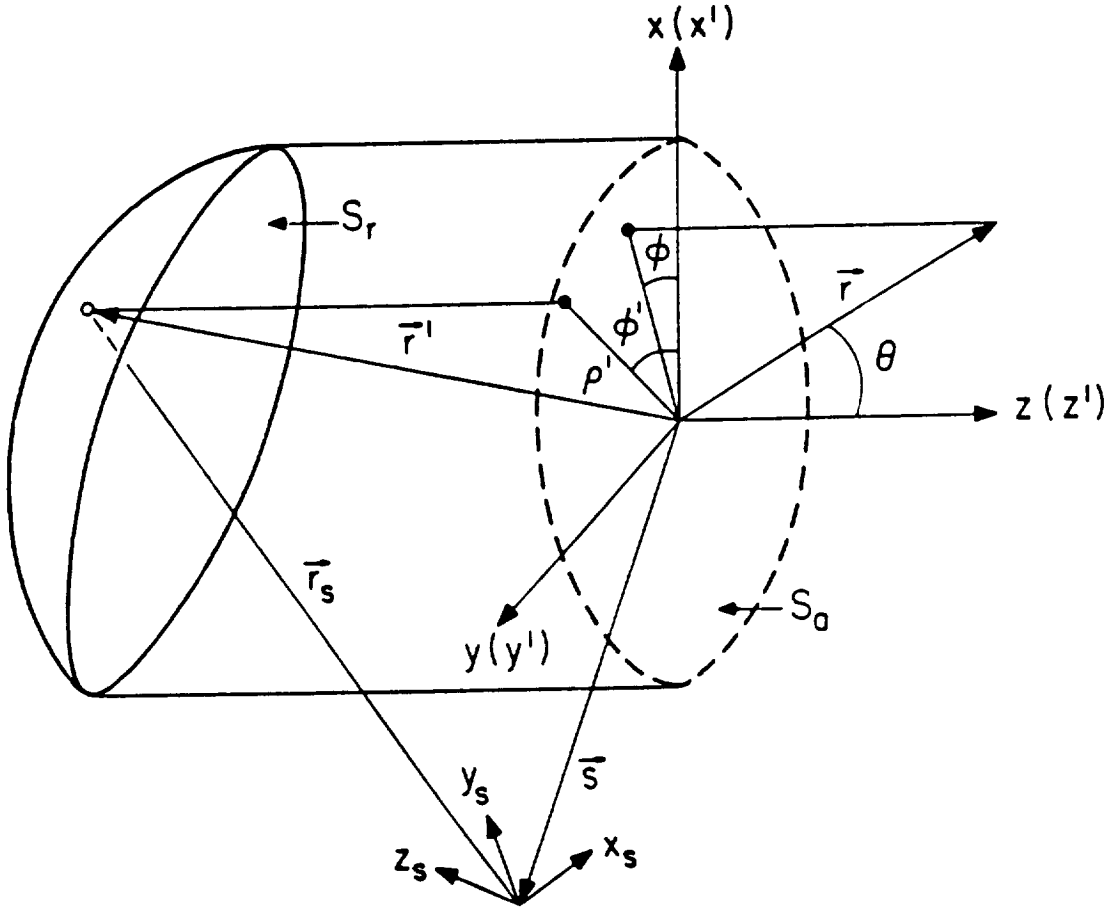

Figure 5.4-1. Geometry defining paraboloidal reflector used in RAP. [52]

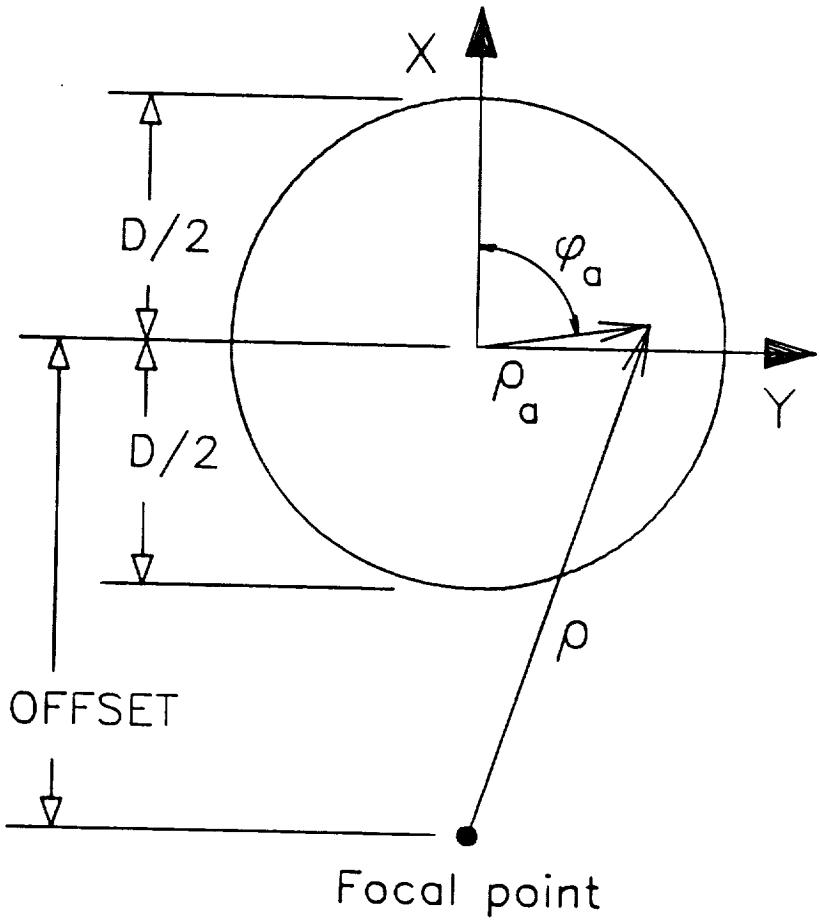

Figure 5.4-2. Geometry defining the radial and azimuthal surface errors.

The first paraboloidal surface distortion case analyzed was periodic as a function of radius. The distortion gives rise to a sinusoidal error in the aperture equivalent current. The radial surface error is given by

$$\zeta = \Gamma \cos\left(\frac{4\pi m \rho_a}{D}\right) \tag{5.4-5}$$

where Γ is the magnitude of the surface error (in λ), m is the number of periods along the radius, and D is the diameter of the aperture. The phase error in the aperture equivalent current is

$$\Phi_E = \phi_E \cos\left(\frac{4\pi m \rho_a}{D}\right) \tag{5.4-6}$$

where $\phi_E = (2\pi/\lambda)\Gamma$.

The second paraboloidal surface distortion case analyzed contained periodic errors in aperture azimuth angle ϕ_a. This distortion gives rise to a scalloped phase error that somewhat approximates the error when a radial rib reflector is used. The azimuthal surface error is given by

$$\zeta = \Gamma\left(\frac{2}{\pi} - \cos \mid \cos m\phi_a \mid\right) . \tag{5.4-7}$$

This error has zero mean. The corresponding phase error in the aperture equivalent current is

$$\Phi_E = \phi_E\left(\frac{2}{\pi} - \cos \mid \cos m\phi_a \mid\right) . \tag{5.4-8}$$

The profiles of both surface distortions are shown in Fig. 5.4-3.

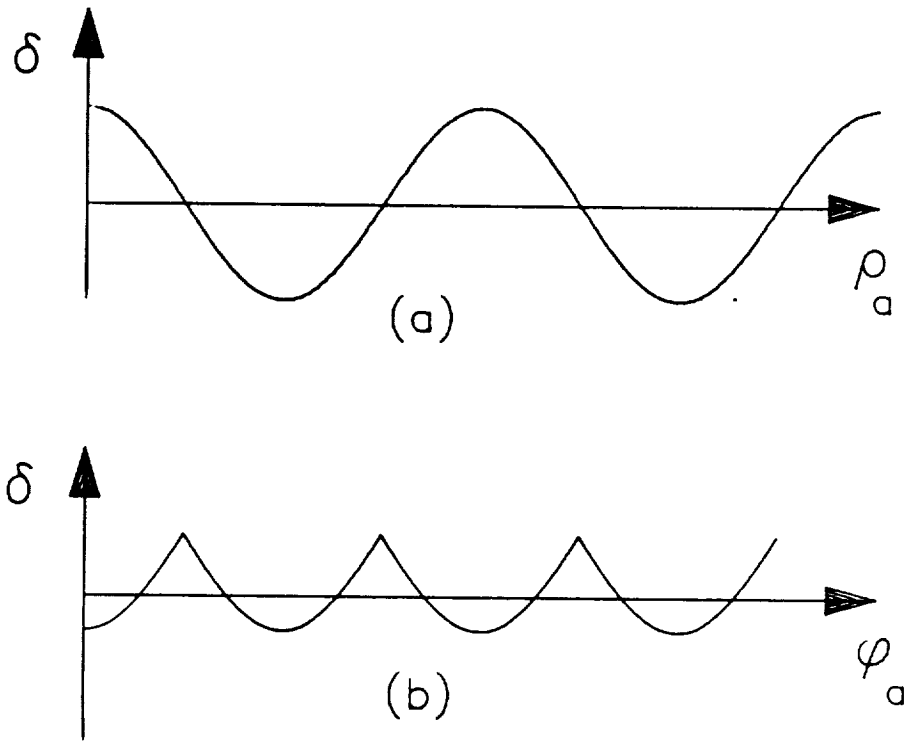

Figure 5.4-3. Surface error profiles for the (a) radial error and the (b) azimuthal error.

5.4.2 RAP INPUT AND OUTPUT

References [52] and [53] describe the RAP input and output files in detail. Example programs are given in the references.

6.0 COMPENSATION RESULTS

Results of studies using both cylindrical and paraboloidal reflectors are presented in this chapter. An extensive scan profile was generated for the cylindrical reflector to evaluate the scanned beams of smooth and distorted reflectors. Compensation results are presented for both cylindrical and paraboloidal reflectors, using displaced auxiliary feeds and fixed array feeds that use individual element amplitude and phase control (electronic compensation) to scan the compensation beams.

6.1 SCANNING STUDIES

6.1.1 PRIME FOCUS CYLINDRICAL REFLECTOR SCANNING STUDY

The pattern synthesis technique correction beams are meant to cause localized constructive effects but the side lobe envelope degrades with increasing scan. This degradation eventually produces a destructive global effect on the radiation pattern. Therefore, the side lobe degradation will ultimately limit the angular range over which the pattern synthesis compensation technique will be effective. For this reason, scanning studies were performed on cylindrical reflectors. Displaced feed scanning (prime focus, Sec. 3.1) and electronic scanning (Sec. 3.2) were evaluated. The scanning studies were used as a guideline for determining the limits over which the compensation technique can be used. In addition, the studies were used to determine whether the amplitude and phase of the scanned beam were significantly different between the smooth and distorted reflector cases.

For the scanning studies, and all the cylindrical prime focus reflector studies, the feed pattern was assumed to be a $\cos^q\theta$ pattern with $q = 3$. This gives a -12 dB edge taper with $F/D = 0.4$. The surface distortion of (5.1-21) and (5.1-22) is used. It sets up a surface error corresponding to a sinusoidal phase error in the equivalent PO aperture plane current.

FEED DISPLACEMENT

Examples of unscanned smooth and distorted reflector patterns computed using RAPCA are shown in Fig. 6.1-1. Note that the pattern angle where the region of high side lobes occurs increases as the frequency of the phase error increases (m increases). Also, the amplitude of the side lobes increases with increasing amplitude of the phase error.

Scanning of the beam causes the side lobe envelope to rise and the gain to drop. Figures 6.1-2 and 6.1-3 show examples of scanned smooth and distorted reflector radiation patterns. Note that while the high side lobe regions caused by the surface distortions appear in nearly the same location relative to the main beam, the main beam is nearly unaffected by the surface distortions. The scanned pattern in Fig. 6.1-3, however, is not usable for compensation as the side lobes are too high. Compensation for this reflector would then be limited to a range inside the location of the scanned beam shown in Fig. 6.1-3.

It is necessary to have amplitude and phase information for the scanned beam in order to apply the pattern synthesis compensation technique (see Sec. 4.2). The amplitudes and phases of the scanned beams produced by lateral displacement of the feed for the smooth and distorted reflector mentioned above were compared (see Table 6.1.1). The important point to note from the scan study is that, while the side lobe regions of the scanned patterns (e. g., Figs. 6.1-2 and 6.1-3) were noticeably affected by the surface distortion, the characteristics of the peak of the scanned beams for the distorted reflector did not vary greatly from the smooth reflector. This means that the amplitudes and phases of the auxiliary beams that will be used for compensation are essentially known based on smooth reflector performance. This is a major result because it implies that knowledge of the actual surface deviations is not required. It is also

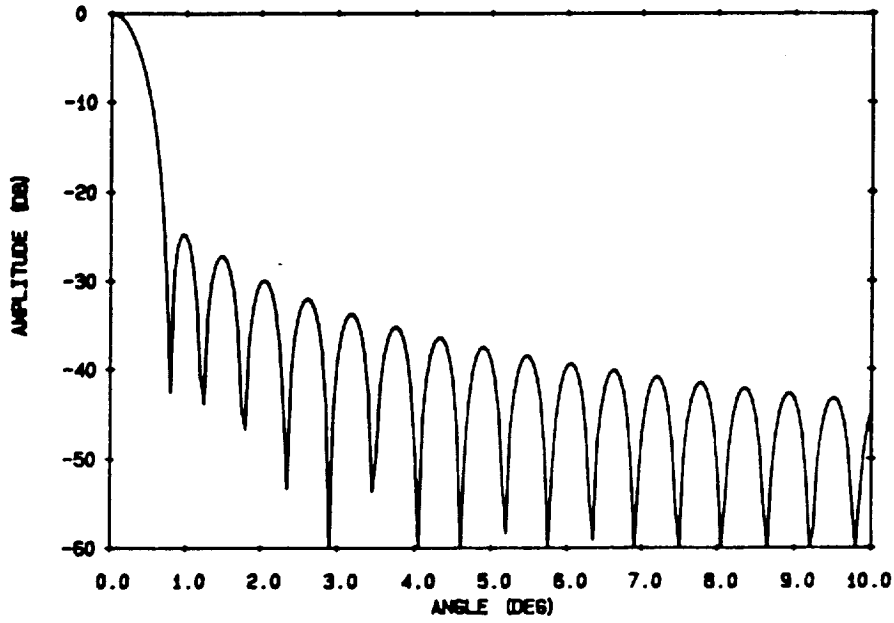

(a)

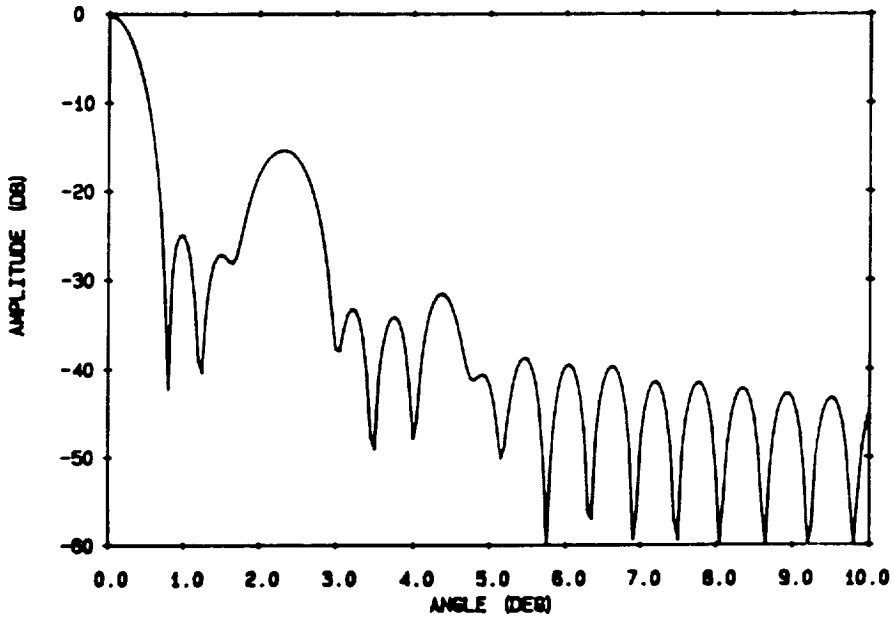

(b)

Figure 6.1-1. Unscanned beam for (a) smooth reflector, (b) distorted reflector with 2 periods of the surface error along the radius, and (c) distorted reflector with 5 periods of the surface error along the radius. The surface errors are such that the sinusoidal phase error of (5.1-23) appears across the aperture with a peak phase error of $\phi_E = 20°$. The $F/D = 0.4$, $D = 100\lambda$.

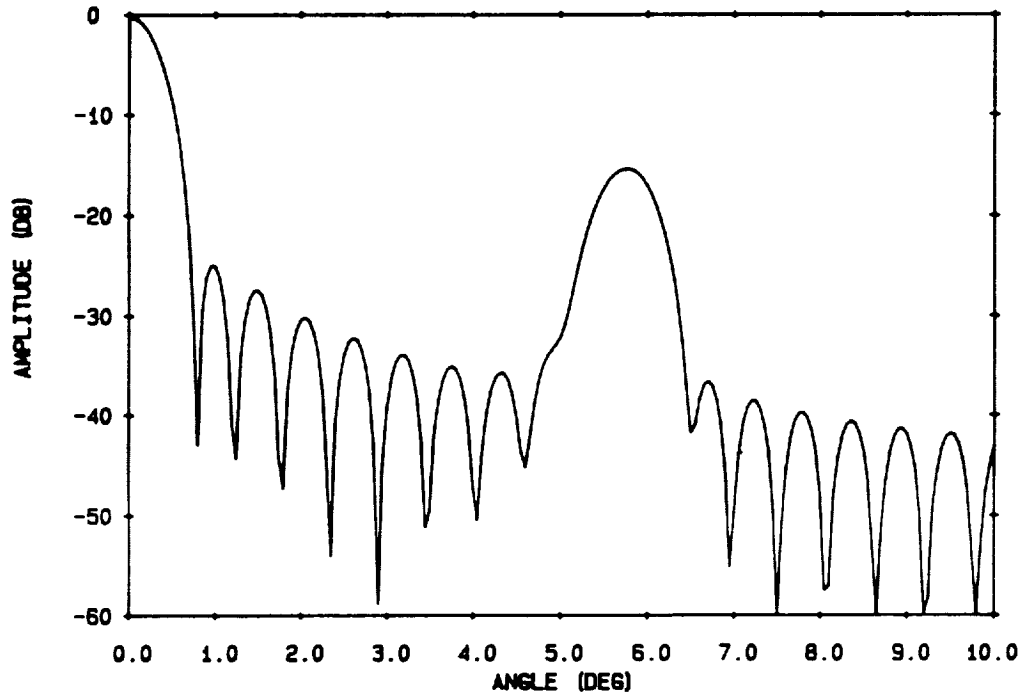

(c)

Figure 6.1-1. (continued)

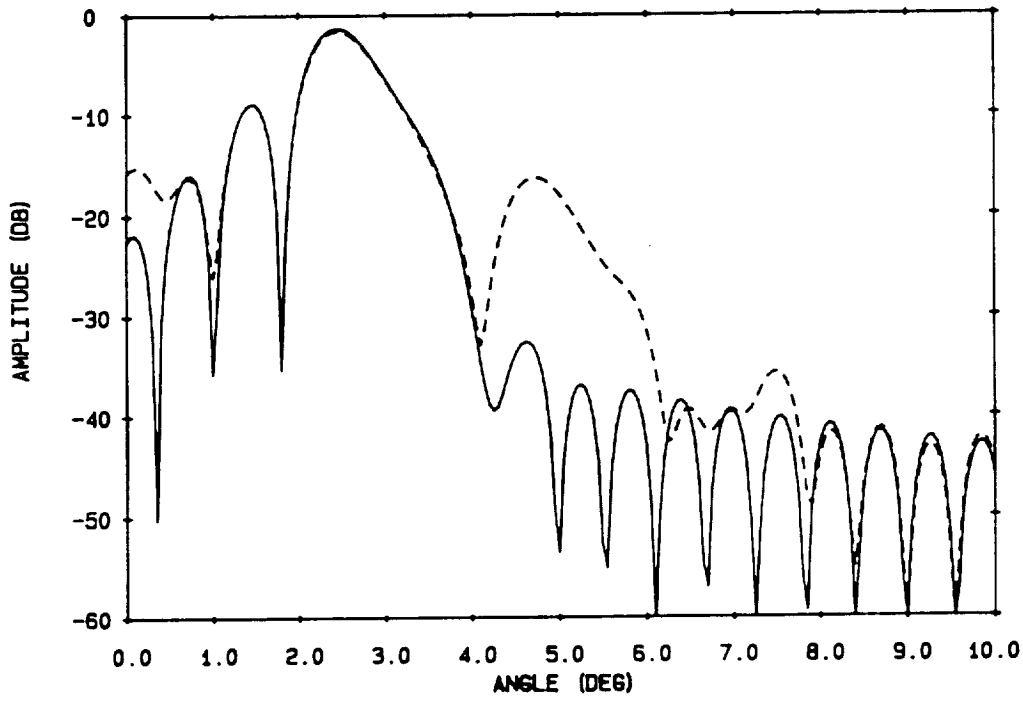

Figure 6.1-2. Scanned reflector patterns for lateral feed displacement of 2λ. The cases are for smooth reflector (solid) and distorted reflector (dashed) with 2 periods of the surface error along the radius ($F/D = 0.4$).

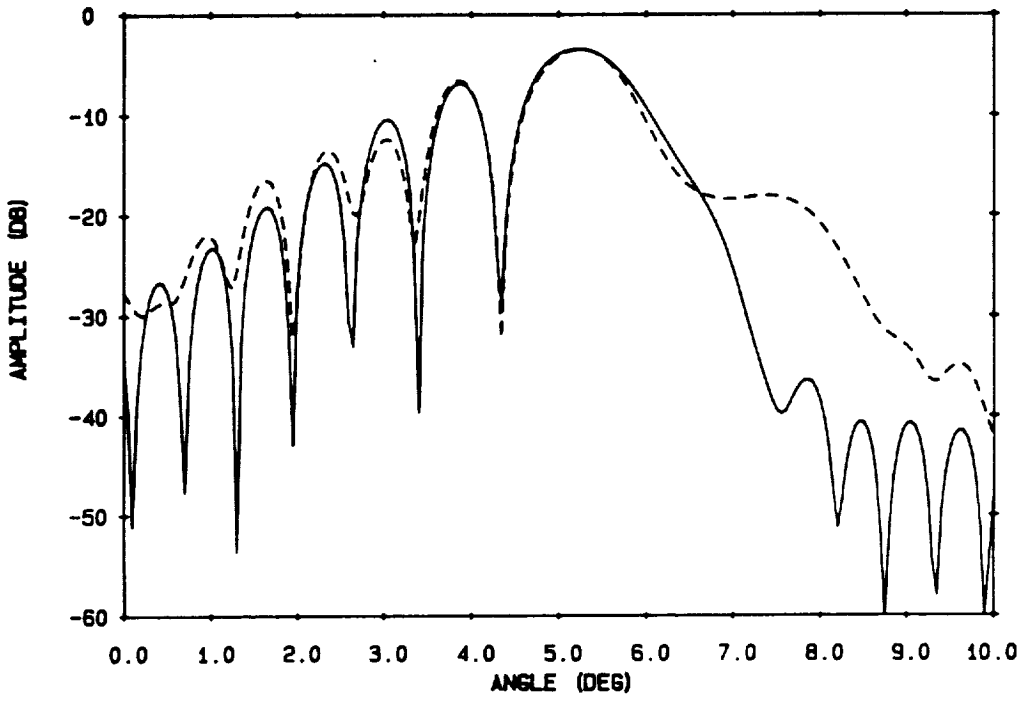

Figure 6.1-3. Scanned reflector patterns for lateral feed displacement of 4λ. The cases are for smooth reflector (solid) and distorted reflector (dashed) with 2 periods of the surface error along the radius ($F/D = 0.4$). This beam is beyond the useful limit of our compensation technique as the side lobes are too high.

Table 6.1-1.

The amplitude (linear field)/phase of the scanned beam peaks for both smooth and distorted reflectors. F/D = 40λ/100λ. The amplitude of the sinusoidal phase error is $\phi_E = 20°$.

	Feed Displacement, wavelengths (Scan Angle/BW of Scan)						
Distortion frequency (m)	X = 0.0 (0°/0BW)	X = 0.5 (0.6°/1BW)	X = 1.0 (1.22°/2BW)	X = 1.5 (1.82°/3BW)	X = 2.0 (2.44°/4BW)	X = 3.0 (3.74°/6.2BW)	X = 4.0 (5.22°/8.7BW)
m = 0	0.43/180.0°	0.43/-178.2°	0.41/-172.5°	0.40/-163,3°	0.37/-150.3°	0.32/-112.4°	0.29/-52.9°
m = 1	0.42/-179.5°	0.41/-177.6°	0.40/-171.8°	0.38/-162.4°	0.35/-148.9°	0.30/-109.2°	0.27/-49.2°
m = 2	0.42/-179.9°	0.41/-178.0°	0.40/-172.2°	0.38/-162.9°	0.36/-149.7°	0.31/-112.1°	0.29/-55.9°
m = 3	0.42/-179.9°	0.41/-178.1°	0.40/-172.4°	0.38/-163.2°	0.36/-150.1°	0.31/-112.7°	0.28/-54.8°
m = 4	0.42/180.0°	0.41/-178.1°	0.40/-172.5°	0.38/-163.2°	0.36/-150.2°	0.31/-112.6°	0.28/-53.9°
m = 5	0.42/180.0°	0.41/-178.1°	0.40/-172.5°	0.38/-163.3°	0.36/-150.3°	0.31/-112.5°	0.28/-53.7°

possible to determine the relative phase of the side lobe by using amplitude only measurements. This phasor analysis is presented in Section 6.2.1.

A presentation by Lee [21] at the NASA Earth Science Geostationary Platform Workshop held at NASA Langley Research Center prompted investigation into extending the scan range by using a higher F/D ratio reflector. Figure 6.1-4 shows scanned beams for a cylindrical reflector with $F/D = 1.0$, $D = 100\lambda$, and $q = 3$. The higher F/D reflector has significantly less increase in the side lobe envelope for a given scan angle than the lower F/D reflector evaluated above. This led to an investigation into extending the useful range of the pattern synthesis compensation technique by using a higher F/D reflector (see Section 6.2.1). The higher F/D reflector, however, would require a larger supporting structure and, if electronic scanning is used, a larger feed array. This, in turn, motivated investigation into a dual reflector configuration (see Sec. 6.4).

ELECTRONIC SCANNING

The cylindrical scanning study concluded with examination of electronic scanning. Again, a 100λ cylindrical reflector with F/D = 0.4 was used. The feed was a 7-element linear array with 0.5λ element spacing, centered on the focal line, and orthogonal to it. The element pattern was the same as the single element in the above laterally displaced feed analysis ($\cos^q\theta$, $q = 3$) .

Figure 6.1-5 shows examples of electronically scanned beams. The excitations of the elements were computed with SCANRAP (Sec. 5.2). Table 6.1-2 gives the element excitations for the electronic scans. Comparison to Figs. 6.1-2 and 6.1-3 reveals that the electronically scanned beams show improved performance compared to the single,

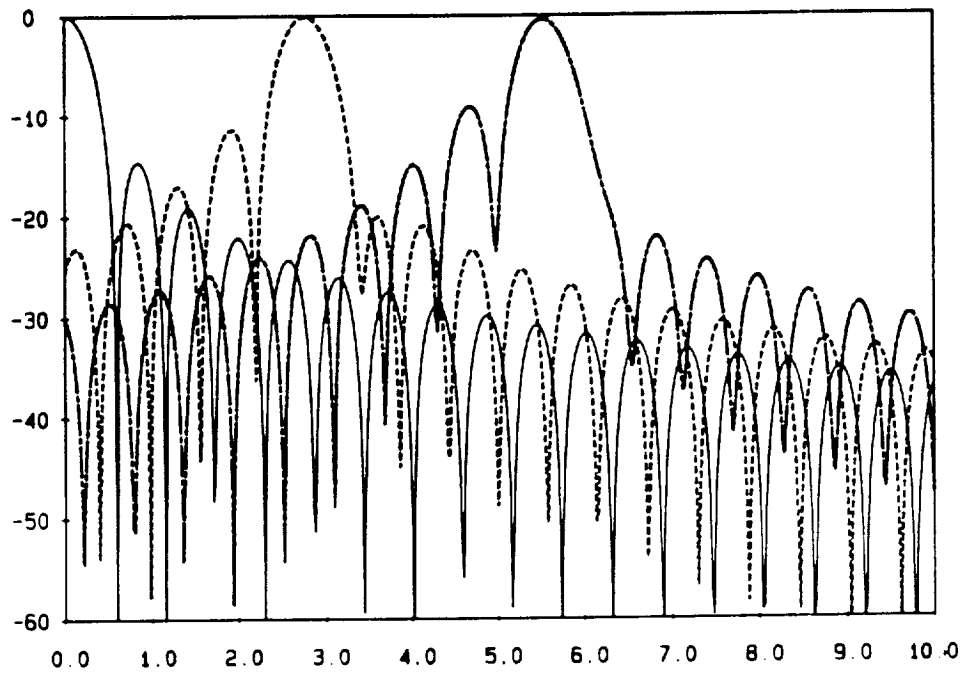

Figure 6.1-4. Radiation patterns for a smooth 100λ reflector with $F/D = 1.0$ for the cases of unscanned (solid), lateral feed displacement of 5λ (dashed), and lateral feed displacement of 10λ (dot-dash).

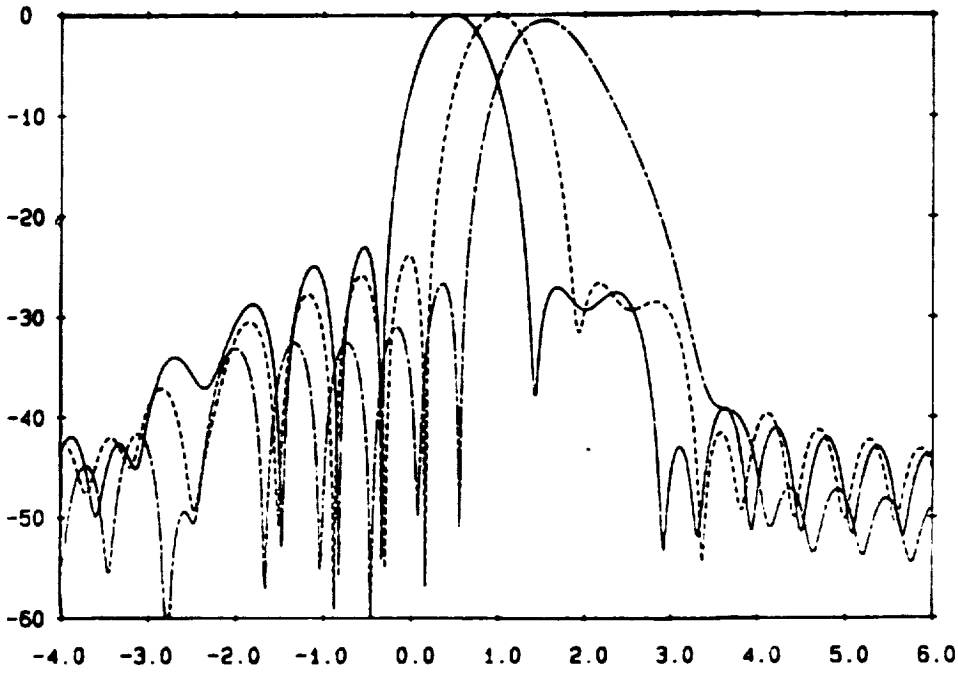

Figure 6.1-5. Electronically scanned beams for a cylindrical reflector with $F/D = 0.4$ and $D = 100\lambda$. A 7-element array feed with 0.5λ -element spacing was used. The element excitations were computed with SCANRAP and are given in Table 6.1-2.

Table 6.1-2.

Feed excitations for the scanned beams of Fig. 6.1-5. The feed elements are located in the focal plane (Z-COORD = 40λ).

FEED EXCITATION FOR 0 DEGREE SCAN

FEED	X-COORD (λ)	AMPLITUDE (LINEAR)	PHASE (DEG)
1	1.5000	.0900	.6204
2	1.0000	.1089	179.6889
3	.5000	.1457	-.8344
4	.0000	1.0000	.0000
5	-.5000	.1457	-.8344
6	-1.0000	.1089	179.6889
7	-1.5000	.0900	.6204

FEED EXCITATION FOR 1 DEGREE SCAN

FEED	X-COORD (λ)	AMPLITUDE (LINEAR)	PHASE (DEG)
1	1.5000	.0465	.3289
2	1.0000	.0586	179.1039
3	.5000	.0709	-1.4059
4	.0000	.0700	178.9586
5	-.5000	.7045	-.4076
6	-1.0000	1.0000	.0000
7	-1.5000	.2934	-178.2593

FEED EXCITATION FOR 2 DEGREE SCAN

FEED	X-COORD (λ)	AMPLITUDE (LINEAR)	PHASE (DEG)
1	1.5000	.0122	-.8269
2	1.0000	.0212	175.9401
3	.5000	.0298	-5.4128
4	.0000	.0373	174.1605
5	-.5000	.0547	-5.3645
6	-1.0000	.2113	-.8740
7	-1.5000	1.0000	.0000

laterally displaced feed. The array feed is able to somewhat compensate for the inherent phase errors associated with scanning a prime focus reflector by capturing more of the energy that is spread in the focal region due to scanning and adding it coherently. With the above 3λ-diameter feed array configuration, the reflector is limited to about ± 3 beamwidths of scan. This limit could be increased by using a larger array.

As with the scanned beams using laterally displaced feeds, it was found that the characteristics of the scanned beam peaks for the distorted reflector using a phased array feed did not vary greatly from the smooth reflector. This means that for the electronic scanned case that the amplitudes and phases of the auxiliary beams used for compensation are essentially known.

6.1.2 DUAL REFLECTOR SCANNING STUDIES

The dual reflector scanning study was performed on an infinite cylindrical axisymmetric Cassegrain reflector (see Fig. 6.1-6). The main reflector had a diameter of $D = 100\lambda$ with $F/D = 0.5$. The subreflector had a diameter of 34λ with eccentricity $e = 3$. The focal length of the equivalent prime focus reflector is [19]

$$F_E = F\,M = 50\,M \tag{6.1-1}$$

where [19]

$$M = \frac{e+1}{e-1} = 2 \tag{6.1-2}$$

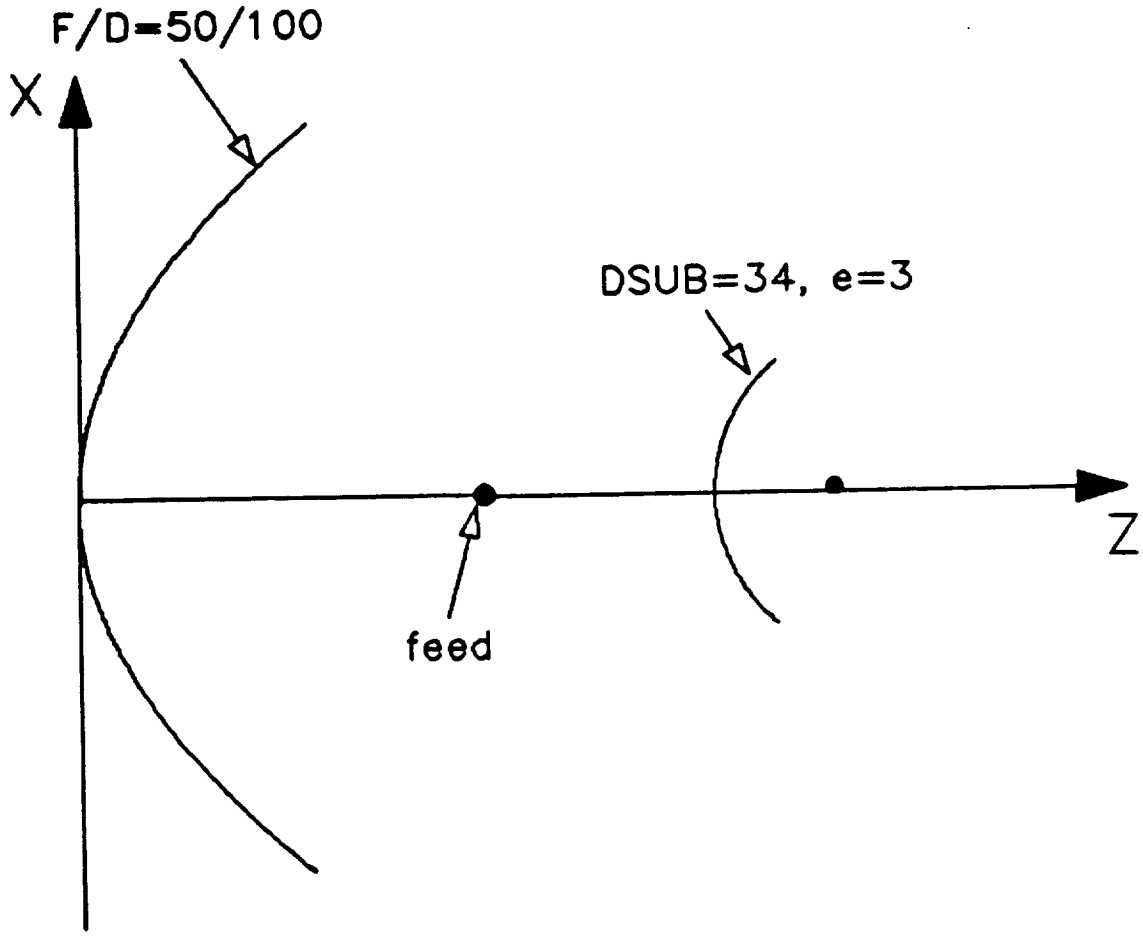

Figure 6.1-6. Infinite cylindrical axisymmetric Cassegrain reflector. The equivalent prime focus reflector has $F_E/D = 1.0$.

so $F_E = 100$. The choices of main reflector and subreflector eccentricity then give rise to an equivalent reflector with $F_E/D = 1.0$. Blockage was neglected. Feeds displaced from the focal point were used to scan the reflectors.

For small angle scans, the Cassegrain exhibits similar characteristics to that of its equivalent prime focus reflector (see Sec. 3.3). The equivalent reflector in this case has $F_E/D = 1.0$ An example of a pattern for the Cassegrain with the feed laterally displaced by 2λ in the minus x-direction is shown in Fig. 6.1-7. Note the phase is reasonably flat across the main beam. For wide angle scans, however, the phase aberrations of the Cassegrain differ significantly from the equivalent prime focus reflector. [13] This is now discussed further.

A quantitative comparison of wide angle dual reflector and prime focus reflector scanning is shown in Fig. 6.1-8. Fig. 6.1-8(a) shows the pattern for the Cassegrain with a feed laterally displaced -9.5λ in the minus x-direction to scan the reflector to 5.7°. Fig. 6.1-8(b) shows the pattern for the equivalent prime focus reflector (a single cylindrical reflector, $F/D = 1.0$) with the feed laterally displaced -10λ in the minus x-direction to scan the reflector to 5.7°. Note that the pattern phase across the main beam of the Cassegrain has a very steep slope while the phase across the main beam of the equivalent parabola is fairly flat. The steep ramp of the phase will make it difficult for the pattern synthesis compensation technique to coherently match the distorted pattern phase over a significant portion of the correction beam. In addition, the main beam of the Cassegrain pattern in Fig. 6.1-8(a) is very broad which impairs the ability of the pattern synthesis technique to act locally on a distorted pattern.

Krichevsky and DiFonzo [15] reported on optimizing the offset Cassegrain scanning performance by displacing the feed laterally and away from the focal plane (see Sec. 3.3). The optimized patterns had considerably better scanned pattern characteristics than those for lateral displacement in the focal plane. [15] The optimum loci for the

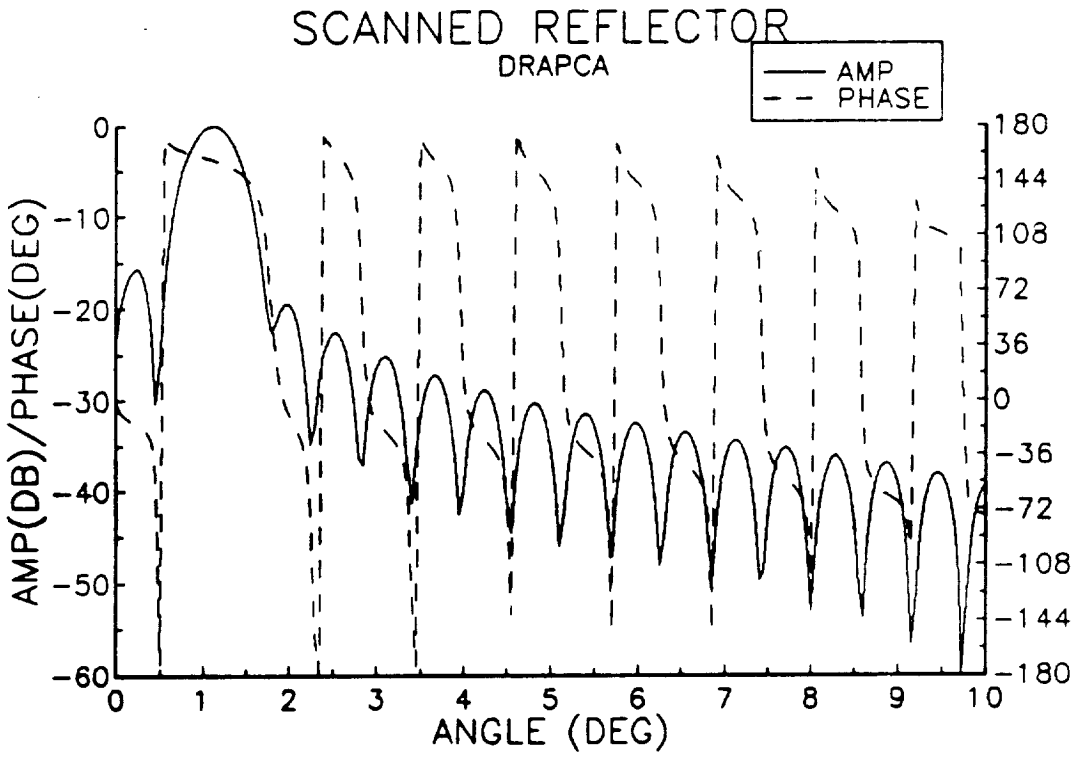

Figure 6.1-7. Scanned reflector pattern for lateral feed displacement of 2λ for an infinite cylindrical Cassegrain reflector. Both the amplitude (solid) and phase (dashed) are shown.

C-3

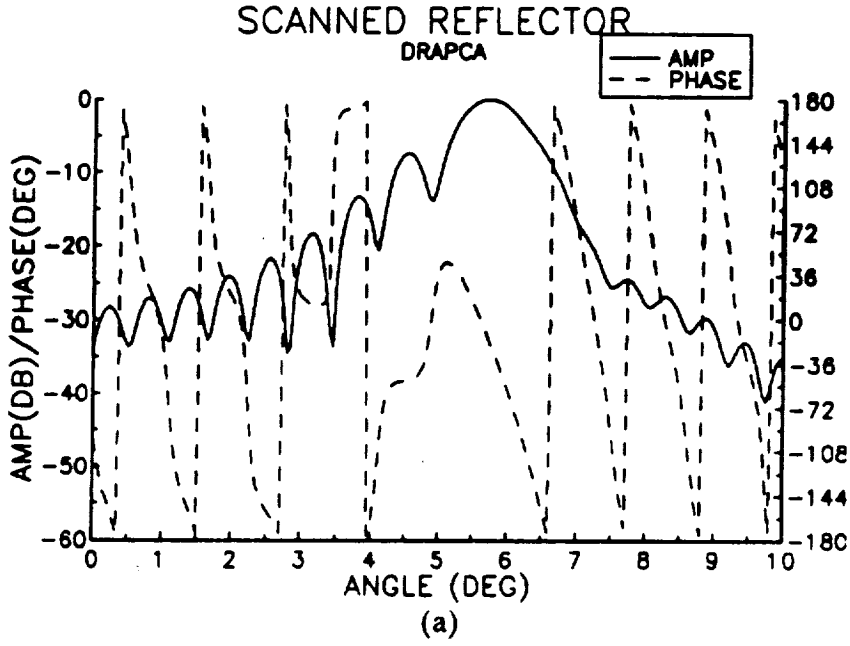

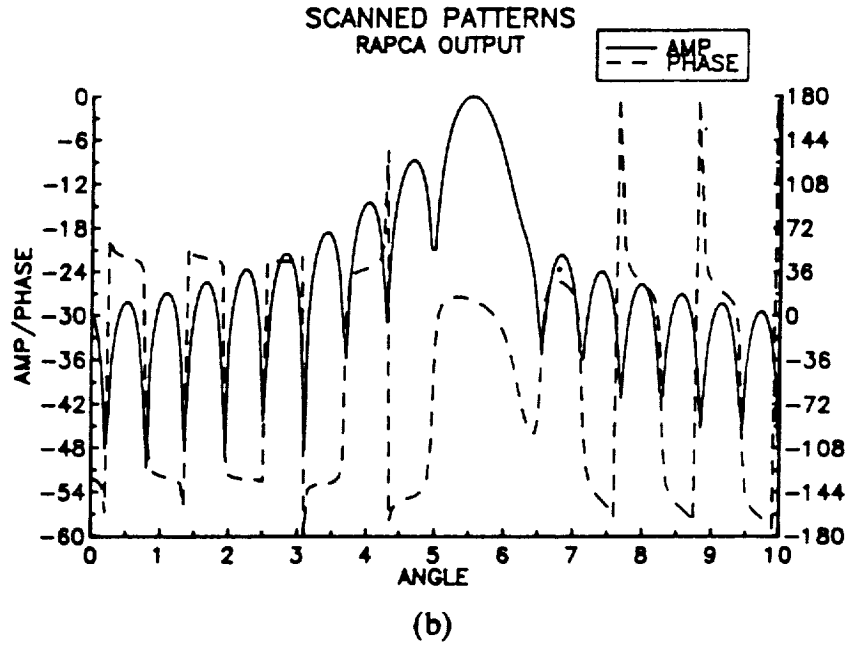

Figure 6.1-8. Amplitude (solid) and phase (dashed) for scanned reflector patterns (scan angle is 5.7°). (a) Dual cylindrical Cassegrain with the feed laterally displaced. (b) Equivalent prime focus reflector. (c) Dual reflector with the feed optimally displaced.

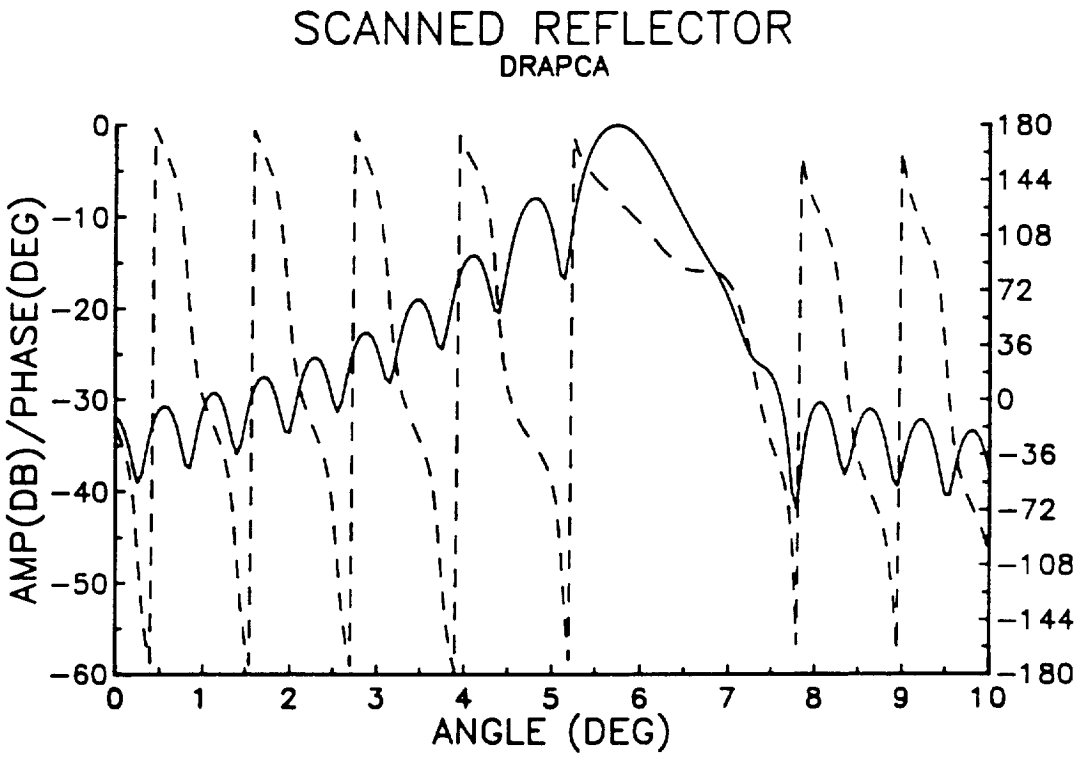

(c)

Figure 6.1-8. (continued)

feeds are along a hyperbola that curves towards the subreflector as the feed is displaced farther from the focal point. [15] Following the offset dual reflector optimum feed location analysis discussed in [15], trial and error was used to find a near optimum feed location for the wide angle scan. The feed was displaced by -9.5λ in the minus x-direction and 4.5λ in the plus z-direction. Fig. 6.1-8(c) shows the pattern for the optimized feed location. The slope of the phase across the main beam is much less severe and the main beam is much narrower.

The wide angle scanned pattern of Fig. 6.1-8(c) can be used for pattern compensation with the pattern synthesis technique. The dual configuration demonstrates improved scanning of the higher virtual *F/D* dual reflector over that of a lower *F/D* prime focus reflector while maintaining a compact feed structure.

6.2 CYLINDRICAL REFLECTOR COMPENSATION ANALYSIS

6.2.1 COMPENSATION WITH AN AUXILIARY FEED

Compensation calculations were run for the F/D = 40λ/100λ distorted reflector corresponding to the pattern in Fig. 6.1-1(b). An auxiliary scanned beam produced by a second feed was used to reduce the peak of the high side lobe caused by the surface distortion. The element pattern of the auxiliary feed was assumed to be the same as the feed at the focal point ($\cos^q\theta$, $q = 3$) and it was aimed along the boresight direction. The excitations $a_n^{(0)}$ were computed using (4.1-19). To illustrate the pattern synthesis

compensation technique with auxiliary feeds, it is useful to view the process from a superposed pattern standpoint. From (4.1-12), the resultant pattern after the single iteration is

$$F^{(1)}(u) = F^{(0)} + \Delta F^{(1)}(u) \quad . \tag{6.2-1}$$

where $F^{(0)}$ is the original distorted pattern and the correction pattern with one feed is

$$\Delta F^{(1)}(u) = a_1^{(1)}\, G_{ref}(u, u_n^{(1)}) \tag{6.2-2}$$

where the $a_1^{(1)}$ is the weight of the correction beam.

The plots in Fig. 6.2-1 show two cases of compensation. In Fig. 6.2-1(a), the auxiliary scanned beams were weighted to produce nulls at the locations of the peaks of the high side lobes. The auxiliary feeds were displaced by $\pm 1.88\lambda$ to scan the correction beams to the locations of the high side lobes. To produce nulls, the $F_a(u_n^{(0)})$ from (4.1-16) would be equal to zero. The weights were computed assuming a smooth reflector to be consistent with actual implementation of the technique. Using the distorted reflector data from Fig. 6.1-1(b) and the assumed smooth reflector scanned pattern data, the amplitude and phase of the correction beam excitations were computed using (4.1-16) and (4.1-18). The feed element excitations for the compensated pattern in Fig. 6.2-1(a) are found in Table 6.2-1. This weighting would produce absolute nulls at the locations of the peaks of the high side lobes if the weights were computed with the scanned correction beams of the actual distorted reflector. Even without knowledge the surface distortion, the pattern synthesis compensation technique produced the pattern of Fig. 6.2-1(a) with significant reduction in the high side lobes of the distorted reflector pattern of Fig. 6.1-1(b).

Figure 6.2-1(b) shows a case where the amplitude of the weights were reduced to produce a 10 dB reduction in the side lobe peaks. Once again, the weights were

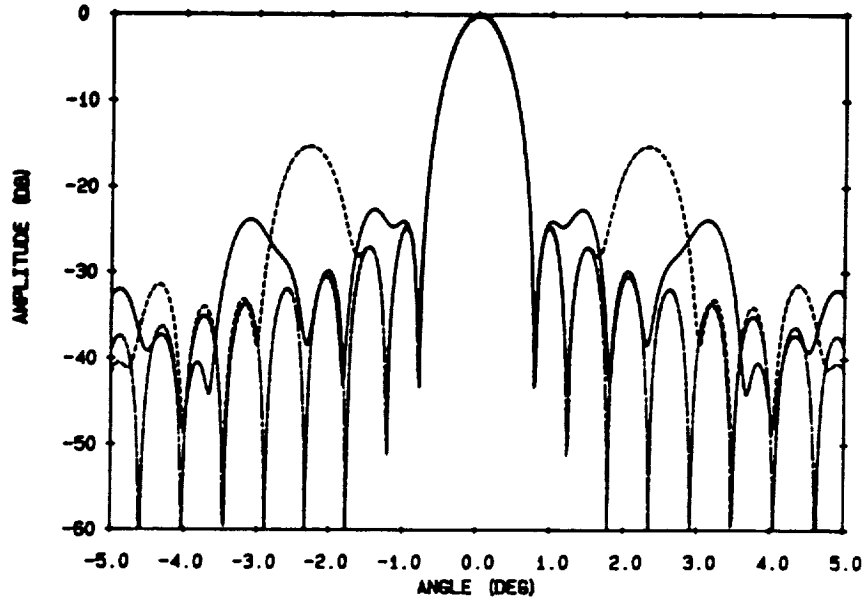

(a)

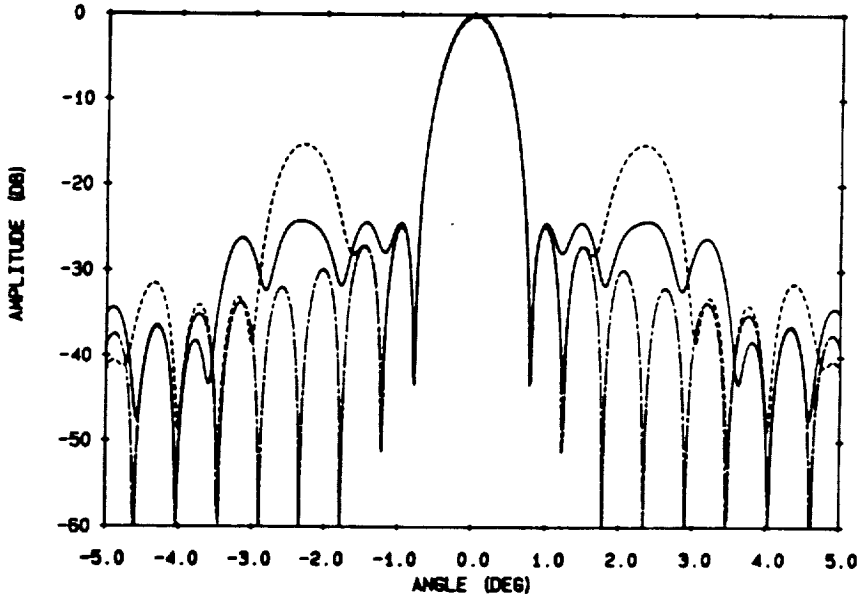

(b)

Figure 6.2-1. Compensation for the high side lobes at $\pm 2.3°$ of the distorted reflector in Fig. 6.1-1(b) using auxiliary scanned beams generated by lateral displacement of two feeds ($F/D = 0.4$). (a) The auxiliary beams are weighted to produce nulls. (b) The auxiliary beams are weighted to reduce the side lobe peaks by 10 dB.

Table 6.2-1.

Feed excitations for the displaced feed compensated patterns in Fig. 6.2-1. The elements are located in the focal plane (Z-COORD = 40λ). The two cases are for (a) placing nulls at the peaks of the high side lobes and (b) reducing the peaks of the high side lobes by 10 dB.

FEED EXCITATION FOR NULL

FEED	X-COORD (λ)	AMPLITUDE (LINEAR)	PHASE (DEG)
1	1.0000	.0000	.0000
2	.1960	-1.8800	99.5300
3	.1960	1.8800	99.5300

(a)

FEED EXCITATION FOR 10 dB REDUCTION

FEED	X-COORD (λ)	AMPLITUDE (LINEAR)	PHASE (DEG)
1	1.0000	.0000	.0000
2	.1340	-1.8800	99.5300
3	.1340	1.8800	99.5300

(b)

computed assuming a smooth reflector. To reduce the peak by 10 dB, the $F_d(u_n^0)$ from (4.1-16) would be equal to $0.316F^{(q-1)}(u_n^0)$. The feed locations and excitations for the compensated pattern in Fig. 6.2-1(b) are given in Table 6.2-1. The advantage to the reduced amplitude case is that the lower auxiliary beam amplitude causes less interference with the surrounding side lobe envelope. This is important in keeping the effects of the pattern synthesis compensation technique iterations localized.

EXTENDED RANGE COMPENSATION

Compensation analysis was run on a distorted cylindrical reflector with an F/D = $100\lambda/100\lambda$. The improved side lobe envelope of the scanned beams for the higher F/D-ratio reflector allows compensation to be performed much farther out than the lower F/D-ratio case. Figure 6.2-2 shows a compensation example illustrating the extended range of the higher F/D-ratio reflector; the F/D = 0.4 case was limited to about ±3° compensation range. The correction beam is weighted to reduce the side lobe peak by 10 dB.

SIDE LOBE PHASE DETERMINATION

Figure 6.2-1 was generated assuming that the pattern phase was known. In implementing the pattern synthesis compensation technique, phase data will probably not be available. This problem is overcome with the "amplitude-only" phasor analysis discussed in Sec. 4.2. The auxiliary beam is amplitude weighted as above and steered to the location of the pattern requiring compensation with a blind guess as to the required phase excitation (a good start is to assume the phase excitation is 0°). By drawing a

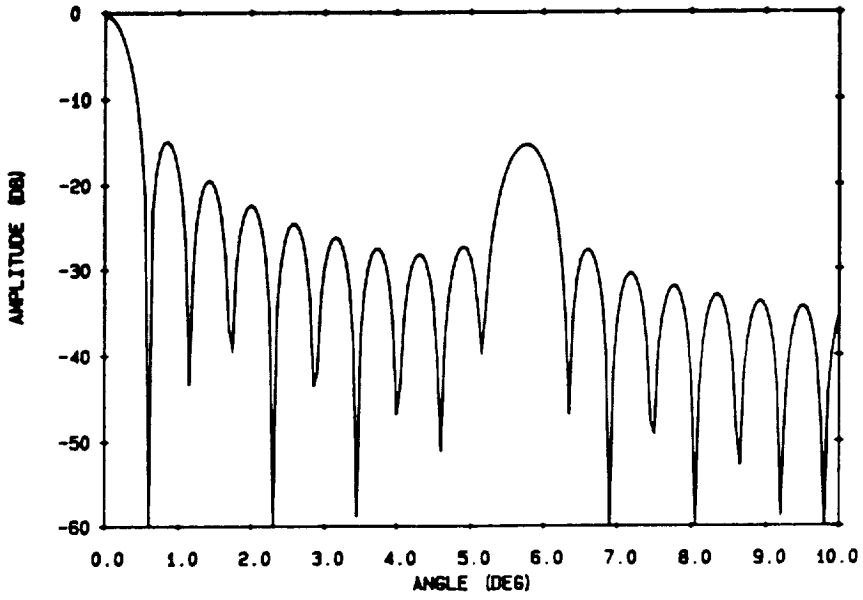

(a)

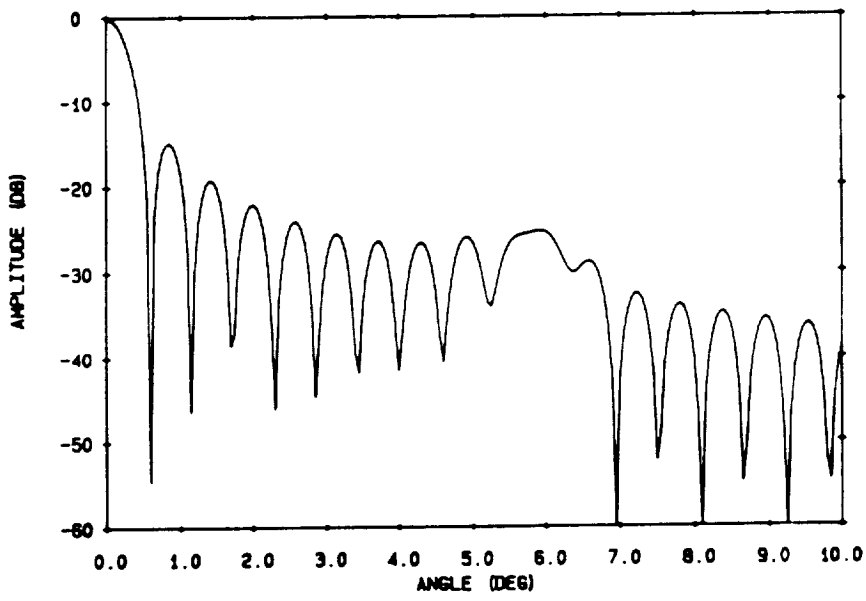

(b)

Figure 6.2-2. Radiation patterns for a distorted 100λ reflector with a distortion having five spatial periods along the radius , $F/D = 1.0$ for the cases of (a) uncompensated and (b) compensated. A second displaced feed was used to generate an auxiliary correction beam positioned at 5.76°.

phasor diagram of the peak of the side lobe before the auxiliary beam is scanned, the peak after scanning, and the (approximately) known amplitude of the auxiliary beam, the relative phase between the side lobe before compensation and the scanned beam can be determined to a reasonable degree of accuracy by determining the angle ϕ, from Fig. 4.2-1. The relative phase is ambiguous as it could lead or lag the phase of the side lobe. Therefore, at least one extra step (possibly two) is required to set the phase excitation to the proper value for compensation.

The above compensation case in Fig. 6.1-1(b) was used as a start point and analyzed without knowledge of the distorted pattern phase. The desired result is to reduce the peak of the high side lobe by 10 dB as was done previously in Fig. 6.2-1(b). Figure 6.2-3 illustrates the process. In the first iteration, the scanned correction beam was weighted with the excitation amplitude from Fig. 6.2-1(b) and a phase of 0°. The resulting pattern (solid curve in Fig. 6.2-3)) actually caused the side lobe peak to increase by 0.22dB. After determining the relative phase with the phasor analysis, the compensated pattern (dashed curve in Fig. 6.2-3)) gave results comparable to Fig. 6.2-1(b). The dot-dash curve in Fig. 6.2-3 is the case where the ambiguity in the relative phase caused an error in determining the phase.

6.2.2 ELECTRONIC COMPENSATION

In this Section, the pattern synthesis compensation technique is implemented with electronic scanning of the correction beams. To illustrate the pattern synthesis compensation technique with electronic scanning, it is useful to view the process from a superposed current standpoint. Using (4.1-15), the composite induced current on the reflector due to the mth feed after this single iteration,

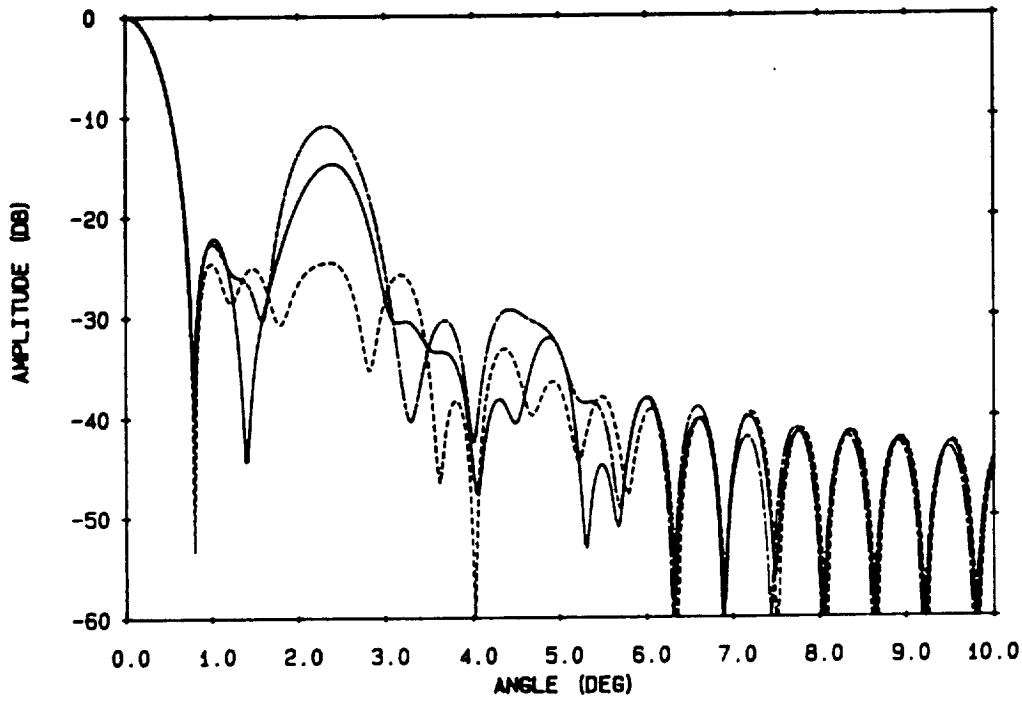

Figure 6.2-3. Radiation patterns of a distorted cylindrical reflector, $F/D = 40\lambda/100\lambda$, for compensation without pattern phase data. The phasor analysis described in Sec. 4.2 was used. The original distorted pattern is that of Fig. 6.1-1(b). The solid curve is the first iteration with auxiliary beam phase excitation of 0°. The dashed curve is the second iteration after the relative phase has been determined. The dot-dash curve is the case where the relative phase ambiguity caused an error in determining the phase.

$$f_{ref,m}^{(1)} = f_{ref,m}^{(0)} + \Delta f_{ref,m}^{(1)} \tag{6.2-3}$$

and, using (4.1-14),

$$\Delta f_{ref,m}^{(1)} = a_1^{(1)} g_{m1}^{(1)} + a_2^{(1)} g_{m2}^{(1)} \tag{6.2-4}$$

where the $a_1^{(1)}$, $a_2^{(1)}$ are the compensation weights for each of the two beams and the $g_{m1}^{(1)}$, $g_{m2}^{(1)}$ are the induced currents on the reflector for each of the two beams due to the mth feed. The composite current of (6.2-3) is then evaluated in the radiation integral to get the compensated pattern.

Electronic compensation was performed on the distorted reflector corresponding to the pattern in Fig. 6.2-4. The distorted reflector has a slightly lower surface error spatial frequency (m) than the reflector from Fig. 6.1-1(b). The feed array was the same seven element array used previously in Section 6.1. Two auxiliary scanned beams (symmetrically placed on each side of the main beam) given in Fig. 6.2-5 were simultaneously used to reduce the high side lobes caused by the surface distortion. The excitations for the scanned beams were computed with SCANRAP assuming a smooth surface. The excitations for scanning the beams were then weighted to reduced the side lobe peaks by 10 dB and superposed to get the compensation excitations using phase information computed from the distorted pattern. The compensated pattern is shown in Fig. 6.2-6. The excitations and locations of the array feed are listed in Table 6.2-2.

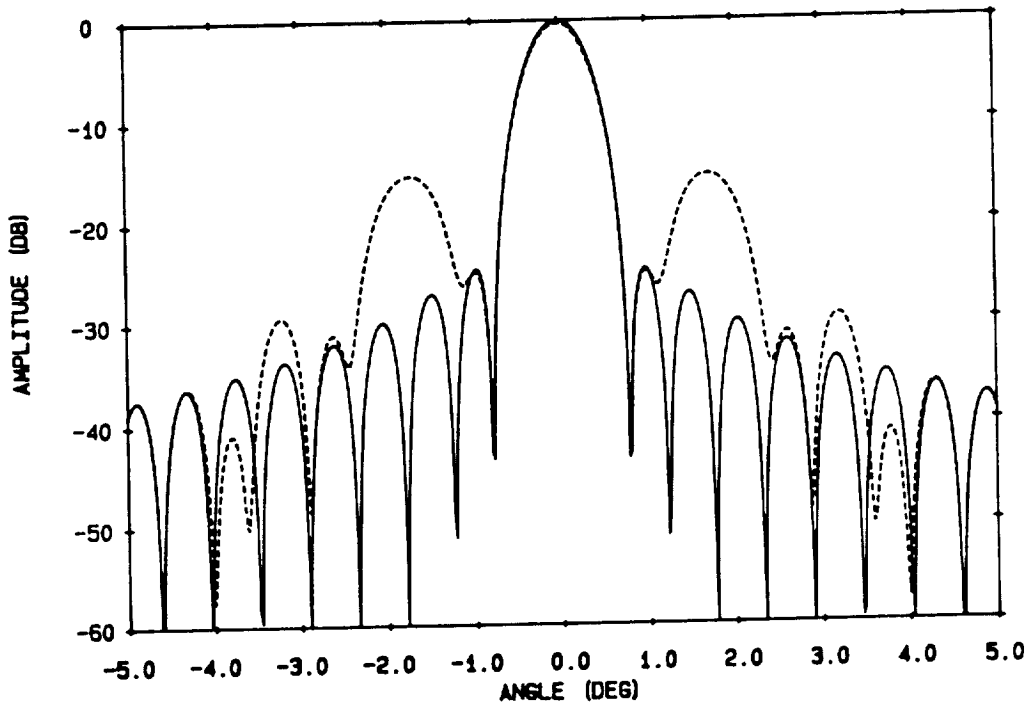

Figure 6.2-4. Unscanned patterns of an axisymmetric reflector for the cases of a smooth surface (solid) and a distorted surface (dashed) with 1.5 periods of the surface error across the reflector. The $F/D = 0.4$ and $D = 100\lambda$. The maximum phase error in the PO current is $\phi_E = 20°$.

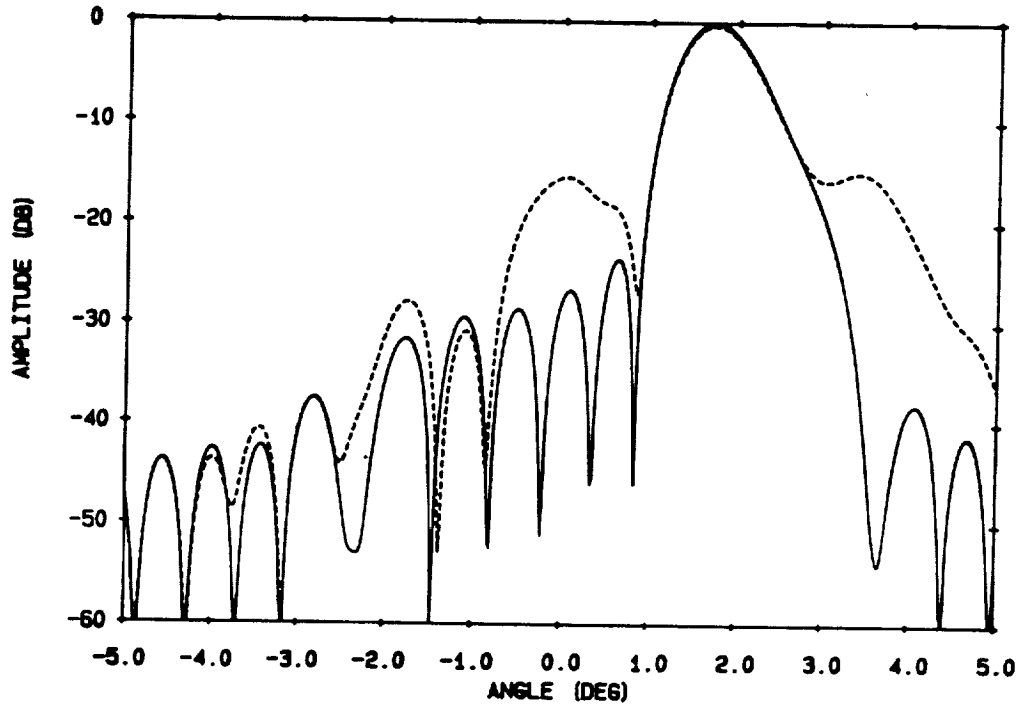

Figure 6.2-5. Auxiliary electronic scanned beam from a linear feed array of seven $\lambda/2$-spaced elements used to reduce the high side lobe at 1.72° caused by the surface error across the reflector of Fig. 6.2-4. The pattern was computed assuming a smooth reflector (solid curve). The actual scanned pattern of the distorted reflector is also shown (dashed). A similar beam is used to reduce the high side lobe at -1.72°.

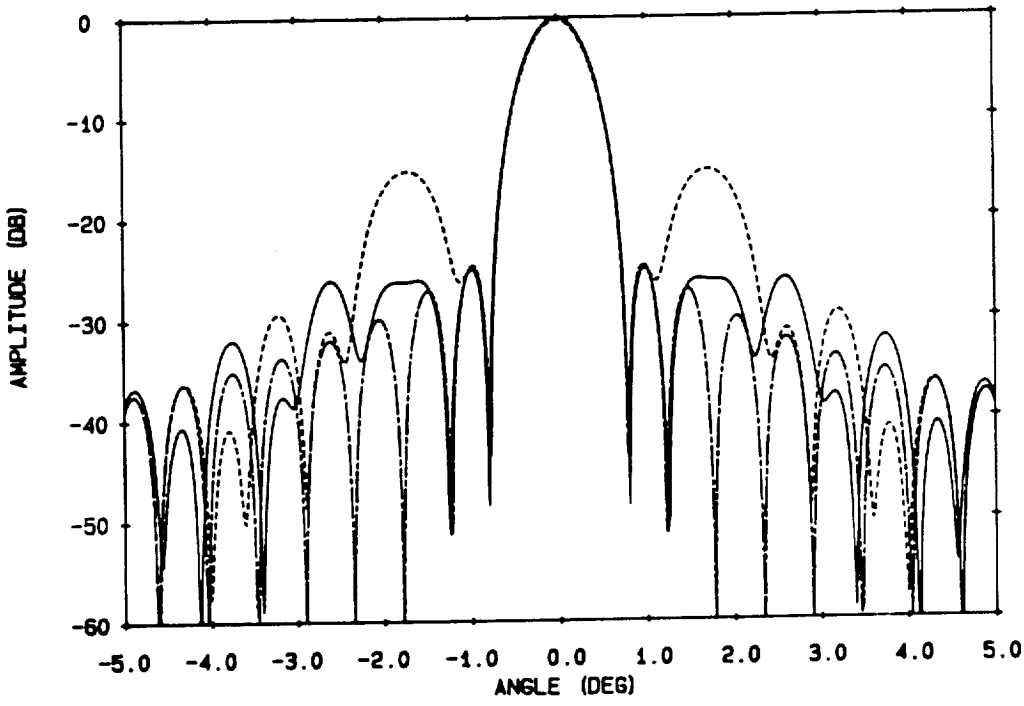

Figure 6.2-6. The pattern resulting from application of compensation for the high side lobes at $\pm 1.72°$ using the auxiliary scanned beams of Fig. 6.2-5 produced by a linear feed array of seven $\lambda/2$-spaced elements (solid). The dashed line is the uncompensated pattern and the dot-dash line is the pattern of a smooth reflector. The amplitudes of the weights were designed to produce a 10 dB reduction in the side lobes.

Table 6.2-2.

Feed excitations for the electronically compensated patterns in Fig. 6.2-6. The elements are located in the focal plane (Z-COORD = 40λ). The excitations were computed to reduce the peak of the high side lobe by 10 dB.

FEED EXCITATION FOR 10 dB REDUCTION

FEED	X-COORD (λ)	AMPLITUDE (LINEAR)	PHASE (DEG)
1	1.5000	.1150	100.2700
2	1.0000	.0620	99.5300
3	.5000	.0017	104.9100
4	.0000	.9990	.1976
5	-.5000	.0017	104.9100
6	-1.0000	.0620	99.5300
7	-1.5000	.1150	100.2700

6.3 PARABOLOIDAL REFLECTOR COMPENSATION ANALYSIS

Compensation calculations were run for distorted prime focus paraboloidal reflectors with $F/D = 0.5$ and $D = 100\lambda$. The feed elements are linearly polarized and have a radiation pattern approximated by a $\cos^q\theta$ with $q = 2.7$ (this q gives an edge illumination of -12 dB). The process uses auxiliary beams that are scanned to the locations in the pattern requiring compensation. The aux beams are then weighted to correct pattern irregularities. The weights are computed assuming a smooth reflector. The pattern synthesis compensation technique was implemented using displaced feed scanning and electronic scanning. The distorted reflectors studied had surface errors that gave rise to periodic aperture plane equivalent current phase errors. The errors were periodic in either the radial or azimuthal directions. The RAP, Version 2.0, subroutine REFLEC that defines the reflector surface was modified to allow implementation of a reflector with surface errors that give rise to the periodic aperture plane current phase errors. The surface functions for the distorted surfaces are given in Sec. 5.4. Both kinds of surface errors produce regions of high side lobes in which the amplitude of the side lobes depends on the amplitude of the phase error and the location depends on the spatial frequency of the error.

6.3.1 COMPENSATION WITH AUXILIARY DISPLACED FEEDS

The radial surface error defined by (5.4-4) and (5.4-5) was chosen so that a sinusoidal error as a function of radius occurred in the aperture plane equivalent current phase. The radial error causes a narrow region of high side lobes. Figure 6.3-1 shows the compensation case where four displaced auxiliary feeds (placed symmetrically about the axis) were used to compensate for high side lobes in the principal planes. The correction beams were weighted to reduce the side lobe peaks by 10 dB. The feed element locations and excitations are given in Table 6.3-1. The actual peak reductions are given in Table 6.3-2.

The azimuthal surface error defined by (5.4-4) and (5.4-7) was chosen so that a scalloped phase error occurred in the aperture plane current. This error somewhat approximates the error that occurs when a radial rib-type reflector is used. The azimuthal surface error causes a distortion over a wider region than the radial surface error does (comparing the distorted patterns from Figs. 6.3-1 and 6.3-2). Figure 6.3-2 shows the compensation case where four auxiliary feeds (placed symmetrically about the axis) were used to compensate for high side lobes in the principal planes. The compensation beams were weighted to reduce the side lobe peaks by 10 dB.

Repeated implementation of the pattern synthesis technique was used to further improve on the E-plane radiation pattern of Fig. 6.3-2a. Two more pairs of auxiliary beams were scanned to each side of the main beam in two separate steps to reduce the side lobe envelope by 10 dB at $\pm 3.4°$ and $\pm 4.6°$. The results are shown in Fig. 6.3-3. The feed element locations and excitations are given in Table 6.3-1. The actual peak reductions are given in Table 6.3-2.

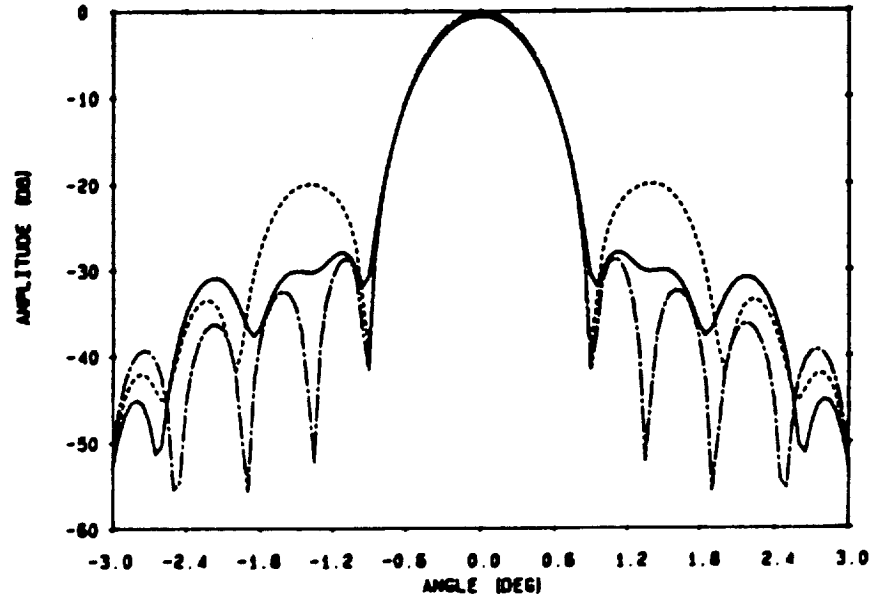

(a)

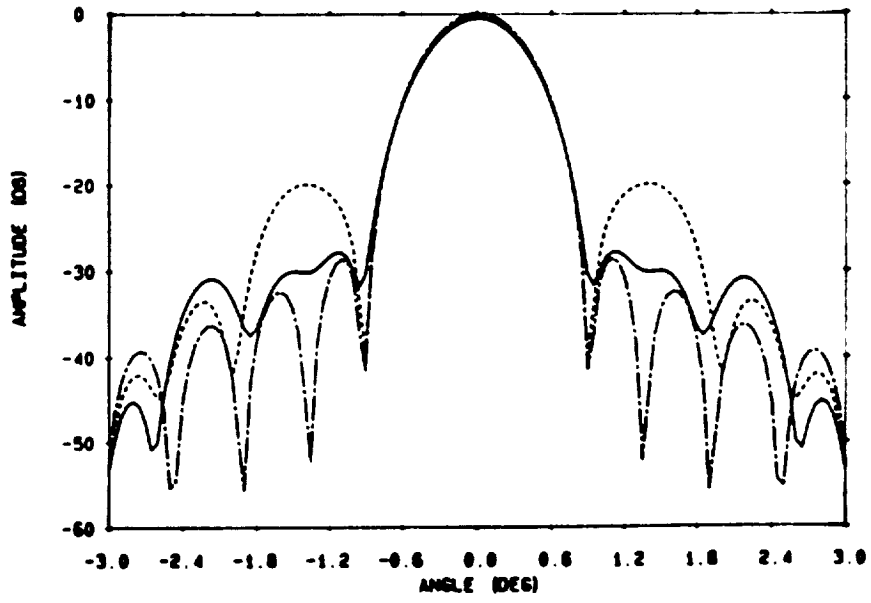

(b)

Figure 6.3-1. Compensation for radial surface distortions in a paraboloidal reflector ($F/D = 0.5$, $D = 100\lambda$)using four feeds displaced symmetrically about the axis. (a) E-plane and the (b) H-plane. The dot-dash curves are the undistorted radiation patterns. The dashed curves are the distorted radiation patterns with a phase error of $\phi_E = 30°$ with one period along the radius. The solid curves are the compensated patterns using displaced feeds to scan the compensation beams.

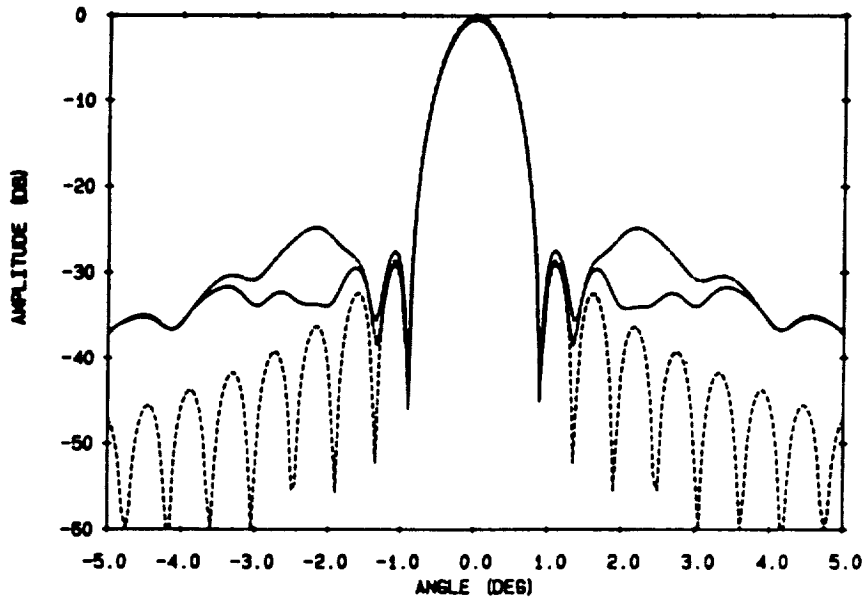

(a)

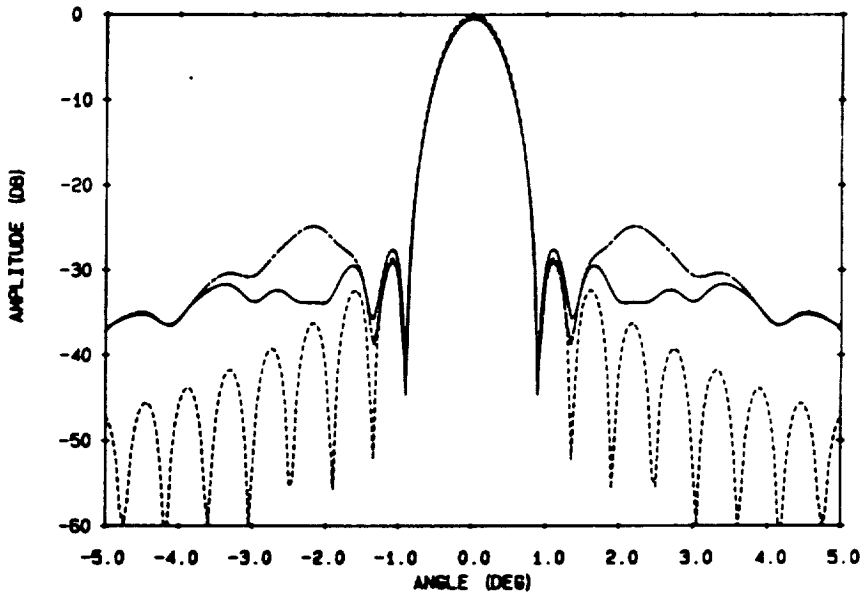

(b)

Figure 6.3-2. Compensation for azimuthal surface distortions in a paraboloidal reflector ($F/D = 0.5$, $D = 100\lambda$)using four feeds displaced symmetrically about the axis. (a) E-plane and the (b) H-plane. The dashed curves are the undistorted radiation patterns. The dot-dash curves are the distorted radiation patterns with a phase error of $\phi_E = 60°$ with 4 periods around the perimeter. The solid curves are the compensated patterns using displaced feeds to scan the compensation beams.

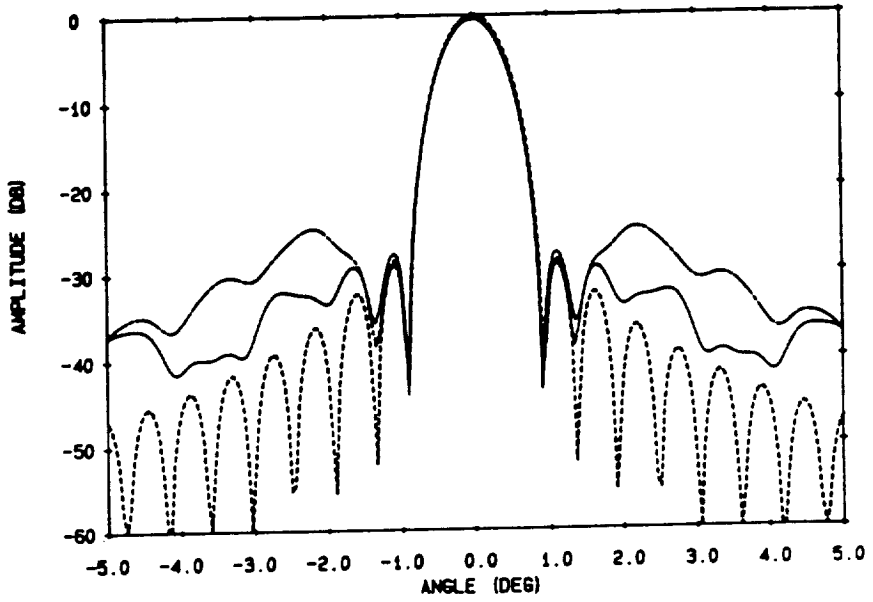

(a)

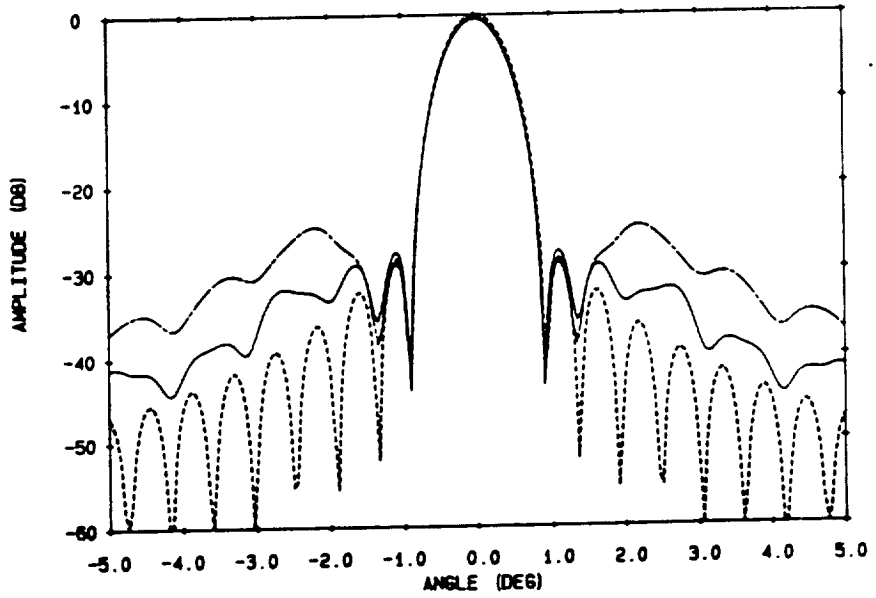

(b)

Figure 6.3-3. Further improvement of the E-plane radiation pattern of Fig. 6.3-2(a). The dashed curves are the undistorted radiation patterns. The dot-dash curves are the distorted radiation patterns. The solid curves are the compensated patterns using displaced feeds to scan the compensation beams. (a) Additional beams are placed at $\pm 3.4°$. (b) Additional beams are placed at $\pm 4.6°$.

Table 6.3-1.

Feed excitations for paraboloidal compensated patterns. The elements are located in the focal plane. The excitations were computed to reduce the peaks of the high side lobes in the principal planes by 10 dB. The two cases are for (a) periodic radial surface errors (Fig. 6.3-1) and (b) periodic azimuthal surface errors (Fig. 6.3-3(b)).

FEED EXCITATION FOR 10 dB REDUCTION - RADIAL ERRORS

FEED	X-COORD (λ)	Y-COORD (λ)	AMPLITUDE (LINEAR)	PHASE (DEG)
1	.0000	.0000	1.0000	.0000
2	1.4400	.0000	.0705	102.3000
3	-1.4400	.0000	.0705	102.3000
4	.0000	1.4400	.0705	102.3000
5	.0000	-1.4400	.0705	102.3000

(a)

FEED EXCITATION FOR 10 dB REDUCTION - AZIMUTHAL ERRORS

FEED	X-COORD (λ)	Y-COORD (λ)	AMPLITUDE (LINEAR)	PHASE (DEG)
1	.0000	.0000	1.0000	.0000
2	2.2000	.0000	.0415	102.3000
3	-2.2000	.0000	.0415	102.3000
4	.0000	2.2000	.0415	102.3000
5	.0000	-2.2000	.0415	102.3000
6	3.4000	.0000	.0180	176.1000
7	-3.4000	.0000	.0180	176.1000
8	4.6000	.0000	.0090	172.4000
9	-4.6000	.0000	.0090	172.4000

Table 6.3-2.

Side lobe peak reduction for compensated paraboloidal patterns. The peak reduction at the location of the correction beam peaks is given in this table. The data are for the distorted reflector patterns in Figs. 6.3-1, 6.3-2, 6.3-3, and 6.3-5.

Figure	Peak Location	SL Peak Reduction
6.3-1	±1.4°	9.6 dB
6.3-2	±2.2°	8.9 dB
6.3-3	±3.4°	8.9 dB
	±4.6°	6.9 dB
6.3-5	±1.4°	8.1 dB

To illustrate the pattern synthesis technique with the repeated implementation using auxiliary feeds, it is useful to view the process from a superposed pattern standpoint. From (4.1-12), the resultant pattern after the three iterations is given by

$$F^{(3)}(u) = F^{(0)} + \sum_{i=1}^{3} \Delta F^{(i)}(u) \quad . \tag{6.3-1}$$

where $F^{(0)}$ is the original distorted pattern and the correction patterns for the three iterations are

$$\Delta F^{(1)}(u) = \sum_{n=1}^{4} a_n^{(1)} \, G_{ref}(u, u_n^{(1)}) \tag{6.3-2}$$

which represents the four correction beams steered to the locations in the principal planes,

$$\Delta F^{(2)}(u) = \sum_{n=1}^{2} a_n^{(2)} \, G_{ref}(u, u_n^{(2)}) \tag{6.3-3}$$

which represents the two correction beams steered to the $\pm 3.4°$ locations in the E-plane, and

$$\Delta F^{(3)}(u) = \sum_{n=1}^{2} a_n^{(3)} \, G_{ref}(u, u_n^{(3)}) \tag{6.3-4}$$

which represents the two correction beams steered to the $\pm 4.6°$ locations in the E-plane.

6.3.2 ELECTRONIC COMPENSATION

Electronic compensation was performed for a distorted paraboloidal reflector with a radial surface error. The feed was a 37-element triangular grid array feed with half-wavelength spacing and 7 elements along the diagonal (see Fig. 6.3-4). The existing computer code RAP, Version 2.0, was used to perform the analysis by repeatedly running the program for each feed and superposing the patterns. The compensation was performed in the principal planes by electronically scanning four correction beams to the desired locations and weighting them to produce a 10 dB reduction in the side lobe amplitude. The method of conjugate field match (ICFM from Sec. 2.3.2) was used to compute the feed excitations required to electronically scan reflector beams to the four locations in the principal planes. RAP was used to compute the far field pattern in the desired direction of scan for each of the individual feeds assuming a smooth reflector. The complex conjugates of the far field pattern values were then used as the excitations for the array feed elements to electronically scan the correction beams (the infinite cylinder electronic compensation case (Sec. 6.2.2) used SCANRAP (Sec. 5.2) and DCFM (Sec. 2.3.2) to compute the element excitations for the correction beams). Each element excitation was then weighted for the compensation. The weighted patterns were then superposed with the original distorted pattern. Figure 6.3-5 shows the results of the electronic scanning. The compensation beams were weighted to reduce the side lobe peaks by 10 dB. The actual peak reductions are given in Table 6.3-2.

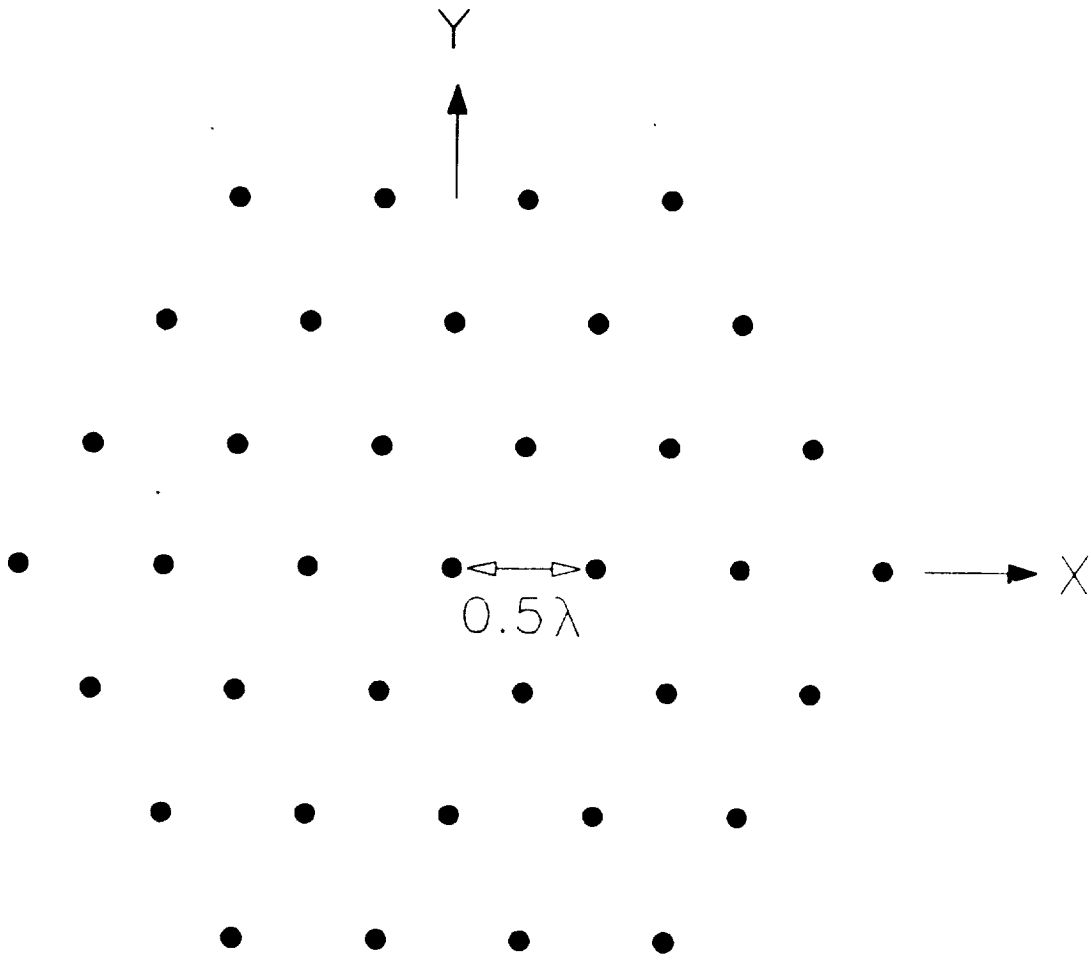

Figure 6.3-4. The geometry for the 37-element triangular grid array feed used to perform electronic compensation with a paraboloidal reflector.

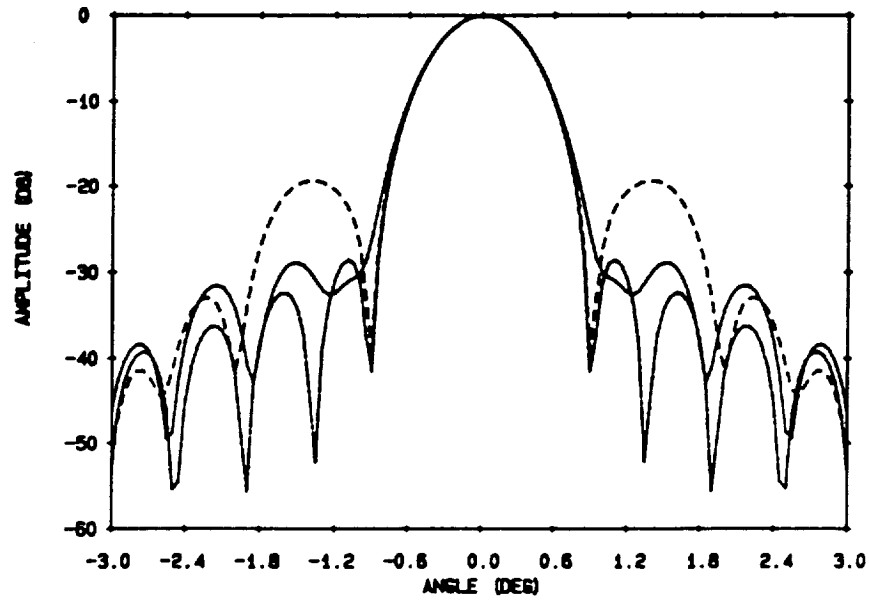

(a)

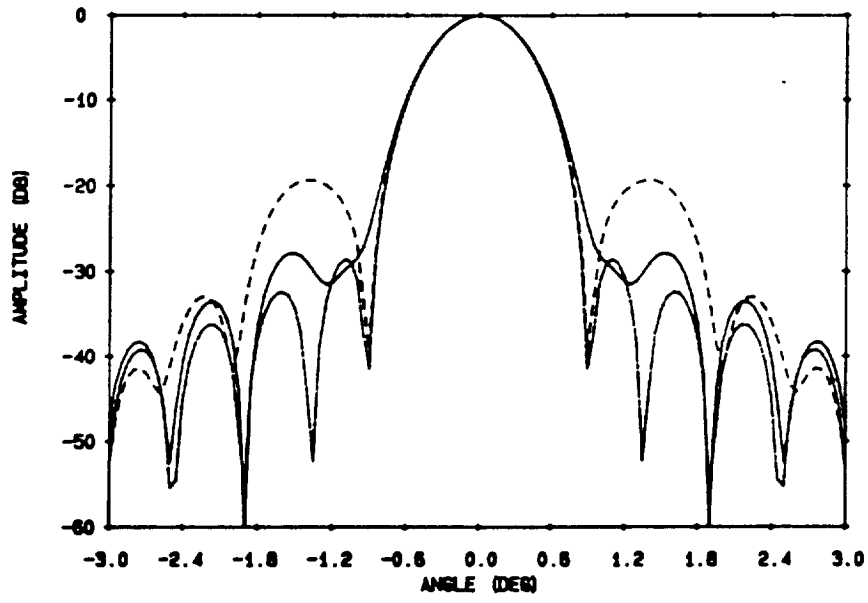

(b)

Figure 6.3-5. Electronic compensation for radial surface distortions in a paraboloidal reflector ($F/D = 0.5$, $D = 100\lambda$)using the 37-element array of Fig. 6.3-4. (a) E-plane and the (b) H-plane. The dot-dash curves are the undistorted radiation patterns. The dashed curves are the distorted radiation patterns with a phase error of $\phi_E = 60°$ with 4 periods around the perimeter. The solid curves are the compensated patterns using displaced feeds to scan the compensation beams.

6.4 DUAL REFLECTOR COMPENSATION ANALYSIS

As discussed in Sec. 3.1, improved scanning is possible using a reflector with a higher F/D. The higher F/D reflector would require a larger support structure for the feed. This motivated investigation into a dual reflector configuration with a higher virtual F/D to extend the compensation range of the pattern synthesis technique.

In this study, the dual reflector analysis is limited to infinite cylindrical problems using the computer code DRAPCA (Sec. 5.3). There were no 3-dimensional dual reflector codes available during this study. The dual reflector is axisymmetric and has a main reflector that is distorted ($F/D = 0.5$, $D = 100\lambda$) with a surface error that produces a sinusoidal phase error in the aperture equivalent current. This is the same type of surface error used in the prime focus infinite cylindrical reflector analysis (eqns. (5.1-21) and (5.1-22)). The subreflector is hyperbolic with eccentricity $e = 3$ and diameter $DSUB = 34\lambda$ (see Fig. 6.1-6).

Figures 6.4-1 through 6.4-3 illustrate an extended range compensation of a high side lobe caused by a distorted reflector. The surface error produces a sinusoidal phase error in the aperture equivalent current with 5 periods along the radius and an amplitude $\phi_E = 20°$. This is the same error that was used for the extended range compensation analysis in Sec. 6.2.1. The distorted pattern is shown in Fig. 6.4-1. The scanned correction beam from a displaced auxiliary feed is shown in Fig. 6.4-2. The correction beam is weighted to reduce the high side lobe by 10 dB and the resultant compensated pattern is shown in Fig. 6.4-3. The feed element locations and excitations are listed in Table 6.4-1.

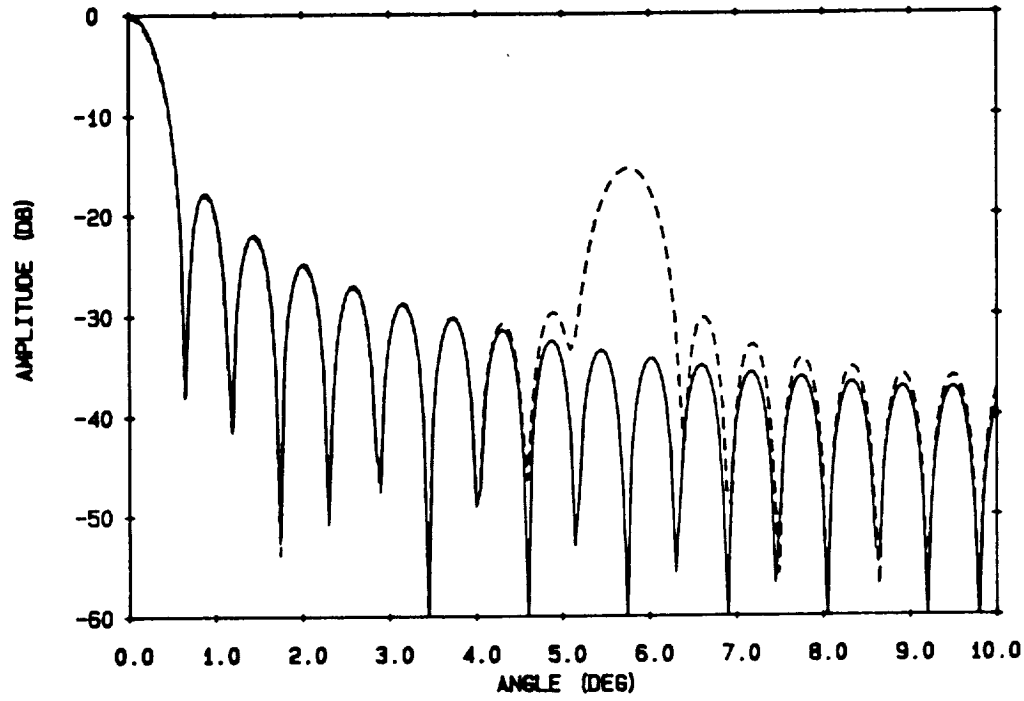

Figure 6.4-1. Unscanned patterns for a dual cylindrical axisymmetric reflector. The $F/D = 0.5$ and $D = 100\lambda$ for the main reflector. The subreflector has $e = 3$ with $DSUB = 34\lambda$. The patterns are for a smooth (solid) and a distorted (dashed) reflector. The distortion gives rise to a sinusoidal phase error in the aperture plane current with 5 periods along the radius and an amplitude of $\phi_E = 20°$.

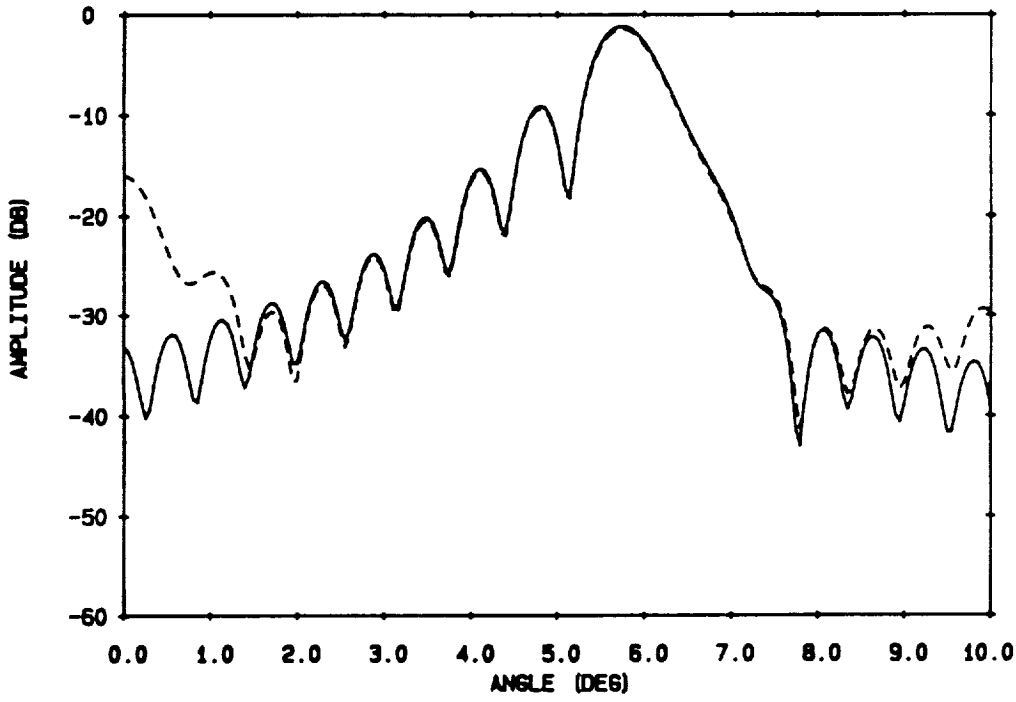

Figure 6.4-2. Scanned patterns for the dual cylindrical axisymmetric reflector. The patterns are for a smooth (solid) and a distorted (dashed) reflector. The scanned patterns are caused by a displaced auxiliary feed. The feed was displaced by 9λ in the minus x-direction and 4.5λ towards the subreflector. The feed was tilted up 10°

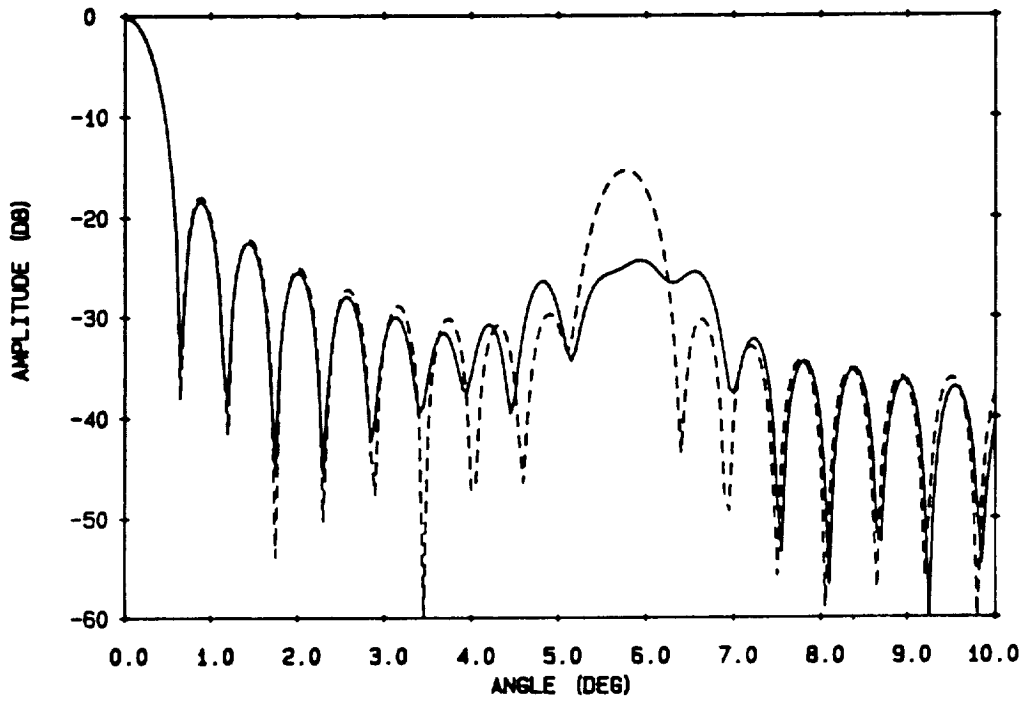

Figure 6.4-3. Compensation for the distorted reflector of. The auxiliary beam of Fig. 6.4-2 was weighted to produce a 10 dB reduction in the side lobe peak.

Table 6.4-1.

Feed excitations for the displaced feed compensated pattern in Fig. 6.4-3. The excitations were computed to reduce the peak of the high side lobe by 10 dB.

FEED EXCITATION FOR 10 dB REDUCTION

FEED	X-COORD (λ)	Z-COORD (λ)	TILT (DEG)	AMPLITUDE (LINEAR)	PHASE (DEG)
1	.0000	26.0000	.0000	1.0000	.0000
2	-9.0000	30.5000	10.0000	.1340	133.4400

The auxiliary feed used for this wide angle compensation was displaced in the x-direction but also had to be moved towards the subreflector (out of the focal plane) and tilted (as opposed to the focal plane displacement for the prime focus reflector with no feed tilt) to achieve an acceptable scanned pattern. This optimized location for the feed was found by trial and error (see Fig. 6.1-8(c)) but follows the general trends in feed locations used to optimize offset dual reflectors. [15, 16]

7.0 SUMMARY AND CONCLUSIONS

The pattern synthesis approach was shown to be a feasible method for electromagnetically compensating for surface errors in large reflectors. The technique was developed using cylindrical reflectors and was extended to paraboloidal reflectors. In this summary we highlight points of note.

Characteristics of previous approaches to electromagnetic compensation:

- They require an accurate model of the surface of the distorted reflector.
- The techniques produce global pattern effects.
- The algorithms are a somewhat blind approach to correcting the patterns (no pattern data).

The pattern synthesis compensation technique is an alternative to those approaches. Characteristics of the pattern synthesis technique:

- It does not require knowledge of the surface.

- It does need radiation pattern data. If surface data are available, however, the pattern data that are required can be computed.

- The pattern synthesis approach uses a localized algorithm in which pattern corrections are directed specifically towards the portions of the pattern requiring improvement. "Customizing" is possible by iterating.

The scan results from Section 6.1 provided important results concerning the auxiliary beams that are used to provide compensation. Results of the scanning study:

- The analysis showed that the scanned beam amplitude and phase of a moderately distorted reflector did not differ significantly from that of the equivalent smooth reflector. This was shown in Table 6.1-1. Therefore, the amplitude and phase of the scanned auxiliary beam is essentially a known quantity.

- The plots provided insight into estimating the angular range over which the pattern synthesis compensation technique is effective (Figs. 6.1-2 and 6.1-3). The limitation is determined by the degradation in the side lobe envelope of the scanned beam.

- Scan range may be increased by using a high F/D reflector (Fig. 6.1-4). This, however, requires a larger feed displacement than with low F/D reflectors.

- The dual reflector scanning analysis showed that for wide angle scanning, a non-planar feed displacement might be required due to the steep phase ramp across the main beam (Fig. 6.1-8).

The compensation results of Sections 6.2, 6.3, and 6.4 showed that:

- The pattern synthesis compensation technique can be used to improve irregularities in the radiation patterns of distorted reflectors without knowledge of the surface distortion.

- The pattern synthesis technique can be implemented by using auxiliary displaced feeds or a fixed array feed.

- The method can be extended to wider angle scans by using a higher F/D reflector (Fig. 6.2-2) or a dual reflector with a higher virtual F/D (Fig. 6.4-3).

- The method for determining the phase of the high side lobes using amplitude measurements only provides a method for overcoming the problem of deciding how to phase the excitation of the auxiliary beam (Fig. 6.2-3).

Recommendations for future efforts to continue the work of this compensation study would be to :

- Implement the method with 3-dimensional dual reflectors.

- Apply the pattern synthesis compensation technique to improve scanned pattern characteristics.

- Investigate hybrid compensation techniques where, for example, CFM would be used as a first iteration to improve the pattern of a distorted reflector. The pattern synthesis technique could be used to further shape the compensated pattern.

- Develop scenarios for obtaining the necessary pattern data.

The pattern synthesis compensation technique was shown by simulation to be a feasible method for pattern correction of the effects of surface errors. Experimental implementation needs to be performed to validate the theory.

8.0 REFERENCES

1. R. J. Acosta, "Compensation of Reflector Surface Distortions Using Conjugate Field Matching," *1986 IEEE AP/S Symposium*, Philadelphia, PA, June, 1986.

2. R. Acosta, A. Zaman, E. Bobinsky, A. R. Cherrette, S. W. Lee, "Case Study of Active Array Feed Compensation with Sidelobe Control for Reflector Surface Distortion," *1988 AP/S International Symposium*, Syracuse, New York, June, 1988.

3. R. N. Assaly, L. J. Ricardi, "A Theoretical Study of a Multi-Element Scanning Feed System for a Parabolic Cylinder," *IEEE Trans. on Ant. and Prop.*, vol. AP-14, no. 5, pp. 601-605, September, 1966.

4. S. J. Blank, W. A. Imbriale, "Array Feed Synthesis for correction of Reflector Distortion and Vernier Beamsteering," *The Telecommunications and Data Acquisition Progress Report 42-86*, April-June, 1986.

5. D. J. Bem, "Electric-Field Distribution in the Focal Region of an Offset Paraboloid," *Proc. IEE*, vol. 116, no. 5, pp. 679-684, May, 1969.

6. M. C. Bailey, "Electronic Compensation for Reflector Surface Distortion to Improve Radiation Pattern Characteristics of Antenna," *NASA Technical Memorandum*, no. 100652, 1988 (yet to be published).

7. S. J. Blank, W. A. Imbriale, "Array Feed Synthesis for Correction of Reflector Distortion and Vernier Beamsteering," *IEEE Trans. on Ant. and Prop.*, vol. AP-36, no. 10, pp. 1351-1358, October, 1988.

8. A. R. Cherrette, P. T. Lam, S. W. Lee, R. Acosta, "Compensation of Distorted Offset Parabolic Reflector Using an Array Feed," *1986 IEEE AP/S Symposium*, Philadelphia, PA, June, 1986.

9. C. Dragone and D. C. Hogg, "Wide-Angle Radiation Due to Rough Phase Fronts," *The Bell System Technical Journal*, vol. 42, no. 5, September, 1963.

10. J. F. Daegele, G. E. Mires, W. V. T. Rusch, R. D. Wanselow, "Grating Lobes of an Umbrella Reflector with Cross-Catenary Tie Supports," *IEEE AP/S Symposium*, June, 1988, Syracuse, pp. 867-870.

11. D. E. N. Davies, "Proposals for Electronic Compensation of Surface Profile Errors in Large Reflectors," *IEE Conference Publication*, no. 21, pp. 80-83, 1986.

12. C. C. Hung, R. Mittra, "Secondary Pattern and Focal Region Distribution of Reflector Antennas Under Wide-Angle Scanning," *IEEE Trans. on Ant. and Prop.*, vol AP-31, no. 5, pp. 756-763, September, 1983.

13. P. W. Hannan, "Microwave Antennas Derived from the Cassegrain Telescope," *IRE Trans. on Ant. and Prop.*, vol. AP-9, pp. 140-153, March, 1961.

14. P. G. Ingerson, W. C. Wong, "The Analysis of Deployable Umbrella Parabolic Reflectors," *IEEE Trans. on Ant. and Prop.*, vol. AP-20, no. 4, pp. 409-414, July, 1972.

15. V. Krichevsky, D. F. DiFonzo, "Optimum Feed Locus for Beam Scanning in the Symmetry Plane of Offset Cassegrain Antennas: Two-Dimensional Case," *Comsat Technical Review*, vol. 11, no. 1, Spring, 1981.

16. V. Krichevsky, D. F. DiFonzo, "Beam Scanning in the Offset Gregorian Antenna," *Comsat Technical Review*, vol. 12, no. 2, Fall, 1982.

17. P. T. Lam, S. W. Lee, D. C. D. Chang, K. C. Lang, "Directivity Optimization of a Reflector Antenna with Cluster Feeds: A Closed-Form Solution," *IEEE Trans. on Ant. and Prop.*, vol. AP-33, no. 11, pp. 1163-1174, November, 1985.

18. D. Lizius, A. D. Olver, "Radiation Characteristics of Offset Radial Rib Reflector Antennas," *ICAP87, IEE Conf. Pub. No. 274*, vol. I, pp. 319-322, 1987.

19. Y. T. Lo, S. W. Lee, *Antenna Handbook*, Van Nostrand Reinhold Company, New York, 1988.

20. Y. T. Lo, "On the Beam Deviation Factor of a Parabolic Reflector," *IRE Trans. on Ant. and Prop.*, vol AP-8, pp. 347-349, May, 1960.

21. S. W. Lee, "A Comparison of Reflector Antenna Designs for Wide-Angle Scanning," oral presentation at the NASA Earth Science Geostationary Platform Technology Workshop held at NASA Langley Research Center, September, 1988.

22. S. LaFleur, "Optical Metrology Technology,", Session at the NASA Earth Science Geostationary Platform Technology Workshop held at NASA Langley Research Center, September, 1988.

23. A. V. Mrstik, P. G. Smith, "Scanning Capabilities of Large Parabolic Cylinder Reflector Antennas with Phased-Array Feeds," *IEEE Trans. on Ant. and Prop.*, vol. AP-29, no. 3, pp. 455-462, May, 1981.

24. A. V. Mrstik, "Scan Limits of Off-Axis Fed Parabolic Reflectors," *IEEE Trans. on Ant. and Prop.*, vol. AP-27, no. 5, pp. 647-651, September, 1979.

25. D. Midgley, "A Theory of Receiving Aerials Applied to the Reradiation of an Electromagnetic Horn," *Proc. IEE*, vol. 108 B, no. 42, pp. 645-650, November, 1961.

26. H. C. Minnett, B. M. Thomas, "Fields in the Image Space of Symmetrical Focusing Reflectors," *Proc IEE*, vol. 115, pp. 1419-1430, October, 1968.

27. A. D. Olver, D. Lizius, "Analysis and Design of Radial Rib Reflector Antennas," *Electromagnetics*, vol. 6, pp. 301-314, 1986.

28. A. Prata, Jr., W. V. T. Rusch, "Radiation Properties of the Optimized Offset-Fed Radial Rib Umbrella Reflector Antenna," *IEEE Trans. on Ant. and Prop.*, vol. AP-35, no. 8, pp. 977-980, August, 1987.

29. J. Ruze, "Antenna Tolerance Theory - A Review," *Proc. IEEE*, vol. 54, pp. 633-640, April, 1966.

30. Y. Rahmat-Samii, "An Efficient Computational Method for Characterizing the Effects of Random Surface Errors on the Average Power Pattern of Reflectors," *IEEE Trans. on Ant. and Prop.*, vol. AP-31, no. 1, pp. 92-98, January, 1983.

31. A. W. Rudge, D. E. N. Davies, "Electronically Controllable Primary Feed for Profile-Error Compensation of Large Parabolic Reflectors," *Proc. IEE*, vol. 117, no. 2, pp. 351-358, February, 1970.

32. W. V. T. Rusch, A. C. Ludwig, "Determination of the Maximum Scan-Gain Contours of a Beam-Scanning Paraboloid and Their Relation to the Petzval Surface," *IEEE Trans. on Ant. and Prop.*, vol. AP-21, no. 2, pp. 141-147, March, 1973.

33. Y. Rahmat-Samii, "A Generalized Reflector/Array Surface Compensation Algorithm for Gain and Sidelobe Control," *1987 IEEE AP/S International Symposium*, Blacksburg, Virginia, June, 1987.

34. Y. Rahmat-Samii, "Effects of Random Errors on Reflector Surface Compensation Using Array Feeds," *National Radio Science Meeting*, January, 1988.

35. Y. Rahmat-Samii, "Large Antenna Measurement and Compensation Techniques," *11th ESTEC Antenna Workshop on Antenna Measurements* , Gothenburg, Sweden, pp. 57-68, June, 1988.

36. Y. Rahmat-Samii, "Spacecraft Antenna Surface-Compensation Techniques," MSAT-X Quarterly, pp. 2-6, 1988.

37. J. Ruze, "Lateral-Feed Displacement in a Paraboloid," *IEEE Trans. on Ant. and Prop.*, vol. AP-13, pp. 660-665, September, 1965.

38. A. W. Rudge, M. J. Withers, "New Technique for Beam Steering with Fixed Parabolic Reflectors," *Proc. IEE*, vol. 118, no. 7, pp. 857-863, July, 1971.

39. A. W. Rudge, K. Milne, A. D. Olver, P. Knight, *The Handbook of Antenna Design*, Vol. 1, Peter Peregrinus Ltd., London, 1982.

40. Y. Rahmat-Samii, V. Galindo-Israel, "Scan Performance of Dual Offset reflector Antennas for Satellite Communications," *Radio Science*, vol. 16, no. 6, pp. 1093-1099, Nov.-Dec., 1981.

41. A. W. Rudge, M. J. Withers, "Design of Flared-Horn Primary Feeds for Parabolic Reflector Antennas," *Proc. IEE*, vol. 117, pp. 1741-1749, September, 1970.

42. Y. Rahmat-Samii, S. W. Lee, "Application of the Conjugate Field Matching Technique to Reflector Antennas - A Critical Review," *URSI Digest*, p. 85, 1984.

43. Y. Rahmat-Samii, "Reflector Antenna Distortion Compensation by Array Feeds: An Experimental Implementation," *Electronics Letters*, vol. 24, no. 18, pp. 1188-1190, September, 1988.

44. Y. Rahmat-Samii, R. L. Cheung, "Nonuniform Sampling Techniques for Antenna Applications," *IEEE Trans. on Ant. and Prop.*, vol. AP-35, no. 3, pp. 268-279, March, 1987.

45. Y. S. Shiffrin, *Stastical Antenna Theory*, Golem Press, Boulder Colorado, 1971.

46. S. H. Stewart, W. L. Stutzman, *Multiple Feed Reflector Antenna Analysis*, Report No. EE SATCOM 86-2, VPI & SU, Center for Innovative Technology, Institute of Information Technology, Grant No. INF-85-013, July 1986.

47. S. Silver, *Microwave Antenna Theory and Design*, Peter Peregrinus Ltd., London, reprinted 1986.

48. W. L. Stutzman, "Synthesis of Shaped Beam Radiation Patterns Using the Iterative Sampling Method," *IEEE Trans. on Ant. and Prop.*, vol. AP-19, no. 1, pp. 36-41, January, 1971.

49. W. L. Stutzman, "Sidelobe Control of Antenna Patterns," *IEEE Trans. on Ant. and Prop.*, vol. AP-20, no. 1, pp. 102-104, January, 1972.

50. W. L. Stutzman, E. L. Coffey, "Radiation Pattern Synthesis of Planar Antennas Using the Iterative Sampling Method," *IEEE Trans. on Ant. and Prop.*, vol. AP-23, no. 6, pp. 764-769, Nov., 1975.

51. W. L. Stutzman, "Shaped-Beam Synthesis of Nonuniformly Spaced Linear Arrays," *IEEE Trans. on Ant. and Prop.*, vol. AP-22, no. 4, pp. 499-501, July, 1972.

52. W. L. Stutzman, S. Stewart, T. Pratt, "Innovative Design of Satellite Earth Terminal Antennas," Virginia Tech EE Dept. SATCOM Report 85-4, submitted to Reynolds Metals and CIT, November, 1985.

53. W. T. Smith, W. L. Stutzman, "A Comparison of Physical Optics and Geometrical Optics Methods for Computation of Reflector Surface Error Effects," Virginia Tech EE Dept. SATCOM Report 87-2, submitted to NASA Langley Research Center, Antennas and Microwave Research Branch, NASA Contract NAS1-18471, December, 1987.

54. S. S. Sandler, "Paraboloidal Reflector Patterns for Off-Axis Feed," *IRE Trans. on Ant. and Prop.*, vol AP-8, pp. 368-379, July, 1960.

55. W. L. Stutzman, G. A. Thiele, *Antenna Theory and Design*, John Wiley & Sons, Inc., New York, 1981.

56. W. M. Truman, C. A. Balanis, "Optimum Design of Horn Feeds for Reflector Antennas," *IEEE Trans. on Ant. and Prop.*, vol. AP-22, pp. 585-586, July, 1974.

57. R. Visocekas, "Non-Cassegranian Indirect System for Aerial Illumination," *Proc. IEE*, vol. 111, no. 12, pp. 1969-1975, December, 1964.

58. W. H. Watson, "The Field Distribution in the Focal Plane of a Paraboloidal Reflector," *IEEE Trans. on Ant. and Prop.*, vol. AP-12, no. 5, pp. 561-569, September, 1964.

59. W. C. Wong, "On the Equivalent Parabola Technique to Predict the Performance Characteristics of a Cassegrain System with an Offset Feed," *IEEE Trans. on Ant. and Prop.*, vol. AP-21, pp. 335-339, May, 1973.

60. P. J. Wood, *Reflector Antenna Analysis and Design*, Peter Peregrinus Ltd, London, 1980.

9. APPENDIX A: EXAMPLE COMPUTER INPUTS AND OUTPUTS

A.1 RAPCA INPUT AND OUTPUT

The Reflector Analysis Program for Cylindrical Antennas (RAPCA) was discussed in Sec. 5.1. In this section, an example is presented to illustrate the use of the program. The example is that of a smooth axisymmetric reflector with diameter $D = 100\lambda$ and $F/D = 0.4$. The feed is a seven element linear array with $\lambda/2$ -spacing located symmetrically about the focus in the focal plane. The feed elements each have a $\cos^q\theta$ field pattern with $q = 3.0$.

It is desired to electronically scan the reflector to $\theta_s = 1.5°$. The excitations for scanning the reflector were computed with the program SCANRAP (see Sec. A.2). The input file for the analysis is shown in Table A.1-1. The file containing the Gauss quadrature zeros and weights is shown in Table A.1-2. The output file for the RAPCA analysis is shown in Table A.1-3.

Table A.1-1.

RAPCA input file for an axisymmetric reflector with a seven element linear array feed. Refer to Tabs. 5.1-1 and 5.1-2 for the format and variable descriptions. The element excitations were computed using SCANRAP (see Sect. A.2). The direction of scan is $\theta_s = 1.5°$.

```
      7
.30003E-01   179.8680    1.5000   40.0000   0.0000
.41161E-01    -1.8880    1.0000   40.0000   0.0000
.51191E-01   177.2723     .5000   40.0000   0.0000
.59228E-01    -2.8996     .0000   40.0000   0.0000
.56011E-01     -.5240    -.5000   40.0000   0.0000
.10000E+01      .0000   -1.0000   40.0000   0.0000
.83784E+00      .3778   -1.5000   40.0000   0.0000
    3.0000       0.00      0.00
 100.0000     0.0000   40.0000
    -5.0        5.0       0.1
      20
```

Table A.1-2.

Input file containing the Gauss quadrature zeros and weights for order 20. The format is outlined in Tab. 5.1-3.

0.9931285992	0.0176140071
0.9639719273	0.0406014298
0.9122344283	0.0626720483
0.8391169718	0.0832767416
0.7463319065	0.1019301198
0.6360536807	0.1181945320
0.5108670020	0.1316886384
0.3737060887	0.1420961093
0.2277858511	0.1491729865
0.0765265211	0.1527533871

Table A.1-3.

RAPCA output file for an axisymmetric reflector with a seven element linear array feed. The direction of scan is $\theta_s = 1.5°$.

RAPCA, VERSION 2.0, SEPTEMBER 12, 1988

**********FEED DATA**********

THERE ARE 7 FEEDS
THEIR EXCITATIONS (LINEAR AND DEGREES)
AND LOCATIONS (WAVELENGTHS) ARE:

FEED	AMP	PHASE	X-COORD	Z-COORD	TFEED
1	.30003E-01	179.8680	1.5000	40.0000	.0000
2	.41161E-01	-1.8880	1.0000	40.0000	.0000
3	.51191E-01	177.2723	.5000	40.0000	.0000
4	.59228E-01	-2.8996	.0000	40.0000	.0000
5	.56011E-01	-.5240	-.5000	40.0000	.0000
6	.10000E+01	.0000	-1.0000	40.0000	.0000
7	.83784E+00	.3778	-1.5000	40.0000	.0000

THE FEED COSINE EXPONENT = 3.0000
THE MAX PHASE ERROR = .0000 DEGREES
THE NUMBER OF PERIODS OF THE PHASE ERROR = .0000

**********REFLECTOR DATA**********

REFLECTOR DIAMETER (WAVELENGTHS) = 100.0000
REFLECTOR OFFSET (WAVELENGTHS) = .0000
REFLECTOR FOCAL LENGTH (WAVELENGTHS) = 40.0000
REFLECTOR F/DP = .40000

ILLUMINATION AT THE TOP OF THE REFLECTOR (DB) = -24.7339
ILLUMINATION AT THE BOTTOM OF THE REFLECTOR (DB) = -24.3993

**********OUTPUT PATTERN**********

THETA MIN = -5.0000
THETA MAX = 5.0000
THETA INC = .1000

Table A.1-3 (cont.).

**********INTEGRATION DATA**********

THE QUADRATURE IS ORDER 20

ZERO	WEIGHT
-.99313E+00	.17614E-01
-.96397E+00	.40601E-01
-.91223E+00	.62672E-01
-.83912E+00	.83277E-01
-.74633E+00	.10193E+00
-.63605E+00	.11819E+00
-.51087E+00	.13169E+00
-.37371E+00	.14210E+00
-.22779E+00	.14917E+00
-.76527E-01	.15275E+00
.76527E-01	.15275E+00
.22779E+00	.14917E+00
.37371E+00	.14210E+00
.51087E+00	.13169E+00
.63605E+00	.11819E+00
.74633E+00	.10193E+00
.83912E+00	.83277E-01
.91223E+00	.62672E-01
.96397E+00	.40601E-01
.99313E+00	.17614E-01

THE MAXIMUM PATTERN VALUE IS .41827E+00 AT 1.5000 DEGREES

ANGLE (DEG)	MAGNITUDE (DB)	PHASE(DEG)
-5.000	-50.7742	161.4400
-4.900	-47.0391	160.1114
-4.800	-46.5008	159.5966
-4.700	-48.8605	158.7413
-4.600	-57.3711	153.5934
-4.500	-56.8248	-10.0209
-4.400	-48.1858	-14.8784

Table A.1-3 (cont.).

-4.300	-45.5103	-15.7190
-4.200	-45.7109	-16.2188
-4.100	-49.1133	-17.4229
-4.000	-62.7939	-31.1731
-3.900	-52.2489	171.4322
-3.800	-46.1372	168.9309
-3.700	-44.4495	168.3735
-3.600	-45.7089	168.0314
-3.500	-51.6651	166.8671
-3.400	-59.1566	-5.0962
-3.300	-46.1309	-9.4387
-3.200	-42.1262	-10.0111
-3.100	-40.9736	-10.5191
-3.000	-41.9847	-11.5695
-2.900	-45.6230	-14.6369
-2.800	-54.8777	-31.8958
-2.700	-55.6846	-156.5971
-2.600	-50.9732	-168.5477
-2.500	-56.0384	-151.7078
-2.400	-50.4225	-23.2950
-2.300	-40.7853	-11.2526
-2.200	-35.9868	-8.5411
-2.100	-33.4517	-7.4036
-2.000	-32.5962	-6.8187
-1.900	-33.4387	-6.5476
-1.800	-36.7134	-6.6495
-1.700	-47.0390	-8.8907
-1.600	-42.9594	176.7147
-1.500	-35.1966	175.3999
-1.400	-32.4636	174.9644
-1.300	-32.1787	174.4784
-1.200	-34.2833	173.5245
-1.100	-40.8624	170.0813
-1.000	-48.2606	9.4087
-.900	-36.0942	-1.5671
-.800	-32.6204	-3.4681
-.700	-32.2052	-4.9715
-.600	-34.7020	-7.5061
-.500	-43.7974	-19.5694
-.400	-40.9616	-170.9099
-.300	-33.0929	-179.2939
-.200	-30.6321	177.9581
-.100	-31.2431	175.2531
.000	-36.2634	168.3990
.100	-44.3099	32.5350
.200	-31.0636	5.5284

Table A.1-3 (cont.).

.300	-26.9084	1.8071
.400	-26.4214	-.2921
.500	-31.3524	-3.7723
.600	-32.5226	-173.9667
.700	-19.4570	-179.1498
.800	-13.1654	179.5663
.900	-8.9631	178.7519
1.000	-5.9232	178.0840
1.100	-3.6844	177.4714
1.200	-2.0636	176.8753
1.300	-.9527	176.2746
1.400	-.2815	175.6563
1.500	.0000	175.0112
1.600	-.0698	174.3334
1.700	-.4583	173.6198
1.800	-1.1352	172.8708
1.900	-2.0696	172.0919
2.000	-3.2284	171.2945
2.100	-4.5757	170.4970
2.200	-6.0750	169.7234
2.300	-7.6927	168.9980
2.400	-9.4049	168.3375
2.500	-11.2056	167.7404
2.600	-13.1118	167.1799
2.700	-15.1655	166.6032
2.800	-17.4292	165.9359
2.900	-19.9777	165.0876
3.000	-22.8822	163.9546
3.100	-26.1829	162.4335
3.200	-29.8255	160.4955
3.300	-33.5347	158.4514
3.400	-36.6811	157.3768
3.500	-38.5219	158.4827
3.600	-39.0151	161.0152
3.700	-38.9999	163.1452
3.800	-39.3983	164.2240
3.900	-40.8872	164.3876
4.000	-44.2708	163.6748
4.100	-52.1304	160.4922
4.200	-58.9859	-4.9786
4.300	-48.4672	-13.0130
4.400	-46.1446	-14.6340
4.500	-47.1148	-15.5939
4.600	-52.0485	-16.1098
4.700	-76.4941	148.1520
4.800	-51.3888	160.6499
4.900	-47.1369	160.1774
5.000	-46.4112	159.5018

A.2 SCANRAP INPUT AND OUTPUT

The SCANned Reflector Analysis Program (SCANRAP) was discussed in Sec. 5.2. SCANRAP is used to compute the excitations for the array feed elements for the axisymmetric reflector example in Sec. A.1. It is desired to electronically scan the reflector to $\theta_s = 1.5°$. The reflector is a smooth axisymmetric reflector with diameter $D = 100\lambda$ and $F/D = 0.4$. The feed is a seven element linear array with $\lambda/2$-spacing located symmetrically about the focus in the focal plane. The feed elements have $\cos^q\theta$ field pattern with $q = 3.0$. The input file for the analysis is shown in Table A.2-1. The output file for the SCANRAP analysis is shown in Table A.2-2.

Table A.2-1.

SCANRAP input file for an axisymmetric reflector with a seven element linear array feed. Refer to Tabs. 5.2-1 and 5.2-2 for the format and variable descriptions. The direction of scan is $\theta_s = 1.5°$.

```
      7
 1.5000      40.0000      0.0000
 1.0000      40.0000      0.0000
  .5000      40.0000      0.0000
  .0000      40.0000      0.0000
 -.5000      40.0000      0.0000
-1.0000      40.0000      0.0000
-1.5000      40.0000      0.0000
 3.0000
100.0000      0.0000     40.0000
  1.50
    20
```

Table A.2-2.

SCANRAP output file for an axisymmetric reflector with a seven element linear array feed. The direction of scan is $\theta_s = 1.5°$.

SCANRAP, VERSION 1.0, NOVEMBER 17, 1988

**********FEED DATA**********

THERE ARE 7 FEEDS

FEED	X-COORD	Z-COORD	TFEED
1	1.5000	40.0000	.0000
2	1.0000	40.0000	.0000
3	.5000	40.0000	.0000
4	.0000	40.0000	.0000
5	-.5000	40.0000	.0000
6	-1.0000	40.0000	.0000
7	-1.5000	40.0000	.0000

THE FEED COSINE EXPONENT = 3.0000

**********REFLECTOR DATA**********

REFLECTOR DIAMETER (WAVELENGTHS) = 100.0000
REFLECTOR OFFSET (WAVELENGTHS) = .0000
REFLECTOR FOCAL LENGTH (WAVELENGTHS) = 40.0000
REFLECTOR F/DP = .40000

**********SCAN ANGLE**********

THE SCAN ANGLE (DEG) = 1.5000

Table A.2-2 (cont.).

**********INTEGRATION DATA**********

THE QUADRATURE IS ORDER 20

ZERO	WEIGHT
-.99313E+00	.17614E-01
-.96397E+00	.40601E-01
-.91223E+00	.62672E-01
-.83912E+00	.83277E-01
-.74633E+00	.10193E+00
-.63605E+00	.11819E+00
-.51087E+00	.13169E+00
-.37371E+00	.14210E+00
-.22779E+00	.14917E+00
-.76527E-01	.15275E+00
.76527E-01	.15275E+00
.22779E+00	.14917E+00
.37371E+00	.14210E+00
.51087E+00	.13169E+00
.63605E+00	.11819E+00
.74633E+00	.10193E+00
.83912E+00	.83277E-01
.91223E+00	.62672E-01
.96397E+00	.40601E-01
.99313E+00	.17614E-01

**********OUTPUT**********

FEED FEED	EXCITATION AMP (LINEAR)	PHASE (DEG)	X-COORD	Z-COORD	TFEED
1	.30003E-01	179.8680	1.5000	40.0000	.0000
2	.41161E-01	-1.8880	1.0000	40.0000	.0000
3	.51191E-01	177.2723	.5000	40.0000	.0000
4	.59228E-01	-2.8996	.0000	40.0000	.0000
5	.56011E-01	-.5240	-.5000	40.0000	.0000
6	.10000E+01	.0000	-1.0000	40.0000	.0000
7	.83784E+00	.3778	-1.5000	40.0000	.0000

A.3 DRAPCA INPUT AND OUTPUT

The Dual Reflector Analysis Program for Cylindrical Antennas (DRAPCA) was discussed in Sec. 5.3. An example of its use is presented in this section. DRAPCA is used to compute a pattern for an axisymmetric dual cylindrical reflector. The geometry for the reflector is shown in Fig. 6.1-6. The pattern is scanned by displacing the feed from the focus. This example is the scanned pattern shown in Fig. 6.4-2 (smooth reflector).

The feed is displaced by 9λ in the minus x-direction and by 4.5λ in the plus z-direction. The feed is tilted up by 10°. The input file for the analysis is shown in Table A.3-1. The output file for the DRAPCA analysis is shown in Table A.3-2.

Table A.3-1.

DRAPCA input file for the axisymmetric dual cylindrical reflector of Fig. 6.1-6. Refer to Tabs. 5.3-1 and 5.3-2 for the format and variable descriptions. The direction of scan is $\theta_s = 5.7°$.

```
0
1                2
1.0000      0.0000      -9.0000      30.5000      10.0000
10.0000     0.0000       0.0000
100.0000    0.0000      50.0000
34.0000     3.0000      24.0000       0.0000       0.0000
0.0000     10.0000       0.1000
20
```

Table A.3-2.

DRAPCA output file for the axisymmetric dual cylindrical reflector of Fig. 6.1-6. The direction of scan is $\theta_s = 5.7°$.

```
 DRAPCA, VERSION 1.0, JANUARY 21,1990

 **********FEED DATA**********

 THERE ARE  1 FEEDS

 THE FEED LOCATIONS ARE IN THE PRIMED COORDINATE      SYSTEM

 THEIR EXCITATIONS (LINEAR AND DEGREES)
   AND LOCATIONS (WAVELENGTHS) ARE:

FEED        AMP      PHASE  X-COORD  Z-COORD     TFEED

  1       1.0000      .0000   -9.0000   30.5000   10.0000

 THE FEED COSINE EXPONENT =    10.0000
 THE MAX PHASE ERROR =      .0000 DEGREES
 THE NUMBER OF PERIODS OF THE PHASE ERROR =      .0000

 **********MAIN REFLECTOR DATA**********

 MAIN REFLECTOR DIAMETER (WAVELENGTHS) =   100.0000
 MAIN REFLECTOR OFFSET (WAVELENGTHS) =      .0000
 MAIN REFLECTOR FOCAL LENGTH (WAVELENGTHS) =    50.0000
 MAIN REFLECTOR F/DP =     .50000

 ILLUMINATION AT THE TOP OF THE MAIN REFLECTOR (DB) =   -12.7122
  ILLUMINATION AT THE BOTTOM OF THE MAIN REFLECTOR (DB) =
-5.8027

 **********SUBREFLECTOR DATA**********

 SUBREFLECTOR DIAMETER (WAVELENGTHS) =    34.0000
 SUBREFLECTOR OFFSET (WAVELENGTHS) =      .0000
 FEED PHASE CENTER OFFSET (WAVELENGTHS) =      .0000
 INTERFOCAL DISTANCE (WAVELENGTHS) =    24.0000
 SUBREFLECTOR ECCENTRICITY =     3.0000
 EQUIVALENT VIRTUAL FOCAL LENGTH (WAVELENGTHS) =   100.0000
 EQUIVALENT VIRTUAL F/DP =     1.0000
 INTERFOCAL AXIS TILT (DEGREES) =      .0000
 F1 COORDINATE SYSTEM TILT (DEGREES) =      .0000
 ILLUMINATION AT THE TOP OF THE SUBREFLECTOR (DB) =   -17.3176
 ILLUMINATION AT THE BOTTOM OF THE SUBREFLECTOR (DB) =    -5.8308
```

Table A.3-2. (cont.)

**********OUTPUT PATTERN**********

THETA MIN = .0000
THETA MAX = 10.0000
THETA INC = .1000

**********INTEGRATION DATA**********

THE QUADRATURE IS ORDER 20

ZERO	WEIGHT
-.99313E+00	.17614E-01
-.96397E+00	.40601E-01
-.91223E+00	.62672E-01
-.83912E+00	.83277E-01
-.74633E+00	.10193E+00
-.63605E+00	.11819E+00
-.51087E+00	.13169E+00
-.37371E+00	.14210E+00
-.22779E+00	.14917E+00
-.76527E-01	.15275E+00
.76527E-01	.15275E+00
.22779E+00	.14917E+00
.37371E+00	.14210E+00
.51087E+00	.13169E+00
.63605E+00	.11819E+00
.74633E+00	.10193E+00
.83912E+00	.83277E-01
.91223E+00	.62672E-01
.96397E+00	.40601E-01
.99313E+00	.17614E-01

THE MAXIMUM PATTERN VALUE IS .28422E+00 AT 5.7000 DEGREES

ANGLE (DEG)	MAGNITUDE (DB)	PHASE(DEG)
.000	-31.9438	-18.9909
.100	-33.4471	-34.2327
.200	-37.3744	-65.3321
.300	-38.1297	-133.8692
.400	-33.4901	-172.6599
.500	-31.0264	170.3503
.600	-30.8535	157.1399
.700	-32.9799	139.5007
.800	-37.1144	98.2908
.900	-35.4026	31.0677
1.000	-31.1502	1.4702

Table A.3-2. (cont.)

1.100	-29.3102	-13.7232
1.200	-29.6899	-27.4507
1.300	-32.4222	-48.7230
1.400	-35.9800	-101.7306
1.500	-32.3844	-160.1923
1.600	-28.7308	176.2502
1.700	-27.4486	162.0109
1.800	-28.3462	147.2063
1.900	-31.5846	120.7678
2.000	-33.6274	58.4323
2.100	-29.1714	11.3999
2.200	-26.1020	-8.4003
2.300	-25.2881	-22.2649
2.400	-26.6288	-38.6047
2.500	-30.1238	-71.3956
2.600	-30.2574	-136.9776
2.700	-25.6991	-174.6383
2.800	-23.0753	167.8565
2.900	-22.5825	154.1416
3.000	-24.2049	136.4060
3.100	-27.6440	98.2948
3.200	-26.3505	34.0248
3.300	-21.8655	1.8649
3.400	-19.4118	-14.1400
3.500	-18.9634	-27.2309
3.600	-20.5522	-44.4493
3.700	-23.9544	-81.8968
3.800	-22.5893	-146.4935
3.900	-17.8227	-178.4675
4.000	-15.0170	166.3728
4.100	-14.0875	155.0060
4.200	-14.9926	142.0730
4.300	-18.0966	118.1600
4.400	-20.3602	56.2266
4.500	-15.0781	6.9875
4.600	-10.8693	-11.2422
4.700	-8.5954	-21.5467
4.800	-7.8371	-29.8961
4.900	-8.5675	-38.9930
5.000	-11.2262	-53.3059
5.100	-16.3169	-93.7612
5.200	-13.5250	-170.5952
5.300	-7.5566	163.0560
5.400	-3.9387	151.9990
5.500	-1.7509	144.7387

Table A.3-2. (cont.)

5.600	-.5155	138.7667
5.700	.0000	133.2159
5.800	-.0731	127.6729
5.900	-.6467	121.8964
6.000	-1.6477	115.7486
6.100	-3.0013	109.2123
6.200	-4.6215	102.4612
6.300	-6.4116	95.9413
6.400	-8.2733	90.3684
6.500	-10.1181	86.5111
6.600	-11.8727	84.7364
6.700	-13.5000	84.5438
6.800	-15.0529	84.5123
6.900	-16.7036	82.7866
7.000	-18.6791	77.4579
7.100	-21.1105	66.2449
7.200	-23.7309	46.3416
7.300	-25.5969	18.4428
7.400	-26.3587	-8.3027
7.500	-27.2863	-28.3221
7.600	-29.7146	-44.7486
7.700	-35.2893	-67.2161
7.800	-41.8928	-160.7856
7.900	-33.9064	144.0989
8.000	-30.7186	128.2787
8.100	-30.4240	115.9502
8.200	-32.5034	99.7713
8.300	-36.8574	64.4989
8.400	-36.9405	-3.7418
8.500	-32.8848	-38.7310
8.600	-31.0580	-55.3581
8.700	-31.4204	-68.8361
8.800	-34.0282	-86.7004
8.900	-38.7078	-127.6477
9.000	-37.6045	163.5279
9.100	-33.6837	132.8955
9.200	-32.1658	117.3623
9.300	-32.8236	103.8998
9.400	-35.7792	84.7363
9.500	-40.4364	38.0176
9.600	-38.2254	-27.7945
9.700	-34.5773	-54.5917
9.800	-33.3671	-68.9905
9.900	-34.3358	-82.0178
10.000	-37.7479	-101.7240